Systematic studies on the thermodynamic properties of gas hydrates and their formation/dissociation/transformation behaviors

---

Dissertation
zur Erlangung des akademischen Grades
"doctor rerum naturalium" (Dr. rer. nat.)
in der Wissenschaftsdisziplin "Geochemie"

eingereicht an der
Mathematisch-Naturwissenschaftlichen Fakultät
Institut für Geowissenschaften
der Universität Potsdam

Mengdi Pan

Disputation on
10th June 2022

Published online on the
Publication Server of the University of Potsdam:
https://doi.org/10.25932/publishup-55476
https://nbn-resolving.org/urn:nbn:de:kobv:517-opus4-554760

Betreuer

Prof. Dr. Dirk Wagner
Deutsches GeoForschungsZentrum GFZ
Department Geochemie
Sektion Geomikrobiologie
und
Universität Potsdam
Mathematisch-Naturwissenschaftliche Fakultät
Institut für Geowissenschaften

apl. Prof. Dr. Judith M. Schicks
Deutsches GeoForschungsZentrum GFZ
Department Geochemie
Sektion Anorganische und Isotopengeochemie
und
Universität Potsdam
Mathematisch-Naturwissenschaftliche Fakultät
Institut für Chemie

Gutachter

apl. Prof. Dr. Judith M. Schicks

Prof. Dr. Ilko Bald
Universität Potsdam
Mathematisch-Naturwissenschaftliche Fakultät
Institut für Chemie

Prof. Dr. Bertrand Chazallon
Université de Lille
Faculté des sciences et technologies
Département Physique

Selbstständigkeitserklärung

Hiermit erkläre ich, Mengdi Pan, dass ich als Autorin der vorliegenden Dissertation mit dem Titel "*Systematic studies on the thermodynamic properties of gas hydrates and their formation/dissociation/transformation behaviors*", die Arbeit selbstständig und ohne unerlaubte Hilfe angefertigt habe.

Die eingereichte Arbeit oder wesentliche Teile derselben in keinem anderen Verfahren zur Erlangung eines akademischen Grades vorgelegt worden sind. Bei der Anfertigung der Dissertation die Grundsätze zur Sicherung guter wissenschaftlicher Praxis der DFG eingehalten wurden. Ich versichere, dass ich keine anderen als die angegebenen Quellen oder Hilfsmittel verwendet zu haben. Alle Ausführungen, die anderen Schriften wörtlich oder inhaltlich entnommenen wurden, sind als solche kenntlich gemacht.

_____

Abstract

Gas hydrates are ice-like crystalline compounds made of water cavities that retain various types of guest molecules. Natural gas hydrates are CH_4-rich but also contain higher hydrocarbons as well as CO_2, H_2S, etc. They are highly dependent of local pressure and temperature conditions. Considering the high energy content, natural gas hydrates are artificially dissociated for the production of methane gas. Besides, they may also dissociate in response to global warming. It is therefore crucial to investigate the hydrate nucleation and growth process at a molecular level. The understanding of how guest molecules in the hydrate cavities respond to warming climate or gas injection is also of great importance.

This thesis is concerned with a systematic investigation of simple and mixed gas hydrates at conditions relevant to the natural hydrate reservoir in Qilian Mountain permafrost, China. A high-pressure cell that integrated into the confocal Raman spectroscopy ensured a precise and continuous characterization of the hydrate phase during formation/dissociation/transformation processes with a high special and spectral resolution. By applying laboratory experiments, the formation of mixed gas hydrates containing other hydrocarbons besides methane was simulated in consideration of the effects from gas supply conditions and sediments. The results revealed a preferential enclathration of different guest molecules in hydrate cavities and further refute the common hypothesis of the coexistence of hydrate phases due to a changing feed gas phase. However, the presence of specific minerals and organic compounds in sediments may have significant impacts on the coexisting solid phases. With regard to the dissociation, the formation damage caused by fines mobilization and migration during hydrate decomposition was reported for the first time, illustrating the complex interactions between fine grains and hydrate particles. Gas hydrates, starting from simple CH_4 hydrates to binary CH_4—C_3H_8 hydrates and multi-component mixed hydrates were decomposed by thermal stimulation mimicking global warming. The mechanisms of guest substitution in hydrate structures were studied through the experimental data obtained from CH_4—CO_2, CH_4—mixed gas hydrates and mixed gas hydrates—CO_2 systems. For the first time, a second transformation behavior was documented during the transformation process from CH_4 hydrates to CO_2-rich mixed hydrates. Most of the crystals grew or maintained when exposed to CO_2 gas while some others decreased in sizes and even disappeared over time. The highlight of the two last experimental simulations was to visualize and characterize the hydrate crystals which were at

different structural transition stages. These experimental simulations enhanced our knowledge about the mixed gas hydrates in natural reservoirs and improved our capability to assess the response to global warming.

Kurzfassung

Gashydrate sind eisähnliche, kristalline Verbindungen bestehend aus Wasserkäfigen, in denen verschiedene Arten von Gastmolekülen eingeschlossen sind. Natürliche Gashydrate sind CH_4-reich, enthalten aber auch höhere Kohlenwasserstoffe sowie CO_2, H_2S usw. Sie sind stark von den lokalen Druck- und Temperaturbedingungen abhängig. Aufgrund ihres hohen Energiegehalts werden natürliche Gashydrate zur Produktion von Methangas kontrolliert zersetzt. Sie können sich aber auch als Reaktion auf die globale Erwärmung zersetzen. Daher ist es von entscheidender Bedeutung, den Hydratnukleation und des Wachstumsprozesses auf molekularer Ebene zu verstehen. Es ist auch von großer Bedeutung zu klären, wie die Gastmoleküle in den Hydratkäftigen auf die Erderwärmung oder die Gasinjektion antworten.

Diese Arbeit beschäftigt sich mit einer systematischen Untersuchung von einfachen und gemischten Gashydraten unter Bedingungen, die für die natürlichen Hydratvorkommen im Qilian Mountain Permafrost, China, relevant sind. Eine in die konfokale Raman-Spektroskopie integrierte Hochdruckzelle gewährleistet eine präzise und kontinuierliche Charakterisierung der Hydratphase während des Bildungs-/Dissoziations-/Umwandlungsprozesses mit hoher örtlicher und spektraler Auflösung. Anhand von Laborversuchen wurde der Entstehungsprozess von gemischten Gashydraten unter Berücksichtigung der Auswirkungen unterschiedliches Gaszufuhr und Sedimenten simuliert. Die Ergebnisse zeigten eine bevorzugte Einlagerung verschiedener Gastmoleküle in die Hydratkäfige und widerlegen die gängige Hypothese der Bildung koexistierender Hydratphasen aufgrund einer sich ändernden Gasphase. Das Vorhandensein bestimmter Mineralien und organischer Verbindungen in Sedimenten kann ebenfalls erhebliche Auswirkungen auf die koexistierenden festen Phasen haben. Bezüglich der Hydratzersetzung konnte im Rahmen dieser Arbeit erstmals über die Formationsschädigung durch Feinkornmobilisierung und -migration beim Hydratabbau berichtet werden, was die komplexen Wechselwirkungen zwischen feinen Sedimentkörnern und Hydratpartikeln verdeutlicht. Gashydrate, angefangen von einfachen CH_4-Hydraten über binäre CH_4-C_3H_8-Hydrate bis hin zu Mehrkomponenten-Mischhydraten, wurden durch

thermische Stimulation zersetzt, um die Reaktion auf die globale Erwärmung nachzuahmen. Die Mechanismen der Substitution der Gasmoleküle in Hydratstrukturen wurden anhand der experimentellen Daten von CH_4-CO_2-, CH_4-Mischgashydraten und Mischgashydraten-CO_2-Systemen untersucht. Erstmals wurde ein zweites Umwandlungsverhalten während des Umwandlungsprozesses von CH_4-Hydraten zu CO_2-reichen Mischhydraten dokumentiert. In den meisten Fällen wird das Modell des Schrumpfenden Kerns (Shrinking-core-model) unterstützt, während in einigen anderen Fällen die Kristalle mit konstanter Geschwindigkeit umwandelten. Der Höhepunkt der beiden letzten experimentellen Simulationen war die Visualisierung und Charakterisierung von Hydratkristallen, die sich in verschiedenen strukturellen Übergangsstadien befanden. Diese experimentellen Simulationen erweiterten unser Wissen über gemischte Gashydrate in natürlichen Lagerstätten und verbesserten unsere Fähigkeit, die Reaktion auf die globale Erwärmung zu bewerten.

List of figures

List of tables

Nomenclature

α	hydrate conversion ratio
α^*	hydrate conversion ratio after surface nucleation process
Xa	molar fraction of component a
Aa	area of the Raman band of component a
b	stoichiometric factor for component B
d	pore diameter
F	number of degrees of freedom
ΔG	Gibbs free energy change
K	number of components
k	reaction rate constant
n	Avrami exponent
n_i	number of edges in polyhedron
n_w	number of water molecules
m_i	number of faces with n_i edges in polyhedron
p	pressure
γ	surface tension and
θ	angle
P	number of phases
r	radius
T	temperature
t	time
t^*	time taken for the surface nucleation process
V	volume
μ_g^W	chemical potential of the gas molecules in aqueous solution
μ_w^W	chemical potential of the water molecules in aqueous solution
μ_h^W	chemical potential of the hydrate in the aqueous solution
μ_h^H	chemical potential of the hydrate in the hydrate phase
$\Delta\mu_h$	difference of chemical potential
a	Raman scattering cross-section factor of component

Table of Contents

Chapter 1

1 Introduction

1.1 Introduction on gas hydrates

The first discovery of gas hydrates can be traced back to early 19th century when the British chemist Sir Humphrey Davy performed experiments on the chlorine-water system and accidentally identified chlorine atoms encased in ice crystals [1]. For the following 120 years, gas hydrates were remained merely as a laboratory curiosity. The importance of gas hydrate research was boosted in the 1930's by the recognition of the modern natural gas industry where gas hydrates were responsible for the ice-like plugs formed in gas pipelines at temperatures above the ice point [2]. It was from this point that the importance of gas hydrates to industry was marked. Thereafter, researches on gas hydrates moved to the focus of preventing the destructions of pipelines by gas hydrate plugs and extensive costs caused by blockages. Later in 1960's, Makogon discovered the existence of natural gas hydrates in permafrost regions of Siberia [3]. More attention has been attracted to understand the conditions of gas hydrate existence and further reveal more hydrate deposits, triggering a new era of gas hydrate research.

Gas hydrates are non-stoichiometric crystalline inclusion compounds where the hydrogen-bonded water molecules form a three-dimensional framework of water cavities. The cavities are stabilized by hosting guest molecules of suitable sizes and shapes [4]. Hence gas hydrates fall under the clathrates group of solid gas-water mixtures from a chemical point of view.

For the formation of hydrate structure, each water molecule aligns in a regular orientation and is attached to four other water molecules via hydrogen bonds. The central molecule is tetrahedrally surrounded by the four neighboring ones, forming the smallest unit cell from which the host network of the hydrate structure is generated [5]. There are altogether five different types of polyhedrons formed by hydrogen-bonded water molecules as shown in Figure 1.1 with properties tabulated in Table 1.1 [5]. The nomenclature description of these polyhedrons (n_i^{mi}) is suggested by Jeffrey (1984), where n_i is the number of

edges and m_i is the number of faces with n_i edges [6]. For instance, the pentagonal dodecahedron (12-sided cavity), the smallest cavity in natural gas hydrates, is labeled as 5^{12} since it has 12 pentagonal faces with equal edge lengths and equal angles [5].

Each single cavity formed by water molecules has a maximum occupancy of one suitable guest molecule. But it is also possible that some of the cavities may remain empty. Although methane (CH_4) is in general the predominant gas molecule in natural gas hydrate cavities, other gas compounds such as C_2–C_5, carbon dioxide (CO_2), and hydrogen sulfide (H_2S) can also be enclathrated into the water cavities [7]. While forming hydrate cavities, attracting forces among water molecules exist which are directly towards the center of the cavity. Therefore, those cavities with the existence of a guest molecule are more stable than empty cavities as the guest molecule shields the attractive forces. The repulsive part of the guest-host interactions via weak Van der Waals forces is supposed to be the primary factor for the hydrate formation process and the stability of the hydrate structure [8]. This also explained the reason why nonpolar molecules are preferred in the hydrate structures. These molecules can be assigned to groups of hydrophobic compounds (e.g. CH_4, C_2H_6 etc.) and water-soluble acid gases (e.g. CO_2, H_2S etc.) [9].

Depending on the size of the guest molecule, different polyhedrons form and combine to unit cells of hydrates with cubic structure I (sI) and structure II (sII), and hexagonal structure H (sH) (Figure 1.1) which have all been verified in samples taken from natural gas hydrate occurrences. The pentagonal dodecahedrons (5^{12}) with an average radius of 0.39 nm is the basic building block presented as the small cavity in all three hydrate structures. In structure I, two 5^{12} cavities are combined with six tetrakaidecahedrons ($5^{12}6^2$) into a unit cell. A unit cell of structure II hydrates consists of 16 pentagonal dodecahedrons (5^{12}) cavities and 8 hexakaidecahedrons ($5^{12}6^4$). As for the unit cell of structure H, it contains three types of cavities: three small pentagonal dodecahedrons (5^{12}), two medium irregular dodecahedrons ($4^3 5^6 6^3$) and one large icosahedron ($5^{12}6^8$). Small guests such as CH_4, C_2H_6 and CO_2 form structure I hydrate, whereas large molecules such as C_3H_8 and iso-C_4H_{10} form structure II hydrate. Larger guest molecule such as neo-hexane form structure H with the presence of helping gas (e.g. methane) occupying the small cavities [10]. However, gas molecules which individually form structure I hydrates may also form structure II in a mixture, as demonstrated by the CH_4–C_2H_6 binary system with certain proportions [11].

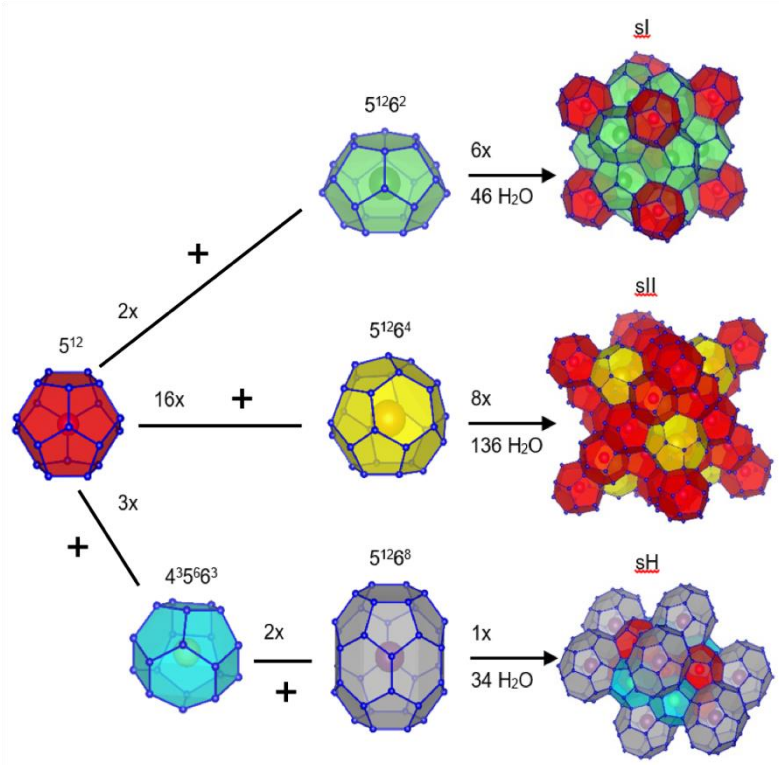

Figure 1.1 Molecular drawing of sI (top), sII (middle) and sH (bottom) hydrates. (modified from [12]).

Table 1.1 Hydrate crystal structure and geometry of cavities [5].

Hydrate structure	**I**		**II**		**H**		
Crystal system	Cubic		Cubic		Hexagonal		
Space group	Pm3n		Fd3m		P6/mmm		
Cavity type	Small	Large	Small	Large	Small	Medium	Large
Description	5^{12}	$5^{12}6^2$	5^{12}	$5^{12}6^4$	5^{12}	$4^35^66^3$	$5^{12}6^8$
Average cavity radius [nm]	0.395	0.433	0.391	0.473	0.391	0.406	0.571
Number of cavities per unit cell	2	6	16	8	3	2	1
Number of water molecules per unit cell	46		136		34		

To investigate the limitations of guest molecules in each hydrate cavity, the size and the shape of the guest molecule are the critical aspects to be considered.

Schrader et al. [13] suggested a method for the determination of an upper size limit for a guest molecule to enter a specific cavity. Initially, the radius of the water molecule which is approximate 0.14 nm is subtracted from the average cavity radius whose values are given in the above Table 1.1. Then the guest molecule radius is divided by the before-calculated difference, which was commonly denoted as the guest-to-cavity ratio shown in Table 1.2. For this work, the values of the molecular diameters and the cavity diameters (Table 1.2) are derived from Sloan and Koh, 2008 [5]. Note that a cavity size ratio between 0.75 and 1.0 is necessary for the stabilization of a hydrate cavity[14]. When the size ratio exceeds unity, the molecules are too large to be fit within the specific cavity without distortions. On the other hand, when the ratio is significantly less than 0.76, the repulsive interaction of the small guest molecule and the surrounding water molecules might become too weak to contribute to the stability of the cavity [5].

It is apparent from the table that CH_4 is able to enter all four cavities of sI and sII hydrates. CO_2 also fits in small and large cavities of sI and sII hydrates. C_2H_6 is slightly larger and therefore can only enter the large cavities of both sI and sII. C_3H_8 and iso-C_4H_{10} fit into the large cavity of sII hydrates with a size ratio of 0.94 and 0.98, respectively. Both molecules can form sII hydrates with the small cavities being vacant. In contrast, the linear n-C_4H_{10} has a guest-to-cavity ratio of 1.18. Effectively, this molecule would be too large to fit into the large cavities of sII hydrates. However, n-C_4H_{10} was verified as a sII former both in laboratory experiments and natural hydrate samples [15,16]. It will not form a hydrate unless there's a help gas like CH_4 or H_2S in the system to stabilize the small cavities of the hydrate structure [15,17].

It should be noted that n-C_4H_{10} has two well-known rotational isomers, trans and gauche, since it is a linear alkane and the CH_3CH_2 fragments can rotate around the central C–C bond. The trans form is the energetically most stable conformer of n-C_4H_{10} [18] but it is supposed to be too large (0.786 nm) even to fit into the $5^{12}6^4$ cavities on the basis of size considerations. From dielectric relaxation as well as Raman measurements it is assumed that n-C_4H_{10} is probably incorporated into the hydrate cage as its gauche conformer [15,17]. Luzi et al. [19] further proved with the help of Raman spectra, single crystal X-ray diffraction data and quantum mechanical calculations, that only the gauche conformation of n-C_4H_{10} can be incorporated into the distorted cage structures and an optimization process of the hydrate structure is requested before the successful

incorporation of n-C_4H_{10}. These results provided deeper insights on the influence of guest molecular shapes on the formed hydrate cavities.

Table 1.2 Properties of guest molecules as well as the guest-to-cavity ratio of each component in sI and sII hydrate. Except for the solubility data from Air Liquide Germany GmbH, all the other data were taken from Sloan and Koh, 2008 [5]

Molecule	Solubility (mmol/L) [1]	Guest diameter (Å)	Guest-to-cavity ratio			
			5^{12} (sI)	$5^{12}6^4$ (sI)	5^{12} (sII)	$5^{12}6^4$ (sII)
CH_4	1.6	4.36	0.86	0.74	0.87	0.66
C_2H_6	2.2	5.50	1.08	0.94	1.10	0.82
C_3H_8	1.8	6.28	1.24	1.07	1.25	0.94
iso-C_4H_{10}	1.0	6.50	1.28	1.10	1.29	0.98
n-C_4H_{10}	1.6	7.10 (gauche)	1.40	1.21	1.41	1.07
		7.86 (trans)	1.55	1.33	1.57	1.18
CO_2	38.6	5.42	1.07	0.92	1.08	0.82

[1] Solubility in water at 20 °C and under normal pressure.

1.2 Gas hydrates in nature

1.2.1 Occurrences of gas hydrates in nature

The formation of gas hydrates in nature requires low temperatures, elevated pressures, and substantial amounts of gases and water, which limits their global distribution to marine sediments at all active and passive continental margins, permafrost areas, deep lakes or in locations with similar conditions [5,20]. The vertical extent over which the above-mentioned requirements are met at one location and gas hydrates remain stable is known as gas hydrate stability zone (GHSZ). Figure 1.2 illustrates the phase diagrams where methane hydrates are stable in two major geological settings. Methane hydrates can only exist at depths where the increased temperature determined by the geothermal gradient with respect to increasing depth in Earth's interior (red curve) is lower than the maximum stability temperature (black curve). In permafrost sediments (Figure 1.2a), the top of the GHSZ typically occurs about 0.2 to 0.3 km below the land surface, often within an interval of permafrost layers and extend to 2.0 km below the land surface. In marine setting (Figure 1.2b) where high pressures are generated by the overlying water, the top of the GHSZ occurs within the water

column. Hydrate can be found in depth up to around 1.2 km depending on the local p–T conditions [21].

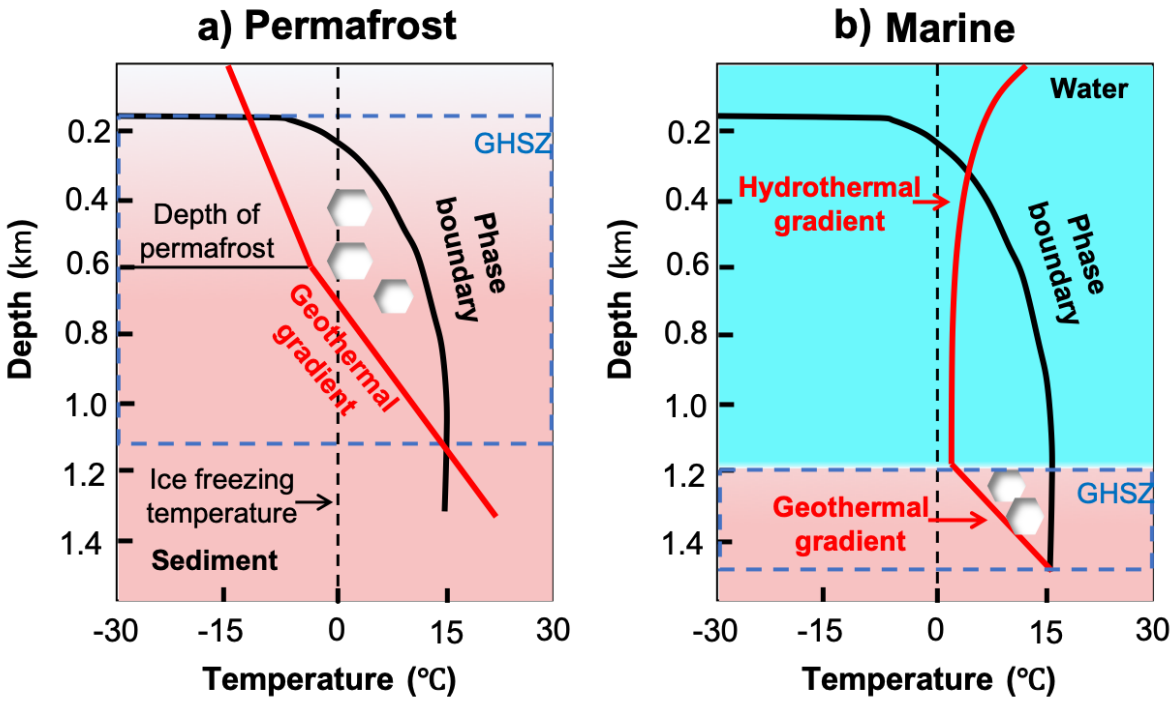

Figure 1.2 Phase diagram illustrating where gas hydrates are stable in permafrost (a) and marine (b) settings. Temperature data are derived either from geothermal gradient (sediments) or hydrothermal gradient (water). Hydrates can only exist at depths where the temperature (red curve) is less than the maximum stability temperature (black curve). (modified from Kvenvolden [22] and Beaudoin et al. [23]).

Similar to other fossil fuels, the guest hydrocarbons in hydrate systems are products of organic matter transformation. They are supplied either from microbial gases or thermogenic gases, or a combination of both origins [24]. Methane to ethane + propane ($C_1/C_2 + C_3$) ratios and methane $\delta^{13}C$ values were used to determine the origin of hydrocarbon gases [25]. Biogenic gas is formed by the activities of methanogenic bacteria on organic matter at non-oxidizing conditions and mainly consists of methane gas. At greater depths and higher temperatures, thermogenic gas is generated through thermo-catalysis which contains heavier hydrocarbon gases e.g., C_2H_6 and C_3H_8. To form hydrates, the generated gas has to migrate through faults and fissures from the place of origin to shallower depths where there's enough water and the p–T conditions are within the GHSZ [26].

Figure 1.3 depicts the global occurrence of natural gas hydrates that are confirmed or inferred taken from Waite et al. [27] . The confirmed gas hydrates (red circles) are biased toward deposits accessible by drilling cores or by videotaped from a vehicle near the sea floor. The existence of gas hydrates is considered inferred primarily when more than one factors (e.g. seismic data, borehole logs, or certain geochemical characteristics) match anomalies known to characterize gas hydrates, shown as yellow circles. Blue symbols in Figure 1.3 denote inferences based only on bottom simulating reflections and are plotted within the region of the bottom simulating reflection.

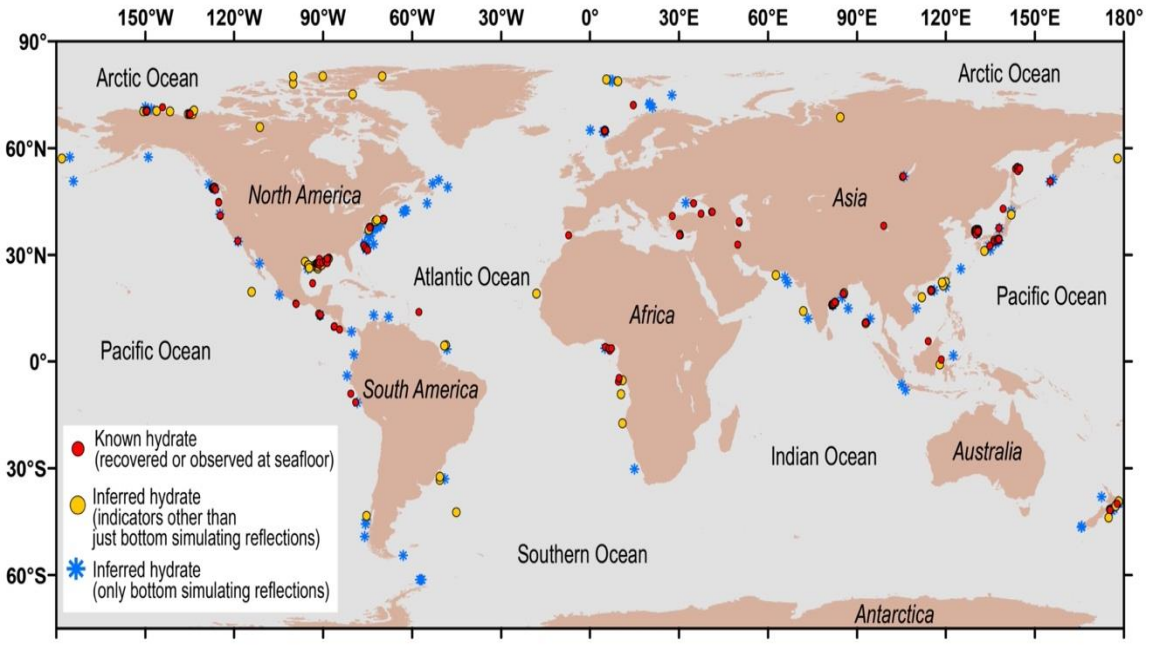

Figure 1.3 Global map of recovered or observed gas hydrates (red circles) and inferred gas hydrates (yellow circles and blue symbols) [27]

Since Trofimuk's first resource assessment in 1973 [28], estimates of the global inventory of gas hydrate deposits have been commonly based on different empirical calculations including the results of field observations or mechanistic models [29]. The maximum and minimum values varying by several times of magnitude [30–35]. Notably, the global estimates of natural gas hydrate resources decreased gradually over time due to improved knowledge towards the limiting factors of natural gas hydrate distribution, concentration, and much reliable volumetric parameters validated by drilling results. Despite this, the most often cited estimate for the amount of carbon stored in natural hydrates still reaches 10,000 Gt, which would double the amount of conventional fossil energy

including natural gas, oil and coal [22]. On the basis of the huge amount alone, gas hydrates are considered as a promising energy resource for future.

Hydrates occur primarily as pore-filling gas hydrates with saturations less than 10 % in fine-grained sediments and much higher saturations (50 % to 90 %) in coarser sands or silt (Boswell et al.,[36] and the references therein), as massive solids in association with rising gas bubbles [37], and as grain-displacing aggregations (nodules and veins) in poorly compacted fine-grain sediments [38]. The morphology of the hydrates is largely affected by the skeleton and capillary forces, which depend on the burial depth and grain size of the hosting sediments [39].

In natural environments, gas hydrates usually contain a mixture of gas molecules, which originate from microbial activities and/or thermogenic conversion of organic matters. The amount of additional gases besides CH_4 varies from less than 1 mol% (e.g., Black Sea) to more than 40 mol% (e.g., Caspian Sea, Gulf of Mexico) in recovered hydrate reservoirs [21]. The feed gas mixtures are also highly dependent on the local conditions of the hydrate system. Regarding hydrate formation in nature, it is questionable whether the feed gas phase is available continuously or whether it is disrupted. The limitation of gas migration may be caused by the formation of hydrate plugs in pore necks or fractures, permeability changes due to mineral diagenesis, or periodical geotectonic movements in geological times. Against such background, the gas supply condition plays a significant role in the formation process of mixed gas hydrates.

The formation of gas hydrates from a gas mixture, however, may result in a coexistence of hydrate phases with different structures and compositions. This has already been verified in natural gas hydrate deposits. In 2007, a complex hydrate sample containing n-pentane and n-hexane in addition to CH_4 and lighter hydrocarbons were identified from Barkley Canyon on the northern Cascadian margin. For the first time the coexistence of sII and sH hydrate phases could be proved in nature [40]. Later, in 2010, Klapp et al. reported the occurrence of sI and sII gas hydrates as coexisting phases from the Chapopote Knoll in the southern Gulf of Mexico [41]. Similar results were observed from the South China Sea by Wei et al. [42], who analyzed gas hydrate samples and confirmed the coexistence of sI and sII gas hydrates. Even hydrate samples from Lake Baikal showed the coexisting hydrate phases with different structures and compositions [43]. Under certain conditions the formation of a more-or-less homogeneous mixed hydrate phase may be difficult in the presence of a gas mixture, as indicated by the above-mentioned examples. However, the reason for

the formation of coexisting hydrate phases can be diverse and are not yet fully clarified. A possible explanation may be fluctuations of the composition of the feed gas flux from deeper sources or a fractionation of the gas in shallower sediments as a result of CH_4 consumption and/or H_2S production due to biological processes such as the anaerobic oxidation of CH_4 [44,45]. In some cases, the migration of the feed gas is limited and the local conditions can be described as a "closed system". Since some gases are preferentially encased into the hydrate structures compared to CH_4 [46], the hydrate formation process may induce a fractionation of the feed gas and result in the formation of coexisting hydrate phases with changing compositions in accordance with the changing feed gas composition [47]. Another possible approach to explain these observations is to consider different hydrate formation kinetics: The formation of CH_4 hydrate seems to be kinetically preferred compared to the formation of mixed hydrates [48]. This, however, is only a selection of possible formation scenarios. For other locations such as the Lake Baikal other theories for the formation of coexisting hydrate phases are discussed [43,49].

1.2.2 Gas hydrates in Qilian Mountain permafrost

The occurrence of mixed gas hydrates has been proved in Qilian Mountain permafrost (QMP) since 2008 during Scientific Drilling Projects of Gas Hydrates, a mid-latitude region of high-elevation in northwest China (Figure 1.4 taken from[50]). The altitude of the area investigated in the drilling project is between 4026 m and 4128 m with a permafrost thickness generally varying between 60–95 m. Although the permafrost layer is relatively thin, totally 14 scientific drilling test wells have been carried out and 7 of which successfully obtained gas hydrate samples below the permafrost at depth of 133–396 m [16,50].

Permafrost zone in QMP is located in the northern margin of Qinghai-Tibet Plateau with a permafrost area of about 10×10^4 km^2 [51]. Its tectonic units are usually divided into three parts, the northern structural zone, the middle block and the southern Qilian belt. Qilian Mountain has undergone continental rift stage, the ocean floor expansion and the trench-arc-basin system stage, orogenic stage and then formed the present tectonic pattern [52]. Large NW–SE trending thrust faults are developed in this area. These thrusts or fractures may serve as pathways for gas to migrate upwards from the deeper layers and some of the fractures may also serve as temporary hydrate bearing reservoirs [53]. There are four main sets of depositions containing relatively high abundant of organic matter, which can potentially serve as source rocks [54,55]. The Carboniferous layer consists of marine-facie limestone and mudstone. The Lower Permian

stratum is made up of marginal marine-facie carbonate or sandstone, siltstone, and mudstone. The Upper Triassic formations consist of marine-facie and onshore-facie sandstone and mudstone inter-bedded with limestone. The Middle Jurassic layer are composed of fluvio-lacustrine to marsh facie coal-bearing sandstone, mudstone, and oil shale. Besides, the local pressure and temperature conditions in the permafrost area meet the conditions for mixed gas hydrate formation.

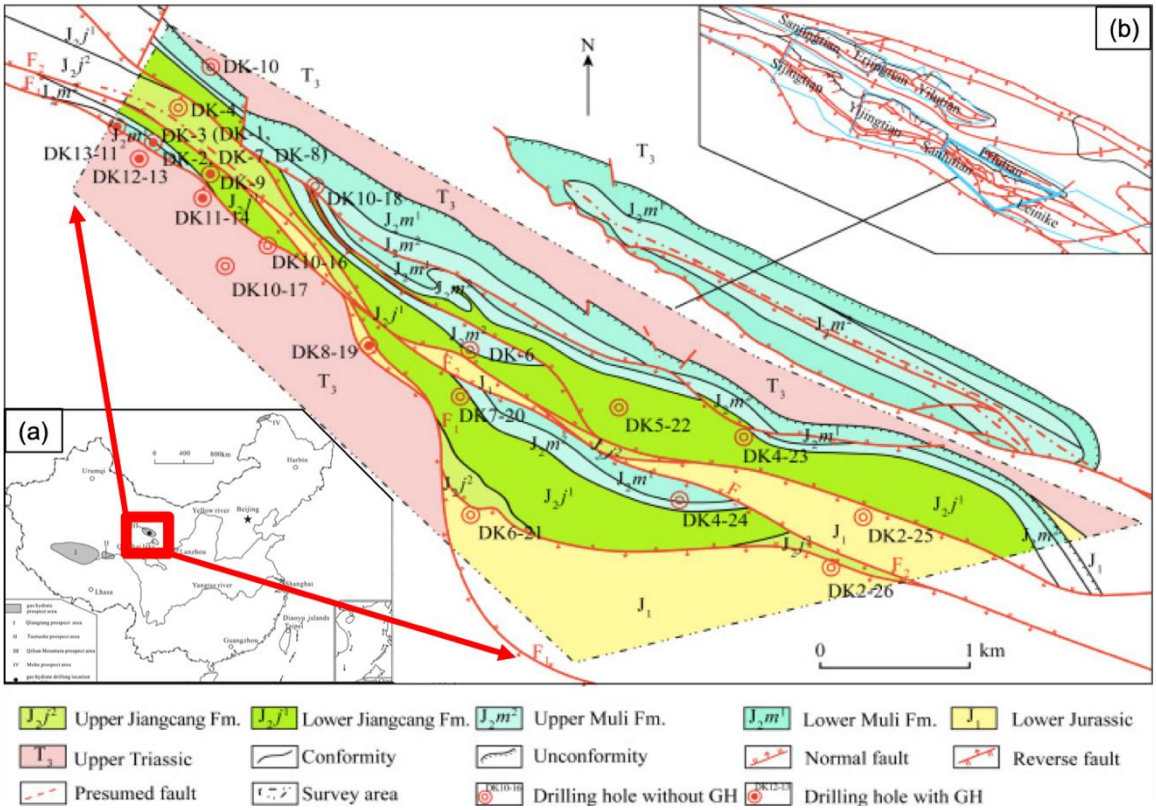

Figure 1.4 Geological characteristics and borehole locations of the gas hydrate reservoir in QMP area (modified from Lu et al., 2020 [56]).

In 2011, China Geology Survey conducted a test production of natural gas hydrates in the Muli area of the QMP through a single straight well. After the first detection of gas hydrate occurrence in hole DK–8, submersible high-pressure pumps were started at the bottom of the well to drain for different hydrate layers at a well depth of 146-305 m. With the decreasing of the water level, the pressure of the hydrate reservoir decreased to release methane from hydrate dissociation. Later in 2016, a second test production was carried out in the same area, using the epsilon-shaped horizontally butted wells in order to improve production efficiency and gas production amount. A main well (SK–0) and two branch wells (SK–1 and SK–2) with a horizontal distance up to 629.7 m

was drilled as shown in Figure 1.5. The production was also achieved by drainage depressurization method, but with a higher yield of the gas production as compared to that in the single straight well.

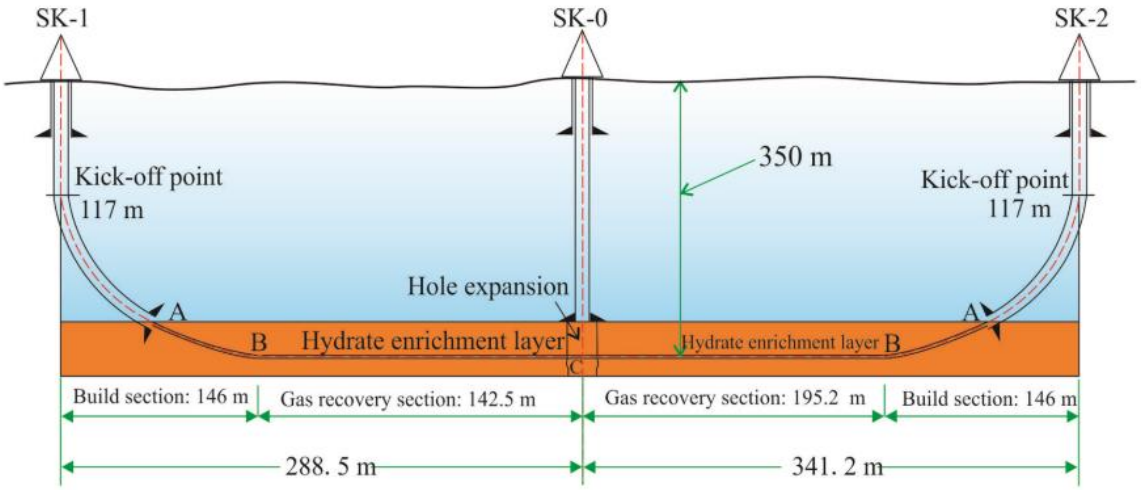

Figure 1.5 Schematic illustration of the horizontal well applied in the test production in Muli area of Qilian Mountain permafrost [57].

The drilling and experimental results show that gas hydrates in QMP are generally preserved in the Jiangcang Formation of Middle Jurassic age. Fracture-filling hydrates are the main reservoir type and manifest as thin layers, flakes or blocks on the fractured surface of siltstone, mudstone, and oil shale [58]. Pore-filling hydrates which occur in the pores of sandstone can only be indirectly observed by continuously emerging bubbles and water droplets, as well as by abnormally low temperatures that are measured using infrared imaging from the core [50,59].

Further analysis also revealed that the Qilian gas hydrate system is an epigenetic hydrocarbon reservoir that is mainly controlled by a gaseous source, exists in permafrost conditions, and contains a system of faults over a deep potential hydrocarbon reservoir. The reservoir occurs at a shallower depth below thinner permafrost and is characterized by more complicated gas components compared to other well-documented permafrost hydrate reservoirs [16,50,60]. Composition and carbon isotope of gases dissociated from gas hydrates suggest that the gas source for this hydrate reservoir is composed mainly of deep or crude oil-concomitant gases originating from the coal layers of Middle Jurassic period, occasionally mixed with microbial source in shallower depths. In other words, the gases are primarily with thermogenic source from deeper depths [61–63]. Previous studies on the geological settings of the Qilian gas hydrate system

unveiled a complex system of faults over a deep potential hydrocarbon reservoir [64,65]. The hydrocarbon reservoir is therefore mainly controlled by faults and fractures with discontinuous distributions in vertical direction [66,67]. The law of hydrate distribution in the lateral areas between drilling holes is also not apparent due to the rock fracture system.

It turns out that the gases obtained from hydrate dissociation contain about 60% CH_4. In addition to CH_4, there's a high percentage of other gas components like C_2H_6, C_3H_8, C_4H_{10} and even heavier hydrocarbons [50]. These larger molecules occupy large cavities of the hydrate structures while CH_4 molecules are mainly in small cavities as indicated by the Raman spectroscopic measurements, suggesting that the gas hydrate belongs to structure II hydrate [68,69]. The encasement of higher hydrocarbons besides CH_4 into the hydrate structure results in a shift of the stability conditions to higher temperatures, lower pressures and an increase of the dissociation enthalpy compared to pure CH_4 hydrate because the large molecules better stabilize the hydrate cavities due to a better guest-to-cavity ratio [48,70,71]. Thus, the occurrence of higher hydrocarbons in the feeding gas phase is a prerequisite for the formation of a hydrate phase under these mild pressure and temperature conditions. However, the feed gas mixtures are highly dependent on the local conditions of the hydrate system in QMP. It is likely that both the changes in the gas migration pathways and hydrocarbon reservoirs will impede the upward gas flow or vary the feed gas composition. As a result, the formation of the mixed gas hydrates from a changing gas phase may lead to the coexistence of different gas hydrate phases.

Apart from the gas supply conditions, the particle size of the host sediments and the mineral composition may also affect the gas hydrates equilibrium conditions and growth kinetics: A high concentration of fine grains (<125 μm) led to an explicitly faster gas hydrate formation compared to medium or coarse sands [72]. Previous researches have shown that hydrate growth is inhibited within fine-grained sediments by a combination of reduced pore water activity in the vicinity of hydrophilic mineral surfaces, and the excess internal energy of small crystals confined in pores. The excess energy can be thought of as a "capillary pressure" in the hydrate crystal, related to the pore size distribution and the state of stress in the sediment framework [73]. Certain mineral surfaces can promote heterogeneous nucleation of hydrate [74]. Some organic substrates such as kerogens or biofilms may also possibly promote hydrate precipitation [73]. In the drilling cores from QMP, the major strata encountered include the Middle Jurassic lacustrine coal-bearing Jiangcang formation and below it the

Muli formation. The Jiangcang formation is mainly composed of black, gray oily shale and mudstone, mixed with gray siltstone, fine-grained sandstone; the Muli formation consists mainly of gray whitish siltstone, fine-grain sandstone [75]. Less is known about the potential effects of these sediments and mineral compositions on the mixed gas hydrate formation kinetics and the thermodynamic properties in the QMP.

1.2.3 Exploitation of natural gas hydrate reservoirs

Even though only a small proportion of natural gas from natural gas hydrate reservoirs is recoverable, it is still considered as a promising energy resource for the future and worth exploiting. Driven by the high demand of energy and limited conventional hydrocarbon resources, several countries involving the USA, China, India, Canada and Japan have launched national projects on the exploration and exploitation of gas hydrate resources.

Natural hydrate deposits can be classified in 3 classes in terms of geological characteristics and reservoir conditions [76]. Class 1 hydrate deposits contain a hydrate interval with high hydrate saturation in the pore space and an underlying two-phase fluid zone with free gas. It is the most desirable class for exploiting since the local pressure and temperature conditions are quite close to the hydrate equilibrium [76,77]. Class 2 deposits comprise a hydrate-bearing zone overlying a mobile water zone without any free gas phase. Class 3 deposits feature only one single hydrate zone with an absence of the underlying mobile fluids zone.

Gas hydrates are fundamentally different from the other unconventional natural gas sources. Gas molecules in the hydrate reservoir are trapped in the cages formed by the water molecules via hydrogen bonds [78]. Therefore, the techniques used to recover methane from gas hydrate sources are much more complicated than just creating conduit for free gas to flow out of the formation in natural gas reservoirs. Up to now, many gas production techniques have been proposed in considering the complex hydrate reservoir conditions. Depressurization, thermal stimulation, chemical stimulation are the three most commonly proposed and used techniques in gas hydrate exploiting for both field trials and lab experiments [76,77,79–82]. Depressurization process lowers the inside pressure of the well and therefore shifts the mechanical equilibrium of the reservoir, promoting the natural gas hydrates to dissociate. Thermal stimulation involves injecting a heat source (e.g. hot water, steam) into the hydrate stability zone to bring up the temperature and decompose the gas hydrates. Production of

hydrates can also be realized by distortion of the chemical equilibrium in the system by injection of inhibitors. For the conventional methods, natural gas hydrates dissociate in response to the pressure–temperature conditions being shifted outside of the hydrate stability zone [76]. Although these methods have been successfully employed to produce gas from marine or permafrost hydrates, there are still some concerns of decomposing natural gas hydrates based on these stimulations. One important aspect that needs to be accounted is the change of mechanical properties of hydrate-bearing sediments as a result of hydrate dissociation which may trigger slope instability and subsidence [83,84].

Another technology for the production of gas from natural gas hydrates is a variant of the chemical stimulation namely the injection of CO_2. In this scheme, the chemical disequilibrium between the initial CH_4 hydrate and the CO_2 gas phase induces the transformation of the original CH_4 hydrate into a CO_2-rich hydrate. Ideally, this process may not result in a dissociation of the hydrate phase, but a replacement of the hydrate-bonded CH_4 with CO_2 molecules and thus resulting in the production of CH_4 and simultaneously the capturing of CO_2 in the hydrate phase. In addition, CO_2 is thermodynamically favored in the hydrate phase compared to CH_4 at relevant conditions and they both form structure I hydrate [5], as do mixtures of these gases [85]. Hence, the gas replacement may be considered as an emission-free approach with higher stability of the hydrate-bearing sediments and reduced geo-hazards [86,87].

In field trials, it is also widely agreed that a combination of the techniques mentioned above may enhance the effectiveness of gas production. The field test at Mallik site in 2002 has been conducted applying thermal stimulation [88]. Other field tests such as the Mount Elbert well in Alaska North Slope in 2007 [89], as well as Mallik sites in 2007–2008 [90,91] were done by depressurization. In 2011, field trials in QMP were implemented using depressurization combining with hot air and hot steam stimulation [92]. In 2012, Conoco Phillips, DOE and JOMEC conducted a field production test, also known as the Ignik Sikumi gas hydrate filed trial, by injecting a CO_2-N_2 gas mixture as a first step and depressurization as a second step [93]. With the exploration of two horizontal butted wells in 2016, a gas hydrate production test was again operated in QMP for 23 days, yielding 1078m^3 gases in total which indicated a significant increase in the production of gas compared to the single-well production test [92,94]. The above-mentioned tests were all onshore field tests since they were carried out in permafrost areas. In 2013, the first marine gas hydrate field production test was conducted in Nankai Trough in Margin of the Daini Atsumi Knoll by

depressurization [95]. In 2017, China also conducted the first production tests of offshore natural gas hydrate by applying the formation fluid extraction method for 60 days [96].

It is noted from the above production trials that production values increased progressively over the tests. Yet the low production efficiency, ice/hydrate regeneration, and sand production problems are still commonly encountered during the field trials. To ensure a safe long-term exploitation of natural gas hydrates, more scientific issues concerning gas hydrate formation and dissociation still need to be discussed.

1.3 Dissociation of gas hydrates with regard to climate changes

Ideally, CH_4 hydrate concentrates CH_4 by around 169 times on a volumetric basis as compared to gas under 273 K and atmospheric pressure [20]. The large amount of CH_4 gas bound in hydrate structures and their worldwide occurrences make them interesting not only as a potential energy resource but also as a possible climate-relevant factor. As concerns about global warming gradually deepened in the past decades, there is raised awareness of the significance of CH_4 released from the destabilization of gas hydrate deposits [97]. The Intergovernmental Panel on Climate Change (IPCC) [98] stated in their recent assessment that over a 20-year period, methane is deemed 84 times more potent than carbon dioxide (CO_2) as a potential greenhouse gas. The massive release of CH_4 has been invoked as a contributing agent to the rapid warming events in geological times such as the Paleocene–Eocene Thermal Maximum [99] and Quaternary glacial-to-interglacial transitions [100]. Some estimations predict that 1 % of annual atmospheric CH_4 may originate through dissociation of global CH_4 hydrates [101–104]. It has been shown that CH_4 is an important component of Earth's carbon cycle on geological time scales and the release of CH_4 into the atmosphere can exacerbate global warming [105].

In turn, climate warming is not only directly affecting the hydrate distribution, but also responsible for the thawing of permafrost, thus resulting in the decomposition of the hydrate layer that within or beneath the permafrost. This has been recorded as atmospheric methane-concentration oscillations in polar ice cores [106,107]. Since the climate warming mainly shifts in temperature, hydrology, vegetation, landscape disturbance and sea levels, the susceptibility of gas hydrates to warming climate should be evaluated individually according to their geographical occurrences. It is assumed that deep marine sediments host around 95,5%% of the world's gas hydrate, typically at water depths of 500 m or

greater [101]. Therefore, the vast majority of hydrates require a sustained warming over thousands of years to trigger dissociation. Gas hydrates, particularly those associated with thin permafrost layers, are more likely to be affected by the climate processes. Chuvilin et al. [108] investigated the effects of temperature increase on the frozen sand and silt containing metastable pore methane hydrates. The results indicated that the dissociation of intrapermafrost hydrates began and ended before the onset of pore ice melting when exposed to warming. The critical temperature sufficient for gas hydrate dissociation ranged from −3.0 °C to –0.3 °C, depending on lithology and salinity of the host frozen sediments. Considering an almost gradientless temperature distribution during degradation of subsea permafrost, even minor temperature increases could be expected to trigger large-scale dissociation of intrapermafrost hydrates.

In addition to the effects on climate warming, gas hydrate decomposition may also destabilize the seafloor causing subsequent threats of potential tsunamis and other geohazards on hydrate bearing sediments. With sufficient concentration, gas hydrates serve to strengthen sediments [109]. A significant consequence of gas hydrate decomposition due to climate change is the release of gas especially methane, which may alter the behavior and mechanical properties of the marine sediments leading to slope failures.

The knowledge of the accurate composition of the gas encased into the hydrate phase is also important for the assessment of the hydrate dissociation behavior. Depending on the guest molecules and the structure of the hydrate phase, the dissociation kinetics of the mixed gas hydrate changes, e.g. structure I hydrates show a different dissociation behavior compared to structure II hydrates [110].

As mentioned above, natural gas hydrates were found below thin permafrost layers at shallow depth of around 133~396 m in QMP, which located in the northern margin of Qinghai-Tibet Plateau [50]. This area has received considerable attention not only due to its vast amounts of hydrocarbons in forms of gas hydrates, but also its high sensitivity to climate changes. Previous researches have confirmed that the active layers of permafrost which thaws and freezes seasonally are getting thicker in the Qinghai–Tibetan Plateau under the impact of global warming [111]. On the other hand, recent numerical simulations by Luo et al. [112] indicated that the permafrost area has decreased rapidly by a total of 26% with an increase of the mean active layer thickness by 0.46 m for the past 30 years. For the next 60 years, around 8.5–35% of the permafrost in Qinghai-Tibetan Plateau will continue to degrade under different trends of climate warming. Inevitably, the degradation of permafrost affects the stability of

the gas hydrates and causes the GHSZ migration and reduction, resulting in a higher CH_4 emission in this area. It should be noted that the dissociation of hydrates may also destabilize spontaneously the hydrate-bearing sediments in QMP. The release of fresh water may cause the migration of the fine particles resulting in the permeability damage. Thus, gas and water production at longer time scales will be hindered by the low permeability of the hydrate reservoir [113].

Considering the environmental effect, a proper understanding of hydrate dissociation behavior under specific conditions is important for the stability of natural gas hydrate deposits with respect to climate change.

1.4 Thermodynamic properties of gas hydrates

1.4.1 Phase diagram

Thermodynamic properties of a hydrate phase describe the phase behavior including stability conditions for the specific phase, decomposition conditions as well as metastable states and transition processes. Based on thermodynamics, Gibbs' Phase rule provides the theoretical principle for characterizing the chemical state of a system which are completely described by the variables pressure (p) and temperature (T) in thermodynamic equilibrium. The rule assumes that the components in the system do not react with each other. It describes the possible number of degrees of freedom F which designates the maximum number of phases and the number of components at equilibrium conditions. According to Gibbs' Phase rule [114],

$$F = K - P + 2 \tag{1.1}$$

where P is the number of phases present and K is the number of components.

Application of the Gibbs' Phase rule can be illustrated by considering the binary mixture of methane and free water phase, where K=2. Since these two components form a solid methane hydrate phase, the number of phases present P=3. It can be determined that F=1, indicating the system is univariant, only one intensive property must be specified to determine the state of the system. For instance, at any given temperature, a single value of pressure at equilibrium conditions is directly attained.

The Gibbs' Phase rule allows the constructing of phase diagrams to represent and interpret phase equilibria in heterogeneous systems. Figure 1.6 illustrates a typical phase diagram for a mixture of water and a hydrocarbon gas system whose application is so fundamental in this study. In this system, gas hydrates

formed from water and hydrocarbon gases constitute a solid phase where the two main components are not chemically bounded but through physical van der Waal forces. The symbols represent *I* (ice), L_W (liquid water), *H* (hydrate), *V* (vapor) and L_{HC} (liquid hydrocarbon), respectively. The diagram includes a logarithmic pressure scale to obtain almost straight lines. This two-component system is represented on the phase diagram as an area (two phases), a line (three phases) or a point (four phases). Point Q_1 is the quadruple points indicating the coexistence of four phases: I–L_W–H–V while point Q_2 for L_W–H–V–L_{HC}. The temperature for Q_1 is similar for almost all hydrate formers (approximately 273 K) whereby the quadruple pressures vary for specific hydrate formers. It should be noted that in the binary system of methane + water, a second quadruple point Q_2 does not exist as the critical point of pure methane lies at 190.6 K, having no intersection with the L_W–H–V line of methane hydrates [5,115]. The blue line is of most concern as it forms the hydrate equilibrium boundary. Hydrate can only form at high pressures and low temperatures in the areas to the left of this line. At conditions within the right areas to this line, no gas hydrates can form. The dash-dotted red line is the I–L_W equilibrium curve with a solid ice phase to the left and liquid water phase to the right. The dashed green line lies in the V–L_{HC} hydrocarbon equilibrium curve. The hydrocarbon will be in the liquid state above the V–L_{HC} equilibrium curve whereas in the vapor state below it. The areas between the three-phase lines stand for two-phase areas. For instance, the area between H–V–L_{HC}, I–H–V and L_W–H–V three-phase lines accounts for either the H–V region or H–L_W region, depending on whether water is excess or gas is excess when forming hydrates (K=2). The formation of hydrates with limited water and excess gas leads to the presence of only hydrate phase and vapor phase at equilibrium (P=2). For this study, experiments were mainly carried out with a continuous gas flow and a certain amount of liquid phase. It is assumed that water molecules will be completely consumed at the end of the experiments. Therefore, F equals to 2 in the area between the three-phase lines, indicating that both the pressure and temperature should be specified for the determination of the state of the system.

The complexity of the phase behavior diagram changes with the composition of the system. Gas hydrates, containing N_2 beside methane are less stable than pure methane hydrates: the stability field of these hydrates is shifted to higher pressures and lower temperatures as compared to the stability conditions of pure methane hydrates [116]. In contrast, the encasement of H_2S, CO_2 or higher hydrocarbons besides CH_4 into the hydrate structure results in a shift of the

stability conditions to higher temperatures and lower pressures and an increase of the dissociation enthalpy since the large molecules better stabilize the hydrate cavities [48,70,71].

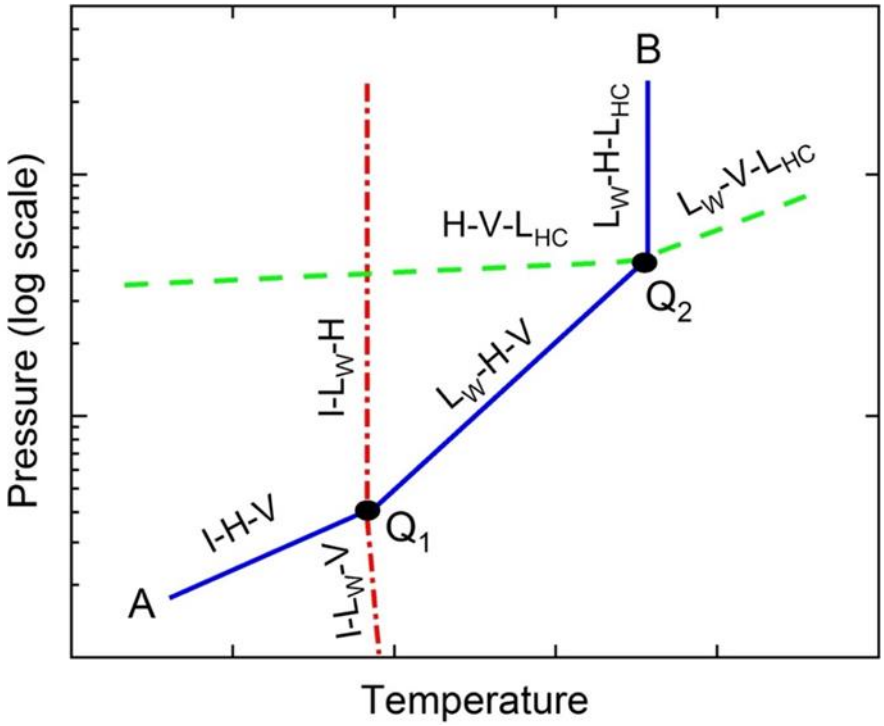

Figure 1.6 Typical pressure–temperature diagram of a binary hydrocarbon + water system (modified from Sloan and Koh, 2008 [5]).

On the basis of the published experimental data, the phase boundaries for the gas hydrates with different components have reached reasonable accuracy (within experimental error) for most common sI and sII hydrate formers. These data have been incorporated into a multiphase flash program called CSMGem. CSMGem is a software written for the prediction of the thermodynamically stable hydrate structures and cage occupancy of a multiphase system at any given pressure and temperature using an algorithm based on Gibbs energy minimization [5]. This software is also used frequently to predict and verify the experimental results in this study.

1.4.2 Driving force for the hydrate formation process

In general, gas hydrate formation is a phase change rather than a chemical reaction, where no chemical bonds are generated or broken. In a three-phase system of a one-component gas, an aqueous solution and a crystalline hydrate of the gas, the chemical equation for the hydrate formation "reaction" can be formulated as follows

$$\text{Gas} + n_w\, H_2O \rightleftharpoons \text{Gas}\cdot\, n_w\, H_2O \tag{1.2}$$

where n_w is the number of water molecules.

Chemical potential characterizes the possibilities of a substance, to react with other substances (chemical reaction); to change into another form of state (phase transition); redistribute in space (diffusion). A chemical reaction, phase transition or diffusion can only take place voluntarily if the chemical potential in the initial state is greater than in the final state. This concept was initially introduced by Josiah Willard Gibbs who established the mathematical beauty of thermodynamics by formulating the fundamental equation of thermodynamics of a system [114]. According to Kashchiev and Firoozabadi [117], the chemical potentials of the gas and the water molecules in aqueous solution were denoted as μ_g^W and μ_w^W, respectively. Referring to the thermodynamic relation between chemical potentials in reaction equilibria and equation 1.2, μ_h^W was denoted as the chemical potential of the hydrate building unit in the water phase

$$\mu_h^W = \mu_g^W + n_w \mu_w^W \tag{1.3}$$

Kashchiev and Firoozabadi defined that the driving force for new phase formation was the difference between the chemical potentials of the old (aqueous phases) and the new phase (hydrate crystal). They called this difference supersaturation which was commonly denoted as $\Delta\mu$. Therefore, the chemical potential of the hydrate building unit μ_h^W corresponds to the old phase (aqueous phase) while the chemical potential μ_h^H stood for the new hydrate phase. Consequently, the supersaturation can be expressed as:

$$\Delta\mu_h = \mu_h^W - \mu_h^H \tag{1.4}$$

Nucleation and growth of gas hydrates are only possible if $\Delta\mu_h > 0$, where $\mu_h^W > \mu_h^H$ and the solution is supersaturated by the gas. If $\Delta\mu_h = 0$, the solution is saturated and the system is in phase equilibrium, indicating that the dissolved and crystalline hydrate phases can coexist. When $\Delta\mu_h < 0$, the solution is undersaturated: as then $\mu_h^W < \mu_h^H$ and hydrate crystals cannot nucleate in the solution, and existing ones are subject to dissolution. The authors also pointed out that this concept of supersaturation was also applicable for the formation of hydrates from ice and the decomposition of hydrates to gas and ice. For the transformation process, it is also widely accepted that the driving forces is the difference in the chemical potential between the initially formed hydrate phase and the transformed new gas phase, e.g. in the CH_4–CO_2 swapping process, the difference in the chemical potential between the coexisting CH_4 hydrates phase

and the surrounding gas phase when exposed to a CO_2 gas is the driving force for further transformation process [118].

At constant pressure and temperature conditions, chemical potential is the partial molar Gibbs free energy. Therefore, the difference between the chemical potentials of the "reactants" and "product" corresponds to the Gibbs free energy change ΔG for the reaction as follows

$$\Delta G = -(\mu_g^W + n_w \mu_w^W) + \mu_h^H \tag{1.5}$$

Considering equation 1.3 and 1.4, the formation of hydrates is only possible if $\Delta G < 0$ resulting in a diminishment of the Gibbs free energy.

1.5 Kinetics of gas hydrate formation

1.5.1 Hydrate crystallization from water

Historically, there are three main hypotheses proposed to explain the mechanism of hydrate nucleation from water. These hypotheses treat the hydrate nucleation qualitatively on a molecular level. First, Radhakrishnan and Trout [119] proposed the *local structuring nucleation hypothesis* based on the Landau free energy calculations. The study on the CO_2 hydrate nucleation at the water-liquid CO_2 interface lead to the assumption that the guest molecules arrange in a configuration similar to that in the hydrate crystal due to the thermal fluctuations. Afterwards, the water molecules rearrange around the locally ordered guest molecules. When the number of the CO_2 molecules in the arrangement with a local order reaches a critical size, hydrate nuclei starts to form. Second, Long [120] and Kvamme [121] presented their *hypothesis of heterogeneous nucleation at the interface* between the gas phase and the liquid phase. Gas molecules are assumed to be transported to the water-gas interface, absorbed at the aqueous surface where they are at first partially and thereafter completely encased into hydrate cavities made of water molecules. These clusters agglomerate and grow from the water surface to the gas phase. However, this model is not a satisfying concept for the hydrates with a higher density compared to the density of water since a preferential hydrate nucleation and growth on the subsurface rather than in the vapor phase could be observed [122].

Apparently, both of the above two hypotheses have limitations with the first one only applicable to CO_2 hydrates and the second one requiring the presence of a vapor phase. *The labile cluster nucleation hypothesis* proposed by Sloan and his co-workers [123,124] shows a higher universal validity as it can be applied for the hydrate nucleation process with/without a free gas or liquid phase of the guest molecule. The quintessence of this hypothesis is the formation of labile ring

structures of pentamers and hexamers by water molecules around the dissolved guest molecule. The coordination number of the surrounding water molecules depends on the size of the gas molecule. According to Christiansen and Sloan, 1 CH_4 molecule was surrounding by 20 water molecules whereas 24 water molecules surround 1 C_2H_6 molecule. These labile clusters agglomerate by sharing faces on one side of the interface until they reach a critical size for hydrate growth. This assumption is supported by Ludwig [125] who probed the structure of the water phase from ab initio calculations. The results turned out that it is very like to have ring structures in the water phase besides the tetrahedrally coordinated water molecules. Walsh et al. [126] further developed the hypothesis from their molecular dynamic simulations of the growth of CH_4 hydrates. Small 5^{12} cavities around a methane molecule are observed to form first, favoring structure II. Jacobson et al., [127] described the nucleation of hydrates from different guest molecules as a multistep mechanism. They observed that clusters of guest molecules and their surrounding water molecules in the aqueous phase formed the so-called "blobs" which could be considered as large analogues of the labile clusters proposed by Christiansen and Sloan [124]. When the cluster of clathrated cages become a critical size, the nucleus starts to ordering water molecules to cavities and recruits more molecules from the solution, resulting an amorphous hydrate form. Later on, the amorphous hydrate nuclei rearrange to form a polycrystalline structure containing elements for both sI and sII [128].

Investigations on the hydrate formation process via *in situ* Raman spectroscopy support the labile cluster hypothesis in general. Even though the nucleation process takes place very fast, a preferential formation of small 5^{12} cavities of sI is confirmed from the experiments [129]. Also, CH_4 molecules are observed to incorporate into the 5^{12} cavities as a first step during the mixed gas hydrate formation process whereas the formation of other cavity types occurs later [48].

1.5.2 Hydrate crystallization from ice

Gas hydrate formation from ice is a solid-state reaction that takes place at the ice-gas or ice-liquid hydrocarbon interface [130]. The hydrate formation is an exothermal process and consists of two main stages: nucleation and growth. For the nucleation process, Hwang et al. [131] first assumed that the water molecules from the melting ice surface were more mobile and could interact with the CH_4 gas by forming hydrate cavities. Thereby, the ice structures remained stable to a certain extent and acted as "molecular template". Later, Sloan and Fleyfel [123]

proposed a similar theory for the primary nucleation of hydrates from ice. They came up with a concept of "transient liquid water" which might be locally presented on the surface of the ice particle. While forming hydrates, water molecules in the ice lattice were rearranged. The first labile hydrate clusters formed within the liquid film at the interface between gas and ice while melting ice was again described as template for the hydrogen bonds that need to be formed for the hydrate cavities.

In accordance with experimental observations, a thin gas hydrate film rapidly spreads over the ice surface at the initial stage of the hydrate formation [132–135]. To ensure a continuous reaction, the gas phase needs to penetrate through the intervening hydrate layer to the ice-hydrate interface and/or water molecules transport to the outer hydrate interface with the ambient gas. This diffusion-limited growth on the ice surface at the second stage was considered and simulated by various researchers. Henning et al., [136] proposed a two-stage mechanism for the CO_2 hydrate formation from powdered deuterated ice crystals. A simple shrinking core model was applied to fit the diffusion-controlled stage with the equation goes back to the model of Jander [137]. Fujii and Kondo [138] also provided a simplified diffusion theory based on the hydration of tricalcium silicate. A measurable amount of time t^* was introduced in the model after which time the hydrate formation is diffusion-controlled. These approaches were extended by Wang et al. [139] who applied a more complex shrinking core model to study CH_4 hydrate formation kinetics. They adopted a mathematical shrinking core model developed by Levenspiel [140] for the description of the second stage. Later on, Kuhs and co-workers extended the before-mentioned shrinking core model to the occurrence porous microstructure of hydrates in the nanoscale [141–143]. The authors suggested that water and mass transport became easier in case of porous gas hydrates. The enclathration of the guest molecules might become rate-limiting instead of the diffusion of gas or water molecules [142]. A combined Avrami–Erofeev and Ginstling–Brounshtein model was suggested with the initial formation and growth of hydrate nuclei modelled by means of the Avrami–Erofeev theory and a diffusion-controlled stage fitted by Ginstling–Brounshtein theory [144].

Based on the above-mentioned literature findings, the formation of gas hydrates from ice is divided into three stages. During the initial stage, small clusters of water and gas are generated which continue to form hydrate crystals on the surface of ice particles. This process occurs on various active sites on the surface resulting in a thin hydrate film that spreads over the ice particle. The

second stage is supposed to be rate-limiting during which gas molecules diffuse inward through the existing hydrate layer to the unreacted ice core or the opposite transport of water molecules to the hydrate–gas interface. The third stage is the reaction of gas molecules with residual ice. Since the third step of hydrate formation is only observed for a low number of systems and also incompletely, only the first two steps are considered for mathematical description.

The initial hydrate formation stage controlled by the enclathration reaction is modelled using the Avrami rate law [145], which fits for the random nucleation followed by the growth of the nuclei. Although not developed for the description of hydrate formation kinetics, it has been successfully adopted in hydrate formation experiments as well as transformation of CH_4 hydrate into a CO_2-rich hydrate experiments [130,139,144,146,147]. The reaction rate α can be given by a general expression of the Avrami rate law being

$$\alpha = 1 - \exp(-kt^n) \tag{1.6}$$

where α is the hydrate conversion ratio at time t, k is the rate constant for the enclathration-controlled reaction stage of hydrate formation, and n is the Avrami exponent that accounts for the dimension of crystal growth.

The second step of the hydrate formation process is controlled by diffusion. Three physical models can be employed for the description of this process which are all derivatives of the general shrinking core model. Shrinking core model is developed initially for heterogeneous reactions between a gas phase or a liquid phase and a spherical solid particle [148]. The application of the model to gas hydrate formation from ice describes that a thin hydrate layer around the ice particle is formed after the initial enclathration stage. Thereafter, the gas molecules diffuse through the formed hydrate layer to the interface of the unreacted ice core. Thereby, the gas and the boundary of the unreacted ice move towards the center of the ice particle which is illustrated with Figure 1.7. Consequently, the diffusion distance extends due to the growth of the product layer and the reaction surface becomes smaller. The growth rate decreases over time.

The first physical model to describe solid-state reactions mathematically was proposed by Jander in 1927 [149], describing the contact of two non-ideal crystal faces with an immediate formation of a product layer on the surface of one crystal:

$$\frac{2kt}{r^2} = (1 - (1 - \alpha)^{\frac{1}{3}}) \tag{1.7}$$

where r is the radii of the ice particle and α is the conversion ratio at time t. k refers to the formation rate constant. It has to be noted that the Jander equation implicitly assumes that both of the two reacting spherical crystals do not change their sizes during the whole reaction and only the product layer and the diffusion way change. It is also assumed that only the unreacted crystal diffuses through the product layer. However, it completely neglects the decrease of the reaction surface due to the shrinking of the unreacted core and the time taken for the initial enclathration stage.

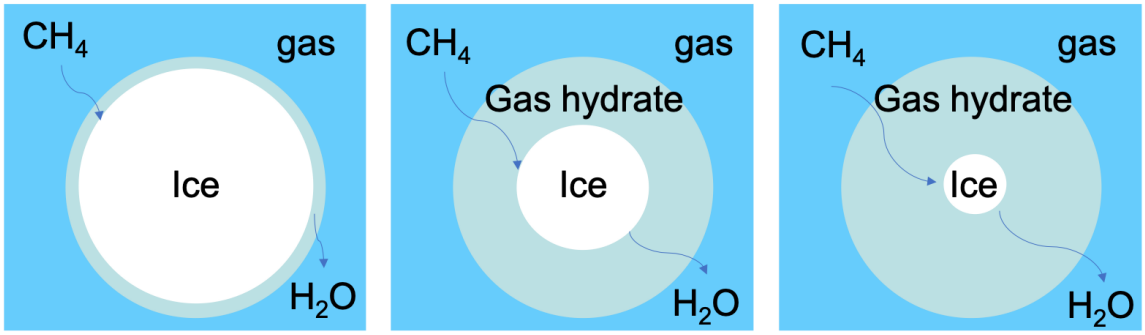

Figure 1.7 Schematic illustration of the shrinking core model during the hydrate formation process (modified from Schmalzried, 1995 [148]).

In some cases, the surface nucleation process may take a measurable amount of time t^*, which can't be neglected. Fujii and Kondo [138] gives the new equation based on the model of Jander considering the time t^* and corresponding mole conversion of the reactant α^*

$$(1 - \alpha)^{\frac{1}{3}} = \frac{-(2k)^{\frac{1}{2}}}{r}(t - t^*)^{\frac{1}{2}} + (1 - \alpha^*)^{\frac{1}{2}} \tag{1.8}$$

It is apparent that the model does not apply to the vicinity of the assumed transition time t^* as it predicts the formation rate constant k to approach infinity. This is due to a simplification of the model, which assumes that the transition from the nucleation stage to the diffusion-controlled stage occurs instantaneously for a single particle while in reality this should occur over a period of time. This model has been successfully employed for the data interpretation of the formation of CO_2 hydrates as well as CH_4 hydrates [136,139].

The model of Levenspiel [140] which is adopted by Wang et al. [139], considers the shrinking core effect. In this model, the concentration gradient of the gas is considered as constant based on the assumption that the shrinking of the unreacted core is far slower than the flow rate of the reactant through the

product layer. Moreover, the stoichiometry of the reaction is also assumed to be constant so that the ratio of the consumed number of gas reactant particles and the solid particles are constant, too. However, care has to be taken when applying the model for gas hydrate formation as they are non-stoichiometry compounds. The general expression of Levenspiel model is as follows:

$$kt = 1 - 3(1-\alpha)^{\frac{2}{3}} + 2(1-\alpha) \tag{1.9}$$

where α is the conversion ratio at time t. k is also the formation rate constant.

All the models described here are not originally developed for hydrate formation kinetics, but the diffusion process in solid-state reactions. In this study, they are carefully employed for the analysis of kinetics during the CH_4–CO_2 swapping process when solid CH_4 hydrates are exposed to CO_2 gas.

1.6 Outline of the thesis

The four-year PhD research program focused on a systematic study about the mixed gas hydrate formation, dissociation and transformation process based on the natural reservoir conditions in Qilian Mountain permafrost. The thesis was divided into 6 main chapters.

This thesis begins with an introductory overview of basic aspects of gas hydrates such as structure, composition, natural occurrences and exploration technologies. Also, a thorough description of the gas hydrates and the reservoir properties in the research area in Qilian Mountain permafrost was given. Based on the background of climate change, the important role of gas hydrates as a key chain in the global carbon circle was presented and potential hazards for gas hydrate dissociation with regard to climate warming was discussed. This chapter also consisted of a literature review of thermodynamic and kinetic fundamentals of hydrate formation process including the mathematical description of existing physical models.

The second chapter was dedicated to the introduction of the experimental set-ups and methods that were developed or applied in this study. It is widely accepted that time-resolved micro-scale analysis are essential to facilitate a systematic study on gas hydrates. That requires a proper experimental reactor which allows for the *in situ* simulation and observation of the hydrate formation, dissociation and transformation process. For this purpose, a new high-pressure cell on the basis of confocal Raman spectroscopy was developed, tested and applied/used in the course of this thesis. A unique feature of this setup was the continuous gas flow system. The whole system ensured the verification of the phase equilibrium data and a semi-quantitative determination of the hydrate

composition during the hydrate formation, dissociation and transformation process simulating natural reservoir conditions. Apart from this, batch pressure vessels and a system for experimental petrophysics (SEPP) were also used to characterize the hydrate formation kinetics and permeability properties, respectively. The other analytical tools also included powder X-ray diffraction (PXRD), Scanning Electron Microscopy (SEM), Mercury Intrusion Porosimetry (MIP). Since the objectives and samples were diverse in each single experiment, only general experimental procedures and data analytical methods were given in this chapter.

The experimental part was separated into three aspects: formation, dissociation and transformation, which were discussed individually in the following three chapters. Hydrate formation process were investigated with regard to possible effects from gas supply conditions and sediments. The results were presented in *Chapter 3*. *Chapter 4* introduced two sets of experiments related to the dissociation process of hydrates. Since an unexpected permeability decrease was observed after hydrate dissociation, possible reasons for this observation were discussed. Also, the dissociation behaviors of sI methane hydrates, sII binary methane-propane hydrates and sII multi-component mixed gas hydrates were investigated in this chapter. The conversion process of CH_4–CO_2 covered an important part of *Chapter 5*. In addition, the transformation from sII mixed gas hydrates to sI CO_2 hydrates and a reversible process from CH_4 hydrates to sII mixed gas hydrates were also studied in *Chapter 5*. The last chapter gave a thorough review and discussions about the aforementioned experiments.

Chapter 2

2 Experiments

This chapter gives an overview of the experimental setups which were developed or applied in the frame of this work, as well as the main analytical techniques namely Raman spectroscopy, Powder X-ray diffraction (PXRD), Scanning Electron Microscopy (SEM), and Mercury Intrusion Porosimetry (MIP). Raman spectroscopy is a non-destructive technique to investigate gas hydrates at a molecular level, mainly delivering information concerning the relative composition of the guest molecules, the possible occurrences of metastable or coexisting phases. A significant feature of the confocal Raman spectroscopy is the capability to measure a small area with a diameter of a few microns. However, the yield of structural information from Raman spectra is limited. Powder X-ray diffraction measurements are therefore applied which is used for the identification of the hydrate structure. In addition, a combination of PXRD, SEM and MIP are applied for the analysis of the properties of natural sediments. Since the focus of the experimental work was on Raman spectroscopy, the development, start-up and operation of the high-pressure cell plus the development of a suitable measuring procedure were an important part of this thesis. This experimental setup was designed for the *in situ* investigations of micro-scale processes in gas hydrates using confocal Raman spectroscopy. The main features of this setup as well as first results were also published by Schicks et al. [150]. Additionally, general experimental methods for the synthesis of gas hydrates and Raman spectra data analysis were introduced. All the experiments were performed at the German Research Centre for Geosciences (GFZ) in Potsdam, Germany.

2.1 Experimental setup

2.1.1 A new high-pressure cell developed for *in situ* micro-Raman spectroscopy

This sub-chapter was mainly taken from the publication Schicks et al., 2021 [150] which I contributed to carry out experiments, analyze the data, optimize the experimental parameters and draft the experimental part of the manuscript.

Raman spectroscopy is a powerful tool to determine the overall composition and the cage occupancy of a hydrate phase. This technique enables to distinguish between guest molecules in the free gas or liquid phase, encased into a clathrate cavity or dissolved in an aqueous phase. This is possible because the position of the Raman band of the respective gas molecules clearly shifts to different wavenumbers. In addition, the band width (full-width at half-maximum) are significantly higher for those gas molecules dissolved into the water phase or enclathrated into a hydrate cavity [44,129,151,152]. For instance, small gas molecules such as CH_4 do not only occupy one cavity type in the hydrate structure. They may be encased into both, small cavities (pentagonal dodecahedra, 5^{12}) and large cavities (tetrakaidecahedron, $5^{12}6^2$) of a structure I hydrate. The Raman spectra of a CH_4 hydrate show therefore, one prominent signal for the CH_4 molecule encased into the large cavities at 2905 cm^{-1} and another band at 2915 cm^{-1}, representing those in the small cavities of sI. The position of the Raman band for CH_4 dissolved into an aqueous phase, however, is at 2910 cm^{-1}, whereas the position of gaseous CH_4 is at 2917 cm^{-1} (see Figure 2.1) [151].

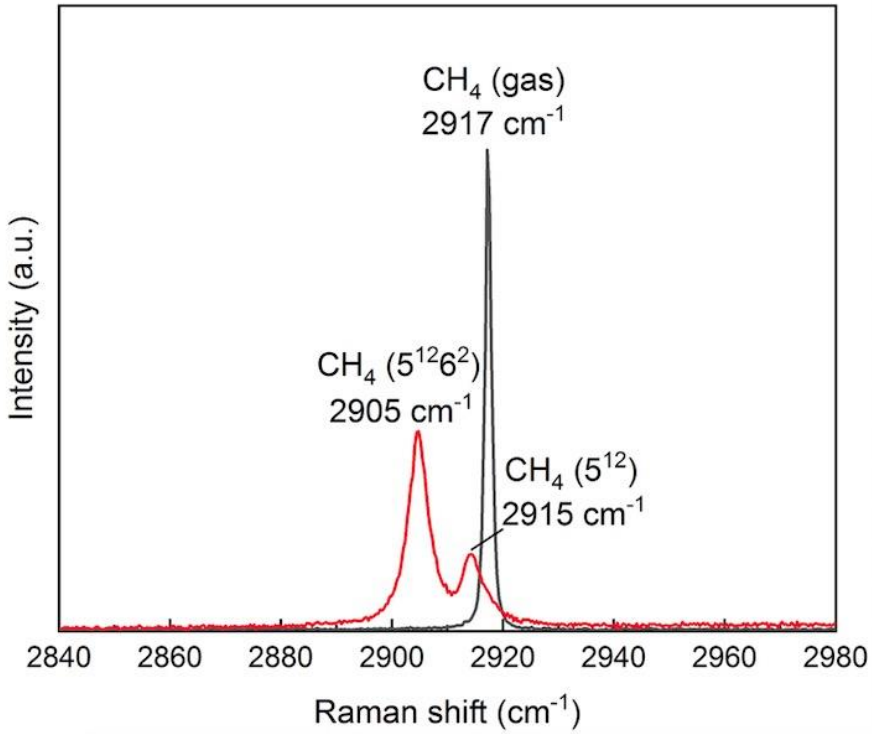

Figure 2.1 Raman spectra of CH_4: The Raman spectrum in red shows one prominent signal for the CH_4 molecule encased into the large cavities at 2905 cm^{-1} and another band at 2915 cm^{-1}, representing the CH_4 molecule encased into the

small cavities of structure I. The black Raman spectrum shows a prominent band for CH_4 in the gas phase.

Raman spectroscopic measurements on natural gas hydrate samples and synthesized gas hydrates are usually single point measurements providing a more general verification of varying hydrate compositions and coexisting phases [41,42]. The combination of Raman spectroscopy with confocal microscopy allows for the determination of spatially resolved gas hydrate compositions in three dimensions with resolution on a micrometer scale. Advanced mapping tools enable to determine heterogeneities in composition, concentration gradients and cage occupancy even within a single crystal [153]. This has been documented e.g. for a gas hydrate sample recovered in 2002 from gas hydrate outcrops on the seafloor in Barkley Canyon (northern Cascadia margin). A hyperspectral map across the hydrate crystal with the spectral region between 2800 cm^{-1} and 3000 cm^{-1} clearly indicated an inhomogeneous distribution of the guest molecules CH_4, C_2H_6 and C_3H_8 within the scanned area [154].

In recent years, a large number of different pressure cells have been developed in which gas hydrates can be formed and investigated using *in situ* Raman spectroscopy. In addition to relatively simple pressure cells with an optical window made of quartz, sapphire or diamond [155–157], piston cells with variable volumes [158], capillary cells [159] as well as diamond [160,161] and sapphire anvil cells [162] were developed and applied for the investigations of gas hydrates. All of these different cell designs are, however, only of limited suitability for investigating the formation of complex, heterogeneous and coexisting gas hydrate phases under natural conditions as this was the aim of this study. In order to be able to mimic some natural boundary conditions, the gas flow in the cell must be varied in a defined manner or the composition must be changed over time. Therefore, an ideal experimental set-up should allow to adjust and measure defined variations of gas fluctuations and changes of the feed gas composition. In this study, a new experimental set-up with a custom-made, high-pressure flow-through cell was introduced. After being integrated to a high-resolution confocal Raman spectrometer, the system enables the experimental implementation of natural hydrate formation processes. Preliminary results show that this experimental set up allows for *in situ* investigations of hydrate formation and transformation processes on a sub-µm to µm level in complex multiphase systems.

I. Raman spectrometer

Raman spectroscopic measurements were performed using a LabRAM HR Evolution dispersive Raman spectrometer from Horiba Scientific coupled to an open microscope Olympus BX-FM. The Raman spectrometer is equipped with two gratings 1800 grooves/mm and 600 grooves/mm and two laser sources: one frequency-doubled Nd:YAG solid-state laser with an output power of 100 mW (max. ~ 48 mW at sample surface) working at 532 nm and one wavelength-stabilized laser diode working at 785 nm with an output power of 300 mW (max. ~ 150 mW at sample surface). Respective edge filters are used to suppress the excitation lasers in the analyzing beam path with a cut-off at ~ 50 cm^{-1}. With a focal length of 800 mm, this spectrometer achieves a maximum spectral resolution (grating 1800 grooves/mm) of 0.5 cm^{-1} (532 nm) and 0.2 cm^{-1} (785 nm), respectively. In order to determine the spectral resolution, a Raman spectrum of neon light can be recorded and the full width at half maximum of the neon band at 1706 cm^{-1} is determined as the actual spectral resolution. A motorized pinhole in the analyzing beam path enables to variably increase the spatial resolution of laser-spot measurements. Using e.g. a 100× Olympus MPlan (NA = 0.9) objective, the maximum spatial resolution in x-y-direction is ~ 0.5 µm and ~ 1.5 µm in z-direction. By using a long-working distance objective (Olympus LMplanFLN 20×, NA = 0.4) and selecting a pinhole number of 30 µm with a 532 nm excitation laser, an optimum spatial resolution of 1.6 µm in the planar and 6.2 µm in the z direction is reached. The Raman spectral positions are calibrated employing the silicon peak (521 cm^{-1}).

A special feature of this Raman spectrometer system is the motorized, software controlled, Märzhauser Scan+ sample stage attached to the microscope. The smallest step size in x-y-dimension is 50 nm with a reproducibility of 1 µm and an accuracy of ± 1 µm. The smallest step size in z-direction is 10 nm. Since gas hydrate samples usually do not have an even, planar surface, it is important to ensure that the laser beam is focused on the samples' surface during line scans or hyperspectral mapping. An automated focus system, using a dedicated software module (ViewSharp™) developed by Horiba Scientific, estimates the samples topography within the selected surface area prior to the mapping process and thus allows for the laser beam to remain focused during the entire mapping acquisition.

Since the weight-loading capacity of the motorized sample stage is limited to ensure accurate function, a small and lightweight pressure cell has to be developed.

II Cell Design

The pressure cell has to fulfill certain requirements needed for the successful conduction of experiments investigating the formation and transformation processes of complex gas hydrate phases simulating different natural processes:

1) To mimic the fluctuations of the composition of the feed gas flux the composition of the gas phase in the sample cell has to be changed without changing pressure or temperature. This requires a continuous gas flow at constant and defined pressure and temperature conditions with an adjustable composition of the feed gas.
2) If the experimental conditions are adapted to mimic a limited gas flow, the possibility to reduce or interrupt the continuous gas flow is needed. In addition, the changes in the composition of the hydrate phase and the coexisting gas phase need to be analyzed *in situ*.
3) To avoid temperature gradients the volume of the sample chamber should be small and the sample should be consistently cooled. A fast and selective tempering of the cell is advantageous.
4) The incoming gas should be cooled before entering the sample area to avoid any heating effects and temperature gradients.
5) A transparent optical window is necessary for microscopic investigation and *in situ* Raman spectroscopic measurements.
6) The material of the sample cell requires high corrosion resistance at variable experimental conditions.
7) Since the manufacturer of the motorized sample stage recommends not to exceed a load of about 500g for its standard configuration, the weight of the pressure cell is limited.
8) Due to the limited distance between the objective and the sample stage (60 mm) the height of the cell including cooling system is limited to approx. 30 mm.

The body of the new pressure cell (Figure 2.2) designed and built at GFZ is made of Hastelloy, to ensure maximum corrosion resistance even if corrosive gases such as H_2S are used. The outer dimensions of the pressure cell are 50 mm x 50 mm x 14 mm. The cell may be operated at pressures up to 10 MPa, using a pressure controller (ER 3000, Tescom) regulating the pressure in the cell with a precision of 2% rel. The volume of the sample chamber in the center of the cell body is about 550 µl. A transparent quartz window (diameter 18 mm) allows for microscopic observation of the processes in the sample chamber and *in situ* Raman spectroscopic investigations.

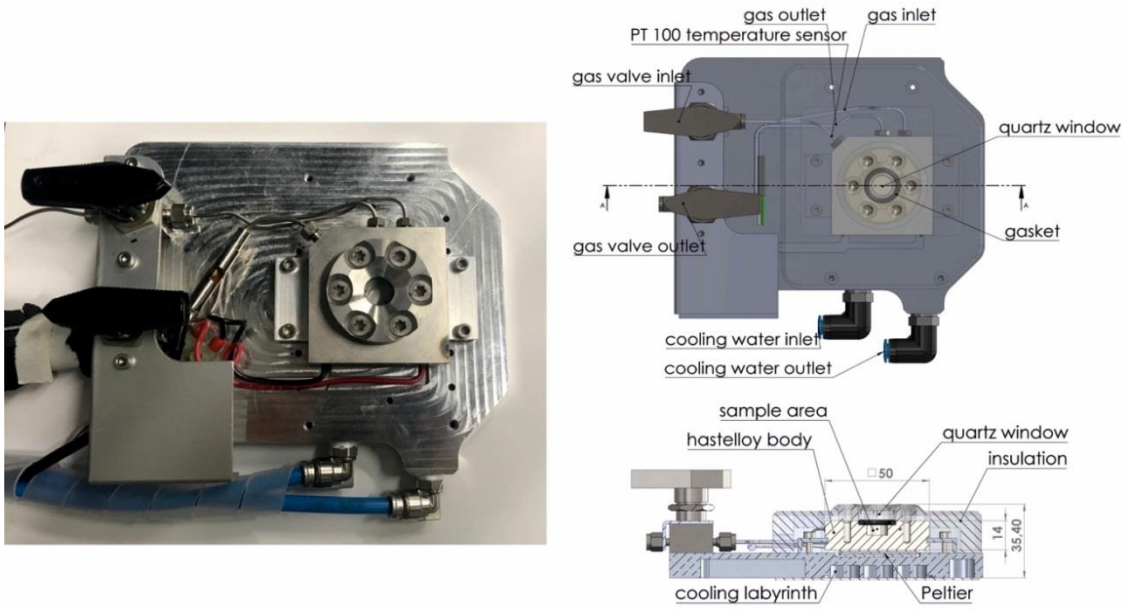

Figure 2.2 Picture of the pressure cell layout (left) as well as a sketch of the pressure cell from a top view (top right) and side view (bottom right). Dimensions are given in mm.

The bottom of the cell body is used for cooling with a Peltier cooler (Laird Technologies, Typ CP1.4-127-045L). For the temperature control a process controller (ESM-4450.1.20.1.1 from EMKO) is employed. In combination with an operational amplifier (OPA549 from Texas instruments) and a 20V/10A power supply, the controller works as a current source for the Peltier element. Water cooling of the Peltier element results in an efficient heat dissipation. This allows for a fast and precise cooling of the complete cell body with defined cooling rates where the desired temperature can be adjusted with a precision of 0.1 K. The temperature of the sample is measured with a PT 100 temperature sensor. Temperature gradients can be neglected due to the small volume of the sample area and the complete cooling of the cell body. A special feature of the pressure cell is the continuous gas flow. The gas flow is measured and regulated in the complete pressure range of the pressure cell with a commercial flowmeter (Bronkhorst HI-TEC digital mass flow controller F230M-AAD-11-K). A supply line with a diameter of max 1.6 mm and a length of 45 mm for the feed gas was drilled into the cell body to allow for the pre-cooling of the feed gas flow before entering the sample area. If the composition of the feed gas phase has to be changed, a valve located between two gas bottles with the specific gases or certified gas mixtures has to be adjusted. Two additional valves at the gas entry

and the exit of the pressure cell can be closed to interrupt the gas flow. Figure 2.3 shows the sketch of the experimental set up.

It should be noted that the initial water-cooling system has popped up with a problem, where small amorphous substances agglomerated and gradually precipitated resulting in blockages at some point of the cooling system. As a result, the pressure cell could not be cooled down to the desired temperature. In order to overcome the problem, a recirculation system was designed and installed as a supplement to the initial cooling system. The cooling liquid was replaced with Glysofor N, an environmental-friendly antifreeze concentrate based on monoethylene glycol, corrosion inhibitors and stabilizers. Since Glysofor N is completely free of nitrites, phosphates, amines, silicates and borates, it can prevent precipitation and silting, providing long-term stable cooling effects during the ongoing *in situ* experiments.

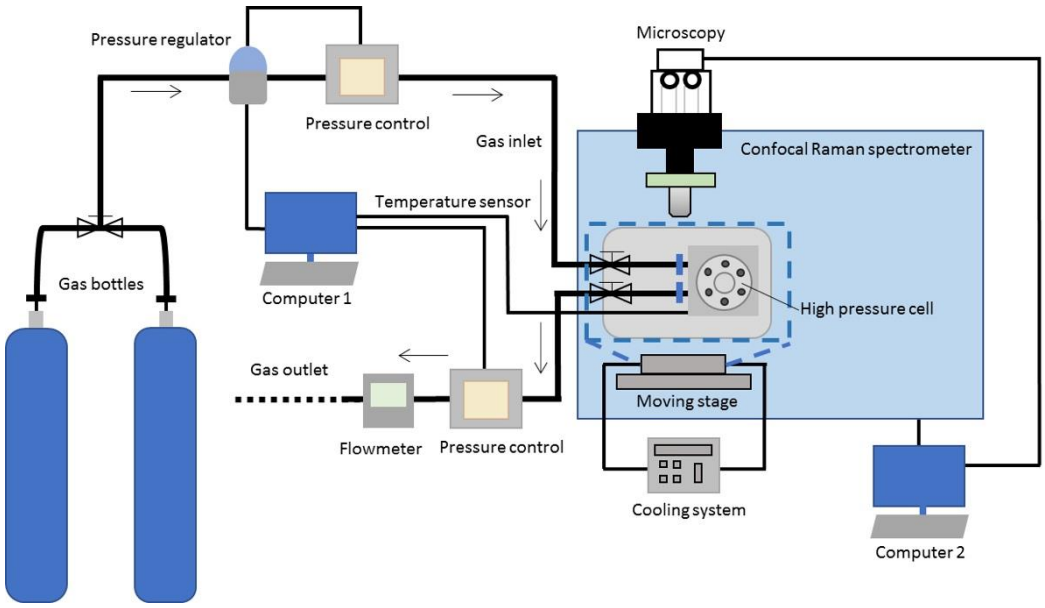

Figure 2.3 Technical sketch of the experimental set-up.

III. Data analysis and preliminary results

Determination of the (heterogeneous) composition of the hydrate phases formed from complex gas mixtures or during a transformation process using Raman spectroscopy was demonstrated in this section. Before the experiment, important Raman instrumental parameters which could affect the resulting spectra were tested and optimized over the same sample spot. For instance, high energy density from the excitation laser may destroy the hydrate sample

inducing the hydrate dissociation. On the other hand, higher laser power offers the advantage of a better signal-to-noise ratio in the resulting Raman spectra. In this case, the excitation power was adjusted via neutral density filters that result in 25%, 50%, 75% and 100% of the output laser power to find a balance between the spectra quality and the sample stability. Among the tested intensities, a 100% intensity was selected for the experiment since it provides the best signal-to-noise ratio while laser irradiation damage at the sample was not observed. With these conditions, the laser power at the sample surface is approx. 48 mW. For this specific case, the pinhole size was defined at 50 μm which offers best spatial resolution. Exposure time and number of exposures were optimized to gain best signal-to-noise ratios according to optimal total measurement times. For this experiment setup, acquisition times of 5 s and 2 averaged exposures were chosen.

For the test of the pressure cell, a gas hydrate phase was synthesized in the new high-pressure cell from water and a certified gas mixture containing 79 mol% CH_4, 8 mol% C_2H_6, 11 mol% C_3H_8, 1 mol% iso-C_4H_{10}, and 1 mol% n-C_4H_{10} at 2.2 MPa and 274 K using a continuous gas flow. This complex gas mixture was chosen because these components were detected in gas hydrate deposits in the Qilian Mountain region. Since a mixture of many different hydrocarbons often also pose a challenge for analysis by means of Raman spectroscopy, this gas mixture is most suitable for this rather methodical proof-of-concept study presented here.

In addition to the hydrate formation using the continuous gas flow, a parallel test was also carried out under identical p–T conditions but with the inlet and outlet valves being closed to mimic a closed system. In both experiments (with and without using the continuous gas flow), selected hydrate crystals were regularly characterized with single point Raman measurements during the formation process. Additional Raman measurements were taken at different depths from the surface to 120 μm below the crystal surface to find out when the hydrate crystals reached a steady state during this process.

Figure 2.4 shows the changes in average composition in the hydrate phase based on single point measurements conducted at the surfaces of 12 selected hydrate crystals and the encasement of the different components into the hydrate phase during the first 76 hours in the open system (Figure 2.4a) and in the closed system (Figure 2.4b). It turned out that C_3H_8 and iso-C_4H_{10} in the open system were enriched into the hydrate phase from the beginning of the formation process when compared to the corresponding concentrations of these components in the feed gas phase. This observation of the preferred encasement

of C_3H_8 and iso-C_4H_{10} into the hydrate phase was in good agreement with observations of Uchida et al [46]. However, the forming hydrate phase in the closed system (Figure 2.4b) revealed a different composition compared to the hydrate phase formed in the open system. It turned out that the average concentration of C_2H_6 was higher while the concentration of C_3H_8 was lower in the hydrate phase formed in the closed system. The result indicated that a limit of gas leads to the enclathration of those components which were not preferred in the open system (e.g. C_2H_6). Unfortunately, the Raman band of n-C_4H_{10} in the hydrate phase (838 cm^{-1}) was either not detectable or showed such low intensities that these data could not be used for a semi-quantitative evaluation. Thus, n-C_4H_{10} was excluded from Figure 2.4.

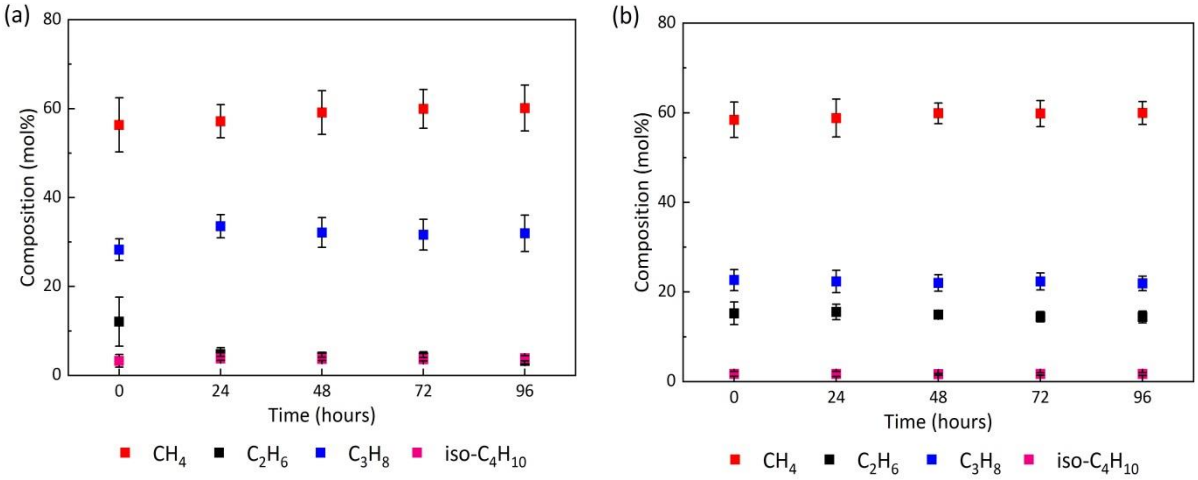

Figure 2.4 Average compositional changes measured on the surfaces of 12 selected hydrate crystals during the hydrate formation process as obtained by *in situ* Raman spectroscopic measurements in the open system (a) and in the closed system (b).

After the hydrate crystals reached a steady state in the open system where no changes were observed over time, a line scan was conducted with 12 Raman measurement points across the surface of selected crystal shown in Figure 2.5.

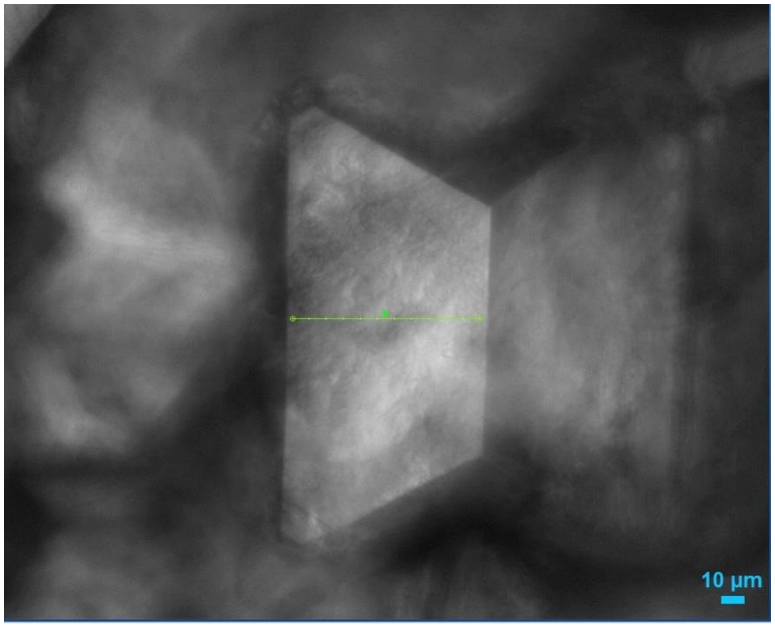

Figure 2.5 Reflected-light photomicrograph of one mixed gas hydrate crystal within the sample chamber formed from a gas mixture containing CH_4, C_2H_6, C_3H_8, iso-C_4H_{10}, and n-C_4H_{10} in the open system. The green line indicates the position of the 12 measurement spots across the crystal.

The line scan measurements on the identical crystal was repeated three times in the open system. Figure 2.6 shows the respective Raman spectra taken at one defined measurement spot of the line scan during the three runs demonstrating the high reproducibility of the Raman measurements with respect to the composition of the hydrate crystal at that specific spot and the measuring range of the motorized sample stage. Raman bands were assigned as listed in Table 2.1 according to literature data.

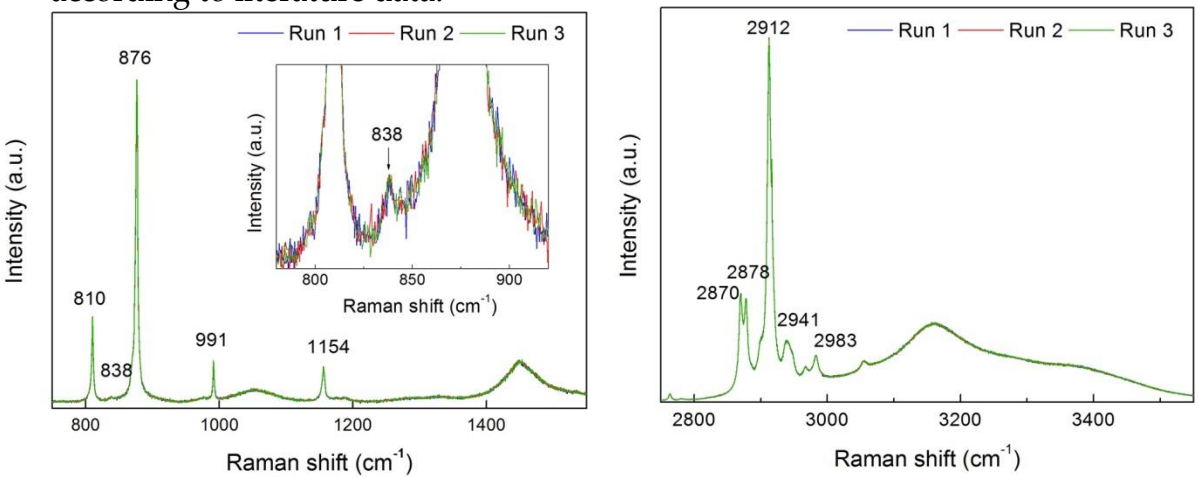

Figure 2.6 Raman spectra taken at the same defined measurement point on the surface of one hydrate crystal during the three runs of the line scan. Left: Raman

spectra taken in the range of 750–1500 cm^{-1}. Right: Raman spectra taken in the range of 2750–3550 cm^{-1}.

Table 2.1 Assignment of measured Raman bands of different types of gas molecules encased into the hydrate structure based on literature data.

Molecule	Vibrational mode	Measured [cm^{-1}]	Literature [cm^{-1}]	Reference
CH_4	C–H stretching	2912	2913	[151]
C_2H_6	C–C stretching	991	992	[163]
	C–H stretching	2941	2940	[46]
C_3H_8	C–C stretching	876	876	[46]
	CH_3 rocking	1154	1157	[164]
	C–H stretching	2870	2870	[44]
		2878	2878	[44]
	CH_2 stretching	2983	2983	[165]
iso-C_4H_{10}	C–C stretching	810	811	[46]
n-C_4H_{10}	C–C stretching	838	837	[15]

Figure 2.7 shows the average values for the composition of the hydrate crystal at each measuring point and the respective standard deviation from three repeated line scans in the open system. The results showed an excellent reproducibility, which, in turn, indicated that the measured variations in local composition of the hydrate crystal demonstrated the non-stoichiometric and inhomogeneous character of hydrate crystals. As mentioned before, the Raman band of n-C_4H_{10} in the hydrate phase (838 cm^{-1}) was either not detectable or showed such low intensities that these data could not be used for the determination of the n-C_4H_{10} proportion in the hydrate phase. It should be noted that the low enclathration of n-C_4H_{10} into the hydrate phase was not unexpected. Since the linear n-C_4H_{10} can only be incorporated into the large cages of a structure II hydrate in its gauche conformation, which nevertheless led to distortions of the cage structure, smaller and more spherical guest molecules were preferred for the enclathration into the hydrate phase [19].

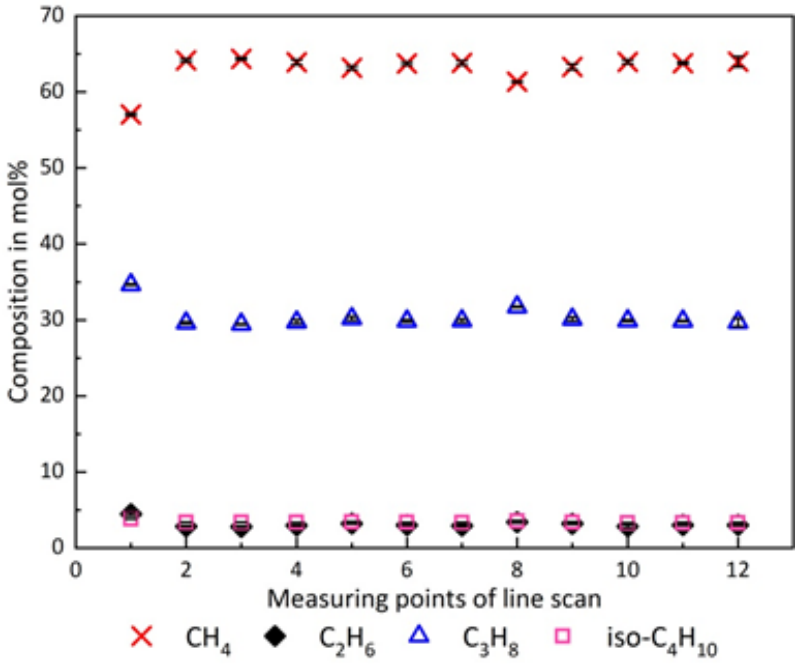

Figure 2.7 Mean values for the different components encased into the hydrate at each of the twelve measuring points across the crystal (see Figure 2.5). The error bars indicated the standard deviation. Since the values for C_2H_6 and iso-C_4H_{10} are in the same range the data points and error bars overlap.

The inhomogeneous nature of hydrates became even clearer when an area of a certain crystal was analyzed. Figure 2.8a shows the measured area of about 50x60 μm^2 on the surface of a hydrate crystal and the 35 measuring points within this area in the open system. Depending on the roughness and/or inclination of the crystal surface, the surface can be analyzed either as was or the topography of the surface must be determined using the special software "ViewSharp". Based on this topographic profile the system focused automatically on the crystal surface to ensure that all Raman spectra taken were focused on the surface and not above or below.

After finishing the mapping of the hydrate surface area, each particular Raman spectrum can be analyzed individually to determine the composition of the hydrate crystal at each specific point as described above. Since this was extensive work, in particular, if the number of measuring points in the Raman maps was higher than our example, an automatic data processing was desirable. Therefore, the LabSpec 6.5 software also offered the opportunity to carry out automated baseline corrections and the calculation of the band integral-area for all spectra and to display the generated data for each component in a color-coded map. Figure 2.8b shows the value of the band integral-area in a color code for C_3H_8.

The absolute values of each measuring point depicted as a pixel in the map that could be read out and transferred to other programs such as Excel etc. These values could also be processed and e.g. corrected with the respective cross section factors of each component.

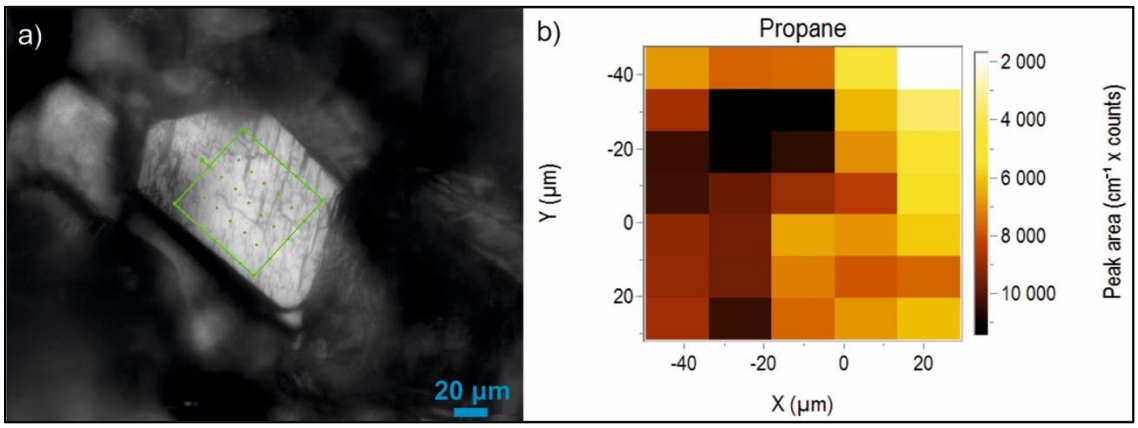

Figure 2.8 a) Scanned area on a hydrate crystal surface in the open system. 5 x 7 measuring points were chosen to analyze the composition of the hydrate crystal. b) Variation of the C_3H_8 band integral-area at 876 cm^{-1} indicating the C_3H_8 content in the hydrate crystal surface in the mapped area. Darker points reflect a higher C_3H_8 content, whereas brighter points represent a lower C_3H_8 content.

In order to verify the quality of the automatic data process options within the LabSpec 6.5 software the Raman bands of CH_4, C_2H_6, and C_3H_8 were chosen and the results of an automatic data processing were compared with the individual analysis of the Raman spectra. For this purpose, the Raman map of the hydrate crystal with 35 (7x5) measuring points was used. It turned out, that the values of the automatically calculated Raman band areas differed from the values we got when every spectrum from each related measuring point was analyzed manually. When the Raman spectra were analyzed manually, in each spectrum the baseline function was adapted individually and adjusted to the spectrum to find an optimal correction. For the automatic analysis, however, one defined baseline function was applied to all spectra, which might result in some cases in a less optimal correction and cause deviations between manually and automatically generated Raman band areas. For Raman bands with a high intensity and a high integrated area (>10000 cm^{-1} x counts) – in our case CH_4 – the statistically deviation between the manually and automatically analyzed peak areas was only about 2% rel. and therefore this statistical error could be neglected. However, for those Raman bands with smaller intensities and integrated band areas (<10000 cm^{-1} x counts) – in our case C_3H_8 – the deviations were between 5% and 10%. It

became even worse for Raman bands with very small intensities and integrated areas (< 1000 cm^{-1} x counts) such as C_2H_6 in our experiment. Here, the deviation between manually and automatically calculated values for the integrated Raman band areas could be up to 25% rel. In these cases, the interpretation of the data was highly affected by the pre-selected data-treatment method.

However, for the depiction of the variation in composition of the hydrate crystal, it was also possible to calculate the ratio of two specific components e.g. C_2H_6 and C_3H_8. In this case the areas of the Raman bands at 991 cm^{-1} for C_2H_6 and 876 cm^{-1} for C_3H_8 could optionally be corrected with or without a base line e.g. using the tool "Map Characterization" of the LabSpec 6.5 software. Figure 2.9 shows the variation of C_2H_6/C_3H_8 ratio with (Figure 2.9a) and without base line correction (Figure 2.9b). Increasing brightness reflected a higher C_2H_6/C_3H_8 ratio, whereas darker points represented a lower ratio. Figure 2.9a and b clearly demonstrated that the application of the base line correction tool leads to completely different results. In our case the results after base line correction were in better agreement with manually calculated data from Raman spectra. Nevertheless, the examples showed that care has to be taken if an automatically processing of the mapping data had to be applied.

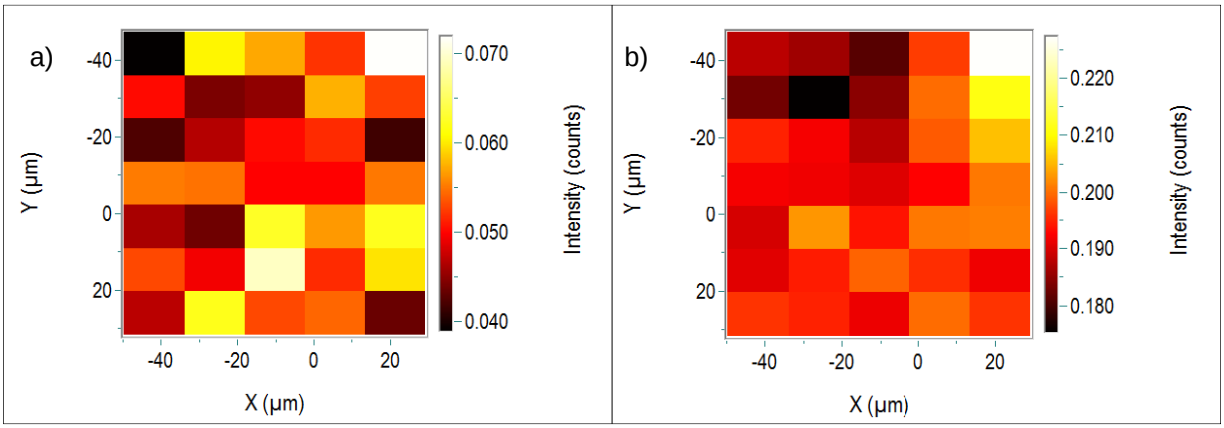

Figure 2.9 Results for the calculated variation of the C_2H_6/C_3H_8 ratio in the mapped area when base line correction was applied (a) and without base line correction (b).

The spatial resolution could be much higher than chosen in this experiment. Depending on the used objective the maximum spatial resolution in x-y-direction might reach ~ 0.5 µm; however, the input of energy due to the laser beam was not negligible and might destroy the temperature-sensitive gas hydrate crystals. Therefore, the chosen number of measuring points within the mapping area should be high enough to provide sufficient data to identify heterogeneities and

transitions to coexisting phases, but also low enough to avoid a dissociation of the hydrate phase due to the high energy impact from the laser beam.

Apart from the above-mentioned formation process, the pressure cell was also applicable for the investigation of a transformation process on a μm scale. For this purpose, a pure CH_4 hydrate was first synthesized following the same procedures as described above. After the pure CH_4 hydrate reached a steady state, the valve between two gas bottles were adjusted to change the feed gas from initial CH_4 gas to pure CO_2 gas at a constant temperature and pressure condition. Continuous Raman measurements were performed on the gas phase and hydrate phase to investigate the transformation process.

It was shown from Figure 2.10 that the CO_2 proportion in the gas phase increased dramatically within the first 500 mins after the feed gas was changed (0 min). Thereafter, the gas exchange slowed down until almost 100% CO_2 was detected in the gas phase. The compositional change in the hydrate phase was faster in the first 2 days after the exchange of feed gas phase compared to the conversion rate that was recorded thereafter. Finally, the average composition of the mixed CH_4–CO_2 hydrate was around 90 mol% CH_4 / 10 mol% CO_2 after more than 6 days.

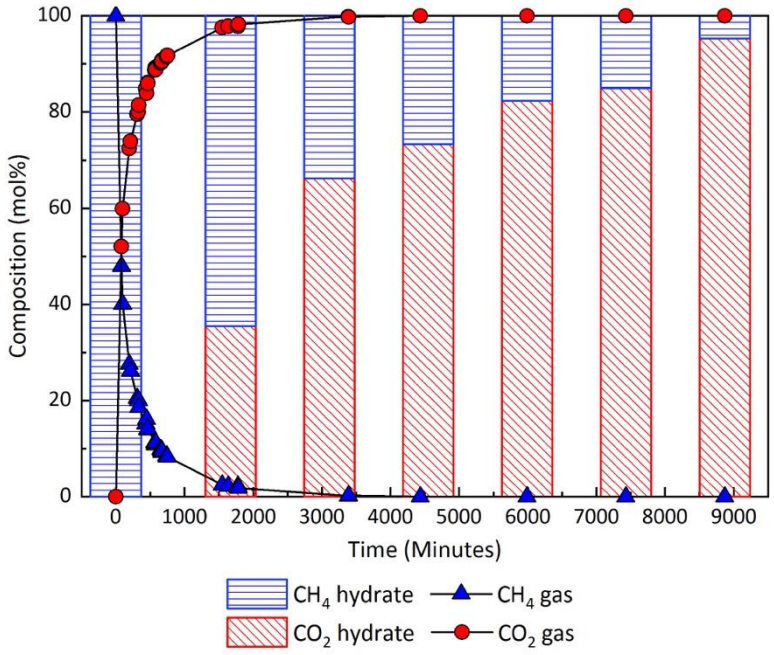

Figure 2.10 Average molar composition changes of 15 selected hydrate crystals indicating the transformation process of pure CH_4 hydrate to CO_2-rich mixed hydrates when the feed gas phase was shifted from pure CH_4 gas to pure CO_2

gas. The blue triangles and red circles illustrate the composition of CH_4 and CO_2 in the gas phase, respectively, whereas the bars indicate the composition of the hydrate phase (red—CO_2, blue—CH_4).

2.1.2 Medium-scale batch pressure vessels

For a medium-scale analysis, batch pressure vessels with a volume of about 420 ml were used in this work. Figure 2.11 shows the picture of the pressure vessels made of stainless steel. The vessels can be sealed after loading ice (with/without additives/inhibitors) into them. They can be pressurized by a specific gas/gas mixture of up to 12 MPa for the formation of gas hydrates. With the help of the pressure sensor located on top of the pressure vessel, the real-time pressure in each vessel can be continuously monitored throughout the whole process by the software catmanEasy V4.2.2. A pressure drop indicates the formation of gas hydrates with gas molecules enclathrated into hydrate structures. Based on the pressure drop and thus the resulting moles of the consumed gas, one can roughly calculate the amount of ice transformed into hydrate. In addition, hydrate samples can be recovered and stored after the vessels are opened for further *ex situ* X-ray diffraction or Raman spectroscopic measurements. It is also possible to collect the gas phase through the outlet of the pressure vessel for further analysis.

Figure 2.11 Picture of the stainless-steel pressure vessels. Each of them has a volume of 420 ml.

2.1.3 A System for Experimental Petrophysics (SEPP)

As shown in Figure 2.12, a system for experimental petrophysics (SEPP) was applied for sediment permeability measurements and hydrate formation /decomposition. SEPP consists of an autoclave with a heating/cooling jacked containing the sample setup. The inner diameter is 70 mm, and the usable length of the vessel is 250 mm. It is designed for a maximum pressure of 80 MPa. The sample setup is mounted at the top closure of the autoclave containing the feedthroughs for confining pressure oil, pore fluid inlet and pore fluid outlet, and the signal lines. The sample is separated from the confining pressure oil by means of a Viton jacket and the Hastelloy end caps. To control the sample temperature, a Pt100 temperature sensor is attached to the Viton jacket. The fluid feedthroughs in the end caps allow for pumping the pore fluid through the sample, to apply a certain pore pressure or to exchange the pore fluid. To simulate in situ pressure and temperature conditions, the autoclave is connected to a syringe pump (ISCO 100DM) to build-up the confining pressure and to a thermostat (Huber K6 s-CC-NR) to temper the sample. A detailed description of SEPP is provided elsewhere [166].

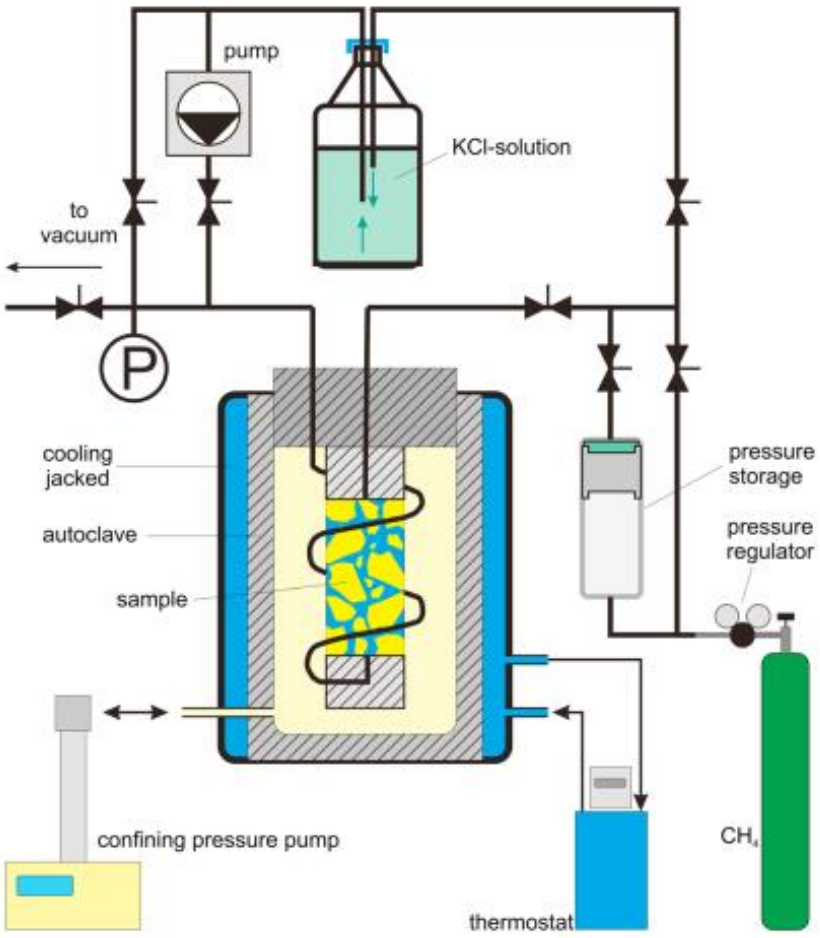

Figure 2.12 Schematic of SEPP setup.

2.1.4 Other analytical techniques

Mercury Intrusion Porosimetry (MIP)

Mercury intrusion porosimetry (MIP) is one of the most effective techniques used for the characterization of pore size, volume, distribution, density, average as well as other porosity-related characteristics of bulk materials. MIP is conducted with a Fison Instruments WS 2000 mercury porosimeter (Macropore 120, Porotec). The method is based on the pressure-dependent intrusion of mercury as a non-wetting liquid into a porous material. By penetrating mercury into the pores of a specimen, the volume of penetrated pore diameter as a function of pressure is measured. The mercury volume that intrudes at each pressure increment, corresponds to the volume of pores of each size class. With a maximum pressure of 200 MPa the pore sizes can be measured from 3.7 to 7500 nm and the range can be extended to 120 μm. Pore diameter d can be calculated from the Washburn equation [167]

$$D = -\frac{4\gamma \cos\theta}{p} \tag{2.1}$$

where p is the mercury intrusion pressure, γ is the surface tension and θ is the contact angle of mercury. A common value for γ is 0.48 N/m and θ is taken as 140° [168]. Data are analyzed using the software Pascal 140/240/440 version 1.02 by CE Instruments ThermoQuest, Milano, Italy. When the cumulative volume of intruded and extruded Hg is plotted as a function of pressure, the intrusion curves typically show a S-shaped form in the present case. The extrusion curves depict a similar form but with a small hysteresis. This behavior suggests a conical form of the pore model used for specific surface area calculations in the software.

Powder X-ray diffraction analysis (PXRD)

A Powder X-ray Diffraction analysis is a method in which a beam of X-rays is directed at a fine powder of randomly oriented grains of crystalline substances. The X-rays are scattered in directions that depend on the crystal structure of the sample and the resulting X-ray diffraction pattern can uniquely identify the material. The method is used to identify individual minerals in randomly oriented bulk rock powder samples (grain sizes <62 μm for qualitative analysis, <10 μm for quantitative analysis), or in oriented samples (size fraction < 2 μm for clay mineralogy analysis).

Sediment samples are powdered in an agate mortar and mounted onto the sample holders. XRD patterns are collected using a PANanalytical Empyrean powder diffractometer with CuKα radiation, automatic divergent and antiscatter slits and a PIXcel^{3D} detector. The diffraction data are recorded from 5 to 85 °2Θ via a continuous scan with a step size of 0.013 and a scan time of 60 s per step. The generator settings are 40 kV and 40 mA. The characterization of the minerals in the powdered samples is done with the program "EVA" (by Bruker), and the open-source program "Profex" is used to quantitatively assess the proportion of the mineral phases [169].

For the *ex situ* analysis of gas hydrate samples, the powder X-ray diffraction patterns are obtained also with the Empyrean theta-theta system (PANalytical) with Cu Kα radiation (λ = 0.15406 nm) generated at 40 kV and 40 mA. The measurements are carried out in a continuous scan mode in step width of 0.028 in the 2θ range of 8°–55° with a total scan time of 312 s. The diffracted X-rays are detected with the PIXcel^{3D} detector. The spectra are computational processed to evaluate the hydrate structure and the ratio of ice:hydrate using EVA v11.0.0.3 and AutoQuan v2.7.1.0, respectively.

Scanning Electron Microscopy (SEM)

Scanning Electron Microscope (SEM) allows for the characterization of surface morphology with a high resolution. A focused beam of high-energy electrons is used to generate a variety of signals at the surface of solid specimens. Sediment particles are placed on the SEM stub by adhesion with carbon tape. Sediment samples are coated with Au–Pd at 20 mA for 120 s using BAL–TEC MED 020 to avoid charging effects during imaging. SEM images are obtained using a secondary electron detector and a backscattered electron detector in a Zeiss Ultra Plus Field Emission-Scanning Electron Microscope (FE–SEM) in a high vacuum mode and cryo mode at acceleration voltages between 10 to 20 kV with 60 µm aperture size and between 1.5 to 3 kV with 10 to 20 µm aperture size, respectively. Elemental analysis of the samples is performed at 20 kV with 120 µm aperture size in point and shoot option using a Thermo Scientific Ultra Dry Energy Dispersive Spectrometry (EDS) detector.

2.2 Experimental methods

The experiments in this study are mainly carried out following two general procedures for the formation of gas hydrates in the high-pressure cell used for Raman spectroscopy and in pressure vessels, respectively. Based on each

specific objective, small variations are made when performing each single experiment as discussed in the following chapters.

2.2.1 General experimental procedures for the formation of gas hydrates

The experiments in the high-pressure cell using for Raman spectroscopy start with the preparation of the cell. For this purpose, the pressure cell and all supply lines are first flushed with the respective gas or gas mixture for about one hour with a gas flow of 1 ml/min. Thereafter, 150 µl of deionized and degassed water are filled into the sample cell. The cell is carefully sealed and flushed again with the respective gas or gas mixture to avoid contamination with air. Afterwards, within around 60 seconds, the pressure is set above the equilibrium pressure at given temperature of the expected hydrate phase. When the final pressure is reached and the flowrate of the gas is constant, the cell is cooled down to 253 K with ca. 2 K/min to induce the spontaneous crystallization of hydrate and ice. The growth of both ice and gas hydrate crystals can be observed over time via optical microscopy through the quartz window. Subsequently, the cell is slowly warmed up to allow dissociation of ice and most hydrate crystals until there are only a few hydrate crystals left. Then, the cell is cooled down again to a temperature below the equilibrium temperature of the hydrate phase at given pressure, but above the melting temperature of ice. Under these set conditions, euhedral gas hydrate crystals are allowed to grow. The "melting-cooling" process is carried out three times before temperature at given pressure is fixed at desired temperature. Figure 2.13 shows the picture of the hydrate formation process that was observed in the pressure cell.

Raman measurements are usually performed both on the gas phase and at different depths in the hydrate phase from the surface to the core of each crystal with a confocal pinhole of 100 µm to record the progression of the hydrate crystals. For this purpose, the laser beam is first focused on the surface of the crystal, subsequently, the position of the motorized sample stage is varied vertically (z direction) in 15 µm or 30 µm steps in such a way that the focus of the laser beam moves into the hydrate crystal. In order to obtain more information on the spatial composition of the guest molecules in the hydrate phases, a specific area of a well-structured crystal with large flat surfaces can be selected for area mapping. The selected area is scanned step by step automatically in one direction for line scans and both x-y-directions for the area maps. Typically, it takes 5–6 days until the hydrate composition in the system reaches a steady state through the hydrate crystals where no further

changes in the hydrate compositions with regard to the cage occupancy are recorded. Please note that the term "steady state" is used for a state in which the composition of the hydrate phase remains approximately constant for hours. The composition of the hydrate phase at a steady state, however, does not necessarily correspond to the composition of the equilibrium state [170].

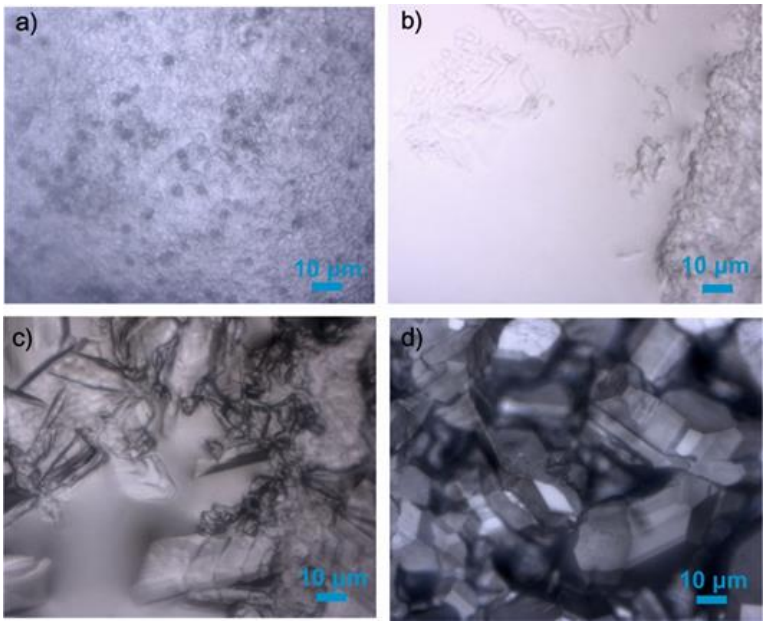

Figure 2.13 Steps of gas hydrate synthesis from liquid water. (a) Formation of ice and gas hydrates, (b) melting of ice with only a few hydrate structures left, (c) formation of gas hydrates at a temperature above ice point, and (d) euhedral hydrate crystals formed.

As an alternative hydrate formation process and for *ex situ* characterization techniques using e.g. PXRD, fine grained ice was filled into the pre-cooled batch pressure vessels. The ice was initially prepared by spraying deionized water into liquid nitrogen bath and milled in a 6750 Freezer Miller (SPEX CertiPrep) to obtain a fine ice powder [71]. Afterwards, the vessels loaded with ice powder are sealed and pressurized with the respective gas or gas mixture at desired pressure. The vessels are then stored in a freezer which is pre-cooled to the experimental temperature for several weeks. A pressure drop at the beginning of the storage indicates the formation of gas hydrates. After several weeks, no changes in pressure can be detected and the amount of ice transformed into gas hydrates can be calculated from the relative pressure drop in each vessel. Finally, gas hydrate samples are recovered from the pressure vessels and quenched into liquid nitrogen for further analysis with *ex situ* X-ray diffraction.

Table 2.2 includes the gas mixtures that are used in this work. The gas mixtures are supplied as certified gas mixtures by Rießner–Gase GmbH, Germany. The ordered gas compositions of these gas mixtures are similar to the gas mixtures released from natural hydrates recovered in QMP, containing various species of hydrocarbons as well as CO_2, besides CH_4. Since the defined composition (± 0.1 mol% rel) of the gas mixtures is only guaranteed by the manufacturer for storage at certain temperatures and for a limited period of time, Raman spectroscopic measurements are carried out on the gas phase without water before the formation of gas hydrates in each experiment.

Table 2.2 List of gas mixtures used in this work.

Composition (mol%)	CH_4	C_2H_6	C_3H_8	iso-C_4H_{10}	n-C_4H_{10}	CO_2	Chapter
Pure CH_4	100	–	–	–	–	–	4.1, 4.2, 5.1, 5.2
Pure CO_2	–	–	–	–	–	100	5.1, 5,2
Gas mixture 1	79	11	8	1	1	–	3.1
Gas mixture 2	63	15	15	–	–	7	3.2, 4.2
Gas mixture 3	71	4	8	1	1	15	4.2, 5.2

2.2.2 Raman spectra data analysis

The molar compositions in the gas and hydrate phase are determined on a semi-quantitative basis following the same calculation routine as described in Beeskow–Strauch et al. [122]. Raman peak areas of the components in a mixed system are proportional to the number of molecules present in the sample, thus the molar fraction of a component a (can be calculated using the following equation:

$$X_a = \frac{\left[{}^{A_a}/_{(\sigma_a \xi_a)}\right]}{\Sigma\left[{}^{A_i}/_{(\sigma_i \xi_i)}\right]} \tag{2.2}$$

where A_a represents the area of the Raman band of component a, σ_a is the Raman scattering cross-section factor of component a and represents instrumental efficiency. The index i represents the values for all species present in the sample and Σ is their sum.

For the determination of the band areas in the Raman spectra, the software package Labspec 6.5 is used. Each spectrum is fitted to a Gauss/Lorentz function after an appropriate background correction to estimate the band areas and positions (Raman shift). The Raman band areas are then corrected with wavelength-independent cross-section factors for each specific component. The Raman band areas are corrected with wavelength-independent cross-section factors for each specific molecule type, assuming that the cross-section factors do not vary with pressure, inclusion of the component into different cage types of the hydrate phase or the presence of other components in the different phases [171–173]. Table 2.3 presents relative normalized differential Raman scattering cross-section factors for defined vibrational modes of the guest molecules that were used in this work. The composition of the guest molecules in the hydrate phase and in the gas phase are given as mol%, assuming that the total Raman band areas for the guest molecules in each phase are set to 100%. Given the fact that the relative changes of hydrate composition over time were compared and discussed, this method for the determination of the semi-quantitative composition of the hydrate phase is sufficient. If a more precise determination of the hydrate composition is necessary, the transferability of Raman cross section factors of gas in fluid phase to gas hydrate phase remains doubtful. The varied gas concentrations under different pressures should be considered. Therefore, the method developed by Qin and Kuhs [174] should be considered as they calibrated the Raman cross section factors and determined relative Raman quantification factors.

Table 2.3 Relative normalized differential Raman scattering cross-section factors for vibrational modes of particular hydrocarbons

Molecule	**Raman shift/cm^{-1}**	**Cross-section factor**	**Reference**
CH_4	2917	8.63	[171]
C_2H_6	993	1.17	[172]
C_3H_8	870	1.60	[172]
iso-C_4H_{10}	794	2.80	[175]
n-C_4H_{10}	827	1.90	[175]
CO_2	1285	0.80	[171]
	1388	1.23	[171]

Chapter 3

3 Formation of mixed gas hydrates

Although the equilibrium thermodynamic and structural properties of gas hydrates have been well characterized in previous studies, there still remains a need for a fundamental understanding of the gas hydrate formation process. The formation of mixed gas hydrates is complicated, especially in natural reservoirs where a large number of factors such as p–T conditions, fractures, sediments, salinity etc. play significant roles in the equilibrium and formation kinetics. A comprehensive understanding of the formation mechanisms under reservoir conditions will be critical to the development of the new and improved technologies for controlling gas hydrate formation in commercial pipelines and/or for the controlled extraction of methane from natural hydrate reservoirs.

The context of this chapter presented results from two separate experiments simulating the mixed gas hydrate formation process based on the reservoir conditions in QMP. The two sub-chapters discussed the influence of gas supply conditions and sediments, respectively. The results obtained from *in situ* Raman spectroscopy and XRD measurements has laid a solid foundation to advance our knowledge on the mechanisms of the formation process.

3.1 Influence of gas supply conditions on the formation of mixed gas hydrates

This sub-chapter was mainly taken from the publication Pan et al., 2021 [176].

Natural gas hydrates occurrences contain predominantly methane, however, there are increasing reports of complex mixed gas hydrates and coexisting hydrate phases. Changes in the feed gas composition due to the preferred incorporation of certain components into the hydrate phase and an inadequate gas supply is often assumed to be the cause of coexisting hydrate phases. This could also be the case for the gas hydrate system in QMP where gas hydrates are mainly controlled by pores and fractures with complex gas compositions.

In this study, the results from the experiments simulating three potential different hydrate formation conditions based on the background in QMP were presented. Hydrates were synthesized from water and a gas mixture under

different gas supply conditions to study the effects on hydrate formation process, namely an open system with a continuous gas flow, a semi-closed system with interrupted outlet gas flow and a closed system with no further gas supply after first pressurization. *In situ* Raman spectroscopic measurements and microscopic observations were applied for the investigations on the mixed gas hydrates

3.1.1 Materials and methods

The experiments were carried out in the high-pressure cell (introduced in *Chapter 2.1.1*). Mixed gas hydrates were formed from deionized water and a complex gas mixture. The ordered gas composition was similar to the gas mixtures released from natural hydrates recovered in QMP, containing 71 mol% CH_4, 11 mol% C_2H_6, 15 mol% C_3H_8 , 2 mol% iso-C_4H_{10} and 1 mol% n-C_4H_{10} [50]. The p–T condition was finally fixed at 2.20 MPa and 274 K for the formation of mixed gas hydrates. The moment when the p–T condition first reached the desired point is defined as time zero (t = 0 min).

To investigate the hydrate formation process simulating natural reservoir conditions, three different test scenarios were carried out with different gas flows but under identical p–T conditions (Table 3.1). In test scenario 1, the inlet and outlet valves outside the sample cell were kept open throughout the whole experiment mimicking a continuous gas supply in natural gas hydrate reservoirs. Test scenario 2 was carried out with the inlet and outlet valves being closed right after initial pressurization to mimic a system with a limited gas supply. To simulate a condition that the hydrate reservoir was partially closed, the outlet valve was closed in test scenario 3 while the inlet valve was open. In this case, the gas flow was regulated in the sample cell, but not continuously, as in the first case of the continuous gas flow. In all these three tests, at least 12 hydrate crystals were selected and continuously characterized with single point Raman measurements to record the formation process of mixed gas hydrates. It took 5–6 days until the hydrate reached a steady state where the system reached a steady state. Each test was repeated for at least two times and similar results have been achieved as discussed in the following chapters. Raman spectra obtained from the experiment were analyzed according to the procedures described in *Chapter 2.2.2*. All data from this experiment are available through GFZ Data Services [177].

Table 3.1 Experimental conditions of the 3 parallel tests regarding the inlet valve and outlet valve of the Raman pressure cell.

	Gas inlet	Gas outlet	System
Test scenario 1	open	open	Open system
Test scenario 2	closed	closed	Closed system
Test scenario 3	open	closed	Semi-closed system

3.1.2 Results

1. Raman spectra of mixed gas hydrates

Experimental investigations were performed applying *in situ* Raman spectroscopy at 274 K and 2.20 MPa for the gas mixture containing CH_4, C_2H_6, C_3H_8, iso-C_4H_{10} and n-C_4H_{10}. Single point Raman measurements on more than 12 crystals showed the formation of sII mixed hydrates with the incorporation of CH_4 mainly in small 5^{12} cavities and other hydrocarbon molecules in large $5^{12}6^4$ cavities. Figure 3.1 depicts the Raman spectra of the mixed gas hydrates in the region between 700 cm^{-1} and 1100 cm^{-1} (related to C–C stretching vibrations, Figure 3.1a) and 2800 cm^{-1} and 3500 cm^{-1} (related to C–H stretching and O–H stretching vibrations, Figure 3.1b). The measured and assigned Raman band positions and corresponding literature data are summarized in Table 3.2.

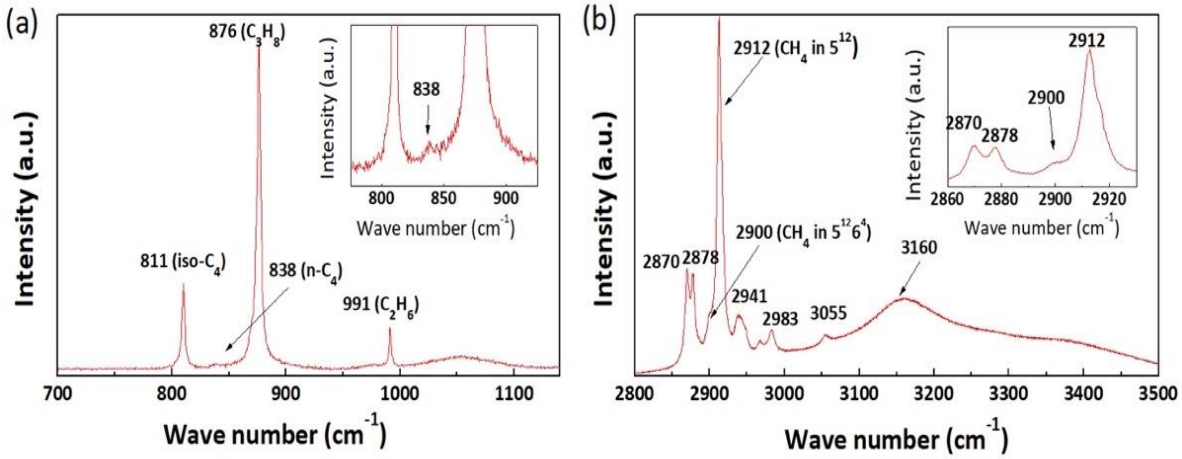

Figure 3.1 Raman spectra of the mixed gas hydrates. (a) C–C stretching vibrational modes ranged from 700–1350 cm^{-1}, and (b) C–H stretching vibrational modes and O–H stretching modes ranged from 2800–3500 cm^{-1}. The inset in Figure 3.1(a) shows the enlarged Raman band at 838 cm^{-1} whereas the inset in Figure 3.1(b) depicts the enlarged Raman bands ranged from 2860–2940 cm^{-1}.

Table 3.2 Assignments of measured Raman bands based on literature data.

Component	Vibrational mode	Cavity type	$\nu_{measured}$ (cm^{-1})	$\nu_{literature}$ (cm^{-1})	References
CH_4	C–H symmetric stretching	sII 5^{12}	2912	2912	[46]
		sII $5^{12}6^4$	2901	2901	
C_2H_6	C–C symmetric stretching	sII $5^{12}6^4$	991	991	[16]
C_3H_8	C–C symmetric stretching	sII $5^{12}6^4$	876	876	[16]
iso-C_4H_{10}	C–C symmetric stretching	sII $5^{12}6^4$	811	811	[46]
n-C_4H_{10}	C–C symmetric stretching	sII $5^{12}6^4$	838 (gauche)	838	[15]

Between 700 cm^{-1} and 1100 cm^{-1}, four characteristic Raman bands were recorded of which the largest Raman band at 876 cm^{-1} can be assigned as the C–C stretching vibration of C_3H_8 enclathrated in the large cavities of sII hydrate [44]. The Raman band with the second highest intensity was detected at approximately 991 cm^{-1}. Notably, the Raman band arose at 1000 cm^{-1} was reported by previous researches as an indication of C_2H_6 encased in the large cavities of sI hydrate whereas the Raman band at 991 cm^{-1} was for C_2H_6 in sII hydrate [178,179]. Hence, we assigned the obtained 991 cm^{-1} Raman band to the C_2H_6 encased in the large $5^{12}6^4$ cavities of sII hydrate. The positions of these two Raman bands agreed very well with the data reported from Lu et al. who also performed Raman spectroscopic measurements on natural gas hydrate samples recovered from QMP [16]. The striking Raman band in the C–C area for iso-C_4H_{10} was located at around 811 cm^{-1}. It was consistent with the Raman data for iso-C_4H_{10} encased into the hydrate phase reported by Klapp et al. [41], Subramanian and Sloan [15], and Uchida et al. [46]. The intensity of the Raman band at 838 cm^{-1} was extremely low and thus zoomed in as shown in the inset of the figure. This Raman band was related to the n-C_4H_{10} in the large $5^{12}6^4$ cavities of the sII hydrate phase [41]. The relatively low signal-to-noise ratio can be attributed to the low concentration of n-C_4H_{10} in the hydrate phase.

The existence of the CH_4 molecules in both cavities of the sII hydrate was exhibited in the Raman spectrum of the C–H stretching vibration mode. In Figure 3.1b, a prominent Raman band can be observed at 2012 cm^{-1} for the CH_4 in 5^{12} cavities. The small shoulder at approximately 2900 cm^{-1} may be an indication for a small amount of CH_4 molecules in $5^{12}6^4$ cavities of the sII hydrate. A minor Raman peak at around 3055 cm^{-1} (Figure 3.1b) indicative of CH_4 in the hydrate phase [7] could also be detected. It was important to mention that the Raman bands of CH_4 in this complex sII mixed hydrate system appeared to have a slight redshift as compared to previous sII hydrate systems with less components [46,71,151]. However, it is in good agreement with previous Raman observations on natural hydrate samples collected from QMP hydrate reservoir [68]. The band position difference could be attributed to the influence of higher hydrocarbon molecules in adjacent cavities. The double Raman bands appeared at around 2870 cm^{-1}, 2878 cm^{-1} were assigned to the C–H stretching mode of the C_3H_8 molecules in sII hydrates. They were good indicators of C_3H_8 in hydrate lattices [44]. Further signals at 2941 cm^{-1}, 2967 cm^{-1} and 2983 cm^{-1} were probably those of the C–H stretching vibrations of C_2H_6, iso-C_4H_{10} and n-C_4H_{10} [41]. Additionally, Figure 3.1b also shows the O–H stretching vibration for water molecules (3000-3500 cm^{-1}) which can be analyzed to further verify the formation of a hydrate phase. A broad Raman band can be observed at around 3160 cm^{-1} which corresponded to increased hydrogen bonds due to the formation of a well-structured hydrogen-bonded network in the hydrate phase [180]. In summary, these results confirmed that sII hydrates are formed from the gas mixture under the chosen experimental conditions. C_2H_6, C_3H_8, iso-C_4H_{10} and n-C_4H_{10} molecules are encaged only into the large cavities ($5^{12}6^4$) of sII hydrate whereas CH_4 predominantly occupies the small 5^{12} cavities of sII hydrate.

2. Enclathration sequence of gas components into the hydrate structures

Real-time Raman spectra provided information of the hydrate phase during the experiments and clarified the enclathration sequence for different components being encased into the hydrate cavities. It is worth mentioning that the sequence refers to the order of Raman bands being detected for each specific component by the Raman system and observed in the Raman spectra. Even though the induction time which indicated the first detectable signal for the enclathration of gas molecules into a hydrate cavity varied significantly under different gas supply conditions, the enclathration sequence was generally similar and independent of the gas supply conditions. Taken the results from one test as an example, Figure 3.2 shows the compiled Raman spectra taken on the surface

of a single hydrate crystal in the open system. The crystal was closely monitored during the first 3 hours. At the beginning of the experiment, only Raman bands at 2917 cm^{-1}, 993 cm^{-1} and 869 cm^{-1} were detected in the system which could be assigned to CH_4, C_2H_6 and C_3H_8 in the gas phase, respectively. It should be noted that with the use of a confocal system, Raman signals for the surrounding gas phase were limited, however, not completely avoided during the measurements of hydrate phase, especially when the measurements were carried out on the surface of the crystal.

The first indication of C_2H_6 encased into the large $5^{12}6^4$ cavities of sII hydrate came at around 16 mins when a tiny Raman band was observed at 991 cm^{-1} next to the Raman band at 993 cm^{-1} assigned to C_2H_6 in the gas phase. At the same time, a shoulder at 2912 cm^{-1} could be observed in the Raman spectra suggesting the enclathration of CH_4 molecules in the small 5^{12} cavities of sII hydrate. After around 25 mins, two small Raman bands occurred at 811 cm^{-1} and 876 cm^{-1} indicating the formation of a mixed gas hydrate phase encasing iso-C_4H_{10} and C_3H_8 in the large $5^{12}6^4$ cavities of sII hydrate. Unfortunately, we were not able to detect the Raman band for n-C_4H_{10} due to its low concentration in both the gas phase and hydrate phase during the measuring time period. With an increasing number of guest molecules being trapped into the hydrate cavities over time, the intensities of Raman bands also increased as the experiment proceeded.

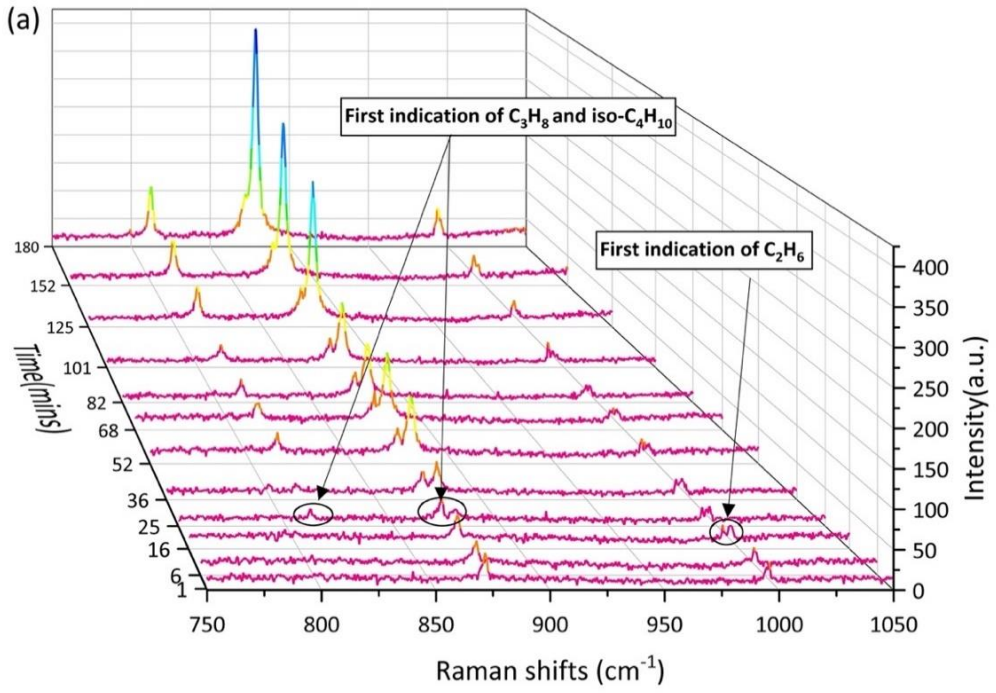

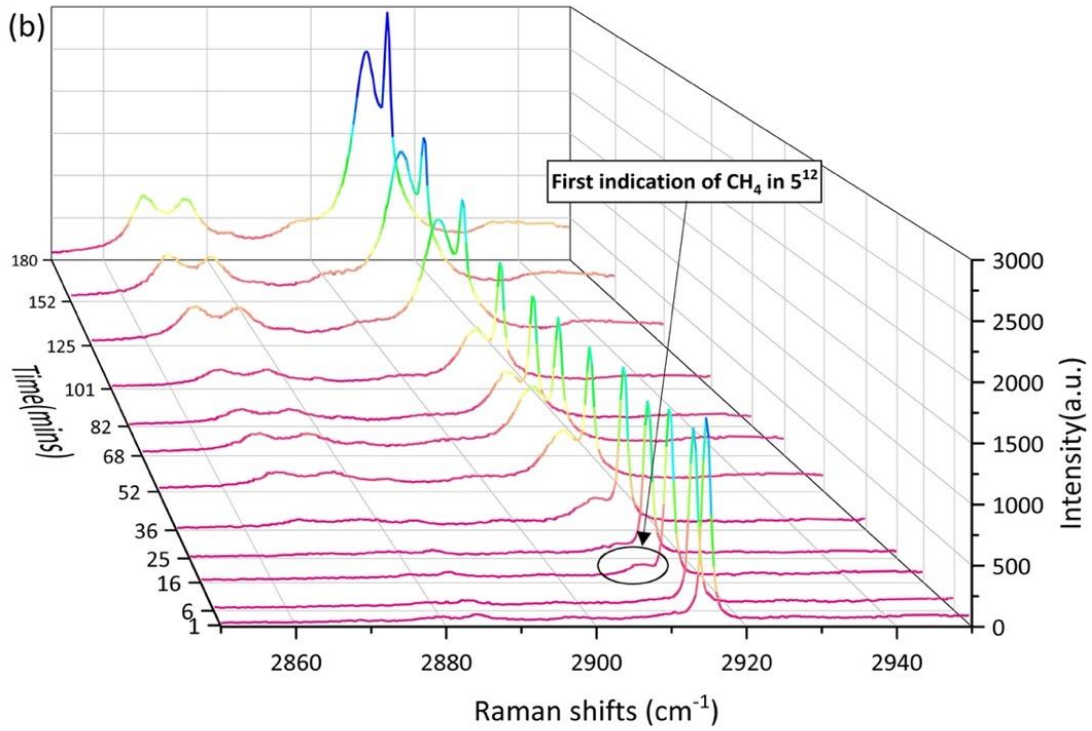

Figure 3.2 Time-resolved overview of Raman spectra in the (a) C–C stretching vibrational modes ranged from 700–1100 cm^{-1}, and (b) C–H stretching vibrational modes ranged from 2840–2950 cm^{-1} recorded on surface of a hydrate crystal in the open system during the first 180 mins.

3. Composition of the feed gas mixture

Since it was possible that the composition of the gas phase had changed over time during transportation, storage or during the experiments and their repetitions, Raman spectroscopic measurements were carried out on the pure gas phase without water (274 K, 2.20 MPa) before the experiments were conducted to determine the actual composition of the gas mixture flowing into the pressure cell. The composition of the gas phase at the beginning of the experiments and the changes of the gas phase composition during the experiments are presented in the following paragraphs. Once the mixed hydrates started to form from the feed gas mixture, the inlet and outlet valves located outside the pressure cell were set to the desired position (either open or closed) to control the supply gas flow. These changes on the gas flow were maintained throughout the whole formation process. In all three experimental systems, Raman spectra continuously recorded potential changes of composition in the gas phase over the formation period.

In the open system, investigations on the gas phase showed no significant changes over the whole formation period indicating a stable gas flow. The absolute pressure in the sample chamber was maintained at 2.20 MPa. In addition, the composition of the feed gas was the same as the initial pure gas which was composed of 71.2 ± 2.2 mol% CH_4, 11.3 ± 0.9 mol% C_2H_6, 15.4 ± 1.5 mol% C_3H_8, 1.5 ± 0.3 mol% iso-C_4H_{10}, 0.6 ± 0.2 mol% n-C_4H_{10}.

In comparison, the ongoing formation process in the completely closed system after initial pressurization resulted in a varying gas phase in the sample cell. Figure 3.3 a depicts the changes of absolute pressure in the closed system once the formation process started. Initially, the pressure in the sample cell was 2.20 MPa. With the enclathration of guest molecules into the hydrate cavities, the absolute pressure decreased to 2.13 MPa within the first 3 hours. Thereafter it became steady at around 2.11 MPa, a pressure that was higher than the equilibrium pressure of mixed gas hydrates at 274 K. This intermediate plateau lasted for several hours before the hydrate continued to form slowly until it reached a steady state. Here, we calculated the partial pressure of each gas component from five Raman measurements taken at different time during the ongoing process (7 mins, 180 mins, 1200 mins, 4450 mins and 8000 mins after initial pressurization) as shown in Figure 3.3b. Within the first 180 mins, the composition of the gas phase changed significantly and became more CH_4-rich, since C_3H_8 molecules were preferentially encased into the hydrate phase and therefore removed from the vapor phase. This resulted in a rapid decrease in pressure during the first seven minutes as shown in Figure 3a. After around 180 mins, the formation process slowed down as indicated by the "plateau" period. Thereafter, hydrocarbons (C_2H_6, C_3H_8, iso-C_4H_{10} and n-C_4H_{10}) were further removed from the vapor phase but at a slower rate as compared to that within the first 180 mins. Finally, the gas phase was composed of more than 90 mol% CH_4. This observation can be summarized as a two-step formation process which was consistent with previous findings from Uchida et al. [44] on the CH_4–C_3H_8 mixed gas hydrates formed in a batch-type reactor.

As for the semi-closed system where the outlet gas was interrupted, the gas phase changed less pronounced compared to that in the closed system due to the supplemented gas flow from the inlet. However, it was also slightly different from the gas in the open system, containing a higher concentration of C_2H_6 and C_3H_8 but a lower concentration of CH_4 from the beginning of the experiment. The absolute pressure decreased due to the enclathration of gas molecules into hydrate structures likely accompanied with a depletion of certain gas

components in the gas phase. With a pressure decrease of more than 0.05 MPa the pressure regulator was activated and corrected the pressure in the sample cell to 2.20 MPa. However, the depletion of certain gas components between two pressure regulation surges was not detected with the individual measurements. The average gas composition was around 67.0 ± 1.8 mol% CH_4, 13.0 ± 1.3 mol% C_2H_6, 17.6 ± 2.0 mol% C_3H_8, 1.6 ± 0.3 mol% iso-C_4H_{10}, 0.8 ± 0.5 mol% n-C_4H_{10} during the ongoing process.

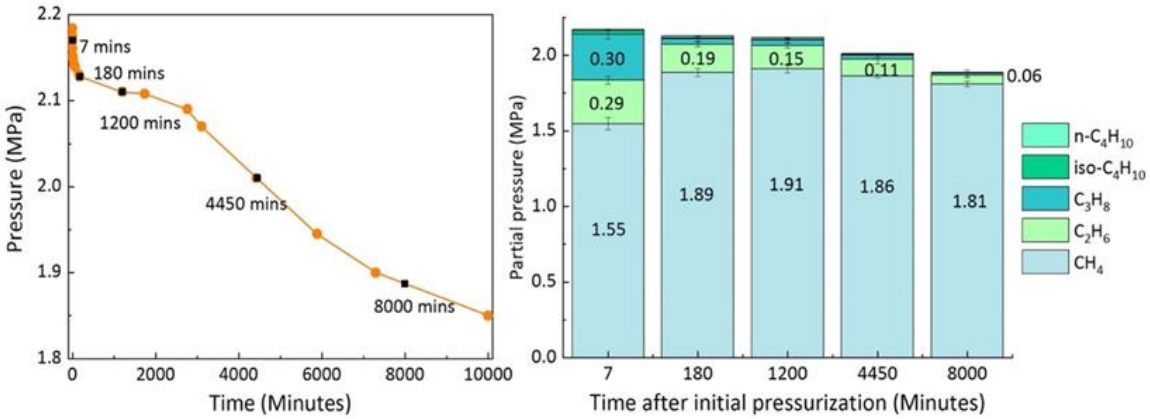

Figure 3.3 Changes in the absolute pressure of the sample cell (Figure 3.3a) and the partial pressure changes of each component measured at different time in the closed system (Figure 3.3b). The black squares in Figure 3.3a indicated the specific measuring time during the ongoing experiments.

4. Composition of the mixed gas hydrates

Our systematic Raman spectroscopic investigations on the mixed gas hydrates revealed the whole formation process of sII hydrate by detecting the enclathration of CH_4, in small 5^{12} cavities and C_2H_6, C_3H_8, iso-C_4H_{10} and n-C_4H_{10} in large $5^{12}6^4$ cavities. In this section, we determined the composition of the formed mixed gas hydrates under different formation conditions with regard to the gas supply. It was noteworthy that the accuracy of Raman measurements was calibrated before the experiment on a mixed gas hydrate crystal with a few measuring points. A good reproducibility of the measurements was confirmed with an average standard deviation of 0.2 mol% for the measuring points over three repeated tests. Therefore, the scattered composition of hydrate crystals detected during the experiments indicated the heterogeneity of the hydrate phase in the systems.

Figure 3.4 shows the changes of composition in the hydrate phase based on single point measurements on the surfaces of 12 selected hydrate crystals in three systems. Surprisingly, the concentration of C_2H_6 in the hydrate phase was higher

at the very beginning of the hydrate formation process but decreased over time whereas the content of CH_4 in the hydrate phase slightly increased with time in the open system (Figure 3.4a). As for C_3H_8 and iso-C_4H_{10}, the concentrations did not change significantly over time. Unfortunately, Raman bands for the n-C_4H_{10} in the hydrate phase was either not detectable or with low intensities, and was therefore excluded from this figure. In the closed system which was carried out under identical p–T conditions but with no gas supply after initial pressurization, the formation process slowed down as indicated by the microscopic observations. Figure 3.5 shows two microscopic pictures of hydrate crystals taken in the open (Figure 3.4a) and closed system (Figure 3.4b) after 30 mins, respectively. Instead of transforming to well-developed sharp-faceted euhedral crystals, the crystals in the closed system were small and without sharp edges after the same time. Apparently, the concentration of C_2H_6 and CH_4 in the closed system increased on the first day, whereas the concentration of C_3H_8 and iso-C_4H_{10} declined as seen from Figure 3.4b. Only a small variation was observed for the 12 hydrate crystals regarding the composition at a steady state. In the semi-closed system (Figure 3.4c), the composition for the selected hydrate crystals scattered over a wide range, especially on the first two days, showing a high heterogeneity of the hydrate phase. It turned out that the concentration of C_2H_6 declined sharply on the first day of the experiment whereas the concentration of CH_4 increased. This trend was consistent with the findings in the open system (Figure 3.4a). Afterwards, the composition of the hydrate phase stabilized and the whole system reached a steady state. The data presented in Figure 3.4 were obtained from one of the tests for each gas supply condition. However, similar phenomenon was observed when repeating the experiments as can be seen from the supporting information (see supporting information, Figure S1).

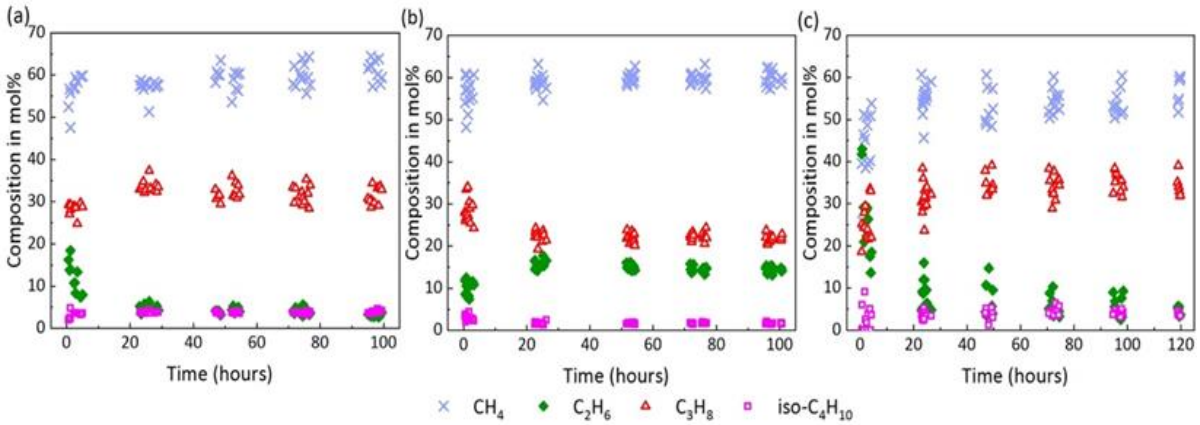

Figure 3.4 Composition changes measured on the surface of selected mixed

hydrate crystals over the formation process in the open system (a), the closed system (b), and the semi-closed system (c).

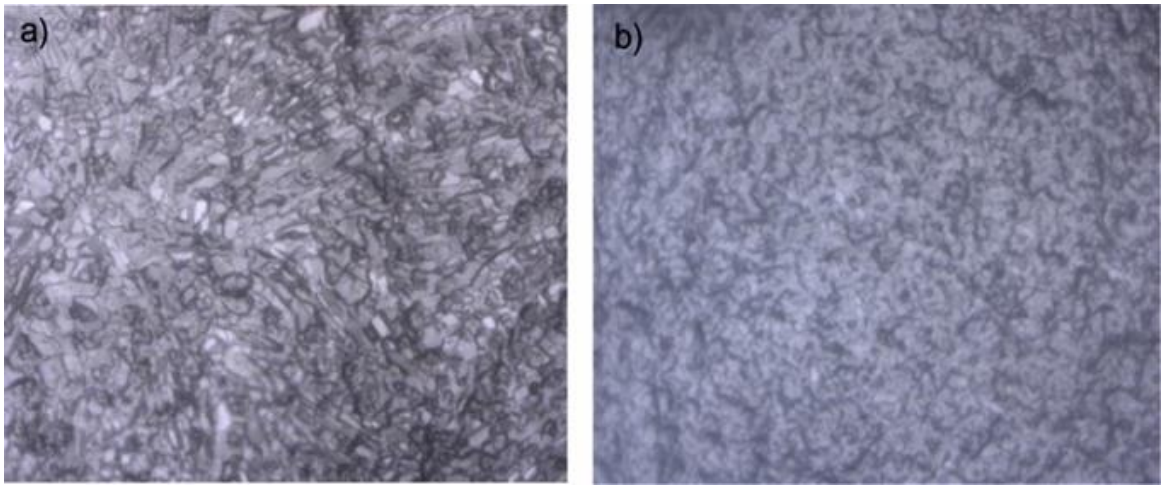

Figure 3.5 Microscopic pictures of hydrates crystals formed (a) in the open system and (b) in the closed system at t = 30 mins after initial pressurization.

As demonstrated from the above Figure 3.4, significant changes in the concentration of guest molecules always occurred within the first day of the experiment. After 5–6 days, the systems were assumed to reach steady states when no significant changes regarding the composition of the hydrate phase were observed. Therefore, the average composition of the hydrate phase was analyzed after first 30 mins, after first 4 hours and after 5 days at a steady state, respectively. The results were summarized in Table 3.2 and presented in Figure 3.6. Errors bars were calculated from standard deviation of average compositions over the repeated experiments.

Table 3.3 Average composition of the hydrate phase formed under different gas supply conditions.

Experimental condition	**Time**	**Average concentration of each component in the hydrate phase (mol%)**				
		CH_4	**C_2H_6**	**C_3H_8**	**iso-C_4H_{10}**	**n-C_4H_{10}[1]**
Open	After 30 mins	58.4	11.1	27.8	2.7	0.0
	After 4 hours	60.6	5.7	29.5	3.7	0.6
	After 5 days	64.3	2.8	29.0	3.3	0.5
Closed	After 30 mins	59.6	8.5	28.0	3.9	0.0
	After 4 hours	58.4	9.8	28.7	3.1	0.0

	After 5 days	60.8	14.3	21.5	1.6	1.8
Semi-closed	After 30 mins	32.2	41.0	21.2	5.6	0.0
	After 4 hours	49.1	17.9	27.8	3.9	1.3
	After 5 days	54.8	4.7	35.5	3.8	1.1

[1] n-C_4H_{10} was not detected in the Raman spectra after 30 mins.

In the open system, the most noticeable change with regard to the composition of the hydrate phase after 30 minutes and 4 hours was the decrease in the proportion of C_2H_6 (Figure 3.6). It should be noted, however, that the composition of the crystals varied much more after 30 minutes than after 4 hours. As seen from the left side of Figure 3.6, larger molecules such as C_3H_8 and iso-C_4H_{10} were preferentially enriched into the hydrate phase from the beginning of hydrate formation when compared to the corresponding concentrations of these components in the gas phase. Finally, the average composition of the resulting mixed hydrate crystal at a steady state was around 64.3 mol% CH_4, 2.8 mol% C_2H_6, 29.0 mol% C_3H_8, 3.3 mol% iso-C_4H_{10}, 0.5 mol% n-C_4H_{10} (Figure 3.6). This composition was very close to the equilibrium composition of the hydrate phase calculated with CSMGem which was 61.6 mol% CH_4, 2.6 mol% C_2H_6, 30.5 mol% C_3H_8, 5.0 mol% iso-C_4H_{10}, and 0.5 mol% n-C_4H_{10}. CSMGem is a software that is developed by Colorado School of Mines and is widely used for the prediction of thermodynamically stable hydrate structure and cage occupancies in specific systems [5]. Our experimental results clearly indicated a preferred enclathration of the C_2H_6 in the hydrate cavities at the beginning of the experiment. However, the ability of C_2H_6 molecules to stabilize the cavities was supposed to be less pronounced compared to C_3H_8 or iso-C_4H_{10} which led to a decrease in the concentration at the end of the experiment indicating that C_2H_6 was not enriched in the hydrate phase [181]. In contrast, C_3H_8 and iso-C_4H_{10} were enriched in the hydrate phase; their concentration was higher in the hydrate phase as compared to the feed gas phase. Apart from C_2H_6, the proportion of the other components in the hydrate phase increased slightly as the experiment proceeded.

In the closed system the composition of the hydrate crystals also varied significantly after the first 30 mins. n-C_4H_{10} could not be detected in the hydrates phase at that time. The formed hydrate phase had a similar composition as that formed in the open system. Thereafter, the composition of the hydrate phase slowly adapted to the changes in the gas phase, which was depleted in C_3H_8. The hydrate phase at a steady state contained around 60.8 mol% CH_4, 14.3 mol% C_2H_6,

21.5 mol% C_3H_8, 1.6 mol% iso-C_4H_{10}, 1.8 mol% n-C_4H_{10}. Obviously, more C_2H_6 was incorporated into the hydrate phase and n-C_4H_{10}, which was though only encased into the hydrate phase in small quantities, was detected in the hydrate phase at steady state (Figure 3.6). The results indicated that a limit of gas supply had led to the enclathration of those components which were not preferred in the open system (e.g. C_2H_6 and n-C_4H_{10}). Accordingly, the proportions of C_3H_8 and iso-C_4H_{10} which were preferentially enriched in the hydrate phase in the open system, were lower in the hydrate phase in the closed system.

Due to a frequent re-adjustment of the gas flow in the semi-closed system, an average composition of 32.2 mol% CH_4, 41.0 mol% C_2H_6, 21.2 mol% C_3H_8, 5.6 mol% iso-C_4H_{10} was recorded in the hydrate phase after the first 30 mins. C_2H_6 and iso-C_4H_{10} were extremely enriched in the initial hydrate phase as compared to those in the other two systems. A decrease in C_2H_6 and iso-C_4H_{10} concentrations was observed after 4 hours with an increasing of CH_4, C_3H_8 in the semi-closed system. This trend was quite similar to that in the open system, but it was much more pronounced in the semi-closed system. For the resulting hydrate phase at a steady state, the composition changed to 54.8 mol% CH_4, 4.7 mol% C_2H_6, 35.5 mol% C_3H_8, 3.8 mol% iso-C_4H_{10}, 1.1 mol% n-C_4H_{10}. This average composition of the hydrate phase at steady state did not yet correspond to the CSMGem calculated composition of the hydrate phase at equilibrium state with 59.8 mol% CH_4, 2.7 mol% C_2H_6, 32.1 mol% C_3H_8, 4.8 mol% iso-C_4H_{10}, 0.7 mol% n-C_4H_{10}. Since the composition of the gas phase in the semi-closed system contained less CH_4 and more C_3H_8 compared to the gas mixture used in the experiments in the open system, a higher C_3H_8 and a lower CH_4 concentration were detected in the resulting hydrate phase. Apart from C_3H_8, iso-C_4H_{10} and n-C_4H_{10} were also enriched in the hydrate phase under this circumstance.

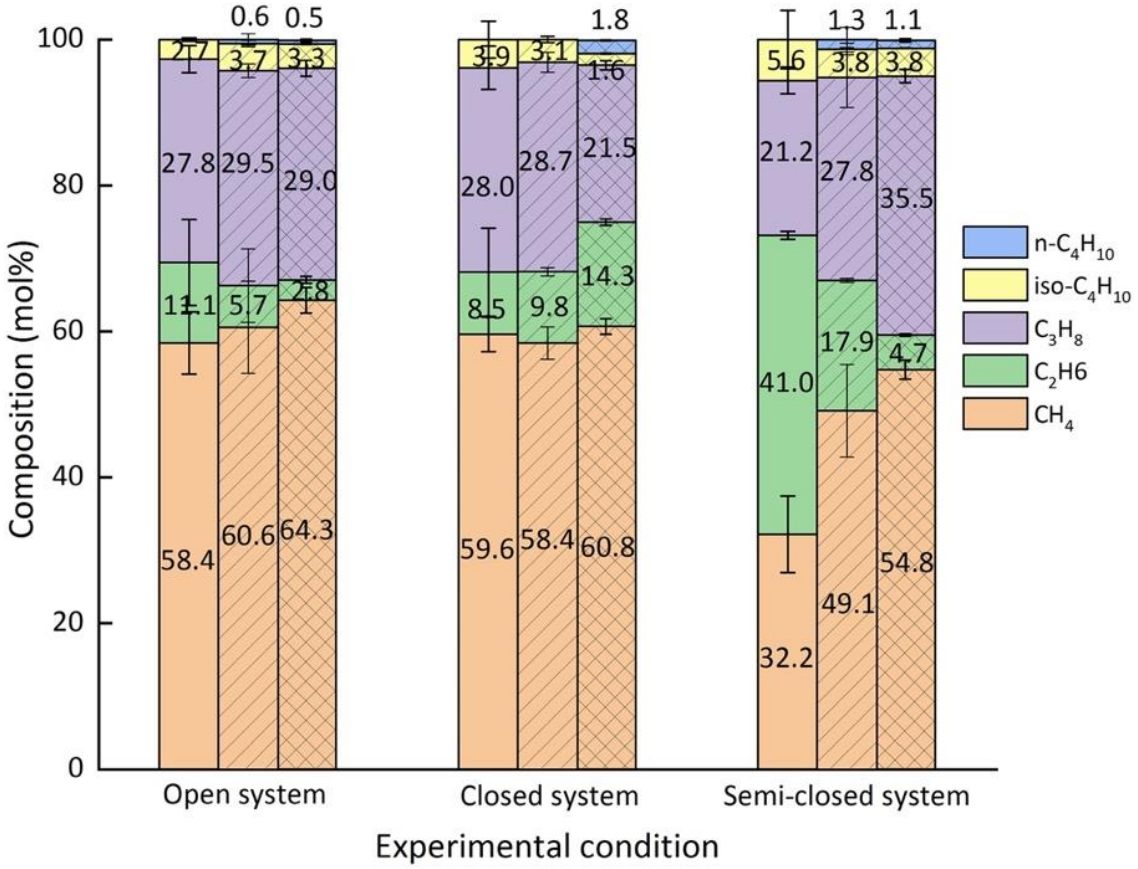

Figure 3.6 Average composition of the measured hydrate crystals formed under different gas supply conditions after 30 mins (blank), after 4 hours (slash shaded) and after 5 days (oblique lines grid). The standard deviation of the average composition in repeated experiments were used for the descriptive error bars.

3.1.3 Discussion

Our time-resolved Raman spectroscopic investigations (Figure 3.2) during the formation process showed a faster incorporation of CH_4 and C_2H_6 in the hydrate phase followed by the enclathration of C_3H_8 and iso-C_4H_{10}. This observation of the enclathration sequence was independent of the gas supply conditions. A possible explanation for this phenomenon may be found in the nucleation process (see details in *Chapter 1.5.1*). It is experimentally challenging to verify which of the three nucleation mechanisms is correct. However, the labile cluster hypothesis shows a higher universal validity when compared to the other two hypotheses and may explain the enclathration sequence observed in our experiments.

It is widely accepted that driving force for the hydrate formation is the difference of chemical potentials between the aqueous phase and the hydrate crystals. To induce the hydrate formation, aqueous phase needs to be

supersaturated as the first step [117]. Based on the labile cluster hypothesis, Walsh et al.[126] and Jacobson et al. [127,128] suggested that the dissolved CH_4 molecule which is surrounded by 20 water molecules in the aqueous phase can easily transform to CH_4 encased into a 5^{12} cavity, whereas the formation of other cavity types is hindered because it requires the incorporation of additional water molecules. This might be a possible explanation for the short induction time of CH_4 as shown in the Raman spectra of our study. Additionally, the initial concentration of CH_4 in the gas phase is the highest of all the guest components in this experiment. As for C_2H_6 and C_3H_8, their solubilities in water phase may play a significant role. Table 3.3 tabulates the properties of guest molecules as well as the guest-to-cavity ratios of each component in sII hydrates. Commonly, C_2H_6, C_3H_8 have slightly higher solubilities under specific p–T conditions when compared to other components. Therefore, a higher concentration of C_2H_6 and C_3H_8 can be expected in the initial water phase which certainly leads to a faster detection of these two components in the hydrate phase. Interestingly, however, the less soluble iso-C_4H_{10} is also incorporated into the hydrate structures at the same time as C_3H_8. This is probably due to a high guest-to-cavity ratio of iso-C_4H_{10} in the $5^{12}6^4$ cavities of sII hydrate. A higher guest-to-cavity ratio is probably also the reason for the observation that the concentration of C_2H_6 decreased gradually over time whereas the concentration of C_3H_8 and iso-C_4H_{10} either increase or at least maintain in the hydrate phase. It is well known that the hydrate cavities are stabilized by the inclusion of guest molecules. According to previous research from Lederhos et al. [14] a guest-to-cavity ratio between 0.75 and 1.0 is conducive to stabilize clathrate cavities. In this case, the ratio for C_2H_6, C_3H_8 and iso-C_4H_{10} are all within this range according to the results shown in Table 3.4. Among them, C_3H_8 and iso-C_4H_{10} are expected to best stabilize the large $5^{12}6^4$ cavities since the guest-to-cavity ratio is close to 1.0 which indicates a minimum energy. Our observation of the preferred encasement of C_3H_8 and iso-C_4H_{10} in hydrate phase throughout the whole formation process is in good agreement with the findings from previous studies [46,48]. The situation for n-C_4H_{10} is much more complicated. It should be noted that n-C_4H_{10} has two well-known rotational isomers, trans and gauche, since it is a linear alkane and the CH_3CH_2 fragments can rotate around the central C-C bond. The trans form is the energetically most stable conformer of n-C_4H_{10} [18] but it is supposed to be too large even to fit into the $5^{12}6^4$ cavities. Thus, only the gauche conformation of n-C_4H_{10} can be incorporated into the distorted cage structures [19] and an optimization process of the hydrate structure is requested before the successful incorporation of n-C_4H_{10}. Nevertheless, the detected average composition of the

hydrate phase was also in good agreement with the hydrate composition at equilibrium state calculated with CSMGem. Figure 3.7 compares the actual gas composition with the respective composition of the formed hydrate phase in three separate systems.

Table 3.4 Properties of guest molecules as well as the guest-to-cavity ratio of each component in sII hydrate. Except for the solubility data from Air Liquide Germany GmbH, all the other data were from Sloan and Koh, 2008 [5].

Molecule	Structure	Solubility (mmol/L) [1]	Guest diameter (Å)	Guest-to-cavity ratio	
				5^{12} (sII)	$5^{12}6^4$ (sII)
CH_4	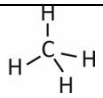	1.6	4.36	0.87	0.66
C_2H_6	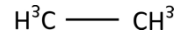	2.2	5.50	1.10	0.83
C_3H_8	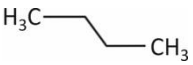	1.8	6.28	1.25	0.94
iso-C_4H_{10}	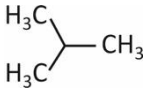	1.0	6.50	1.29	0.98
n-C_4H_{10}	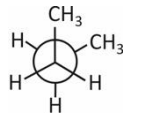 (gauche)	1.6	7.10	1.41	1.07
	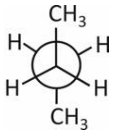 (trans)		7.86	1.57	1.18

[1] Solubility in water at 20 °C and under normal pressure.

In the closed system, the absolute pressure in the sample cell decreased gradually due to the enclathration of guest molecules into the hydrate structures (Figure 3.3). Nevertheless, the p–T conditions were still within the stability field of a mixed gas hydrate as estimated by the CSMGem. In other words, a coexisting hydrate phase with different composition compared to the initial formed hydrate phase could have formed in the closed system from the changing gas phase. After the first 4 hours the measured hydrate crystals showed quite low variations regarding the composition (Figure 3.4 and Figure S1). We therefore calculated the thermodynamically stable hydrate composition in

CSMGem, applying the real-time pressure and gas phase composition after 30 mins, 4 hours and 5 days, respectively. It is noticeable that the measured composition of the hydrate phase after 30 mins corresponded approximately to the equilibrium composition calculated by CSMGem. However, the hydrate composition after 4 hours showed a much higher C_3H_8 concentration and a lower CH_4 concentration as compared to the predicted equilibrium composition. The hydrate phase after 5 days deviated completely from the calculated results. It was also not possible to detect any coexisting hydrate phase in addition to the original hydrate phase, which had a composition corresponding to the p–T conditions and the composition of the actual gas phase at that time. As indicated in Figure 3.3, the formation of hydrates took place mainly within the first few hours. Thereafter, the formation process slowed down with the decreasing pressure in the system. In the framework of this experiment (5 days), the system was far from the equilibrium state but slowly adapted to the changes in the gas phase (Figure 3.7).

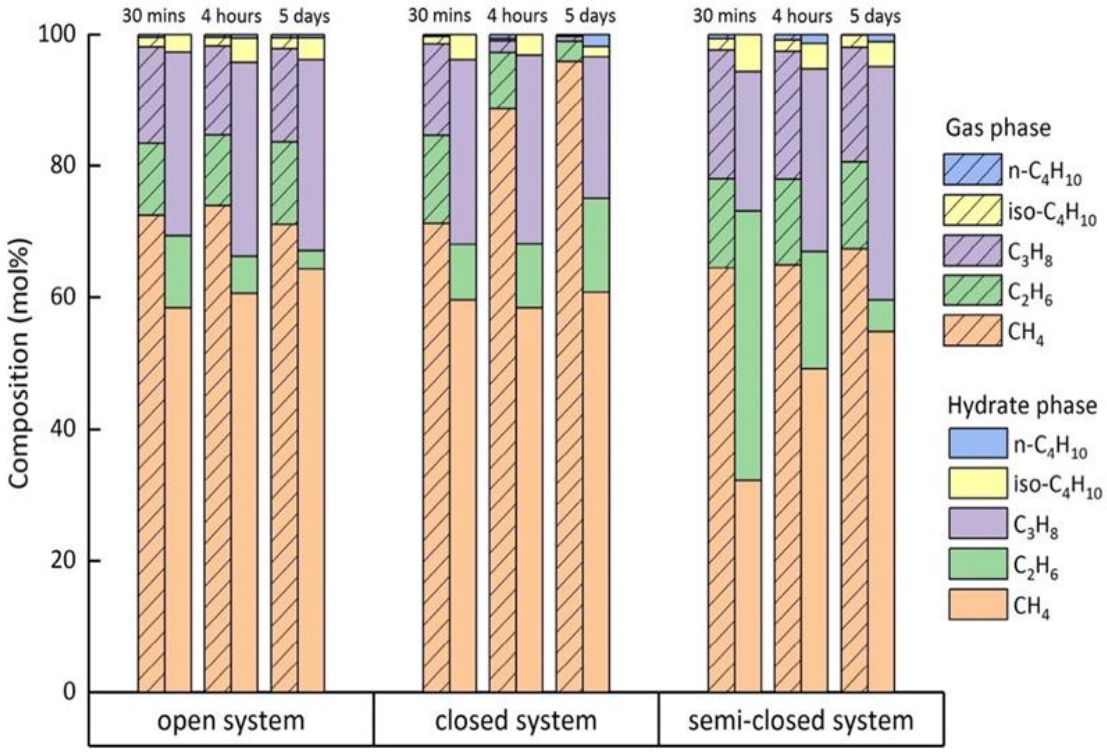

Figure 3.7 Comparison of actual gas phase composition (slash shaded) with the respective composition in the hydrate phase (blank) in all three systems.

For the results detected in the semi-closed system, the composition of the analyzed 12 hydrate crystals were highly heterogeneous and varied strongly within the first 4 hours. Unlike the gas phase in the open system with a

continuous gas flow, the pressure in the semi-closed system decreased slightly due to the hydrate formation until the pressure regulator was initialed to adjust the pressure in the sample cell again to the original value by pumping in fresh gas. During the time when the pressure was slowly decreasing, individual components could become depleted in the gas phase. These gas components, possibly due to diffusion processes, may flow in following the concentration gradient. The frequent turbulence caused by the re-pressurization process in the gas phase may be a potential explanation for the high heterogeneity occurred within the first 4 hours. As the hydrate formation process slowed down after 4 hours, the frequency of pressure regulation also decreased, resulting in a lower heterogeneity in the hydrate composition. Nevertheless, the measured composition of the hydrate phase did not reach the calculated composition at equilibrium state (calculated with CSMGem). It should also be mentioned that some of the selected crystals, especially those with smaller sizes in the semi-closed system, disappeared during the ongoing process and therefore it was not possible to continuously characterize the changes throughout the whole experiment. Instead, new crystals were selected for the Raman measurement during the process. This disappearance of smaller crystals is reminiscent of a process similar to Ostwald ripening [182,183].

3.1.4 Conclusions

In this study, we present the results from our experiments simulating the mixed gas hydrate formation in nature applying *in situ* Raman spectroscopic measurements and microscopic observations. Based on the background in QMP, the experiments were carried out with a complex gas mixture under three different gas supply conditions, namely the open, closed or semi-closed system respectively. Despite the fact that the initial feed gas was almost the same for three experiments, the composition of the gas phase in the pressure cell changed during the experiment in the different systems and therefore the composition of the resulting hydrate phases differed significantly. The semi-quantitative analysis on both the gas phase and hydrate phase during the formation process provided important information about the gas fractionation and high selectivity of guest molecules encased into hydrate structures with regard to the reservoir gas supply conditions. The following points summarized the important findings in this study.

1. The time-resolved characterization of the hydrate phase provides insights into the evolution of guest molecules in the hydrate phase over the formation period. The gas enclathration sequence into the hydrate structures and the

varying hydrate composition indicate a complex competition among different gas molecules incorporating into the hydrate crystals depending on their guest-to-cavity ratio and solubility.

2. In the open system with a continuous gas supply, C_3H_8 and iso-C_4H_{10} are enriched in the hydrate phase. A possible reason for this observation is the higher guest-to-cavity ratio of these molecules compared to the other available gas molecules.

3. In the closed system with no gas supply after initial pressurization, a limit of gas supply has led to the enclathration of those components such as C_2H_6 and n-C_4H_{10} which were not preferentially encased into the hydrate phase in the open system.

4. In the semi-closed system, the changes of hydrate composition over time shared a similar trend with that in the open system, however, this trend was much more pronounced in the semi-closed system. Frequent turbulence in the gas phase caused by pressure regulation between two gas surges may lead to a higher heterogeneity.

5. Despite the fact, that the formation of a coexisting hydrate phase would be theoretically possible in the closed system, we could not observe the formation of such an additional, coexisting hydrate phase with a composition corresponding to the p–T condition and the composition of the actual gas phase.

3.2 Influence of sediments on the formation of mixed gas hydrates

Sediments are unavoidably involved when talking about natural gas hydrates as they are hosted within or beneath permafrost sediments and in marine sediments. The characteristics of host sediments affect the selection of potential gas production strategies. Exploration for hydrates as an energy resource focuses on those within sand reservoirs rather than within fine-grained materials to facilitate extraction while minimizing technical production challenges [33]. It is also a well-established fact that sediments affect and alter the phase boundaries and the growth kinetics of hydrates [73]. To mimic the formation conditions in a natural gas hydrate system to the utmost extent, an understanding of the effects from local sediments to the mixed hydrate formation process is thus essential.

In this study, two parallel tests were carried out in the high-pressure cell for the formation of mixed gas hydrates with two kinds of sediments separately: natural samples from QMP and artificial sands. A background test was performed without sediments under identical p–T conditions. *In situ* Raman spectroscopic measurements and microscopic observation were employed for the investigation of the hydrate formation process on a μm scale. As a supplement,

the same mixed gas hydrates were also synthesized in three pressure vessels with/without sediments for the investigation of hydrate formation kinetics. Combining the preliminary results from both *in situ* and *ex situ* experiments, the influence of local sediments from QMP on the hydrate formation process were revealed.

3.2.1 Materials and Methods

***In situ*:** Mixed gas hydrates were initially synthesized in the high-pressure cell from pure water and a gas mixture at 2.0 MPa and 274 K, following the same formation procedure as described in *Chapter 2.2.1*. It is well-known that the gas components detected from the dissociation of natural hydrates recovered in QMP contains a high percentage of hydrocarbons besides CH_4. Therefore, a similar gas mixture containing 63 mol% CH_4, 15 mol% C_2H_6, 15 mol% C_3H_8, 7 mol% CO_2 was used in this experiment.

To carry out the experiments with sediments, the natural core sample retrieved from QMP (see details in *Chapter* 1.2.2 and *Chapter* 4.1.1) was grinded into homogeneous powders with a grain size of less than 63 μm. The results from powder X-ray diffraction indicated that the main mineral component in the core sample was quartz, which contained 76.5 wt%. Furthermore, it contained 10 wt% feldspar, 6.5 wt% mica, 5 wt% kaolinite, and 2 wt% ankerite/siderite. Considering the fact that it was the sandy sediment that held a higher saturation of gas hydrates in natural occurrences [184], artificial quartz sands were also applied in this experiment. The particle grain size of the quartz sands (~99 wt% SiO_2) was between 500 μm to 1000 μm. The following Figure 3.8 depicts the photo of two sediment samples, with left (a) the sediments from QMP and right (b) the quartz sands.

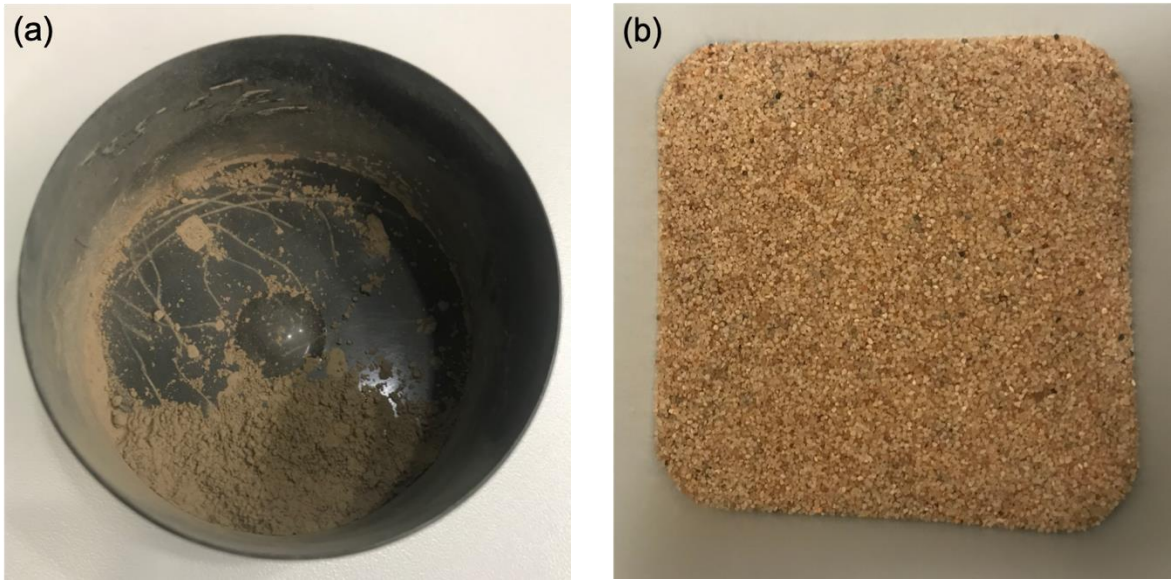

Figure 3.8 Photo of the sediment samples, (a) Powders milled from the drilling core sample retrieved in QMP, (b) artificial quartz sand particles.

During the experiments, 0.02 g of quartz sand were directly transported into the pressure cell before loading 150 μl deionized water. However, it was worth noting that sediment powders from QMP exhibited oily features, thus they were not easy to be dissolved in water. In this case, sediment powders were not loaded into the pressure cell directly. Instead, a sediment load of 0.02 g was first mixed with 150 μl deionized water. The mixture of sediments and deionized water was carefully stirred to ensure a good mixing before loading into the pressure cell. Thereafter, the cell loaded with both sediments and water phase, was sealed and pressurized with the same gas mixture at 2.0 MPa and 274 K in two parallel tests. Figure 3.9 shows the microscopic pictures of the dissolved quartz sands (left) and powdered QMP sediments (right).

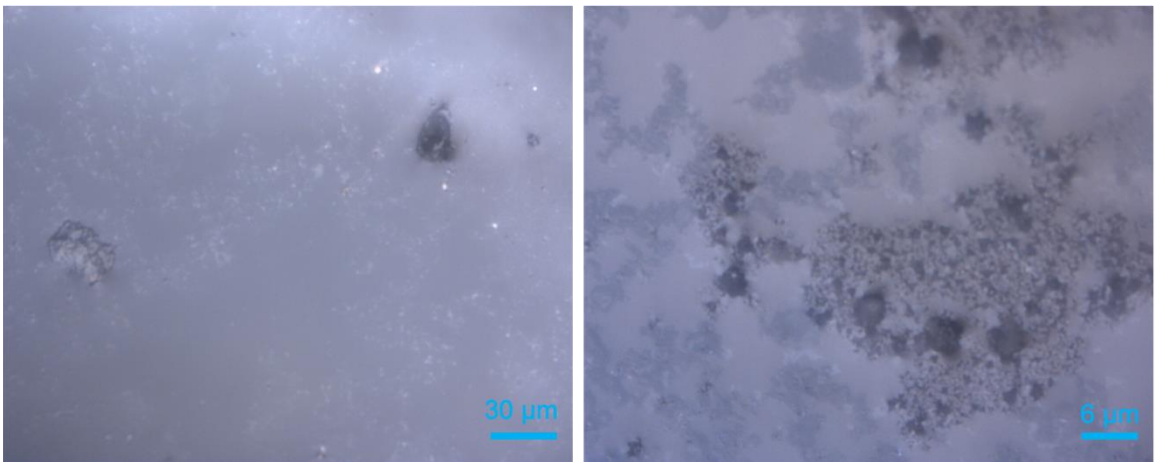

Figure 3.9 Microscopic observations of sediments in aqueous phase before pressurization: (left) quartz sands, (right) QMP sediments.

Once the hydrate crystals started to form, the growth of crystals were continuously characterized on 15 selected hydrate crystals with single-point Raman measurements. For a better understanding on the spatial distribution of the hydrate phases, well-structured crystals were selected for mapping. After 5 days, the mixed gas hydrate composition reached a steady state where no further changes were observed in all three experiments. Each parallel test was repeated for two times. The results from experiments with sediments were compared with those without sediments but under identical p–T conditions to investigate the effects of sediments on the hydrate formation process.

Ex situ: Apart from the above-mentioned *in situ* Raman spectroscopic measurements, mixed gas hydrates were also formed from ice and the same gas

mixture (63 mol% CH_4, 15 mol% C_2H_6, 15 mol% C_3H_8, 7 mol% CO_2) in three batch pressure vessels. Ice was freshly prepared by spraying deionized water into liquid nitrogen and powdered in a Spex 6750 Freezer Mill cooled with liquid nitrogen where ice particles was crushed by a pestle driven by a cryo magnet at 77 K for 120 seconds.

Vessel No.1 contained only 34 ml ice powders. Vessel No.2 was filled with 34 ml ice beads together with 8 g homogeneous powders from QMP while vessel No.3 had the same amount of ice powders but 8 g artificial sands. Afterwards, the three vessels were sealed and pressurized with the same gas mixture at around 3.3 MPa before they were stored in a freezer with the temperature fluctuating between 263 K and 268 K. A fast pressure drop at the beginning of the process indicated the formation of mixed gas hydrates. Later on, the pressure decrease slowed down as the reaction proceeded. After several weeks no changes in pressure was detected and the amount of ice transformed into mixed gas hydrates was calculated from the pressure drop in each vessel. Hydrate formation kinetics was reflected by the rate of pressure decrease over time.

For the *ex situ* X-ray diffraction measurements, the sample materials (hydrate + ice) were quenched and continuously handled in liquid nitrogen right after the vessels were depressurized. All preparation work was carried out in a cooled glove box at 263 K to minimize hydrate dissociation and condensation of air moisture onto the samples. Similar to the above-mentioned ice particles, the samples were also grounded into powders in the freezer mill (Spex CertiPrep) at 77 K for 120 s. The fine crystalline hydrate/ice powders were immediately placed on a pre-cooled sample holder in a low-temperature chamber (153 K) and measured at ambient pressure with the powder X-ray diffraction. The results provided structural information of the formed gas hydrates.

3.2.2 Results and discussion

1. Hydrate formation in batch pressure vessels

In our closed laboratory simulation system (batch pressure vessels), pressure drop was used as an indicator for the formation of gas hydrates as it reflected the enclathration of gas molecules into the hydrate structures, leading to the decrease of the absolute pressure in the system.

Mixed gas hydrates were formed in batch pressure vessels at p–T conditions far within the stability field (274 K, 3.4 MPa). Figure 3.10 gave the absolute pressure in three vessels over time. The curves were shown at two different time scales with (a) during the first 200 minutes and (b) throughout the entire

experiment which lasted for more than 4500 hours. It was clearly shown from Figure 3.10a that all three tests experienced a sharp pressure decrease at the very beginning of the experiments, indicating a quick formation of mixed gas hydrates when the ice powders were first exposed to the gas mixture. Among them, the falling of the pressure in the system containing QMP sediments was the most significant in the first 10 minutes. However, the pressure curve with quartz sand was almost overlapped by the curve without sediments within the first 70 minutes. After around 70 minutes, the formation of hydrates in the vessel with quartz sands accelerated and a higher pressure drop was observed as compared to that in the background test without sediments. This observation indicated a delay of the promoting effect in coarse sand group. After the repetition of the above experiment, similar phenomenon for the hydrate formation kinetics was observed. Correspondingly, previous research also recorded a delay in the induction time of methane hydrates with coarse sand particles (500 μm to 1000 μm), which took around 57 hours, remarkably later than the other groups for the onset of the hydrate formation [185]. Thereafter, the formation process continued but the formation rates were considerably slower in all three tests as the slope of the curves gradually became flat throughout the whole process (Figure 3.10b). The system with QMP sediments led all the way until the end of the experiments after around 4500 hours. Despite a somewhat similar beginning of hydrate formation in the other two systems, the presence of quartz sands still displayed obvious promoting effects since the final absolute pressure was lower than that in the system without sediments, indicating that more ice powders had transferred into mixed gas hydrates.

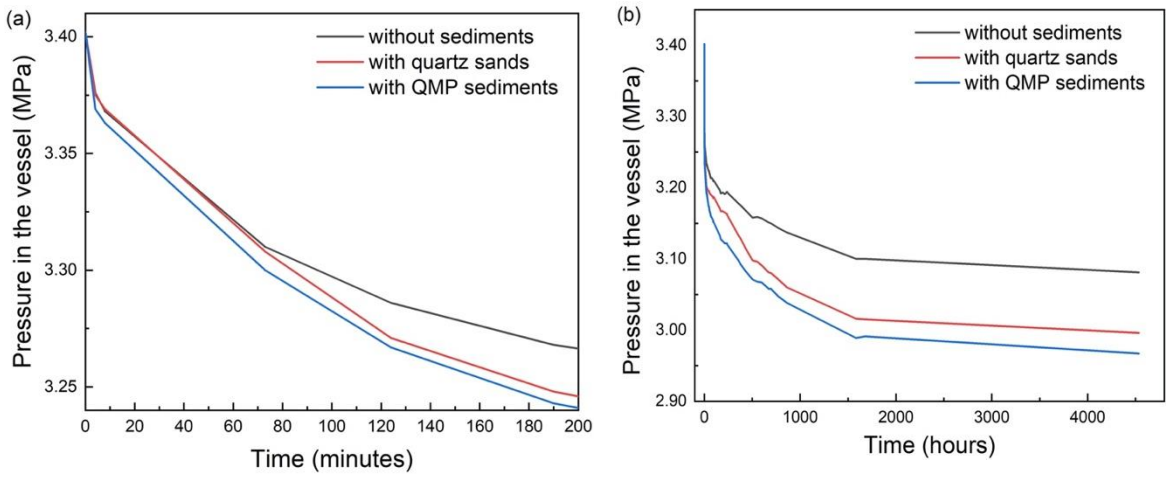

Figure 3.10 Pressure–time diagram of three parallel tests, representing the experiments without sediments (black curve), with quartz sands (red curve) and

with QMP sediments (blue curve), respectively during the first 200 minutes (a) and for the entire experimental period (b).

Apparently, the presence of sediments, regardless of the grain size and species, was favorable for gas hydrate formation. A statistical calculation, based on the pressure drop and the volume of the reactor, revealed that in vessel No.1 without sediments, a total of around 7.7 ml mixed gas hydrates were formed during the experimental period while the amount of hydrates was 9.5 ml in vessel No.2 with quartz sands and 10.2 ml in vessel No.3 with QMP sediments, respectively. There's no doubt that the difference of hydrate formation rate and amount in three batch pressure vessels were governed by the sediments and their matrix characteristics.

The powder X-ray diffraction analysis of the recovered samples in three vessels confirmed the occurrence of sII hydrates. Figure 3.11 depicted the XRD patterns taken from the samples recovered from vessel No.3 within QMP sediments. It should be noted that even in vessel No.3 which gained the highest pressure drop, less than 1/3 of the ice were converted to mixed gas hydrates. In other words, a large amount of ice powders remained in the system after 4500 hours. Hence, strong signals for ice were observed in XRD patterns apart from the weak signals for sII hydrates.

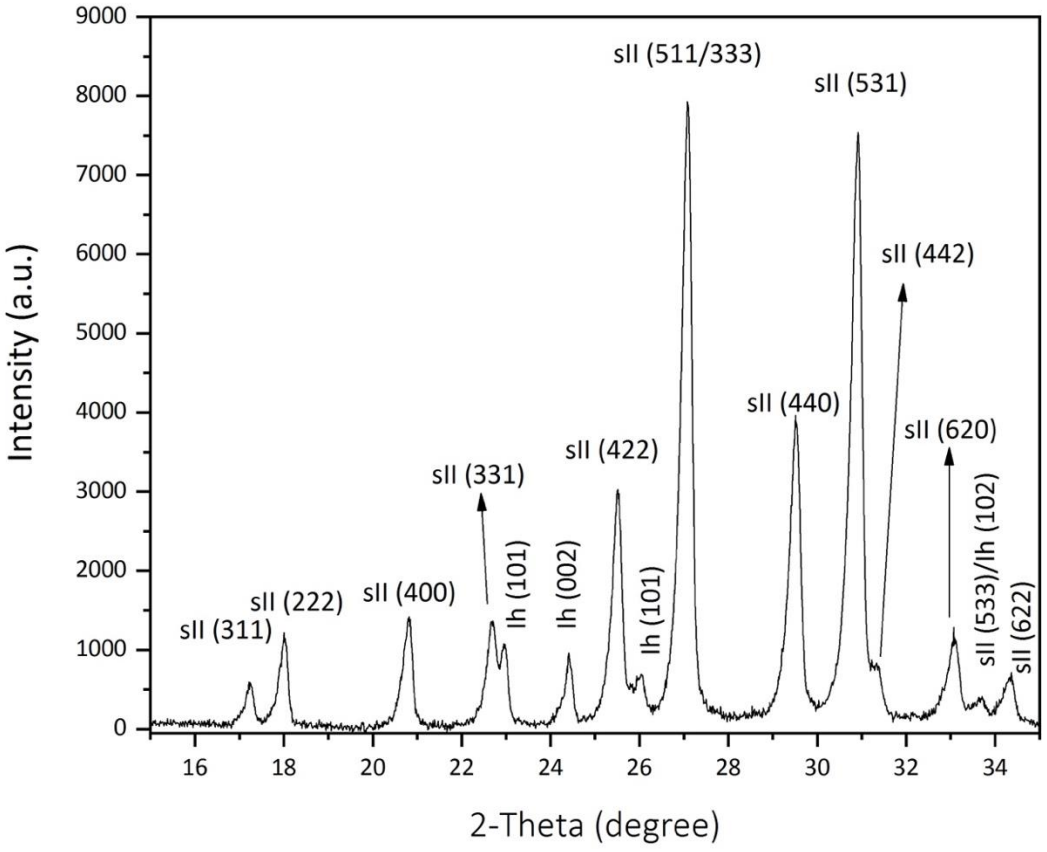

Figure 3.11 Powder X-ray diffraction patterns of hydrate samples formed in the pressure vessel with sediment powders from QMP.

A preferential occurrence of gas hydrate formation in coarse sandy sediments was previously confirmed for both field observations [186,187] and laboratory experiments [188–190]. Clennell et al. [73] ascribed this observation in his conceptual model to higher driving forces for gas hydrate formation in larger pores based on a smaller influence of capillary pressure and a smaller depression of water activity, both caused by fine grain particles. However, the observation of a faster hydrate formation in fine-grained QMP sediments in this study was in good agreement with the results from experimental simulations of Heeschen et al. [185], who reported a shorter induction time for the methane hydrate formation in the sediments group <125 μm as compared to other coarser sediment groups.

It is widely accepted that the guest molecules are first dissolved into the liquid phase before they are encased into hydrate cavities. However, in case of hydrate formation from ice, a liquid water phase is not a prerequisite for hydrate formation. As described by Wang et al., there's a certain possibility that a quasi-liquid layer exists between the forming hydrate layer and the surface of the unreacted ice particle [139]. This layer is believed to be a thin mobile phase of water molecules with mobilities intermediate between those of liquid water and crystalline ice [191]. For hydrate formation, this thin layer of mobile water molecules needs to be supersaturated. With the presence of sediments, a third interface allowed for the reduction of the nucleation work [74]. A smaller grain size range had larger surface area, thus the heterogeneous nucleation opportunities were enhanced, resulting in an increase in the hydrate formation rate [192]. In addition, it may be also related to an earlier local super saturation caused by enhanced sorption of gas molecules on any of the wet mineral phases with smaller grain size.

QMP sediments showed a larger compositional difference as indicated by the aforementioned XRD results. Minerals other than quartz accounted for more than 20 % of the sediments in this sample, mainly including feldspar, mica and kaolinite. In contrast, the sand samples consisted of 99 % quartz. As stated by Blackwell in her PhD thesis [193], specific minerals such as CuO, αAl_2O_3, γAl_2O_3 and $CaCO_3$ acted as the effective gas hydrate nucleators which were also among the best ice nucleators and exhibited small crystal lattice mismatches with ice (hexagonal). The occurrences of these minerals in QMP sediments could possibly offer preferential conditions for hydrate nucleation and/or growth. Adsorption of

water at the enlarged surface of hydrophilic alumosilicas may lead to a reduced free water phase having to be saturated with gas molecules.

The potential influence of salts, which were known to be inhibitors for gas hydrate formation[5], still remained uncertain in this experiment as the initial salinity for these two sediments was not determined.

2. Hydrate formation in the high-pressure cell

Considering the potential changes of the gas composition of the ordered gas mixtures during storage and transportation, it is necessary to determine the exact composition of the gas phase before each experiment. Table 3.5 summarized the information of the ordered gas mixture as well as the actual gas mixtures before six repeated tests. Obviously, the composition of the gases that flew into the high-pressure cell differed from the order composition, containing a lower concentration of CH_4 but higher concentrations of other hydrocarbons and CO_2. The last two tests with quartz sands were carried out with gas mixtures containing even lower concentrations of CH_4. This might be caused by the molecular weight difference in a gas mixture as CH_4 was the lightest molecule and might be released faster when first opened the gas bottle. Accordingly, further discussion and calculations of the hydrate composition at equilibrium in CSMGem (Table 3.5) referred to the measured gas composition rather than the ordered gas composition.

Table 3.5 Results of pure gas phase measurements before the formation of mixed gas hydrates in the high-pressure cell and the calculated hydrate composition from CSMGem.

No.	Sediments	P (MPa)	T (K)	Average mol%			
				CH_4	C_2H_6	C_3H_8	CO_2
Original gas				63	15	15	7
Test 1	/	2.2	274	47.41	19.06	19.08	14.45
Test 2	/	2.2	274	47.40	20.39	17.05	15,.6
Test 3	QMP sediments	2.2	274	47.55	20.26	17.32	14.87
Test 4	QMP sediments	2.2	274	47.53	19.64	19.11	13.72

Test 5	Quartz sands	2.2	274	45.16	20.24	19.45	15.15
Test 6	Quartz sands	2.2	274	45.41	20.11	18.99	15.49
Average gas composition				46.74	19.95	18.55	14.81
Composition of hydrate phase (CSMGem)				58.7	3.9	32.0	5.4

Natural gas hydrates occupy pores in the sediment matrix and hence the pore size distribution characteristics influence the thermodynamic equilibrium curve of the gas hydrates [188,194,195]. Experiments implied that the equilibrium temperature decreased with the decrease of pore diameter at given pressure condition. (see Malagar et al [196] and references therein).

Figure 3.12 presented the p–T diagrams for the studied mixed gas hydrates. The formation condition (blue triangle) of the time-dependent experiments was far within the stability field. All phase data in three separate systems were experimentally determined (displayed as data points). It can be concluded from the figure that the experimental data, in all three different systems, corresponded well with the modelled data (black curve) acquired from CSMGem. In other words, the presence of sediments in the aqueous phase did not affect the hydrate equilibrium conditions in this study.

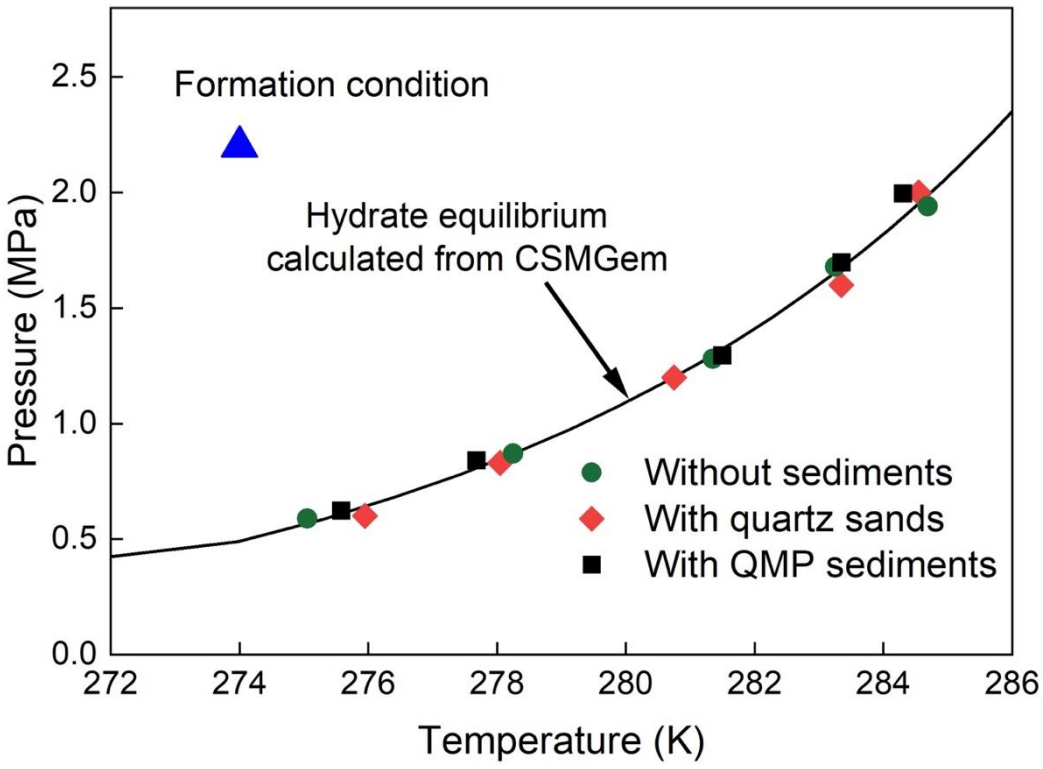

Figure 3.12 Phase diagram of mixed gas hydrates. Experimental data are plotted as data points. The black line represents the modelled data obtained from CSMGem [5]. The blue triangle stands for the chosen p–T condition for the formation of mixed gas hydrate which lies within the stability field.

It has been mentioned earlier that only 0.02 g of sediments were added into the pressure cell together with 150 µl deionized water. A rough estimate showed that the amount of sediments accounted for around 13 wt % of the solution in the system. Hence, sediment particles, no matter fine grains or coarse sands were limited in the high-pressure cell. A recent study from Bhawangirkar et al., [197] investigated the thermodynamics of methane hydrate formation and dissociation in the presence of sediments from natural reservoir at varying concentrations in an aqueous solution. It was concluded from the experiment that natural sediments had an inhibition effect on the hydrate equilibrium, with the equilibrium being shifted towards the lower temperatures and higher pressures. Nevertheless, the inhibition effect was also invisible with the 10 wt % sediment solution, which depicted similar equilibrium curve as the pure methane hydrates without sediments.

3. *In situ* Raman spectroscopic measurements on the mixed gas hydrates

During the hydrate formation process, the gas flow was supplied continuously at constant p–T conditions to avoid the changes in the gas phase. Raman spectra recorded changes of hydrate compositions for the 15 selected crystals over the whole formation period until the system reached a steady state. In the first two tests without sediments (Figure 3.13), it was found that C_3H_8 and CO_2 molecules were preferentially enriched into the hydrate phase from the beginning of formation when compared to the corresponding concentrations in the gas phase. However, the concentration of C_3H_8 in the hydrate phase continued to increase as the experiment proceeded whereas the content of CO_2 in the hydrate phase sharply decreased with time. It also turned out that the concentration of CH_4 in the hydrate phase was much higher at the end of the experiment, following a similar trend with C_3H_8. As described in the previous *Chapter 3.1*, C_2H_6 was such a kind of gas with relatively higher solubility in the water phase than CH_4 and C_3H_8 but a less pronounced ability to stabilize the hydrate cavities, which might be the probable reason for the observation of a decrease in C_2H_6 content. Besides, a large variation of the hydrate composition among crystals were observed at the beginning of the experiment. Finally, the variation became smaller and the system reached a steady state as indicated by the data points in this figure. The

average composition of the resulting hydrate phase contained around 43.6 mol% CH_4, 7.0 mol% C_2H_6, 38.6 mol% C_3H_8, 10.8 mol% CO_2.

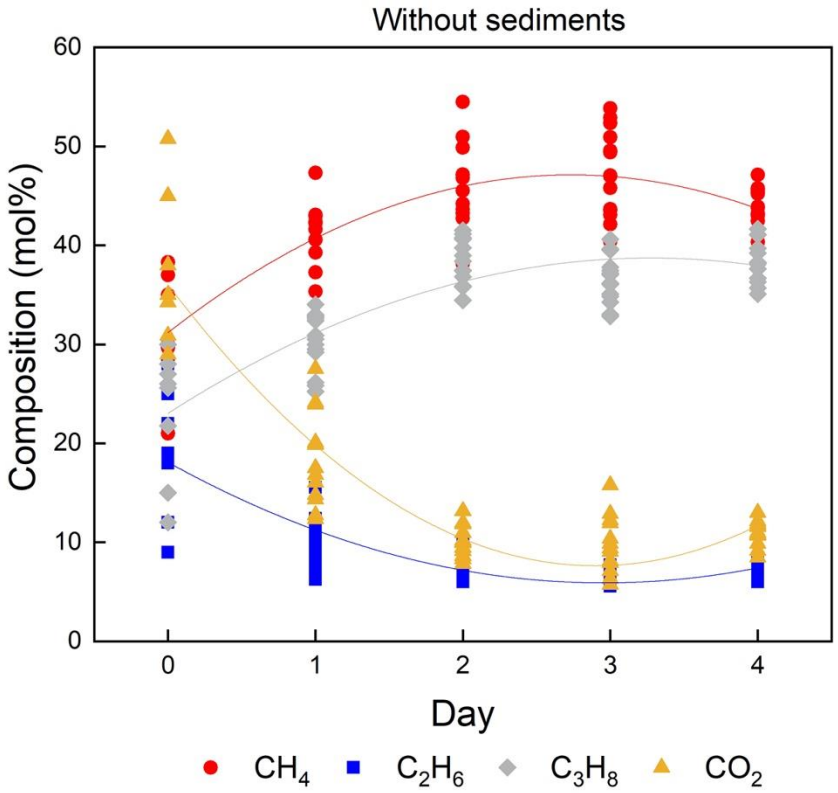

Figure 3.13 Changes of the hydrate composition throughout the whole experimental period which was measured in one of the first two tests without sediments. The straight lines showed the average composition changes in the hydrate phase fitted by smooth curves.

For a better understanding of the spatial distribution of the hydrate phases, a total of five well-structured crystals located in a straight line were selected in the first test without sediments for line mapping. Altogether six measuring points were chosen on the surface of the selected crystals as shown in Figure 3.14. It should be pointed out that the fourth and fifth measuring point were on the surface of the same hydrate crystal. These points were scanned step by step automatically in one direction. The results shown as stacked columns revealed a huge difference in the composition of the hydrate phase for 6 measuring points. Preliminary tests (*Chapter 2.1.1*) showed an excellent reproducibility for the Raman measurements, which, in turn, indicated that the measured variations in local composition of the hydrate crystals (Figure 3.14) demonstrated the non-stoichiometric and heterogeneous character of the hydrate phase.

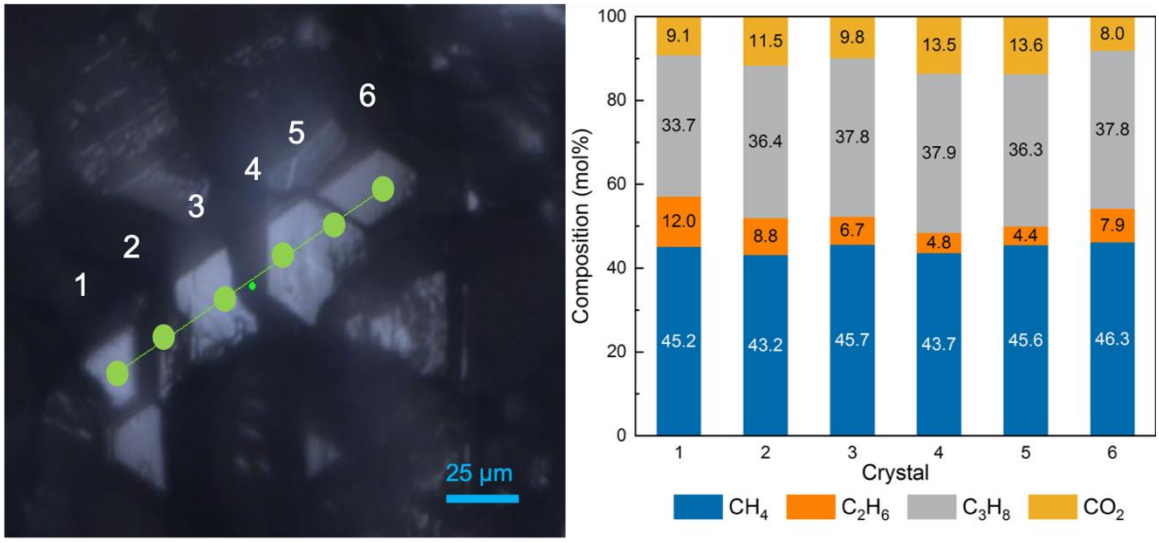

Figure 3.14 (left) Raman line scans across the surface of five hydrate crystals, (right) Composition variations in the hydrate phase at 6 measuring points across the 5 hydrate crystals.

With the occurrences of sediments, no matter quartz sands or QMP sediments, the hydrate compositions were totally different at the beginning of the formation process (Figure 3.15). On the first day, the concentration of CO_2 in Figure 3.13 was considerably high, accounting for more than 35 mol% on average in the hydrate phase. Interestingly, the amount of CO_2 enclathrated into the hydrate structures in Figure 3.15 barely reached 30 mol%. Meanwhile, the other two components CH_4 and C_3H_8 gained relatively higher concentrations on the first day as shown in Figure 3.15. This may indicate that the hydrate formation process progressed much faster with the presence of sediments within the same time period, as compared to that without sediments. More molecules have been encased into the hydrate cavities within a short period of time. Therefore, during the first measurement, a higher concentration of CH_4 and C_3H_8 were already detected in the hydrate phase. The experiments with quartz sands and QMP sediments reflected similar trends as the previous background test for the changes of composition in the hydrate phase over time: the concentrations of CH_4 and C_3H_8 increased with time while the other two molecules decreased. Finally, the formed hydrate composition in all three systems did not show a great difference, leading to a conclusion that the presence of sediments played a minor role in affecting the hydrate composition.

As can be seen from the right part of Figure 3.15, the variation of the hydrate composition was quite high during the first two days which was also observed in the other two tests without sediments and with quartz sands. In the following days, the variation in the hydrate composition measured from the selected hydrate crystals were getting smaller. However, this is not the case with QMP sediments. It was observed that in Day 2 and Day 3, the compositions of a few hydrate crystals were significantly different from the majority of other hydrate crystals.

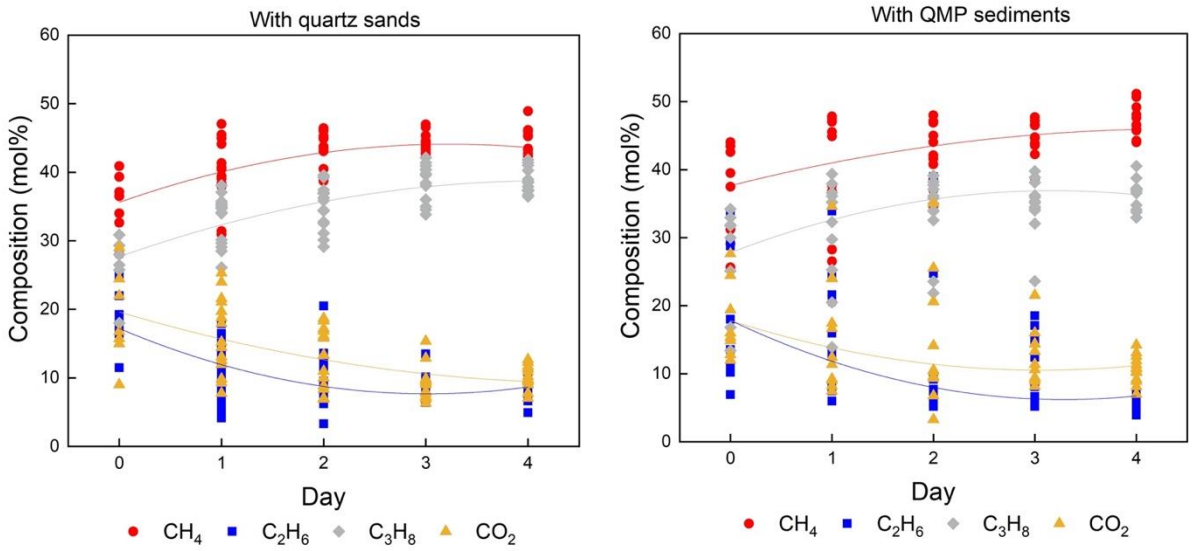

Figure 3.15 Changes of the hydrate composition throughout the whole experimental period which was measured in systems with quartz sands (left) and QMP sediments (right). The straight lines showed the average composition changes in the hydrate phase fitted by smooth curves.

4. Coexisting phases formed with the presence of QMP sediments

There's an increasing number of reports on the coexisting hydrate phases from natural gas hydrate reservoirs as described in *Chapter 1.2.1*. The occurrences of coexisting hydrate phases exhibited either two different structures or the same structure but with a varied hydrate composition. It was demonstrated from Figure 3.11 that only sII hydrates were observed in the system with QMP sediments. The data points collected on the second and third day of measurements with QMP sediments (Figure 3.15) were far from the average composition line, probably indicating the coexistence of hydrate phases with hydrate compositions. Analysis of the Raman spectra for two measuring points gave unexpected results (Figure 3.16). Point A in the figure exhibited as a well-developed hydrate crystal with sharp edges whereas point B seemed to measure

the flat base located below hydrate crystals. It is known that the ratio of large to small cavities for sI and sII hydrates are 3:1 and 1:2, respectively. The relative peak areas of the C–H vibrational modes in the Raman spectra should be good indicators of the hydrate structure. The assigned Raman peaks were summarized in Table 3.6. Finally, it turned out that Raman bands measured on the surface of point A indicated the presence of typical sII hydrate with CH_4 occupied mainly the small cavities of sII but also a small proportion of the large cavities. CO_2, C_2H_6 and C_3H_8 were incorporated into the large cavities of sII hydrates. Nevertheless, point B did not exhibited a typical sI or sII hydrate signal, Instead, weak Raman bands and a very strong CH_4 gas peak were observed indicating a metastable solid phase with only a limited amount CH_4 molecules incorporated into the small cavities. In the O–H stretching region, a prominent broad peak at 3150 cm^{-1} followed by a weak shoulder were observed at point A, whereas this band was less pronounced at point B, leading to the speculation that less hydrogen bonded water molecules existed at point B than point A [180].

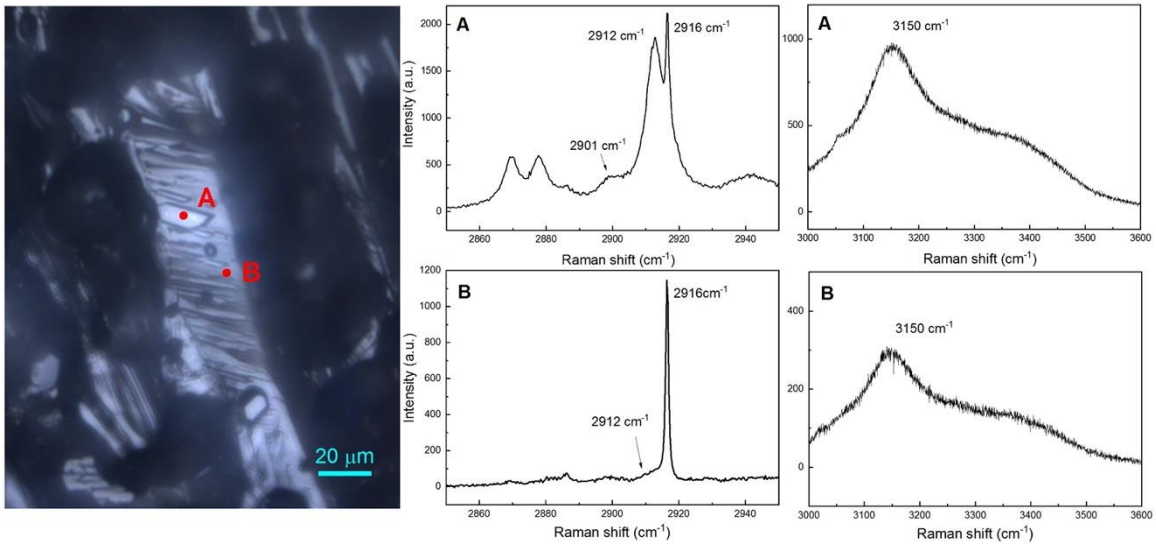

Figure 3.16 Microscopic observation of two selected points and the corresponding Raman spectra for C–H stretching vibrational modes ranged from 2850–2950 cm^{-1} and O–H stretching vibrational region ranged from 3000–3600 cm^{-1}.

Table 3.6 Summary of the Raman band assignments used in this study.

Component	Vibrational mode	Cavity type/ gas phase	$\nu_{measured}$ (cm^{-1})	$\nu_{literature}$ (cm^{-1})	References
CH_4	C–H	Gas phase	2916	2916	[46]

	stretching	sII 5^{12}	2912	2912	[16]
		sII $5^{12}6^4$	2901	2901	
C_2H_6	C–C stretching	Gas phase	993	993	[16]
		sII $5^{12}6^4$	991	992	
C_3H_8	C–C stretching	Gas phase	869	869	[46]
		sII $5^{12}6^4$	877	877	
CO_2	C–O stretching	Gas phase	1285	1285	[198]
		sII $5^{12}6^4$	1274	1275	
	overtone of bending	Gas phase	1387	1388	[198]
		sII $5^{12}6^4$	1381	1381	

By a continuous characterization on the measuring points A and B (Figure 3.16), time-resolved Raman spectra were acquired during the hydrate formation process. In Figure 3.17a and b which referred to the changes in point A, a small Raman band at 2912 cm^{-1} was observed besides the other gas peaks after 10 mins, which could be assigned to CH_4 molecules in the small cavities of sII hydrates. In the meantime, Raman bands at 1274 cm^{-1} and 1381 cm^{-1} for CO_2 in the hydrate phase, together with the peak at 876 cm^{-1} which could be assigned to C_3H_8 in large cavities of sII hydrates, were also detected in the Raman spectra. Thereafter, a Raman band arose at approximately 991 cm^{-1}, corresponding well with the literature data for C_2H_6 molecules in the $5^{12}6^4$ cavities of sII [178,179]. The intensities of these above-mentioned Raman bands increased gradually as the experiment proceeded, showing typical characteristics of sII hydrates. On the other hand, Raman spectra showed a bad signal-to-noise ratio in Figure 3.17c and d for the results from point B. Only gas peaks at 2716 cm^{-1}, 869 cm^{-1}, 993 cm^{-1}, 1285 cm^{-1} and 1387 cm^{-1} were presented during the first few minutes. Later on, CH_4 was shown to be encased into the small cavities of hydrate crystals as a shoulder emerged next to the CH_4 gas peak at around 2912 cm^{-1}. The enclathration of hydrocarbons and CO_2 molecules in the hydrate phase was indicated by various tiny peaks that detected in Figure 3.17c. It seemed that the changes of point B was extremely slow and the intensities did not change over time. Continuous microscopic observations on the hydrate phase revealed that with the expanding of hydrate crystals, the metastable solid phase was totally covered by a layer of the well-developed crystals. Therefore, it was not possible to follow the same measuring point B on the last day. This might explain the

small variation of the hydrate crystals measured on Day 4 as shown in Figure 3.15.

The occurrence of a second solid phase apart from the initial sII hydrates was not observed without sediments or with quartz sand. It was therefore assumed that QMP sediments with unique physical and chemical properties led to the formation of the metastable solid phase during the formation process. As aforementioned in the previous *Chapter 3.2.1*, QMP sediments had oily features which made them difficult to be dissolved into the water phase. Even after careful stirring, a thin layer floated on top of the water surface, suggesting the existence of specific minerals or organic compounds like fats, oils, petroleum products which were hydrophobic. Noteworthy, plagioclase which accounted for 7-9 % in QMP sediments (*Chapter 4.1.1*) was also suggested as a kind of hydrophobic mineral by previous researchers [199]. At specific points around hydrophobic minerals or organic compounds, less water molecules were available which could further agglomerate for the formation of gas hydrates. Inspired by the hydrophobic amino acids as novel kinetic inhibitors for the gas hydrate formation [200], the hydrophobic minerals in some specific areas might also perturbing the arrangement of water molecules. Hence, the nucleation and growth of hydrates in these areas might be retarded or even prevented. As a consequence, Raman spectra of point B exhibited hydrate structural characteristics but with only limited amount of guest molecules.

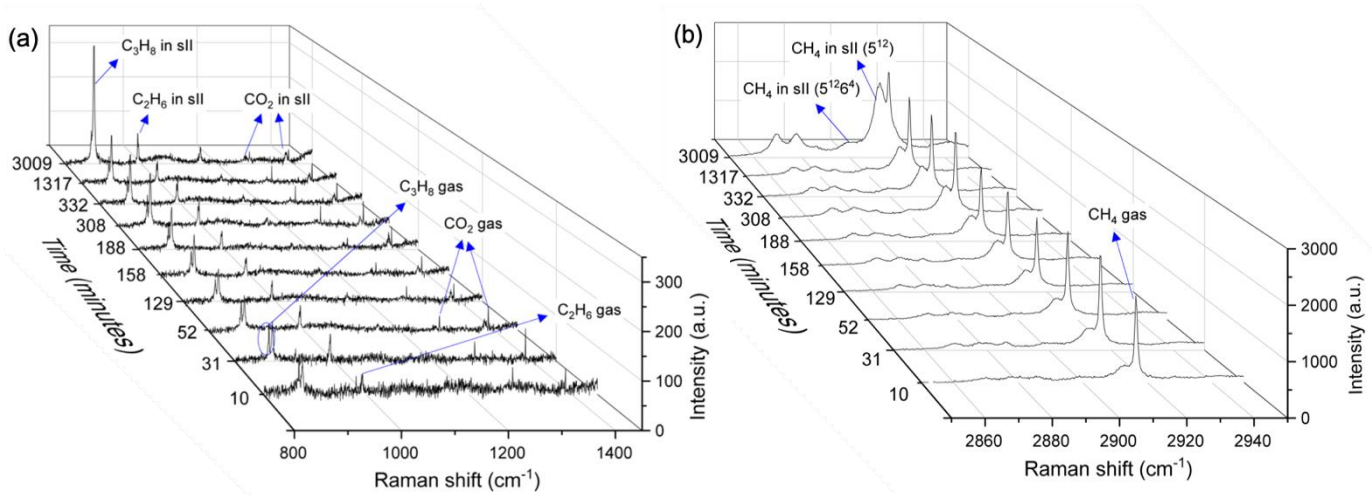

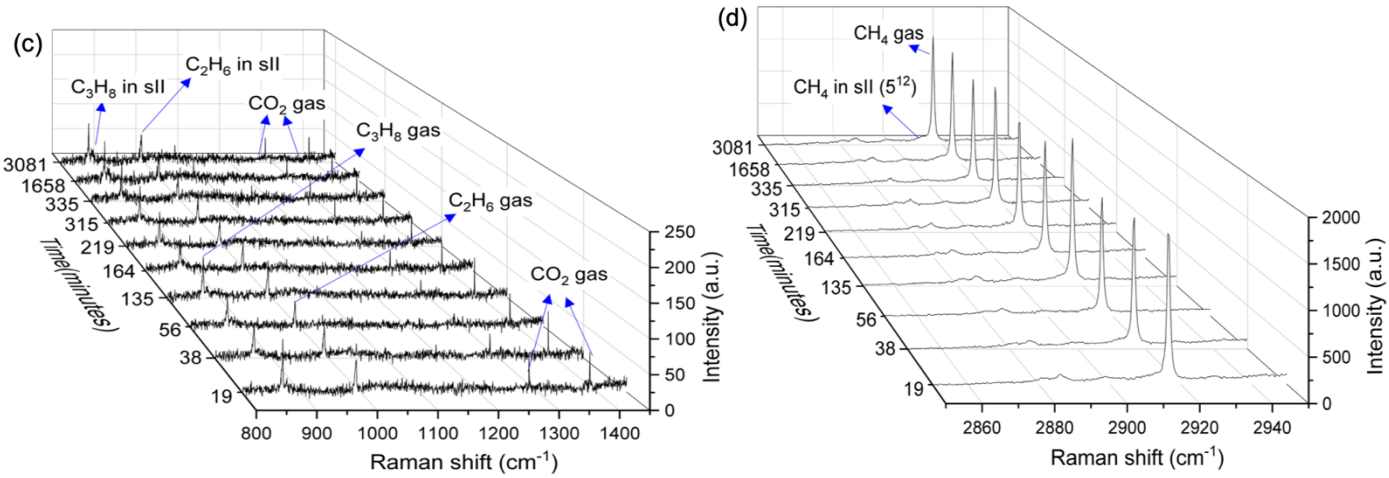

Figure 3.17 Real-time Raman spectra monitoring the two different formation patterns measured from point A (a,b) and point B (c,d), respectively. (a) (c) C–C stretching vibrational modes ranged from 800–1450 cm^{-1}. (b) (d) C–H stretching vibrational modes ranged from 2850–2950 cm^{-1}.

3.2.3 Conclusions

The presented experiments investigated the effects of natural sediments on the formation of mixed gas hydrates simulating natural reservoir conditions in QMP.

By carrying out the formation experiments with/without sediments in batch reactors, time-resolved pressure information was recorded which turned out to indicate the promoting effects of sediments on the hydrate nucleation and growth process. The promoting effects were enhanced in the group with the fine-grained QMP sediments as compared to those in the group with artificial quartz sands.

It revealed from the Raman spectroscopic measurements that the equilibrium of mixed gas hydrates was not shifted with the presence of limited amount of sediments. Despite the heterogeneity of the hydrate phase, the initial composition of the formed hydrates varied in three systems. The presence of sediments led to a lower initial concentration of CO_2 in the hydrate phase. A coexisting solid phase in the system with QMP sediments was also observed, which depicted totally different Raman spectra with those from typical sII hydrate crystals. The existing hydrophobic minerals such as plagioclase or organic compounds in QMP sediments might be a possible reason as they could inhibit the nucleation and growth of hydrates. Instead of the growth of hydrate crystals, some specific points showed limited guest enclathration.

These findings are of importance to understand the mixed gas hydrate system in QMP. With finer grains and a more diverse mineralogy in this area, a fast reformation may occur which enhanced clogging during gas production.

Chapter 4

4 Dissociation of hydrates in natural reservoirs

The interest in gas hydrate research emerges from the awareness that these deposits play critical roles in energy systems as well as in global climate. Gas hydrates may be decomposed either through human interventions for the production of methane gas or due to global climate warming. With regard to the first aspect it is necessary to figure out the physical properties of hydrate-bearing sediments during and after hydrate dissociation to ensure an effective and environmental-friendly field production. On the other hand, accurate knowledge of the hydrate dissociation process with regard to climate change is a prerequisite to alleviate the global warming problems. Therefore, *Chapter 4* is related to the dissociation process of mixed gas hydrates in QMP. The *sub-chapter 4.1* concentrated on the description of an unexpected phenomenon in which the permeability decreased significantly after the dissociation of gas hydrates in the consolidated core samples leading to the reservoir formation damage. The second sub-chapter gave an in-depth comparison of the dissociation behavior of simple sI CH_4 hydrates, sII binary CH_4–C_3H_8 hydrates and complex sII multi-component hydrates. Both results helped deepened the understanding of the dissociation behavior for hydrates in sediments which might be beneficial for future risk assessment prior to the gas hydrate production in a world-wide perspective.

4.1 Reservoir formation damage during hydrate dissociation in sand–clay sediments from Qilian Mountain permafrost, China

This sub-chapter was mainly taken from the publication Wang et al., [113] in which I was the co-first author and carried out experiments, edited the manuscript and helped process the manuscript publication.

Permeability is known as a key factor affecting the gas production effectiveness from the natural gas hydrate-bearing reservoir. It controls fluid migration through sedimentary systems and plays also an important role in heat

and chemical transfer occurring via fluid migration [201]. In hydrate-bearing sediments, permeability determines the accumulation and distribution of dissolved gas, free gas and hydrates [202]. It also affects the ability and efficiency to produce methane gas from hydrate reservoirs [203–205]. Gas and water production at longer time scales may be hindered by formation damage caused by the low permeability of the hydrate reservoir and the fresh water release from hydrate decomposition. The fresh water release may cause clay swelling and clay detachment as well-known from enhanced oil recovery by low-salinity water flooding [206–208]. At a longer time-scale of production from a hydrate-bearing reservoir formation damage may become an important issue. Among all the factors leading to different types of formation damage, the migration of fine particles is often considered as a major cause. Fine particles may physically break away during hydrodynamic flows and may accumulate in pores and thus reduce the permeability [209–211]. Despite the fact that a low permeability caused by sand production or sediments deformation may prevent long-term gas production from hydrate bearing sediments, experimental data are still lacking or insufficient [212].

In this study, we investigated the permeability behavior of natural clayey sand core samples from a natural hydrate-bearing reservoir in the Qilian Mountain permafrost before/after hydrate formation, as well as after hydrate decomposition and discussed the potential reasons for the observations. Hydrate reservoir in this region is a typical Class 3 hydrate deposit with an absence of the underlying mobile fluids zone. The overlying and underlying strata are sand-clay sediments with low permeability. Hence, our work may indicate the interaction between low permeability samples and production effectiveness of this kind of hydrate reservoir.

4.1.1 Materials and methods

The rock samples used in this study were originated from borehole DK–8 and SK–2 (Figure 4.1), which were both drilling sites that recovered gas hydrate samples in northern Muli coalfield. They were gray-black muddy siltstone (DK–8–I) and fine-grained sandstone (SK–2–I, II, III) and their details were listed in Table 4.1. Five distinct hydrate-bearing intervals were detected in the DK–8 profile during drilling and sampling at depths of 147.8–155.9 m, 171.6–175.0 m, 226.3–236.5 m, 265.9–291.2 m and 301.8–304.2 m and three gas hydrate-bearing intervals in SK–2 at depths of 178.0–199.0 m, 250.0–262.0 m and 350.5–354.7 m respectively. In other words, the rock samples were all retrieved from the layers

beneath the hydrate-bearing intervals. Drilling results also indicated that fracture-filling and pore-filling hydrates both occur in these two cores.

Figure 4.1 Samples SK–2–I–III taken from one core piece recovered from borehole SK–2 in 355 m depth. The dimensions of the samples were 61.3 mm length and 24.9 mm in diameter.

Table 4.1 Geoglogical parameters of the samples from Qilian mountain permafrost

Sample	Borehole	Depth (m)	Length (mm)	Diameter (mm)	Porosity (%)	Sample Density (g/cm³)	Matrix Density (g/cm³)
DK–8–I	DK–8	387	48.8	25.0	8.2	2.41	2.62
SK–2–I	SK–2	355	60.5	24.9	4.4	2.41	2.52
SK–2–II	SK–2	355	61.4	24.8	1.7	2.46	2.50
SK–2–III	SK–2	355	61.9	25.0	2.0	2.45	2.50

Experiments were carried out with the system for experimental petrophysics (SEPP) which was introduced in details in *Chapter 2.1.3*. To start, a dry sample was set to the desired confining pressure (6 MPa). A HPLC pump (Knauer Smartline 100) was applied to saturate the initially evacuated sample with a

degassed 5% KCl solution. The temperature at the sample surface was monitored using the Pt100 RTD. The heat generated by hydrate or ice formation dissipated over the sample surface, and the ambient temperature was controlled by the thermostat to be constant at 274 K.

Permeability was estimated using Darcy's law. The permeability can be calculated by the following equation:

$$K = \frac{q\eta L}{A(p_1 - p_2)} \tag{4.1}$$

where K is the effective permeability; q is the injection rate; η is the viscosity of the solution; L is the length of the sample; A is the sectional area of the sample; p_1 is the inlet pressure; p_2 is the outlet pressure.

For the initial experiment without hydrates, the degassed 5 % KCl solution which was used to saturate the sample, was pumped through the setup with rates of 0.5 ml/min, 1 ml/min, 2 ml/min, 3 ml/min, 4 ml/min, 3 ml/min, 2 ml/min, 1 ml/min, and 0.5 ml/min, respectively. For each injection rate, the injection duration was about 5 minutes. The outlet was connected to a fluid sampling container open to air. The pressure on the inlet and the solution injection rate were recorded in real time.

For hydrate formation, the methane gas was injected into the system to displace a part of pore water. Afterwards, the outlet of the setup was closed. The sample was pressurized and maintained at 5.0 MPa for the formation of methane hydrates. The ambient temperature was set to 274 K. After around one week, the free water in pores structures of the sample was transformed into methane hydrates. Thereafter, the injected methane gas pressure was lowered but slightly above the hydrate stability field (3.0 MPa). The valve to the methane cylinder was closed and the connection to the piston pressure storage was opened. The pressure storage contained the same KCl solution, which was now reinjected into the sample by increasing the pressure on the backside of the piston to 5.0 MPa using the pressure regulator of the methane cylinder. The pressure was kept at 5.0 MPa for some days for the formation of hydrate with the injected water.

To measure the permeability of the sample with hydrates, the KCl solution was precooled to 274 K before been injected into the sample to avoid hydrate decomposition by thermal stimulation. The outlet was connected to the pressure storage which was kept at 5.0 MPa. The inlet pressure and the injection rate were recorded in real time.

To initiate hydrate dissociation, the pressure storage located at the outlet was removed so that the outlet was connected to the atmosphere. Afterwards, the

outlet was opened to release methane gas. The volume of the released methane gas was measured by water displacement method. Once the pore pressure in the sample reduced to the atmospheric pressure and no methane gas was released, the hydrate dissociation process was considered as completed. The hydrate saturation before dissociation can be calculated as follows:

$$s_H = \frac{V_g M_H}{v_g \rho_H V_{pore}} \tag{4.2}$$

where S_H represents the hydrate saturation. The gas molar volume, v_g is 2.24 ×10^4 mL/mol in this work. V_{pore} stands for the total pore volume of the sediments assuming that they are incompressible and are considered constant. M_H represents the molar mass of methane hydrates while ρ_H is the densities of the hydrate phase, which is 0.94 g/cm^3 in this work.

4.1.2 Results and discussions

1. Properties of the sample matrix

In this study, the core samples from SK–2 were used for the analysis of the properties of the sediment matrix. Before permeability measurements, the samples were analyzed for particle sizes, pore sizes and mineral components. The results from Mercury Intrusion Porosimetry (MIP) (Figure 4.2) showed that the pore sizes ranged from 0.1–10 μm, and particles sizes ranged from 0.01–30 μm. The pore size of 0.7 μm obtained the highest relative pore volume, and the particle size of 1 μm obtained the highest relative percentage on sample volume. Therefore, the sample was predominantly composed of clay and silty sand. Energy dispersive spectroscopy (EDS) analysis indicated that the main mineral components of the sample from SK–2 were quartz, carbonate, and kaolinite. Meanwhile, the boundary of different components could obviously be found from Figure 4.3.

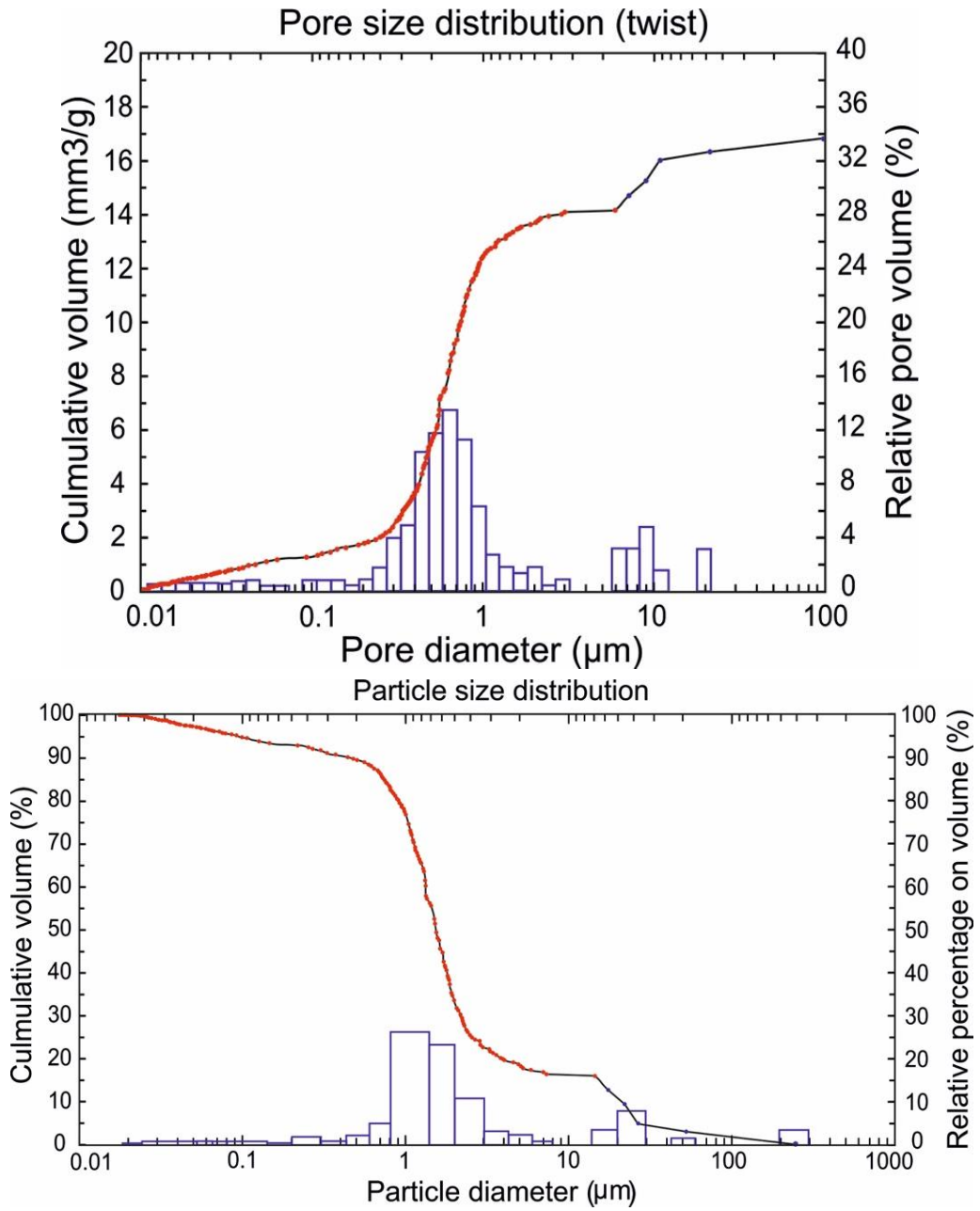

Figure 4.2 Measurements of pore size distribution and particle size distribution for samples from SK–2 site by using Mercury Intrusion Porosimetry (MIP).

Two samples from SK–2 were also ground into homogeneous powders of less than 63 μm for quantitative XRD measurements. During the preparation process, the powders were surprisingly found floating on the water surface instead of dissolving into the water even after stirring. The results from XRD indicated that the main mineral component in both SK–2–I and II was quartz, with 76.5 wt% and 81 wt% respectively. Furthermore, SK–2–I contains 10 wt% feldspar, 6.5 wt% mica, 5 wt% kaolinite, and 2 wt% ankerite/siderite, whereas SK–2–II contains 7 wt% plagioclase, 4.5 wt% mica, 5 wt% kaolinite and 2 wt% ankerite/siderite

(Table 4.2, Figure 4.4).

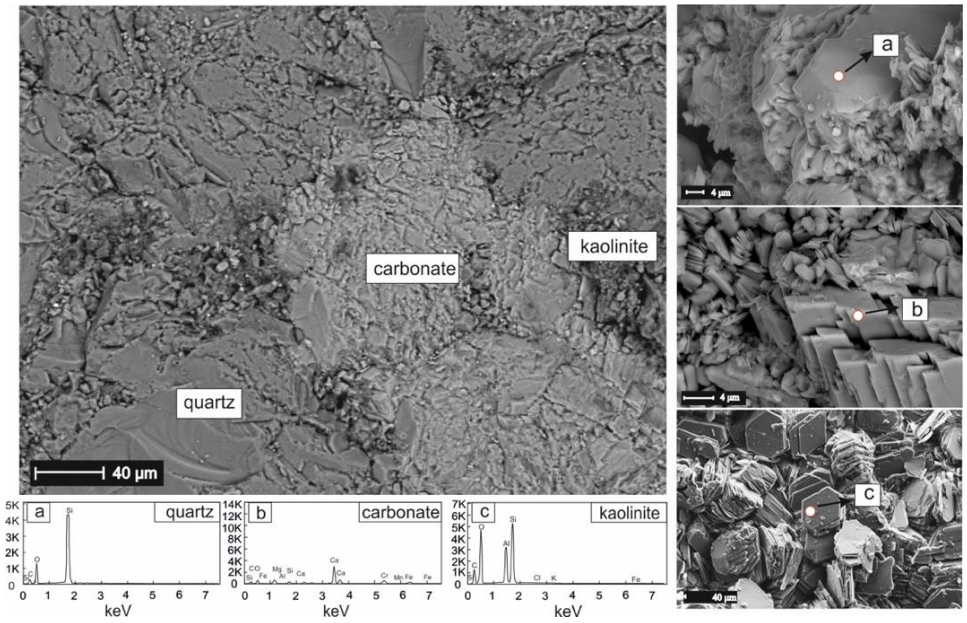

Figure 4.3 SEM–EDS analysis of dry sample from SK–2, Qilian mountain permafrost.

Table 4.2 Quantitative XRD analysis using the open source Rietveld Program "Profex"

Sample	Quartz	Plagioclase	K-feldspar	Mica	Ankerite/Siderite	Kaolinite
SK–2–I	76.5%	9%	1%	6.5%	2%	5%
SK–2–II	81%	7%	n.d.	4.5%	2%	5%

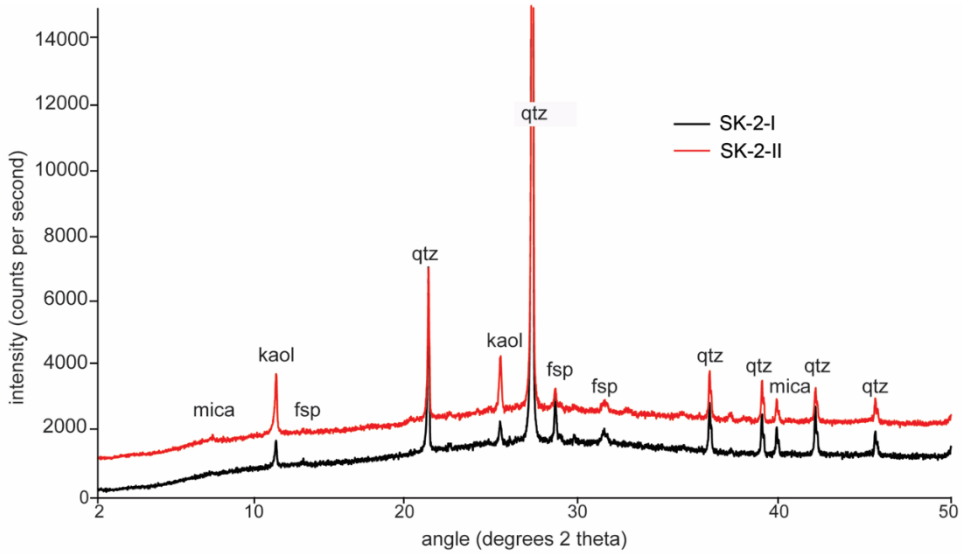

Figure 4.4 XRD patterns of SK–2–I and SK–2–II used for quantitative analysis (kaol=kaolinite, qtz=quartz, fsp=feldspar).

2. Reservoir formation damage by hydrate dissociation

Figure 4.5 showed the changes of the inlet pressure during the initial permeability measurement by brine injection with different injection rates of the sample DK–8–I. Since the outlet was open to air, the inlet pressure measured with a relative pressure sensor, could be considered as the pressure difference of the inlet and outlet. As seen from this figure, the pressure difference was proportional to the injection rate.

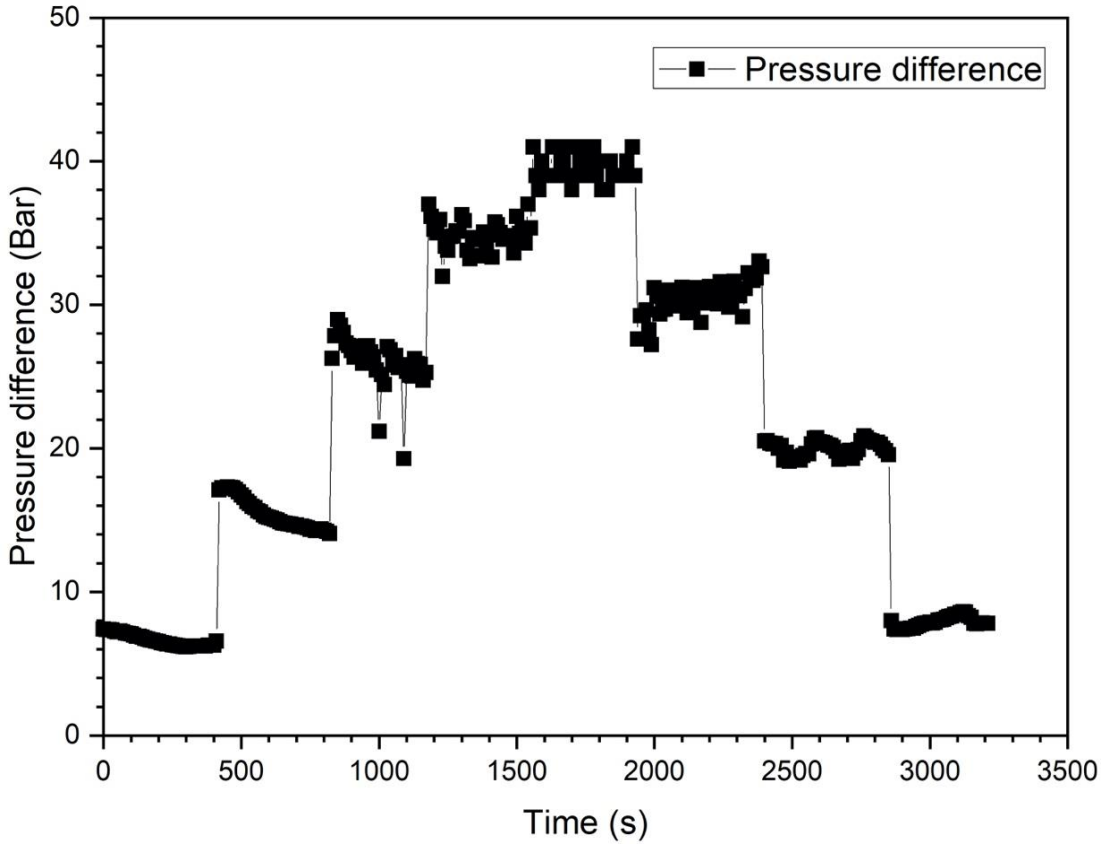

Figure 4.5 Changes of the pressure difference during brine injection with different injection rates.

The permeability can be calculated using Equation 4.1 with the experimental results of the pressure difference shown in Figure 4.5. The results of the calculated permeability were presented in Figure 4.6. However, it turned out that the permeability estimated at the lower injection rates (0.5 ml/min, 1 ml/min) were unstable. It might be due to the fact that the pump was not accurate at lower injection rates. Therefore, the calculated results with injection rates from 2 ml/min to 4 ml/min were selected for the permeability estimation. The average permeability value was considered as the effective permeability for this sample in this test. Therefore, the initial permeability of the sample DK–8–I was 26.2 mD. As also can be seen from Figure 4.6, the permeability of sediment slightly increases after the first injection with a rate of 3 ml/min. It might be due to the fact that the fluid dynamics led to the migration of particles in the porous media.

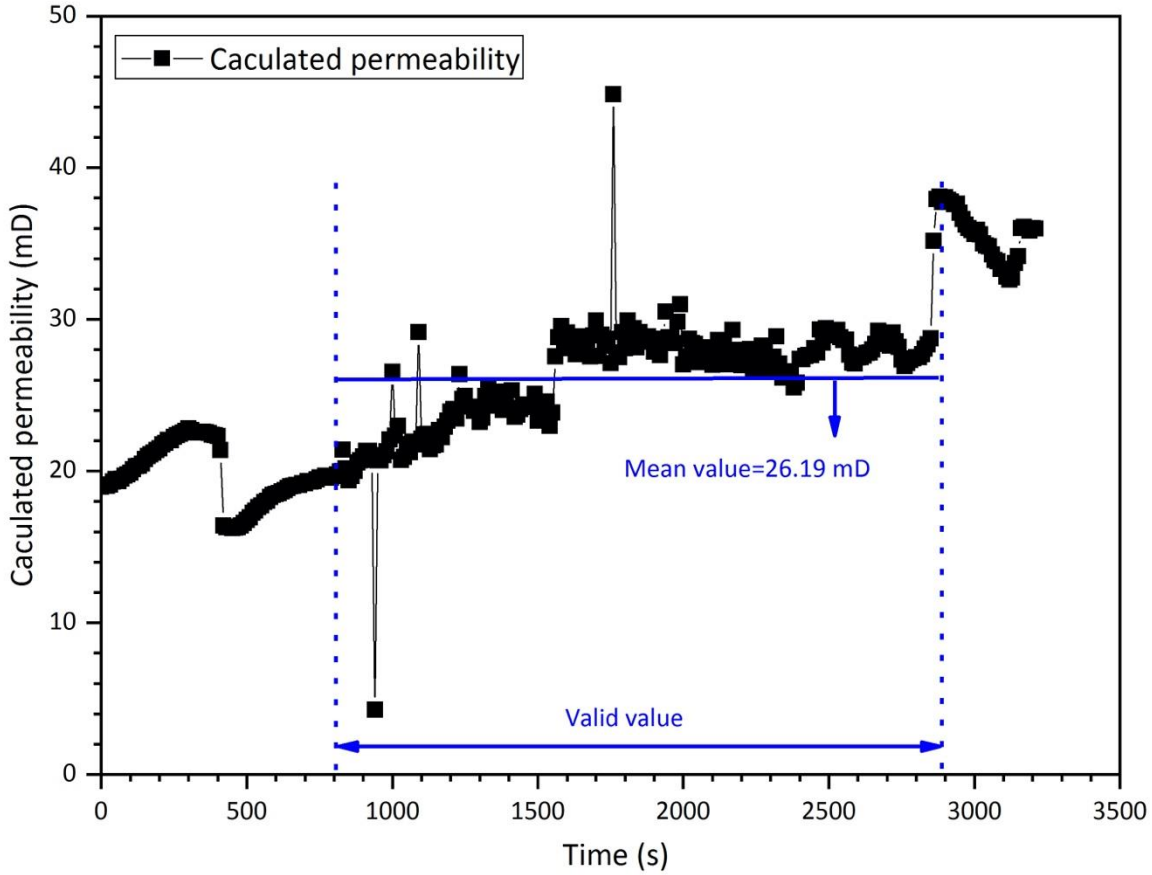

Figure 4.6 Permeability calculated by Darcy's law during brine injection with different injection rates.

After methane hydrate was synthesized in the sample DK–8–I with the hydrate saturation of 33% the permeability was determined to be 15.3 mD (Figure 4.7). The reduction of permeability was due to the fact that the methane hydrate

occupies a part of the pore volume, which originally contributed to the transport network in the sample. This observation was already reported in the past [213–215]. However, in these previous studies, permeability was recovered after hydrate dissociation in the sediments. In contrast, we observed a decrease of the permeability of the sample after hydrate decomposition to 2 mD. The phenomenon can be considered as "reservoir formation damage", which is a generic term referring to the impairment of the permeability of petroleum-bearing formations by various adverse processes. In order to determine the reason for the formation damage after hydrate dissociation, 6 experimental tests were designed. Test 1 was the initial permeability measurement. Test 2 was the permeability measurement after long time brine injection, which was applied for investigating the influence of water flow on the permeability of the sample. Test 3 was the permeability measurement after gas injection, which was applied for investigating the influence of gas flow on the permeability of the sample. Test 4 was the permeability measurement after ice formation and melting, which was similar to those of the methane hydrate. The main difference between ice melting and hydrate decomposition was the release of gas. For ice formation, the samples were firstly soaked in pure water to ensure the pores fulfilled with water, and then the temperature of the soaked sample was decreased to 258 K for ice formation. Thus, the ice saturation in sample was nearly 100%. Afterwards, the temperature was recovered to 298 K for ice melting. Test 5 was the permeability measurement after alternating pure water and brine water injection, which was applied for investigating the influence of the pure water on the permeability. During Test 5, brine water was firstly injected into the sample with the injection rate of 1 ml/min for 5 minutes, and then pure water injected into the sample with the same injection rate for 5 minutes. Test 6 was the permeability measurement after hydrate formation and dissociation. Because each sample could only be damaged once, one sample could not finish all of the tests. The experimental procedures for each sample were shown in Table 4.3. The experimental results were shown in Figure 4.8–10.

Table 4.3 Arrangement of experimental tests for SK–2–I, SK–2–II, and SK–2–III.

Sample	**Test1**	**Test2**	**Test3**	**Test4**	**Test5**	**Test6**
SK–2–I	Yes	Yes	No	Yes	No	Yes
SK–2–II	Yes	No	Yes	Yes	No	Yes
SK–2–III	Yes	No	No	Yes	Yes	No

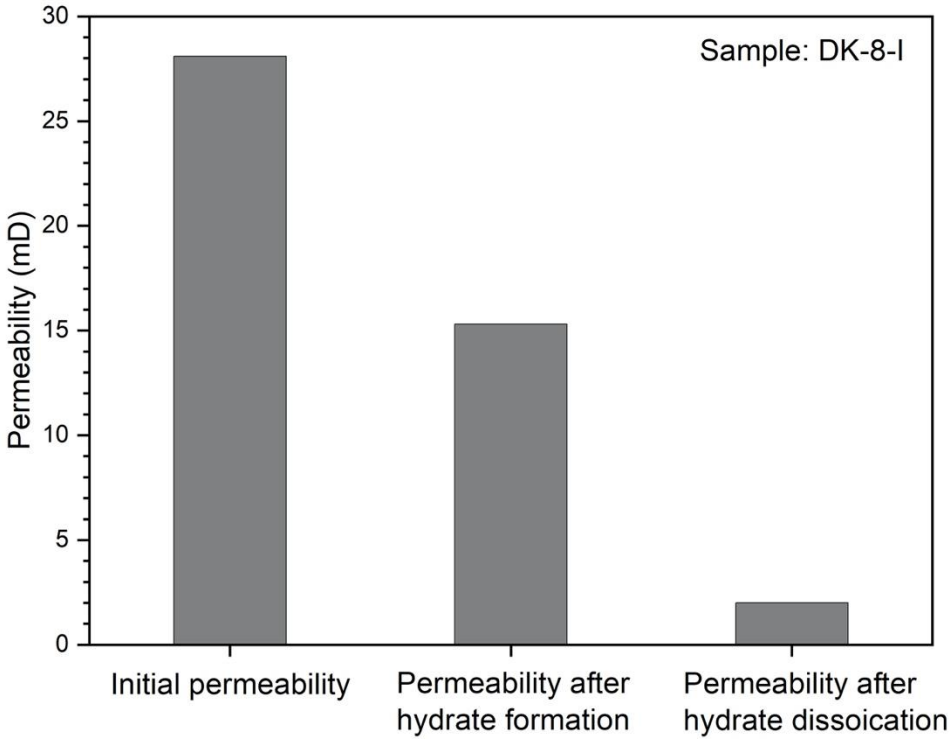

Figure 4.7 Intial permeability, permeability after hydrate formation and permeability after hydrate dissociation of sample DK–8–I.

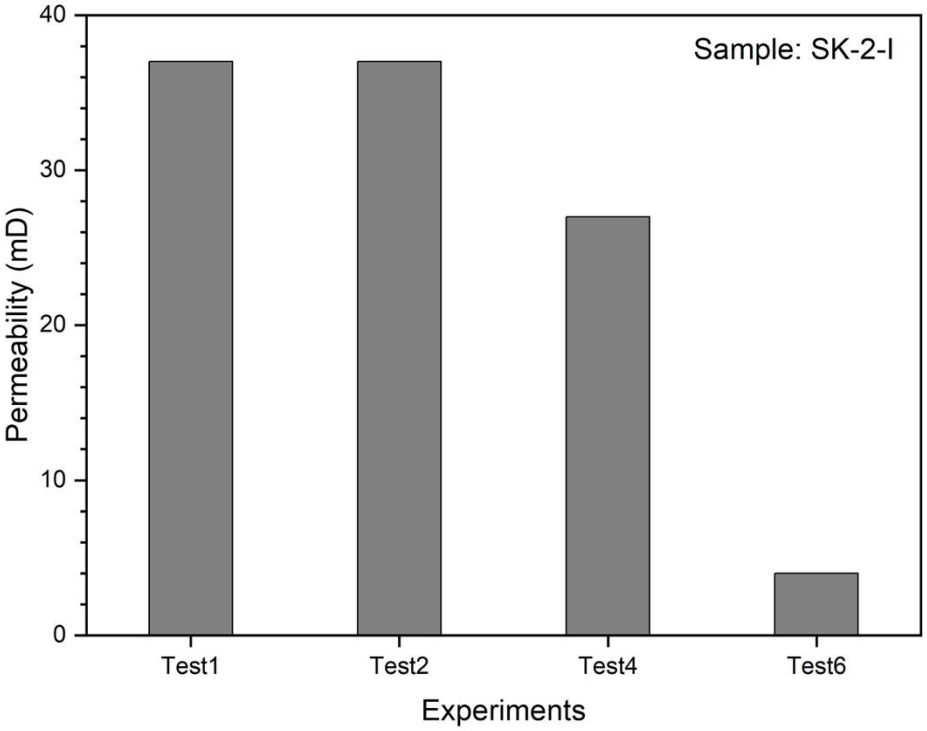

Figure 4.8 Permeability measurement results after experimental test 1, test 2, test 4 and test 6 for sample SK–2–I.

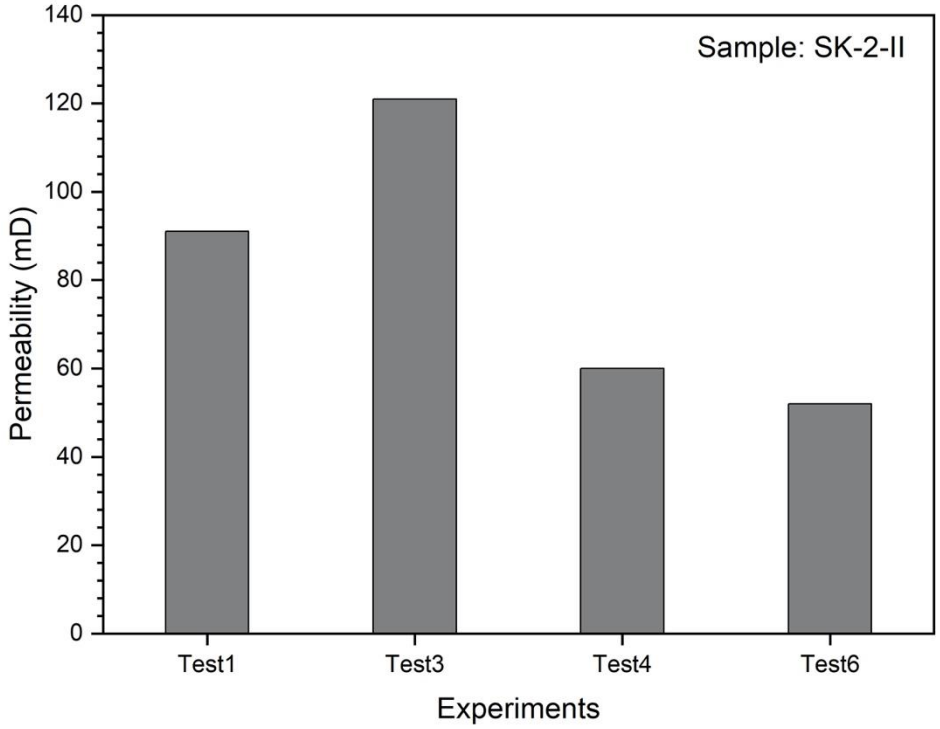

Figure 4.9 Permeability measurement results after experimental test 1, test 3, test 4 and test 6 for sample SK–2–II.

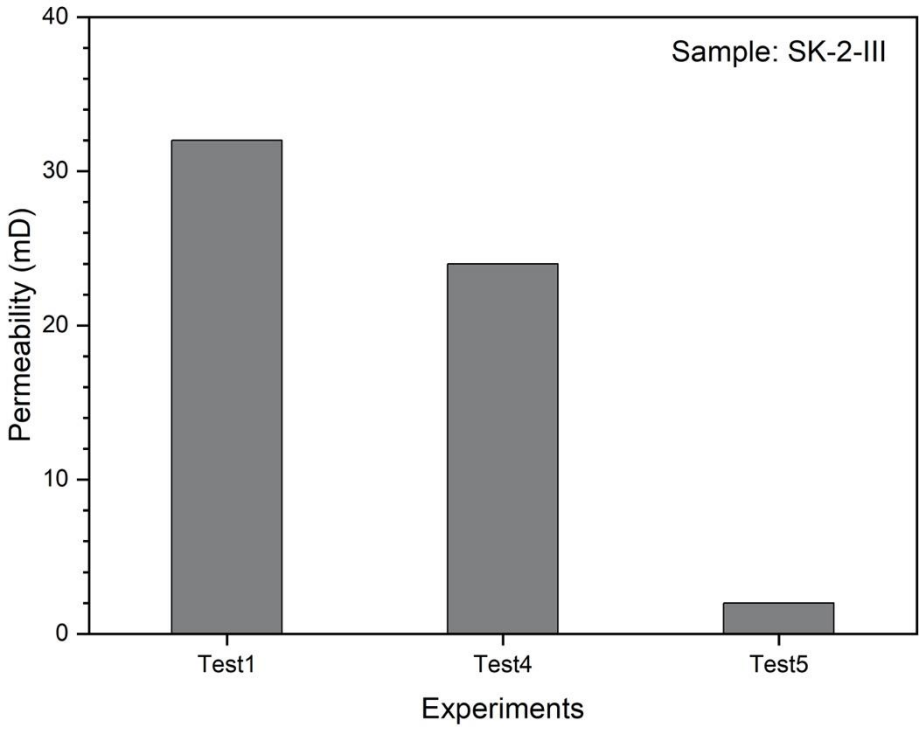

Figure 4.10 Permeability measurement results after experimental test 1, test 4 and test 5 for sample SK–2–III.

As shown in Figure 4.8, after injection of a 5% KCl solution for 24 hours (Test 2), the permeability remained at the initial value of 37 mD. After ice formation and melting (Test 4), the permeability decreased to 27 mD. However, after hydrate formation and decomposition (Test 6, hydrate saturation = 38%), the permeability decreased to 4 mD. The experimental results indicated that the water flow dynamic might not be the reason for reservoir formation damage after hydrate dissociation. As shown in Figure 4.9, after gas injection (Test 3), the permeability of SK–2–II increased from 91 mD to 121 mD. This result indicated that the gas fluid dynamic might also not be the reason for reservoir formation damage. After ice formation and melting (Test 4), the permeability decreased to 60 mD. After Test 6, the permeability decreased to 54 mD. It should be noted, that the hydrate saturation was only 5% for sample SK–2–II, which was much lower compared to that in Test 6 for sample SK–2–I. This might be the reason for a lower decrease in permeability after Test 6 in sample SK–2–II. As shown in Figure 4.10, after ice formation and melting (Test 4), the permeability of the sample SK–2–III decreased from 32 mD to 24 mD. After alternating pure water and brine water injection (Test 5), the formation damage progressed and the permeability declined to 2 mD. The main reason for the formation damage after hydrate decomposition seemed to be the fresh water released from hydrate dissociation. However, Test 5 (alternating pure water and brine water injection) also led to an obvious decrease in permeability. More work should be done to define the relationship of alternating pure water and brine water injection with permeability variety. By summarizing the experimental results from Figure 4.8-10, three conclusions can be drawn for the investigated rock materials: (1) Fluid dynamic is not the main reason for the decrease of permeability. (2) Permeability decrease by hydrate dissociation is related to hydrate saturation – higher hydrate saturations result in the release of larger amounts of water and thus stronger decrease of permeability. (3) Fresh water release from hydrate dissociation induces formation damage: The fresh water released from hydrate dissociation will increase the thickness of the electrical double layer (EDL) at the fluid-mineral interface, because there are less ions available in the pore water to compensate the surface charges at the mineral surface [216]. The extension of the EDL increases the distant effect of repulsive forces especially for small particles like clays with a high surface to volume ratio. This might lead to the separation of clay particles sticking together or at the surface of larger particles and allows them to float in the pore water. These small particles can migrate through the pore network and may get trapped at small pore throats, decreasing or finally blocking the flow through these pores and, therefore, leading to formation

damage and low permeabilities. The theoretical analysis for the reservoir formation damage after hydrate decomposition will be investigated in details in the following paragraph.

3. Detection of the fine migration using SEM

In order to find the evidence for the fine migration during the formation damage process, an unused filter paper was attached on the outlet-side of the sample SK–2–I before the experimental test. The sample was cleaned by ultrasonic cleaners before experiment to avoid free particles on the sample. Thereafter, the initial filter paper and the filter paper used during the test were analyzed with SEM. The microscopic images measured by the SEM are compared in Figure 4.11**.** Fine particles with different sizes could be found on the filter paper, which indicates that the fine migration has happened during the formation damage process. Elemental analysis of the particles indicates that not only quartz but also other minerals (such as plagioclase, mica, carbonate, kaolinite etc.) are involved in the fine migration to the surface of the filter paper (Figure 4.12).

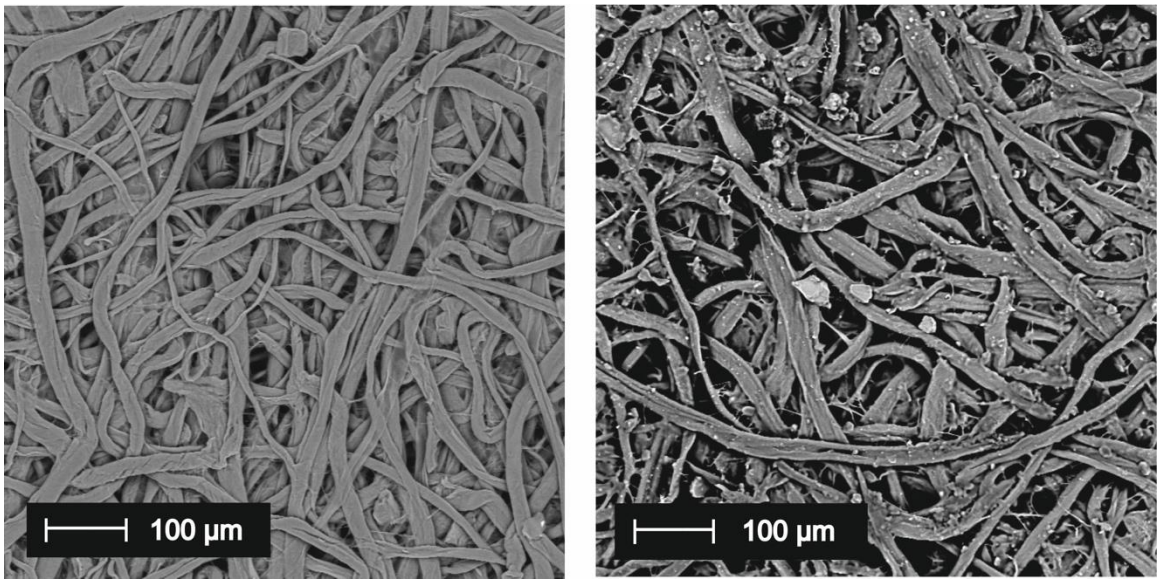

Figure 4.11 SEM microscopic photos of the filter paper before and after reservoir formation damage of sample SK–2–I.

4. Theoretical analysis for the reservoir formation damage

Permeability decrease in the clay–sand sediments due to the change of the injection salinity has been reported in the research of petroleum reservoir engineering for a long time. When the salinity of the solution is lower than the critical salt concentration, clay particles will disperse and migrate causing the

block of pore throats [217,218]. There are many different reasons for this phenomenon like cation exchange and swelling [219]. Since we do not have expandable clay minerals like bentonite or montmorillonite, swelling is not the explanation in our experiments. However, the release of fresh water during hydrate decomposition already causes an increase of the double layer thickness and therefore an increase of repulsion forces between small particles that can release some of these particles from the rock formation. Fluid dynamic of the fresh water will cause the migration of the fine particles resulting in permeability damage.

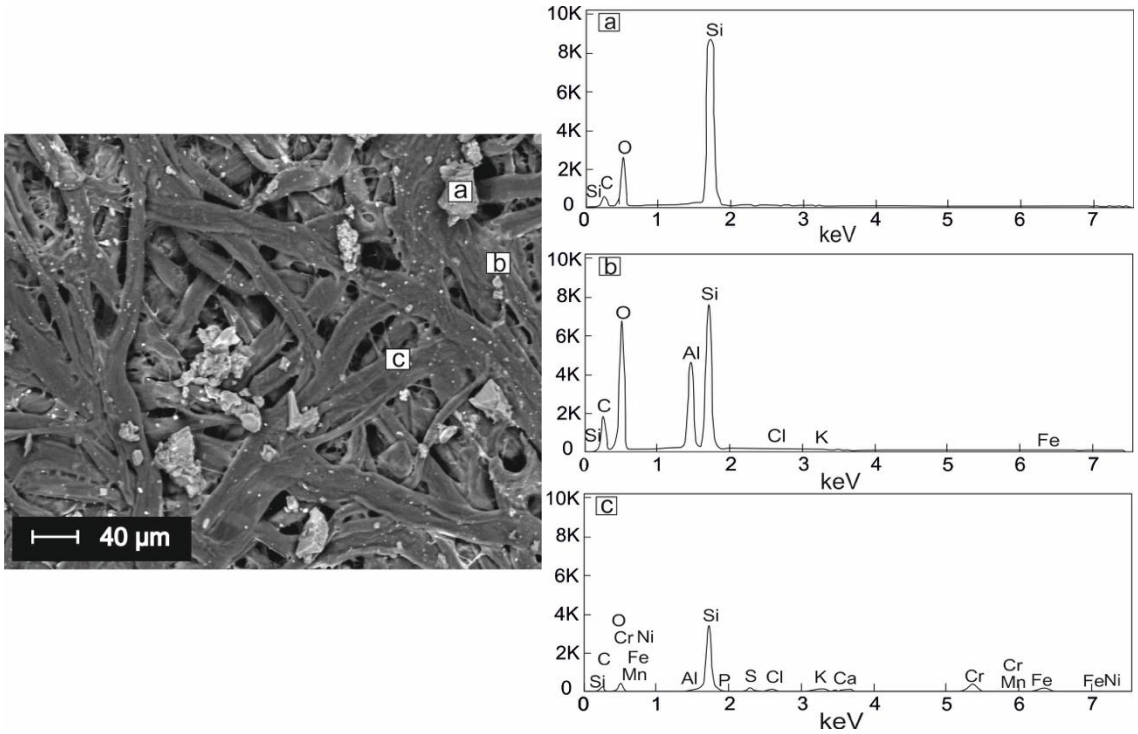

Figure 4.12 Mineral component analysis of the particles on filter paper after reservoir formation damage by SEM and EDS.

4.1.3 Conclusions

The permeability study on sand-clay core samples from the Qilian Mountain permafrost revealed that fines mobilization and migration which occurred during hydrate decomposition led to a significant permeability decrease. This was to our knowledge the first time that formation damage by fines migration during hydrate decomposition was reported. From the results of the experiments the following conclusions can be drawn:

(1) The observed fines mobilization and migration was a result of the freshwater release during hydrate decomposition and the fact that the

simultaneous release of a large methane volume displaced the saline pore water and separated it from the produced freshwater. In our experiments the pore pressure was lowered to atmospheric pressure during hydrate decomposition which resulted in a maximal volume expansion of about 200 liter methane per liter produced water. This effectively displaced the original saline pore water and prevented the mixing of the saline and freshwater.

(2) The methane gas to water volume ratio during production depends on the initial pore fluid pressure (depth) and the pressure drop required to initiate hydrate decomposition. The lower the required pressure drop and the deeper the reservoir, the lower the methane gas to water ratio will be recorded during production. In deep hydrate-bearing reservoirs close to the hydrate stability, the produced gas volume might not sufficiently displace the original saline pore water and separate it from the produced fresh water. This could suppress the above-described formation damage mechanism.

(3) However, the higher the hydrate saturation, the lower the amount of residual saline pore water that may mix with the freshwater during hydrate decomposition. This means that as the hydrate saturation becomes higher and the hydrate-bearing reservoir shallower, the described reservoir damage mechanism in clayey sand reservoirs might become more important during production.

Even though the experimental samples come from the hydrate reservoir in QMP, the observed phenomenon during the experiments are more important rather than the samples or this specific hydrate reservoir. The conclusions are based on the experimental results but at the same time with in-depth analysis of the underlying mechanism. Therefore, a basic understanding of the above-described formation damage scenario is an important prerequisite for the assessment of the economic risk prior to the gas production from clay-bearing hydrate reservoirs in a world-wide perspective.

4.2 Experimental simulations of gas hydrates dissociation in response to global warming

Natural gas hydrates, as a highly concentrated form of methane, are only stable over a range of low-temperature and high-pressure conditions. Oceanic and atmospheric warming caused by climate changes may destabilize the hydrate deposits which are preserved in the sediments of marine continental margins and permafrost areas, leading to an enhanced release of sequestered methane into the overlying sediments. Those methane gas that escaped from the

sediments and reach the atmosphere can in turn exacerbate greenhouse warming. Gas hydrates in QMP occur at a shallow depth beneath the thin permafrost layers which may be more vulnerable to dissociation in response to atmospheric warming. However, the mechanisms of mixed gas hydrate dissociation are still not straightforward and worth discussion.

In order to clarify the response of gas hydrate reservoirs to climate change, a better understanding of the dissociation behavior of the complex mixed gas hydrates is required. Our experiments simulated the dissociation process with regard to thermal stimulation of mixed gas hydrates under reservoir conditions in QMP. For comparison and an in-depth analysis, the dissociation of pure sI CH_4 hydrates as well as simple sII CH_4–C_3H_8 mixed gas hydrates were also investigated in this work. The dissociation processes were based on the thermal conduction and the results were discussed under several isobaric conditions. By applying *in situ* Raman spectroscopic measurements and microscopic observations, information about the dissociation process was revealed on a micro-scale. Single-point Raman measurements on specific hydrate crystals continuously recorded the molecular behaviors of each guest component until the whole hydrate phase was decomposed. These results provided essential information for the estimation of possible methane release from this area in response to future climate warming.

4.2.1 Materials and methods

To ensure a systematic study about the dissociation process, experiments systematically progressed step by step from the simplest methane hydrates to sII binary mixed hydrates and finally the complicated multi-component mixed hydrates for both *in situ* and *ex situ* Raman spectroscopic analysis.

***In situ**:* Initial experiments were carried out with sI methane hydrates formed from the pure methane gas and deionized water in the high-pressure cell. The pressure and temperature conditions were selected at 7.0 MPa and 274 K. It should be noted that a higher pressure (at constant temperature) and a lower temperature (at constant pressure) condition was required for the formation of methane hydrates as compared to the mixed gas hydrates (Figure 4.13). Once sI methane hydrate crystals were well developed, the temperature of the system was increased one step at a time (277 K, 278 K, 279 K, 280 K, 280.5 K, 281 K, 281.5 K, 282 K, 282.5 K, 283 K) to cross the equilibrium curve to induce hydrate decomposition. Since it took some time until the complete system reached an equilibrium temperature, each temperature gradient was maintained for at least

20 minutes. During this period, the compositions of the selected hydrate crystals were measured. The collapse of hydrate structures may occur instantaneously, hence, a smaller step (0.5 K) was made when the temperature approached the equilibrium curve at given pressure.

Mixed gas hydrates were synthesized in the high-pressure cell from deionized water and two gas mixtures. The binary gas mixture contained 98 mol% CH_4 with 2 mol% C_3H_8. The multi-component gas mixture was composed of 63 mol% CH_4, 15 mol% C_2H_6, 15 mol% C_3H_8, 7 mol% CO_2 which shared a similar composition with the natural gas hydrates that recovered from QMP. Both gas mixtures formed sII hydrates at 3.0 MPa, 278 K (Figure 4.13). The hydrate formation conditions are summarized in Table 4.4. Hydrate crystals were analyzed in x-y-z directions to help identify the guest compositions using Raman spectroscopy combined with optical microscopy. Once the mixed gas hydrates reached a steady state as indicated by the Raman spectra in terms of cage occupancy, the temperature of the system which was initially set at 278 K, was gradually increased until the complete decomposition of the hydrate phase. In the binary hydrate system, measurements were taken at 280 K, 281 K, 281.5 K, 282 K, 282.5 K, 283 K, 283.5 K and 284 K respectively. Temperature gradients in the multi-component mixed hydrate system were set at 281 K, 284 K, 286 K, 287 K, 287.5 K, 288 K and 288.5 K. In both systems, selected hydrate crystals were monitored at each temperature gradient. The results from multi-component sII hydrate system was analyzed in comparison with the results from sI and binary sII hydrate systems.

Table 4.4 Experimental conditions for the three tests regarding the p–T conditions.

Experiments	**Gas**	**Pressure (MPa)**	**Temperature (K)**
Test 1	CH_4	7.0	274
Test 2	$CH_4 + C_3H_8$	3.0	278
Test 3	$CH_4 + C_2H_6 + C_3H_8 + CO_2$	3.0	278

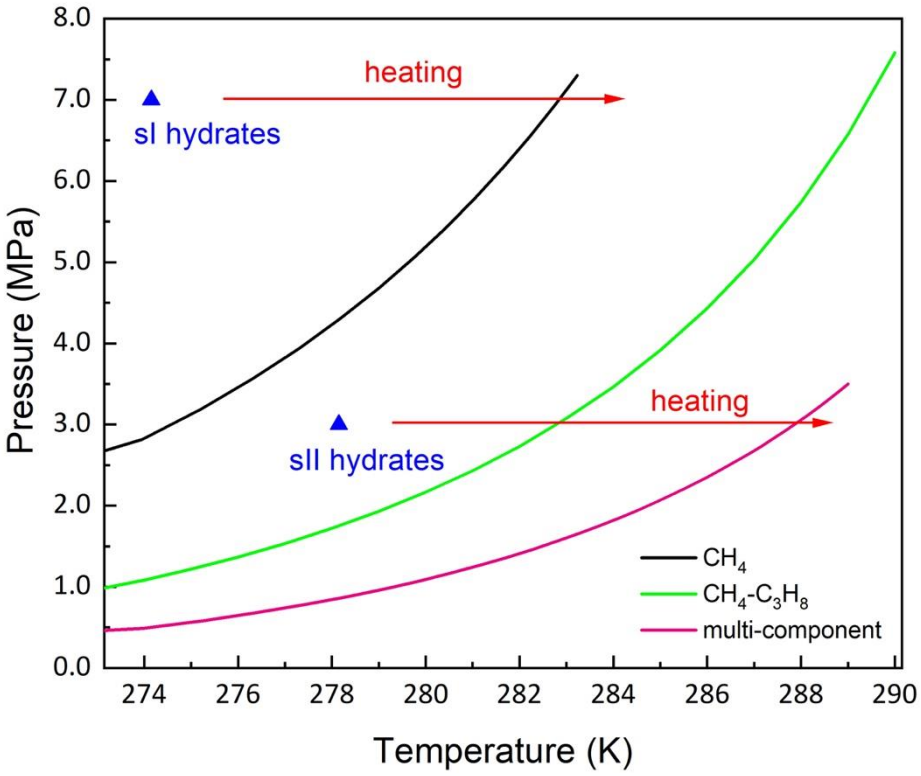

Figure 4.13 Experimental conditions and the corresponding equilibrium curves for pure methane hydrates and two mixed gas hydrates. The formation condition for the pure methane hydrates were 7.0 MPa and 274 K (blue triangle) whereas two mixed gas hydrates were formed at 3.0 MPa, 278 K (blue triangle). The straight lines indicated the equilibrium curves calculated from the software CSMGem [5].

Ex situ: Apart from the above-mentioned *in situ* Raman spectroscopic measurements, sI and sII hydrates were also formed from ice and the same gas /gas mixtures in batch pressure vessels with a volume of 420 ml. The formation of gas hydrates started with the preparation of ice by spraying deionized water into the liquid nitrogen bath. Ice beads were powdered by a pestle driven by a cryo magnet in a Spex 6750 Freezer Mill for 120 seconds. Thereafter, the vessels were loaded with ice powder, sealed and pressurized with the respective gas or gas mixture at desired pressure. Thereafter, the vessels were stored in a cooling box with the temperature fluctuating between 263 K and 268 K for several weeks. When there were no further changes in the pressure of the vessel, gas hydrate samples were recovered and quenched into liquid nitrogen. For further analysis with *ex situ* Raman spectroscopy, the recovered hydrate samples were quickly placed into a Linkam cooling stage at ambient pressure at 168 K. Single Raman spectra were collected continuously using the

aforementioned confocal Raman spectroscopy. The temperature of the Linkam cooling stage was gradually increased until Raman spectra showed no signals of hydrate structures indicating that the hydrates were completely dissociated.

4.2.2 Results and discussion

1. sI methane hydrates

After the formation of methane hydrates (see also *Chapter 2.1.1 and 5.1.2*), time resolved Raman spectra recorded the dissociation process on the surface of hydrate crystals. It should be pointed out that Raman signals for the surrounding gas phase during the *in situ* measurements of the hydrate phase were limited with the use of a confocal system, however, not completely avoided. To refrain from the influence of the gas phase, results from *ex situ* Raman measurements were used for analyzing the behaviors of guest molecules in the hydrates structure. Time-resolved Raman spectra recording the methane hydrates dissociation process was shown in Figure 4.14. Preliminary results showed that Raman band intensities for CH_4 in large and small cavities started to decrease after 86 mins, indicating the release of gas from hydrate structures. Hydrates were totally dissociated after 294 mins.

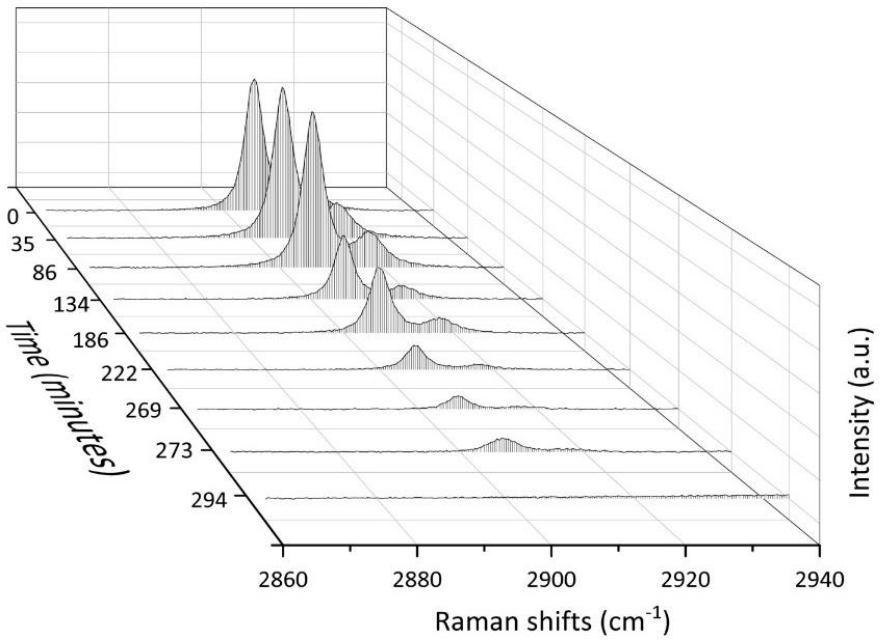

Figure 4.14 Real-time *ex situ* Raman spectra monitoring the dissociation process of methane hydrates in the Linkam cooling stage.

Figure 4.15 illustrated the changes of CH_4 in large and small cavities for a specific hydrate crystal over time. Initially, the integrated Raman intensity of CH_4 in large and small cavities approached the theoretical value of 3:1. As shown

Figure 4.15, the ratio remained for around 190 mins before a slight decrease, indicating that CH_4 gas molecules were released faster from the large cavities than that in small cavities at the end of the dissociation process. It was noteworthy that Raman signals for CH_4 in hydrate cavities were no longer detected after around 275 mins suggesting that all hydrates have been melted. Same phenomenon was also recorded when repeating the dissociation process but the duration time for the complete dissociation in each test was varied.

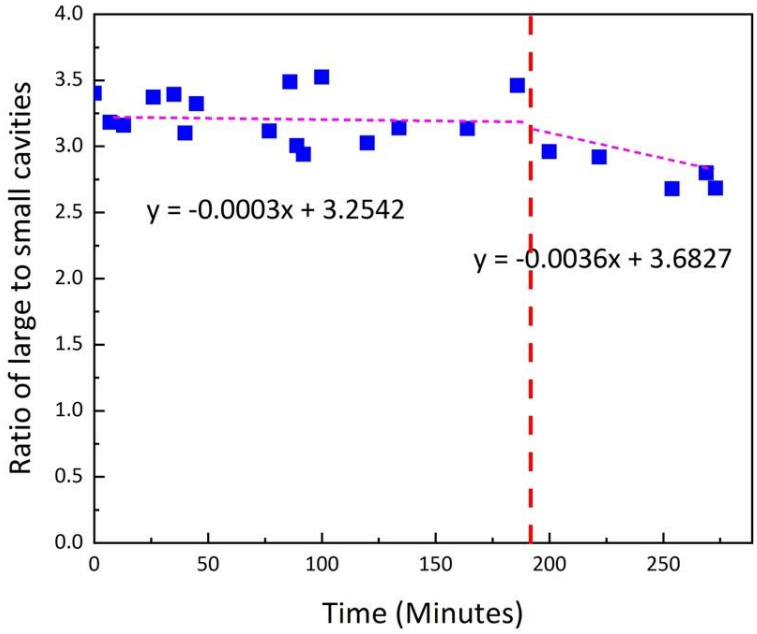

Figure 4.15 Ratio of large to small cavities as a function of time during the dissociation process of methane hydrates.

The unit cell of sI hydrate is comprised of two small cavities (5^{12}) and six large ones ($5^{12}6^2$) with a total of 46 water molecules [5]. In pure CH_4 hydrates, CH_4 molecules occupy both small and large cavities. It is reported by Lederhos et al. [14] that the guest diameter of CH_4 molecules is around 0.436 nm. The corresponding guest-to-cavity ratios for large $5^{12}6^2$ and small 5^{12} cavities are 0.87 and 0.74, respectively. It is a common assumption that the guest to cage ratio should approach the value 1.0 so that the guest molecule stabilizes the cavity well (see also *Chapter 3.1.3*) Apparently, the ratio is much closer to 1.0 for the small 5^{12} cavities which indicates that CH_4 molecules are expected to better stabilize in the small 5^{12} cavities than the large cavities. When the system is gradually heated up and hydrates are temporarily preserved outside the stability field, large $5^{12}6^2$ hydrate cavities are less stable and liberate CH_4 gas fast. CH_4 in small cavities are also released in response to the temperature increase.

2. sII CH_4–C_3H_8 hydrates

The binary sII hydrates were synthesized from a gas mixture containing 98 mol% CH_4 and 2 mol% C_3H_8. In the first step, the pure gas phase was characterized by the *in situ* Raman spectroscopic measurements as shown in Figure 4.16 (a–b). The Raman bands at 2916 cm^{-1} indicated CH_4 molecules in the gas phase while a small band occurred at 869 cm^{-1} can be assigned to C_3H_8 in the gas phase. By calculating from the integrated intensities of the two above-mentioned Raman bands, the verified composition of the gas phase was composed of around 94.8 mol% CH_4 and 5.2 mol% C_3H_8.

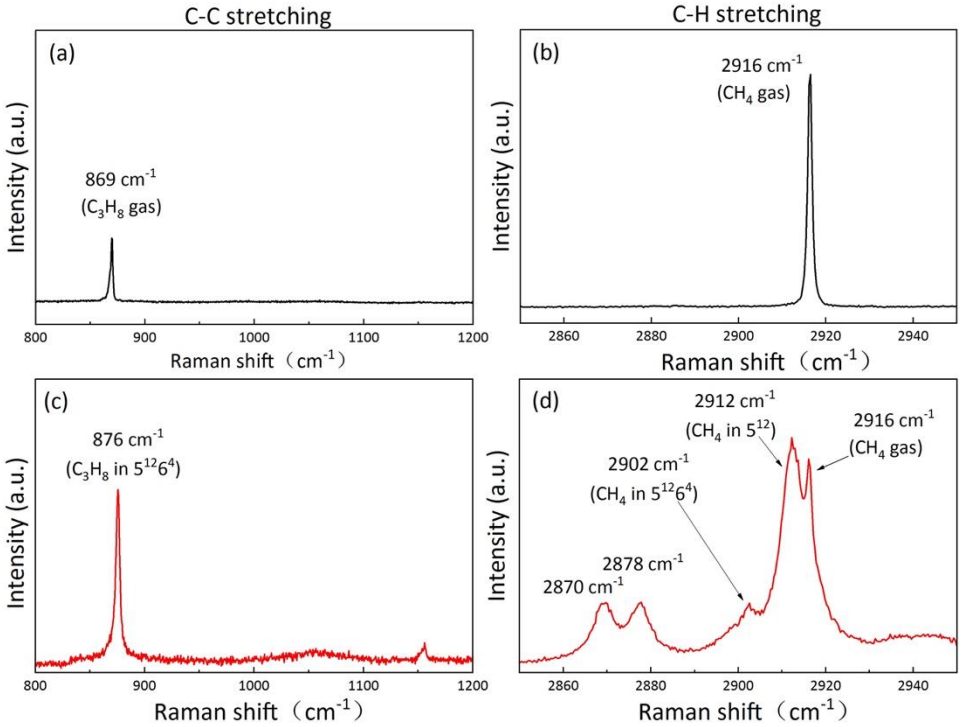

Figure 4.16 Raman spectra of the gas phase (a–b) and binary mixed hydrate phase (c–d), respectively. (a) and (c) Section of the Raman spectrum showing the C–C stretching vibrational modes from 800 cm^{-1} to 1200 cm^{-1}. (b) and (d) Section of the Raman spectrum showing the C–H stretching vibrational region from 2850 cm^{-1} to 2950 cm^{-1}.

The occurrence of hydrates was indicated by the changes of the Raman bands in the spectra (Figure 4.16 c–d). Instead of a signal at 869 cm^{-1} for C_3H_8 in the gas phase, a much stronger Raman band at 876 cm^{-1} from C–C stretching vibrational mode region appeared during the measurements. The two bands at approximately 2870 cm^{-1} and 2878 cm^{-1} indicated the C–H stretching of C_3H_8 molecules in the large cavities of the hydrate lattice. The concentration of CH_4 in

the hydrate phase was calculated from the integrated intensities of the Raman bands for CH_4 encased in the $5^{12}6^4$ (2902 cm^{-1}) plus the 5^{12} (2912 cm^{-1}) cavities of sII, with the dominance of the latter. When the Raman spectra indicated an achievement of a stationary state, showing no further changes regarding the hydrate composition and cage occupancy over several hours, the experimental temperature started to increase for the initiation of dissociation.

The average composition of CH_4 in the hydrate phase was merely 54.4 mol% for the selected crystals at a stationary state whereas C_3H_8 content reached 45.6 mol%. In comparison with the original gas, C_3H_8 molecules were preferred encased into the hydrate structure II within the large cavities based on the statement that the molecular size of C_3H_8 was not able to adequately fit into the small cavities (5^{12}) [6]. Considering that there are 16 small cavities and 8 large cavities in a unit cell of sII hydrates, the measured hydrate composition indicated that some of the small cavities were remained empty. With the increasing of temperature, the enclathration of C_3H_8 and CH_4 into the hydrate phase altered as illustrated in Figure 4.17. At temperatures lower than 283 K, the hydrate composition remained relatively unchanged. At temperature = 283.5 K, which was slightly above the equilibrium temperature at 3.0 MPa as calculated from CSMGem, a larger variation of the hydrate composition was detected, suggesting that the hydrate crystals started to decompose. Later on, a reduction of CH_4 concentrations in some crystals was observed. In contrast, the relative content of C_3H_8 gained a significant rise in most of the hydrate crystals. This finding implied that the release of CH_4 from the hydrate structures were much faster than the release of C_3H_8. The changes in the hydrate composition at higher temperatures were also accompanied by the morphology changes observed on each crystal surface. Taking one crystal as an example shown in Figure 4.18, the surface morphology of the hydrate crystal almost remained unchanged until 283 K, which was in consistent with the results from Raman measurements. When the system was heated up to 283.5 K, the hydrate crystal lost its even surface and sharp edges. The whole hydrate structure collapsed at a temperature of 284 K.

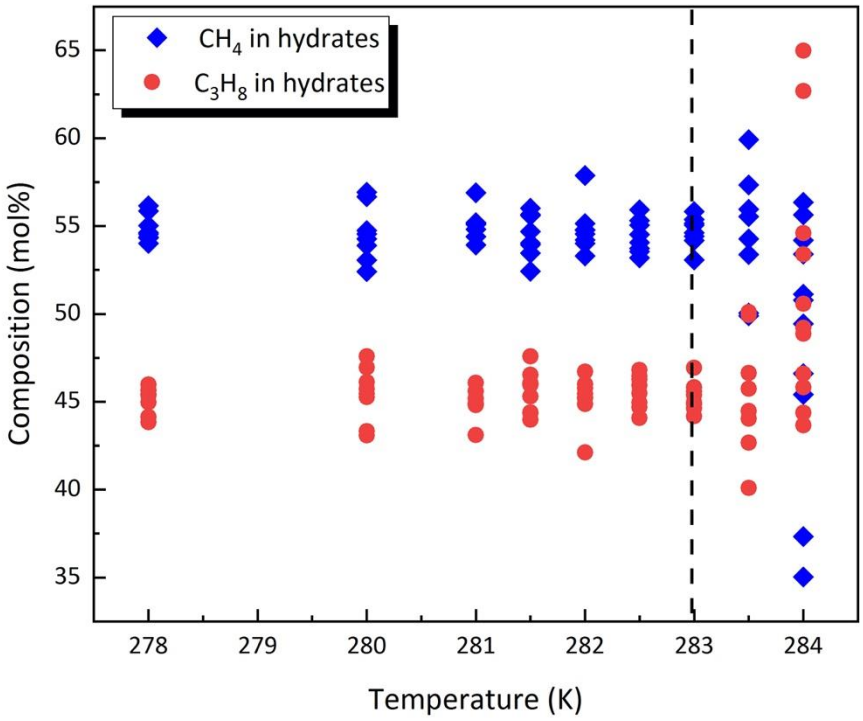

Figure 4.17 Results of Raman spectroscopic measurements illustrating the changes of hydrate composition with regard to the increasing temperature. Blue diamonds represented the data points collected for CH_4 in the hydrate phase while red circles indicated C_3H_8 molecules in hydrate lattice. The black dashed line indicated the equilibrium temperature for the chosen mixed gas hydrate at 3 MPa calculated from CSMGem.

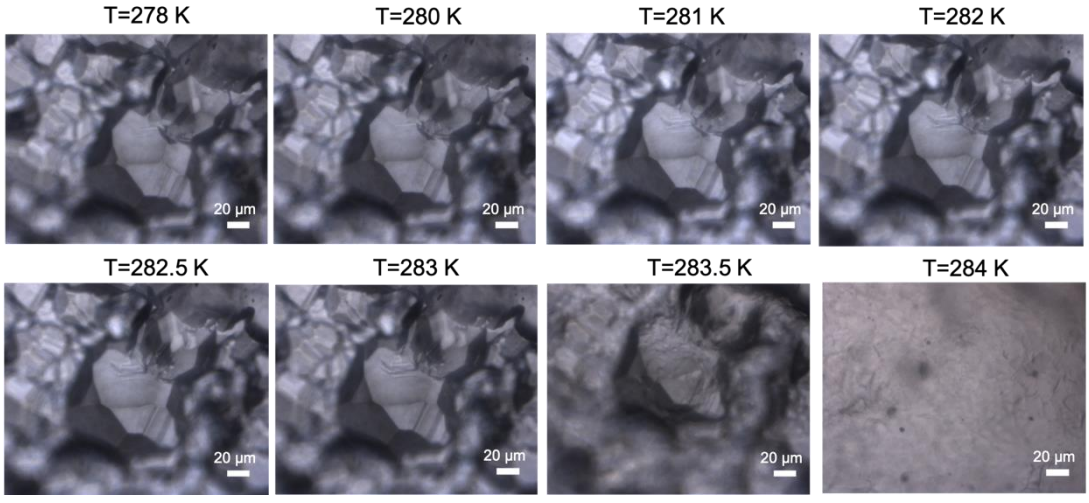

Figure 4.18 Morphology changes observed on the surface of a hydrate crystal with increasing temperatures.

Ex situ Raman measurements on the hydrate phase also implied a differentiated performance of CH_4 and C_3H_8 molecules during dissociation process, where the concentration of CH_4 in the hydrate phase decreased remarkably after around 100 mins (Figure 4.19). Correspondingly, the relative C_3H_8 composition in the hydrate phase ascended which is consistent with the findings from *in situ* Raman measurements (Figure 4.17). To avoid the effects from gas phase, the ratio of CH_4 in large and small cavities throughout the dissociation process were calculated from *ex situ* Raman measurements in consideration of the occupancy of CH_4 in both small 5^{12} and large $5^{12}6^4$ cavities of sII (Figure 4.20). It turned out that the initial ratio for the specific hydrate crystal was less than 0.4, indicating an extremely low content of CH_4 in large cavities of sII. Later on, the ratio revealed a trend of remarkable increase which could be explained by a faster release of CH_4 from small cavities than the release from large cavities of sII. It should be noted that the signal-to-noise ratios were relatively low for the last few measurements due to the low concentration of hydrate phase. Therefore, the last two data points were not precise enough and should be neglected. Interestingly, the simple sI CH_4 hydrates exhibited an opposite trend as shown in Figure 4.15 in which the ratio of large to small cavities dropped over time. Similar phenomenon has been recorded when repeating the dissociation process.

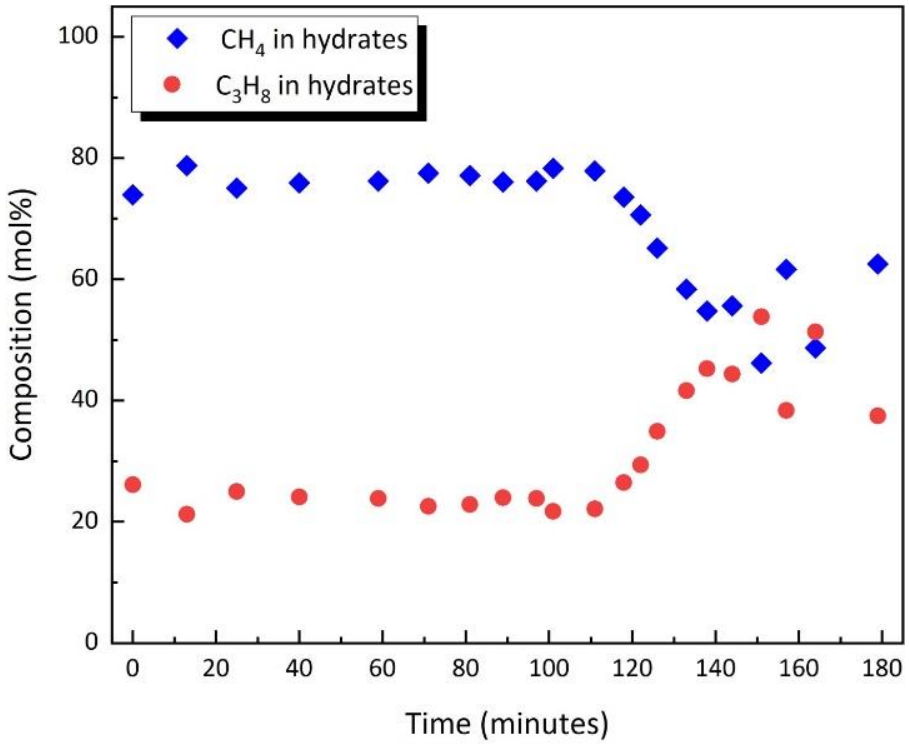

Figure 4.19 Results of *ex situ* Raman spectroscopic measurements illustrating the changes of hydrate composition measured on a specific hydrate crystal over time. Blue diamonds represented the concentration of CH_4 in the hydrate phase while red circles indicated C_3H_8 in hydrate lattice.

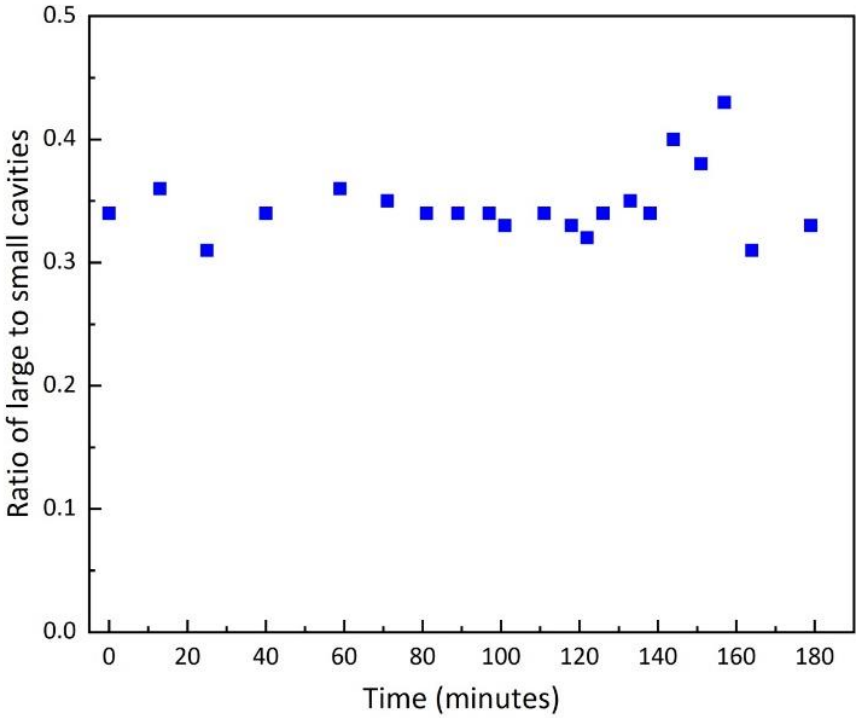

Figure 4.20 Ratio of large to small cavities as a function of time during the dissociation process of the binary CH_4-C_3H_8 hydrates.

In the form of sII hydrate, a total of 16 small 5^{12} cavities together with 8 large $5^{12}6^4$ cavities were presented in a single unit cell. For the binary system, the diameter of C_3H_8 molecule was too big to fit into the small cavities [14]. The preferential enclathration of C_3H_8 molecules in the hydrate phase was not only confirmed in this study but also reported by previous researches who observed the time-dependent overview of the Raman spectra during formation of mixed gas hydrates [44,46,71]. This observation indicated that C_3H_8 molecules can well stabilize the large cavities of sII. Again, CH_4 was enclathrated in both cages. It was concluded from the results that the rate of release for CH_4 was much faster than that for C_3H_8. Furthermore, the number of the small cavities were two times more than the large cavities in a unit cell of sII. Even though some small cavities were left empty as indicated from the hydrate composition, the break-down of more small cavities led to an increase in the ratio of large to small cavities.

Our results with regard to the rate of guest molecules release in different cavities were in good agreement with the data described by Truong-Lam et al.

[220] who simulated the dissociation process of CH_4–C_3H_8 mixed gas hydrates by depressurization. The retainment of C_3H_8 in mixed hydrate phase during dissociation was deducted by Sun et al. [221] as a permeable barrier that hindered the diffusion of gas from the hydrate core. However, other researchers also demonstrated that the hydrate cages collapsed as an entity in sI CH_4 hydrates [222], sI CH_4–CO_2 mixed hydrates [223], and CH_4–C_3H_8 hydrates [224]. The difference might be related to the experimental setups. Notably, previous researches on the dissociation process including the aforementioned examples were mainly induced by depressurization and without a continuous gas supply.

3. sII multi-component mixed hydrates

With the presence of multi-components in the hydrate phase, the dissociation behaviors of the mixed gas hydrates were undoubtedly much more complicated. *In situ* Raman spectroscopic measurements on the initial gas phase showed that composition of the incoming gas flow was 45 mol% CH_4, 20 mol% C_2H_6, 20 mol% C_3H_8 and 15 mol% CO_2. The average composition of the formed hydrates phase was around 41.9 mol% CH_4, 9.1 mol% C_2H_6, 40.4 mol% C_3H_8, 9.6 mol% CO_2. The results were in good agreement with the gas and hydrate composition measured in *Chapter 3.2.2*. The hydrate phase exhibited a high heterogeneity among different crystals. The inhomogeneous nature of hydrates became even clearer when an area of a certain crystal was analyzed (Figure 4.21a). For the depiction of the variation, the ratio of the concentration for two specific components in the hydrate phase, CH_4 and CO_2, were calculate and displayed in a color-coded map (Figure 4.21b).

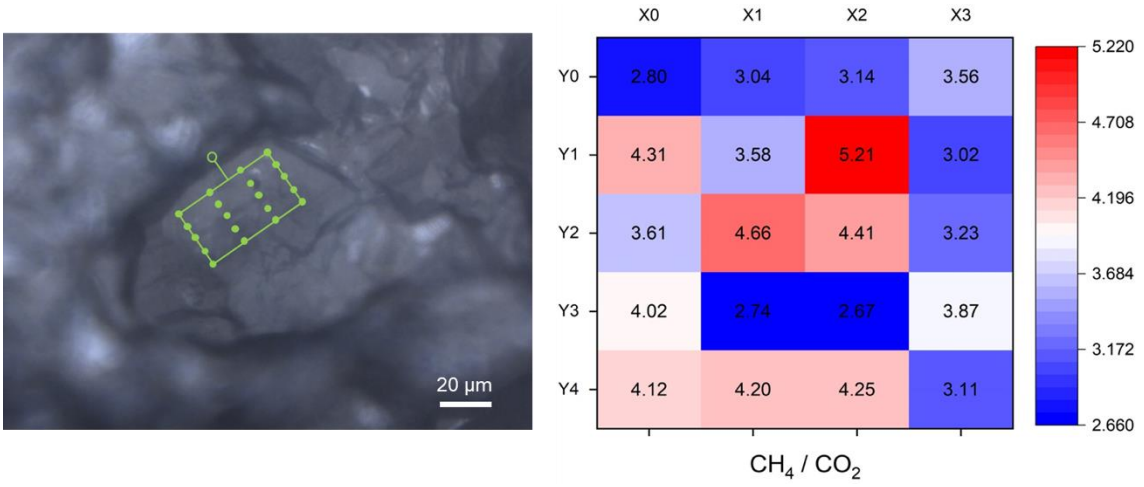

Figure 4.21 a) Scanned area on a hydrate crystal. 4 x 5 measuring points were chosen to analyze the composition of the hydrate crystal. b) Variation of the CH_4/CO_2 concentration ratio of the hydrate crystal surface in the mapped area.

Reddish points reflected a higher CH_4/CO_2 ratio, whereas bluish points represented a lower CH_4/CO_2 ratio.

Once the temperature of the *in situ* system was increased to initiate dissociation, the surface morphology of the hydrate crystals was monitored. A series of snapshots from microscopic observations were presented in Figure 4.22, given a better visualization of the single crystal. Initially, the hydrate crystal was developed with sharp edges and a relative even surface. Cracks were widely distributed on the surface of the crystal, which divided the entire surface to several small parts. With the increasing of temperature, slight changes were recorded from the pictures showing the alternative growing and shrinking of small parts. The whole surface almost remained its original appearance, but the number and positions of cracks on the surface seemed to change, indicating an ongoing process during the process. At t= 287.5 K, a temperature point that approached the equilibrium temperature at 3.0 MPa for this mixed gas hydrates, the edges of the hydrate crystal began to blur which gave a clearer signal for the dissociation. It was difficult to distinguish the boundary of the hydrate crystal when the temperature reached 288 K, as shown in the figure. The other hydrate crystals in the surrounding area also dissociated, with gas bubbles coming out. After a limited time, the hydrate phase was totally dissociated without evidence of a self-preservation effect at t = 288.5 K.

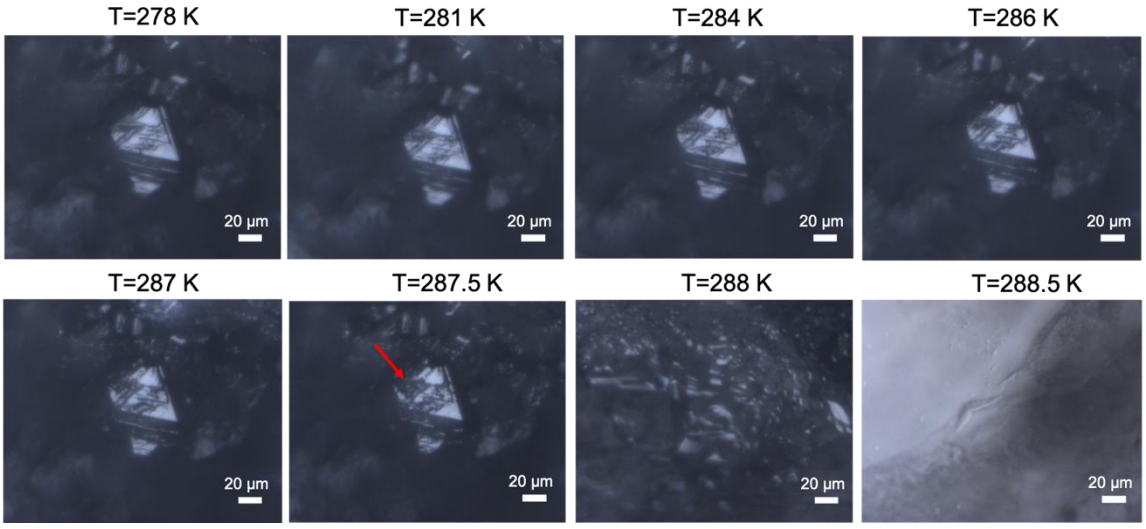

Figure 4.22 Changes in surface morphology of one mixed hydrate crystal at each specific temperature gradient.

More specific observations derived from *in situ* Raman analysis were shown in Figure 4.23 and Figure 4.24 for the dissociation of complex mixed gas hydrates. With the confocal Raman system scanned precisely the hydrate phase, Raman

spectra of specific vibrational regions were collected under different temperature conditions. The peaks at 876 cm^{-1} were from the C–C stretching mode region for C_3H_8 in the sII large cavities, while the peaks at 991 cm^{-1} represented C_2H_6 in the hydrate phase (Figure 4.23a). These two Raman bands appeared along with their corresponding gas peaks at 869 and 993 cm^{-1}, respectively (Figure 4.23a). CO_2 molecules in the hydrate phase were represented by the Raman bands at 1274 cm^{-1} and 1380 cm^{-1} which could be assigned to the ν_1 C–O symmetric stretching and $2\nu_2$ overtone of bending for CO_2 molecules (Figure 4.23b). Small Raman bands occurring at 1285 cm^{-1} and 1388 cm^{-1} for CO_2 in the gas phase could also not be avoided. The bands appeared at approximately 2870 cm^{-1} and 2878 cm^{-1} in Figure 4.23c indicated C–H stretching of C_3H_8 molecules in the hydrate phase. Two strong peaks were observed at 2912 cm^{-1} and 2917 cm^{-1}, which could be assigned to the C–H stretching mode of CH_4 in the small cavities of sII hydrates and the gas phase. Notably, CH_4 in the large cavities is shown as a small shoulder of the nearby peak, occurred at approximately 2901 cm^{-1} (Figure 4.23c). It is important to mention that the Raman bands of CH_4 in both small and large cavities appeared to have a slight redshift as compared to the other sII hydrate systems with less components [46,71,151], highlighting the influences of other higher hydrocarbon molecules in adjacent cavities on the methane molecules. Raman bands for the O–H stretching of water had a broad spectral feature ranging from 3000 cm^{-1} to 3600 cm^{-1} as expressed in Figure 4.23d. It was shown from Figure 4.23 that the intensities the Raman bands were quite similar at 281 K to the initial Raman bands at 278 K. However, the intensities decreased over time as the system was gradually warmed up. At t = 288 K, only a small amount of C_3H_8, C_2H_6 and CO_2 were left in the hydrate structures. CH_4 molecules were released significantly from the small cavities of the hydrate phase and the small "shoulder" was not recognizable. It was also clear that the hydrogen bonds were broken when the temperature increased to 288 K as the Raman band at 3160 cm^{-1} almost disappeared.

Figure 4.24 compared the Raman spectra taken on a specific crystal at the surface (0 μm), and at penetration depths of 30 μm and 60 μm when the temperature was set at 278 K and 287.5 K, respectively. Initially, the intensity of Raman peaks at all penetration depths were similar. However, the measured intensity at 60 μm decreased significantly when the temperature reached 287.5 K. Since the heat came from the bottom of the pressure cell in this system the decomposition of the hydrate phase started also from the bottom which was indicated from the Raman spectra.

In order to figure out the composition changes with regard to the increasing temperature, the concentration of each specific guest component in the hydrate phase were calculated and the results from one of the tests were displayed in Figure 4.25. The hydrate composition exhibited small fluctuations. However, under higher temperature conditions (287.5 K and 288 K), extraordinary variations were observed which could be explained by the differed dissociation behaviors of hydrate crystals. In addition, the relative concentration of CH_4 decreased with increasing temperature while the relative C_2H_6 and CO_2 contents were increased in the final hydrate phase. As for C_3H_8, the relative concentration was increased in some crystals while decreased in others.

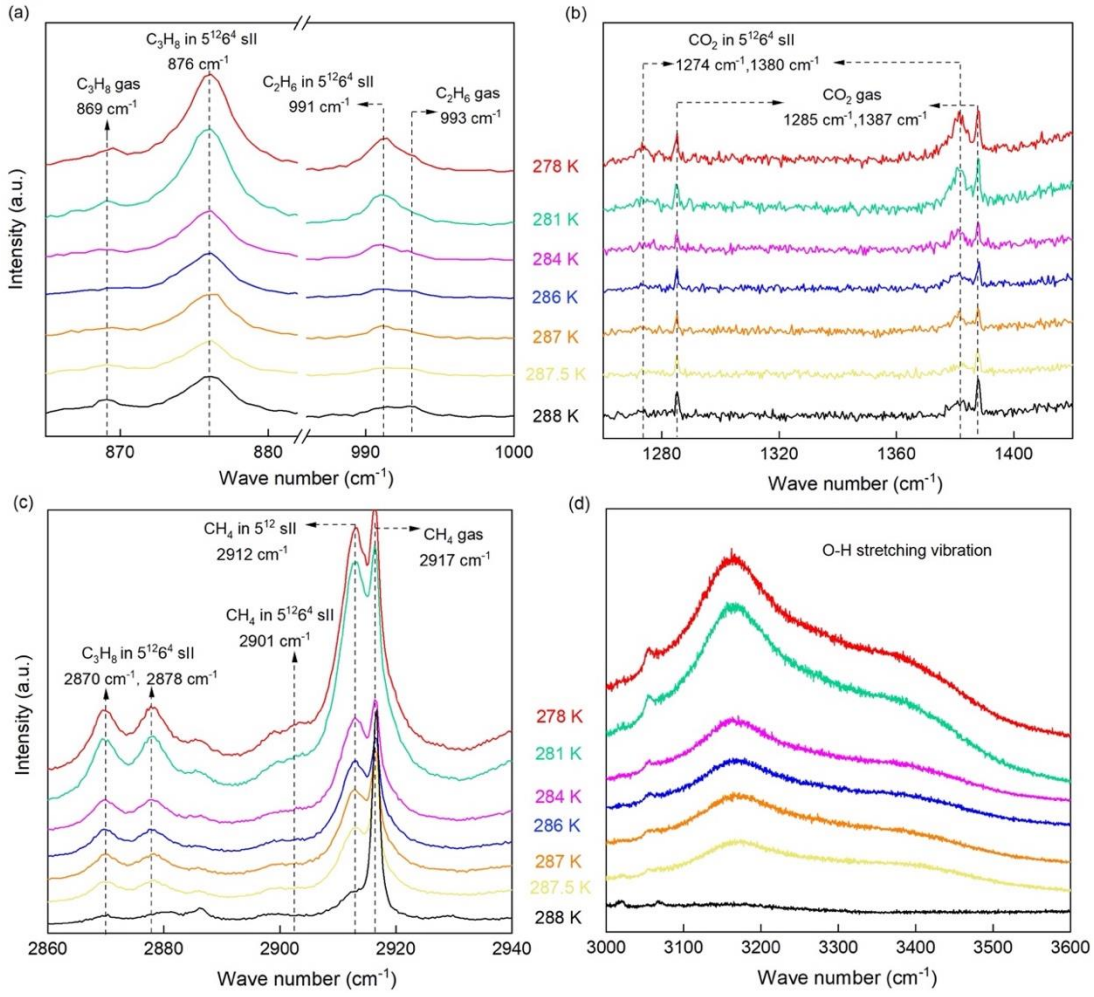

Figure 4.23 Changes of Raman spectra with regard to the increasing temperature. (a) C–C stretching vibrational region from 860 cm^{-1} to 1000 cm^{-1}; (b) C–O symmetric stretching and overtone of bending for CO_2 molecules from 1260 cm^{-1} to 1420 cm^{-1}; (c) C–H stretching vibrational modes ranging from 2860 cm^{-1} to 2940 cm^{-1}; (d) O–H stretching modes ranging from 3000 cm^{-1} to 3600 cm^{-1}.

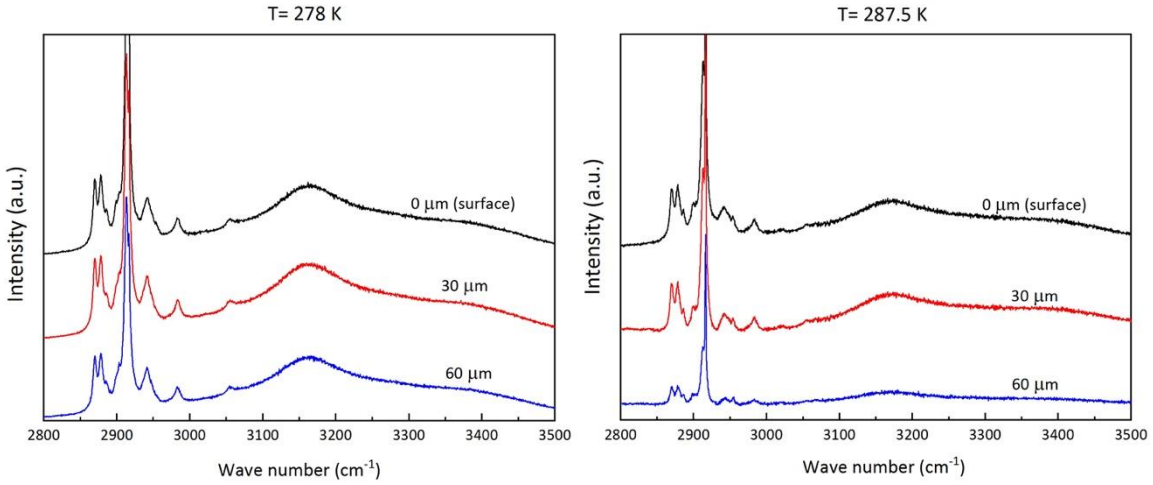

Figure 4.24 Comparison of Raman spectra measured on a specific hydrate crystal at penetration depths of 0 μm, 30 μm and 60 μm at 278 K and 287.5 K, respectively.

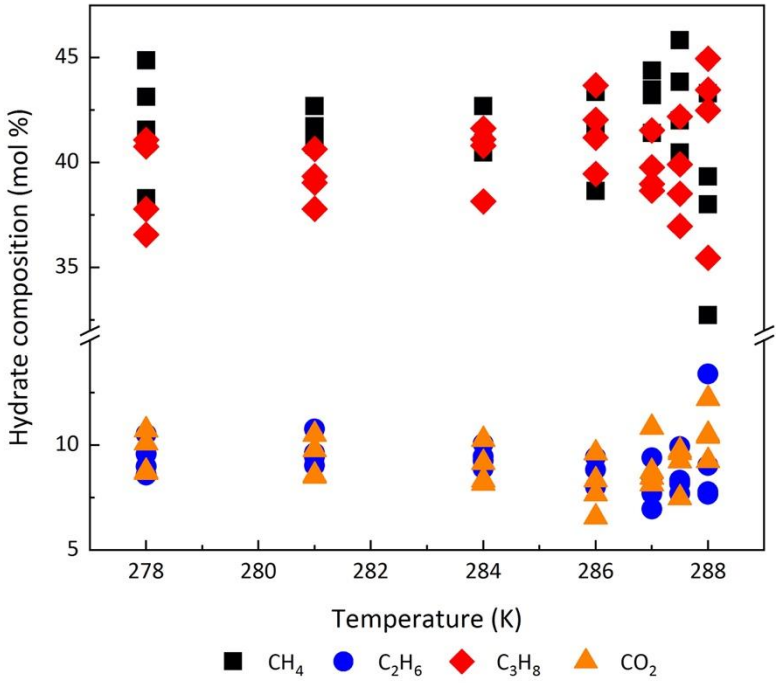

Figure 4.25 Concentrations of the guest components in the hydrate phase with regard to the increasing temperature.

Since it was difficult to differentiated CH_4 in large and small cavities of sII from *in situ* Raman spectroscopic measurements, the preferential dissociation behavior of CH_4 was discussed based on the *ex situ* measurements for the calculation of integrated intensities of Raman bands at 2901 cm^{-1} and 2912 cm^{-1}. Unlike an obvious increase in L/S ratio for CH_4 in the sII binary system, the L/S ratio in the mixed gas hydrate system fluctuated and showed a step growth

increase indicating that CH_4 in small cavities was released faster than that in large cavities (Figure 4.26). The potential dissociation behavior of CH_4 in the sII binary system and mixed hydrate system were slightly different which suggested an unavoidable impact from other guest components on CH_4 in hydrate cavities. Time-resolved hydrate composition recorded from the selected crystal during the *ex situ* Raman spectroscopic measurements was shown in Figure 4.27. Based on the results, CH_4 concentration in the hydrate decreased over time while those for C_2H_6 and CO_2 increased. This was in consistent with the findings from *in situ* measurements. However, C_3H_8 displayed a clear trend of increasing at the end of the dissociation process which varied from the observations from previous *in situ* measurements.

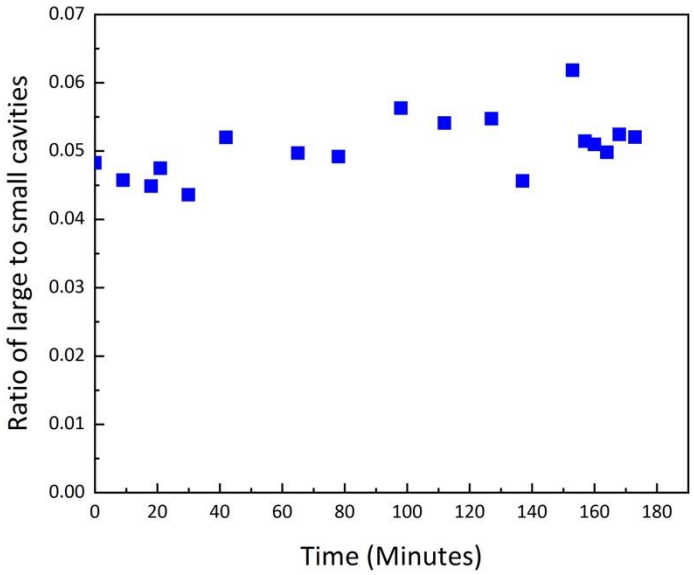

Figure 4.26 Ratio of large to small cavities as a function of time during the dissociation process of the multi-component gas hydrates.

Only a few literatures dealt with the decomposition process of hydrates with multiple hydrocarbons guests [221]. The investigations showed that mixed hydrates had a completely different dissociation process from that of the conventional sI hydrates due to its composition, structure and guest species. In this study, the gas mixture contained four guest components among which CH_4 predominantly occupied small cavities and a small proportion encased in large cavities of sII hydrates like C_2H_6, C_3H_8, CO_2 molecules. There's a clear trend that the ratio of CH_4 in large and small cavities generally decreased over time. Significant influence of larger molecules in large cavities on the nearby CH_4 in small cavities, led to a more complicated dissociation process. The kinetics of the

mixed gas hydrates with multiple hydrocarbons and/or CO_2 will be subject of further experiments.

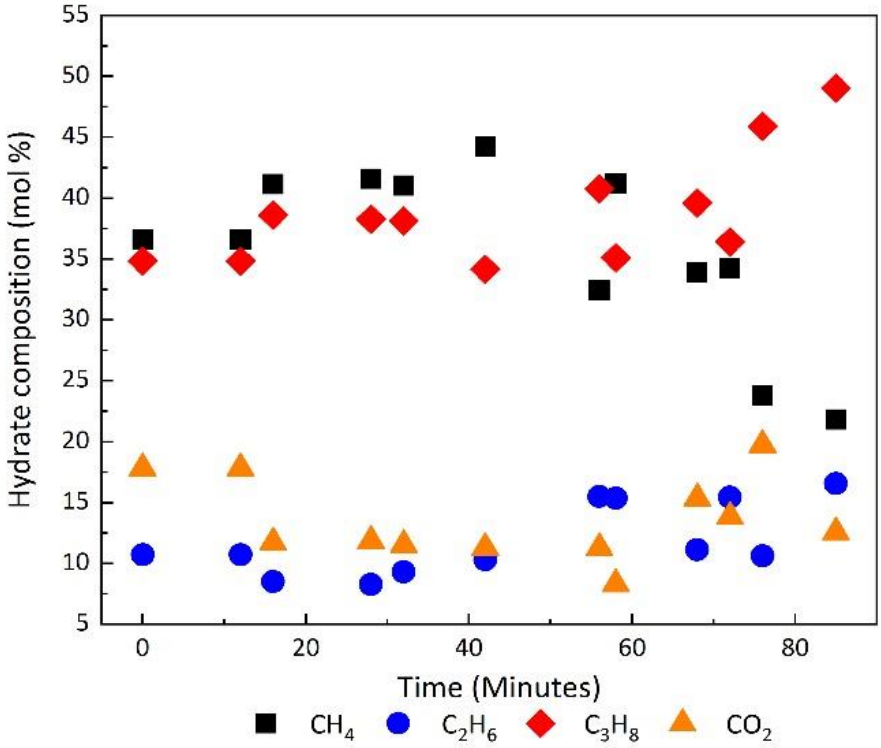

Figure 4.27 Concentrations of the guest components in the hydrate phase with regard to the reaction time from ex situ Raman spectroscopic measurements.

4.2.3 Conclusions

In this context, the experimental data provided from *in situ* and *ex situ* Raman spectroscopy and microscopic observations revealed the dissociation behaviors of sI CH_4 hydrates, sII binary CH_4–C_3H_8 hydrates and sII multi-component mixed gas hydrates. Three different hydrates that formed within the stability field were decomposed by thermal stimulation as it would be possible as a result of global warming. Except for the well-known heterogeneous dissociation behavior of hydrate crystals, CH_4 in large cavities of sI hydrates were released faster than those in small cavities at the end of the dissociation process. In contrast, the break-down of small cavities in the binary sII hydrate system was rapid, followed by the liberating of CH_4 and C_3H_8 in large cavities of sII. With the presence of multiple guests, CH_4 in sII mixed hydrates were largely affected by the surrounding larger molecules. Those CH_4 molecules in large cavities were released slightly faster than those in small cavities of sII hydrates. As compared to CH_4, C_2H_6 and CO_2 remained in the hydrate structures leading to an increase

in the hydrate composition. Changes of the relative concentration of C_3H_8 in the hydrate phase was not clear.

On the basis of these experimental simulations, the dissociation process was visualized, providing advanced insights on the fundamentals of the hydrate dissociation behavior at a μm scale. The knowledge of hydrate dissociation with regard to climate warming may also be critically useful in the assessment of CH_4 release to the atmosphere in nature.

Chapter 5

5 Experimental simulation of gas hydrate transformation processes

Hydrate structural transitions are reported in laboratory experiments from sI to sII and back to sI in a certain composition region of methane + ethane mixed gas hydrates [11,225,226]. In natural deposits, there are also two scenarios which may cause a potential hydrate structural transition: gas production via CO_2 injection or a sudden change in the composition of the feed gas flow which is highly dependent on the local reservoir conditions. It is therefore essential to clarify how the originally formed gas hydrates react when exposed to a new gas flow [117]. *Chapter 5* presents the results from experimental simulations of gas hydrate transformation processes. Experiments began with the replacement of CH_4 to CO_2 in the hydrate structures (*Chapter 5.1*). It was followed by the transformation of multi-component sII hydrates when the feed gas source changed from the gas mixture to CO_2 gas mimicking the production of mixed gas hydrates by CO_2 injection (*Chapter 5.2*). Thereafter, pure CH_4 hydrates were exposed to a multi-component gas mixture simulating a possible gas shift duo to geological events in natural environments (*Chapter 5.3*). The composition changes of the hydrate phase and possible hydrate structural transitions were recorded and interpreted in the following three sub-chapters.

5.1 New insights on a µm scale into the transformation process of CH_4 hydrates to CO_2-rich mixed hydrates

This sub-chapter was mainly taken from the publication Pan et al., 2020 [227].

The global occurrences of natural gas hydrates lead to the conclusion that tremendous amounts of hydrocarbons are bonded in these hydrate-bearing sediments serving as a potential energy resource. For the release of the hydrate-bonded CH_4 from these reservoirs different production methods have been developed during the last decades. Among them, the chemical stimulation via injection of CO_2 is considered as carbon-neutral on the basis of the assumption, that the hydrate-bonded CH_4 is replaced by CO_2.

During the past decades, efforts have been made on experimental studies to investigate the kinetics of CH_4–CO_2 swapping. Lee et al. [228] investigated hydrate samples prepared from powdered ice (particle size of the ice and resulting hydrates were 5–50 μm) in porous silica gel (pore size 15 nm). They injected gaseous CO_2 to the CH_4 hydrate phase and observed the establishment of a steady state after 5 hours with a CH_4 recovery rate of about 50%, which indicated a mixed hydrate phase with 50/50-ratio of CO_2/CH_4. Similar results were observed by Schicks et al. [118] who formed CH_4 hydrate from powdered ice (50–100 mg) with a particle size of <10 μm in a small pressure cell (~400 μl) and exposed the CH_4 hydrate phase to a continuous CO_2 gas flow. Raman spectroscopic measurements indicated the transformation of the initial CH_4 hydrate phase into a mixed hydrate phase with the large $5^{12}6^2$ cavities partly filled with CO_2 and CH_4 and the small 5^{12} cavities filled with CH_4. After 116 hours the gas incorporated into the mixed hydrate phase was composed of 50% CO_2 and 50% CH_4, indicating that 50% of the CH_4 was released from the initial CH_4 hydrate phase. These are two examples carried out with gaseous CO_2, but in the first example a porous medium was used, which may have had an effect on the kinetics of the transformation process. This indication is also given when researchers applied liquid CO_2 to prove the feasibility of replacing CH_4 in hydrates as the following examples might show. Hirohama et al. [229] filled about 560 mL of water (31 mol) into a pressure vessel, pressurized the cell with CH_4 and converted 24 mol of the water into a bulk CH_4 hydrate phase. Thereafter, the CH_4 gas phase was replaced by liquid CO_2 which induced the conversion of the remaining free water phase (7 mol) into CO_2 hydrate. In addition, they observed the transformation of about 15% of the initial CH_4 hydrate into CO_2 hydrate after 800 hours. A higher conversion rate was observed by Ota et al. (2005) [230] conducting similar experiments but on a smaller scale. They formed CH_4 hydrates from 1.05–1.38 mol water and the CH_4 hydrate phase was exposed to liquid CO_2. The results indicated that after 307 hours 37% of the hydrate-bonded CH_4 was replaced with CO_2, which occurred mostly in the large cages whereas CH_4 and water molecules were preferentially reformed in the small cages after decomposition. Zhou et al. [231] conducted the replacement of CH_4 by use of liquid CO_2 under the same conditions as in Ota's experiment. The recovery ratio was about 18.6 % after 96 hours. However, when porous media were added the recovery ratio of CH_4 could be increased to approximately 45% after 288 hours under otherwise identical conditions as reported by Xiong et al., [232]. The effect was even more pronounced when sandstone cores were used: Ersland et al. [84] investigated the swapping process on hydrates in pores of sandstone cores.

After CH_4 hydrate formation the core was exposed to liquid CO_2. Within 300 hours up to 60% of CH_4 was recovered from the hydrate phase. Besides the effects from sediments, additional heat supply can help overcome the mass transfer limitations and thus improve the efficiency of the transformation process as observed by Deusner et al [233]. They investigated production of CH_4 hydrates in quartz sand with pure ice by injecting hot supersaturated CO_2 at 368.15 K in a flow-through apparatus instead of a typical batch fixed bed reactor. This unique method permitted a higher CH_4 recovery rate of 40.7% in a relatively short duration of 44 hours. For a further improvement of the slow transformation process Park et al. [86] investigated the effect of additional N_2 on the transformation kinetics. They synthesized CH_4 hydrate from powdered ice and CH_4 gas in a stirred reactor before exposing about 1 ml of the pure CH_4 hydrate sample to a N_2–CO_2 gas mixture (80% N_2, 20% CO_2). After about 24 hours 85% of CH_4 from hydrate phase was recovered. It is noteworthy that production of CH_4 via CO_2 + N_2 injection was already tested in 2012 at the Alaskan North Slope in the Ignik Sikumi Field Trial [93]. A mixture of 23 mol% CO_2 and 77 mol% N_2 was injected into the target sediments. According to its final report, 70 % of the injected N_2 and 40% of the injected CO_2 were recovered along with 24,210 m^3 of CH_4 during the flowback phase. However, 1421 m^3 of N_2 and 82 m^3 of CO_2 remained in the formation which indicated the occurrence of CH_4–CO_2 replacement in the solid phase or dissolution of the gases into the brine [93,234].

The above-mentioned examples are chosen to show how much the efficiency of transformation process and thus the CH_4 recovery rate differ depending on the chosen scale and experimental conditions. In addition to those studies focusing on the optimization of the process with regard to the recovery rate of CH_4, there are other studies that deal with the transformation process on a µm-scale, to understand the mechanisms on a molecular scale. Due to the high complexity of the experimental systems, only several common assumptions may be allowed from previous researches: 1) the exchange process is incomplete and reversible to a certain degree[118,198]; 2) the kinetics of the replacement process appears to follow a variant of shrinking-core model involving two stages, similar but not identical to the formation of methane hydrate from ice [235,236]; 3) the initial exchange takes place at the interface of the CH_4 hydrate which is rapid and heterogeneous[118,237]; 4) the subsequent reaction, requiring a penetration of gas molecules through the previously formed mixed hydrates is found to be generally slow [238–240]. However, even it is now generally accepted that the driving force for the CH_4–CO_2 swapping process is the difference of the chemical

potential between the coexisting CH_4 hydrate phase and surrounding gas phase when exposed to a CO_2 gas [118], the transformation mechanism on a molecular scale is still under discussion. The replacement process is neither simply the dissociation of the initial CH_4 hydrate followed by the CO_2 hydrate formation, nor the one-to-one replacement of a CH_4 molecule with a CO_2 molecule. A recent study on the CH_4–CO_2 replacement from Mok et al. [241] provides time-dependent information on the guest exchange behaviors and cage occupancies during the replacement process applying *in situ* Raman spectroscopy together with NMR and PXRD. They analyzed quantitatively the CO_2 enclathrated in each cages of structure I hydrate throughout the whole replacement process. However, it is still not yet clarified if this replacement process is correlated with a diffusion of the CO_2 molecules in the hydrate phase through "holes-in-the-cages" as suggested by Falenty et al., 2016 [242], a recrystallization and re-arrangement of the water molecules or a (partial) dissociation and reformation as suggested by e.g. Ota et al. and others [118,238].

The uncertainty of the mechanism originated in the use of different analytical methods such as *in situ* Raman spectroscopy [118,198,230,240,243], PXRD [244,245], NMR [228,246], *in situ* Neutron Diffraction [242,247] and MRI [84,239] to study the *in situ* dynamic replacement reactions or visualize the transformation process on a μm-scale. Among these methods, Raman spectroscopy is the most widely used method for determining the composition and cage occupancies of the hydrate. Since it allows the analysis of compositions of each phase and the changes of molecules in the corresponding hydrate cavities, promising results can be given for the guest replacement experiments. For instance, Yoon et al. [240] investigated the guest replacement reaction applying *in situ* Raman spectroscopy. They monitored the changes in the relative intensities of Raman peaks corresponding to CH_4 and CO_2 in large and small cages of sI hydrate. A sharp increase in the Raman peaks of CO_2 in the hydrate phase was observed in the first 100 mins, but the increase of intensities slowed down after 100 mins which may indicate an effect from the surface shielding of CO_2 hydrate formed in the outer layer. Another example is from Zhou et al. [243] who also studied the swapping process. Real-time Raman spectra monitoring the changes of composition for CO_2 and CH_4 in the hydrate phase depicted no significant fluctuations throughout the transformation process. The observation suggested that the transformation was simply not a dissociation process followed by a reformation process. Up to now, most researches applying Raman

spectroscopy only provided spectroscopic evidence but did not provide enough real-time visualization information for the transformation process.

Against such background, the ultimate goal of our research was to advance our understanding on the transformation process of hydrate-bonded CH_4 with CO_2 on a µm-scale applying *in situ* Raman spectroscopy and microscopic observations. Time-resolved Raman measurements were performed on pure CH_4 hydrates exposed to a continuous CO_2 gas flow, recording changes in compositions and cage occupancies during the whole transformation process. In addition to single point measurements, line scans and Raman maps were also taken from the hydrate phase. With the help of a confocal microscope and a motorized sample stage, hydrate crystals were analyzed in all three dimensions with a high spatial resolution. In this work, the transformation kinetics of CH_4 hydrates to CO_2-rich mixed hydrates are discussed in details based on the experimental data. For a better understanding, the µm-scale investigation results from this research are compared and discussed in consideration of the previous kinetic models which are originally developed for other solid-state reactions. The microscopic investigations on specific hydrate crystals at defined depths expand our understanding on the transformation process and reveal more detailed information.

5.1.1 Materials and methods

The experiment started with the formation of pure CH_4 hydrate by following the same procedures as described in *Chapter 2.2.1.* The system was pressurized to 3.2 MPa at 274 K. The experimental p–T condition allowed the formation of CH_4 hydrates and CO_2 hydrates (see Figure 5.1) without the presence of liquid CO_2. At least 15 of the formed hydrate crystals were selected for continuous *in situ* Raman measurements to record the changes in the hydrate phase. Morphology changes of the hydrate surface were also monitored regularly. It took 5–6 days until the pure CH_4 hydrate reached a steady state.

To initiate the hydrate transformation process, the feed gas composition was changed from the initial CH_4 gas to CO_2 gas conducting similar steps as described in the publication of Beeskow–Strauch & Schicks [198] at constant pressure and temperature. First, the CH_4 gas flow was stopped by closing the gas inlet valve at the sample cell. The gas line was then flushed with CO_2 gas to ensure that the gas flowed into the sample cell from this step onwards was pure CO_2 gas. However, the very last part of the gas line could not be flushed, which resulted in a certain delay until CO_2 entered the sample cell. Afterwards, the gas

inlet valve was reopened to a continuous stream of CO_2 gas into the sample cell at a flow rate of 1 mL/min. Raman measurements were performed both on the gas phase and at different depths in the hydrate phase from the surface to the core of each crystal (surface, 15 μm, 30 μm, 60 μm, 90 μm) with a confocal pinhole of 30 μm to record the progression of the gas replacement process in the crystal in terms of relative guest molecular compositions. In order to obtain more information on the spatial composition of the guest molecules in the hydrate phases, a specific area of a well-structured crystal with large flat surfaces was selected for mapping. The selected area was scanned step by step automatically

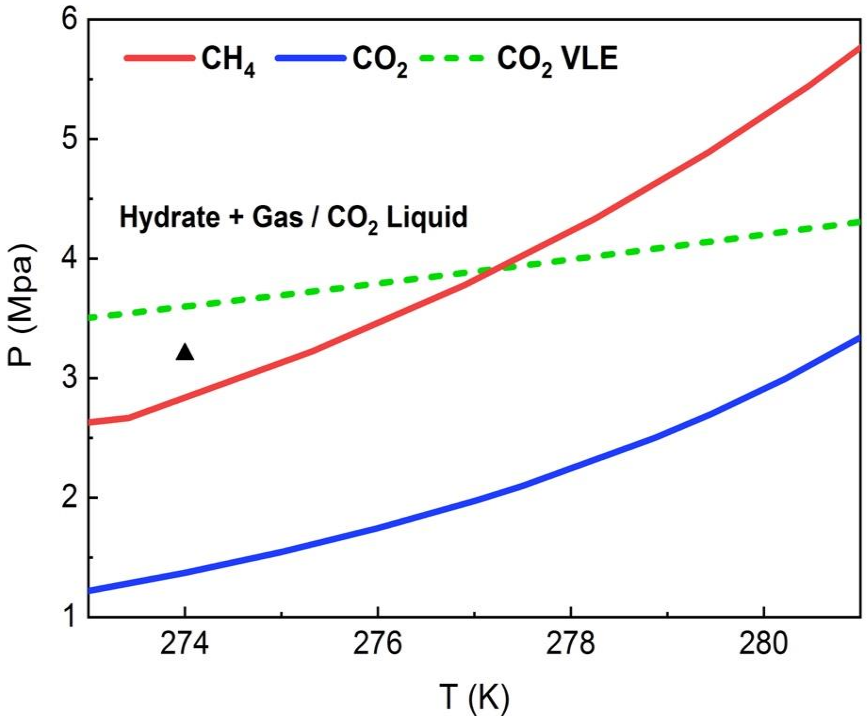

in one direction for line scans and both *x*-*y*-directions for the area maps. The whole experiments have been repeated for 3 times and similar results have been achieved as discussed in the following section.

Figure 5.1 Phase boundaries of hydrates formed from pure CH_4 (red line), and pure CO_2 (blue line) calculated using CSMGem. Also shown are the CO_2 vapor-liquid boundary (green dashed-line) and experimental p–T condition (triangle symbol) at 3.2 MPa and 274 K which is maintained throughout the entire process including CH_4 formation and gas replacement process.

In this study, the molar compositions of the CH_4 and CO_2 in the gas and hydrate phase were given as relative percentages, assuming the total Raman bands for the guest molecules were set to 100%. The measured Raman band

positions were in good agreement with literature data as summarized in Table 5.1.

Table 5.1 Spectroscopic information for the CH_4 and CO_2 molecules in the gas phase and for different cavities in the hydrate phase.

Component	Vibrational Mode	Cavity Type/Gas Phase	$\nu_{measured}$ (cm^{-1})	$\nu_{literature}$ (cm^{-1})	References
CH_4	ν_1 C–H symmetric stretching	Gas phase	2917	2917	[122]
		sI 5^{12}	2915	2915	[171]
		sI $5^{12}6^2$	2905	2905	[171]
CO_2	ν_1 C–O symmetric stretching	Gas phase	1285	1285	[122]
		sI $5^{12}6^2$	1277	1276	[198]
	$2\nu_2$ overtone of bending	Gas phase	1388	1388	[122]
		sI $5^{12}6^2$	1382	1381	[198]

5.1.2 Results

1. CH_4 hydrate formation

During the formation of CH_4 hydrate, initial Raman measurements detected the appearance of Raman bands at 2905 cm^{-1} and 2915 cm^{-1} as shown in Figure 5.2 which illustrated the C–H stretching mode of CH_4 molecules in the hydrate phase. This figure indicated the enclathration of CH_4 molecules into the hydrate cavities with the Raman bands of 2905 cm^{-1} and 2915 cm^{-1} assigned as CH_4 encased into the large $5^{12}6^2$ and small 5^{12} cavities of structure I hydrate respectively, as tabulated in Table 5.1. The ratio for the integrated intensities of the Raman bands at 2905 cm^{-1} and 2915 cm^{-1} were calculated to ensure that the CH_4 hydrate followed the structure I equilibrium 3:1 ratio of large to small cavities. The equilibrium ratio was achieved after 24 hours for some of the well-developed crystals, whereas it took longer than 24 hours for the less-developed crystals to reach the expected equilibrium ratio. After 6 days, the cage occupancy ratio for most of the CH_4 hydrate crystals reached 3.1(± 0.2):1 which indicated that the system was close to an equilibrium state. It should be noted that the presence of CH_4 gas peak in the Raman spectra at 2917 cm^{-1} may have an effect on the calculation of cage occupancy ratio. In this case, the CH_4 gas peak in the

Raman spectra was considered. However, after careful calculation it turned out that the impact from CH_4 gas peak was lower than 2 % rel on average whether it was considered or not.

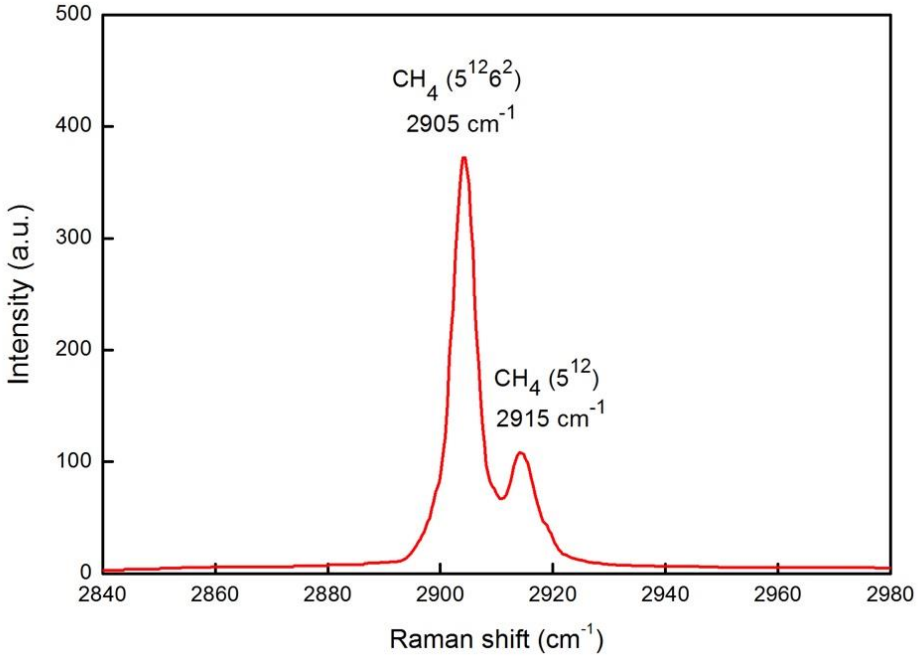

Figure 5.2 Raman spectra for the C–H stretching mode of CH_4 molecules enclathrated into large $5^{12}6^2$ (2905 cm^{-1}) and small 5^{12} (2915 cm^{-1}) cavities of structure I hydrate. The spectral resolution achieves 0.6 cm^{-1} as described in *Chapter 2.1.1*.

Microscopic observations indicated no remaining free water phase after that time. In addition, the shape of Raman bands of the water indicated that at least most water molecules were bonded into the hydrate structure: according to literature, the left shoulder of the band shape (2800–3350 cm^{-1}) is attributable to the strongly hydrogen-bonded water molecules in the hydrate or ice structure, whereas the right shoulder (3350–3800 cm^{-1}) is attributable to weakly hydrogen-bonded water molecules such as in liquid water [248,249]. Please note that in this context the terms "strong" and "weak" refer to the number of hydrogen bonds a water molecule forms with its neighboring water molecules.

2. Changes in compositions of the initial gas and hydrate phase when exposed to CO_2

After there were no further changes in the CH_4 hydrate compositions with regard to the ratio of large to small cavities that signified a steady state condition

has been reached, the gas flow was changed from CH_4 to CO_2 to induce the transformation process at 274 K and 3.2 MPa.

It took more than 50 minutes before the CO_2 could be detected in the gas phase besides CH_4. CO_2 gas was represented by the Raman bands at 1285 cm^{-1} and 1388 cm^{-1} which could be assigned to the ν_1 C–O symmetric stretching and $2\nu_2$ overtone of bending for CO_2 molecules, respectively. The delay in detecting CO_2 in the gas phase may result from several reasons. There might be CH_4 gas left in the pipe line between the gas bottle and pressure cell. Also, the very last part of the gas line could not be flushed. It was also possible that the CO_2 concentration in the cell was too low at the beginning to be clearly detected with Raman spectroscopy. As for CH_4 gas, the Raman band occured at 2917 cm^{-1}. With longer time, the intensities for the CH_4 gas band in the Raman spectra reduced, while the intensities for CO_2 gas bands in the Raman spectra continued to increase as shown in Figure 5.3a. Figure 5.3b shows the changes of gas composition versus time in two separate tests. The blue diamonds and red circles in Figure 5.3b represent the gas composition in test 1 while the pink and light blue symbols show the results from test 2. Within the first 100 minutes after the feed gas was changed, the CO_2 proportion (given as molar composition in %) increased dramatically. Thereafter, the gas exchange process slowed down until almost 100% CH_4 in the gas phase was replaced by CO_2 after 4000 minutes. Even though the respective times of measurements varied slightly in these two tests, similar trends for the gas phase composition were observed when repeating the transformation process, indicating a high reproducibility of the measurements.

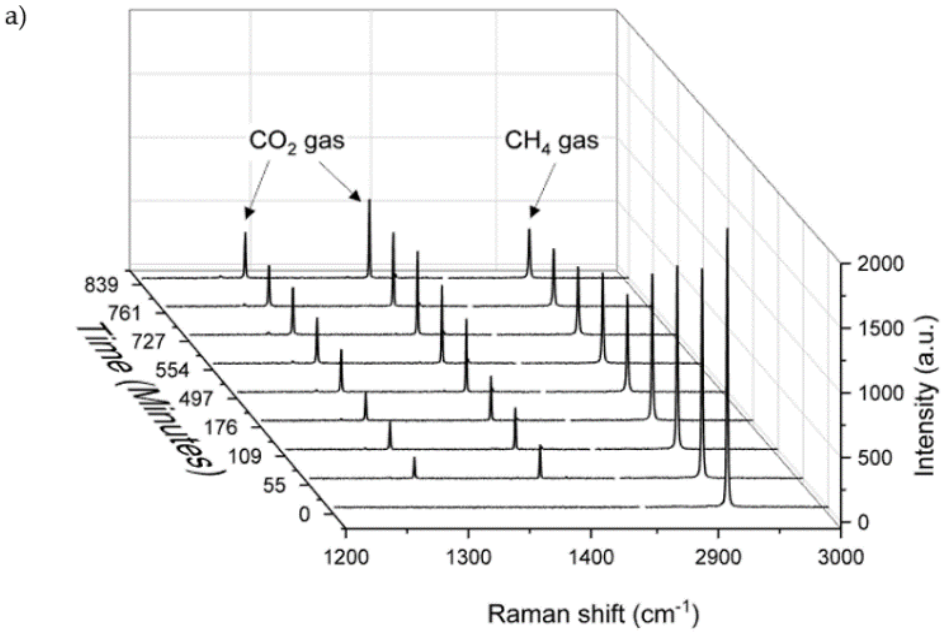

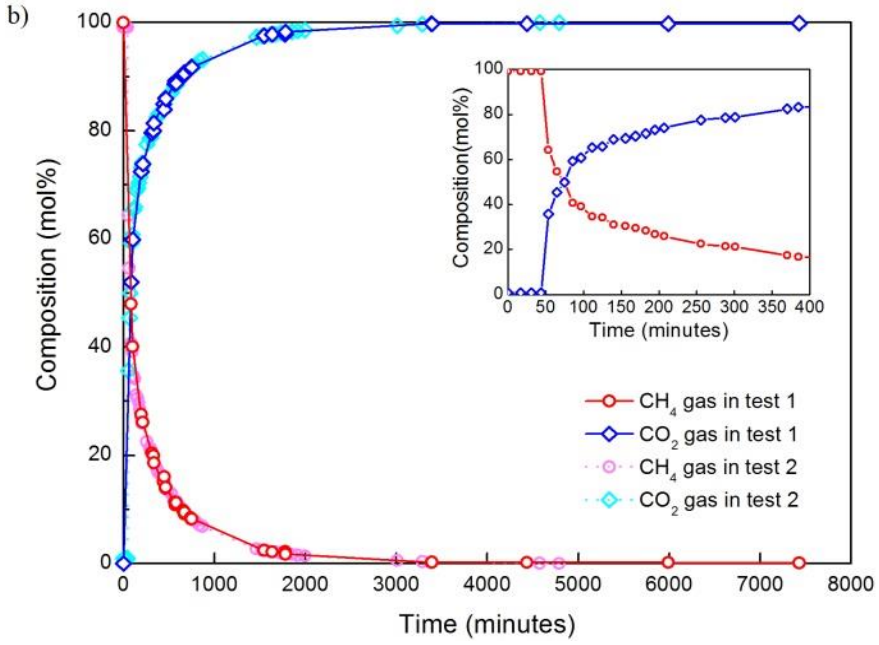

Figure 5.3 Changes of the gas phase composition as a result of the continuous gas flow after the exchange from CH_4 gas to CO_2 gas. (a) shows real-time Raman spectra monitoring, and (b) shows the relative molar composition of the gas phase over time in two separate tests. For a better overview, the time axis in Figure 5.3a is displayed value-independent.

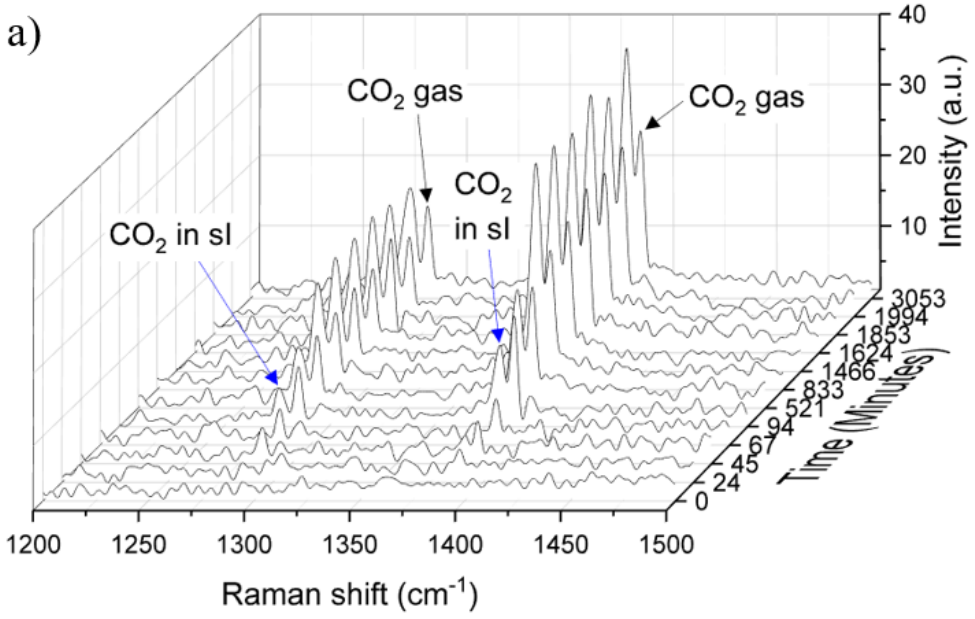

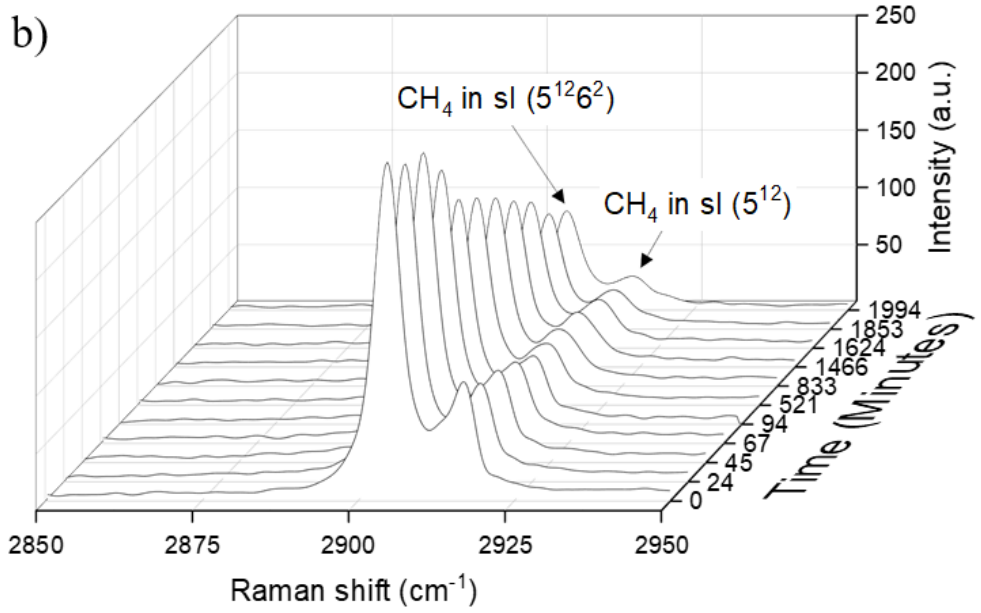

Figure 5.4. Real-time Raman spectra monitoring (a) CO_2 hydrate and (b) CH_4 hydrate for changes in the solid phase as a result of the shift of gas phase from CH_4 gas to CO_2 gas. Blue arrows in (a) point out the first appearance of Raman bands at 1277 cm^{-1} and 1382 cm^{-1} for CO_2 hydrate after around 500 minutes. The time axes are displayed value-independent.

Raman measurements on the hydrate crystal surfaces revealed the enclathration of CO_2 molecules in the hydrate phase by detecting the first appearance of the Raman bands at 1277 cm^{-1} and 1382 cm^{-1} after around 500 minutes (8.3 hours). CO_2 gas peaks were still detectable due to the effects of surrounding gas phase on the hydrate surface during measurements. As shown in Figure 5.4, the intensities for the CO_2 hydrate bands increased with time, while the intensities for Raman bands representing CH_4 in the hydrate phase decreased.

By referring to the plot of changes in composition over time for the selected hydrate crystals in Figure 5.5, it was found that the relative compositions for all the selected hydrate crystals scattered over a wide range. The scattered composition of hydrate crystals indicated the heterogeneity of the hydrate phase with regard to the content of CH_4 and CO_2. Using these data, the average molar composition for CH_4 and CO_2 in the hydrate phase was determined, and plotted on the same graph. Since the experiment has been repeated for 3 times, the standard deviation of the average molar composition was also given in the caption of Figure 5.5. The steep slope from the plot of average molar compositions at the surface of the crystals shown in Figure 5.5 represented a

faster reaction for the transformation of the pure CH_4 hydrate into mixed CH_4–CO_2 hydrate during the first 2 days (around 2880 hours) after the gas flow was changed compared to a much slower conversion that was recorded afterwards. The integrated Raman intensity of CH_4 in the $5^{12}6^2$ cavities and the 5^{12} cavities also changed from nearly 3:1 to a ratio of 2.0 (±0.2) :1 which signified that a mixed hydrate has formed during the exchange process containing CO_2 and CH_4 in the $5^{12}6^2$ cavities and CH_4 in the 5^{12} cavities. It should be noted that no CH_4 gas peaks were observed at that time in the Raman spectra taken from the hydrate phase due to a low concentration of CH_4 in the gas phase. Therefore, CH_4 gas peak did not impact the calculation of cage occupancy ratio. After more than 7000 minutes (116.7 hours) the average composition of the resulting hydrate phase contained ~80% CO_2 and 20% CH_4, which was defined as CO_2-rich mixed hydrates. However, it should be noted that for some of the hydrate crystals the CO_2 concentration is still much less.

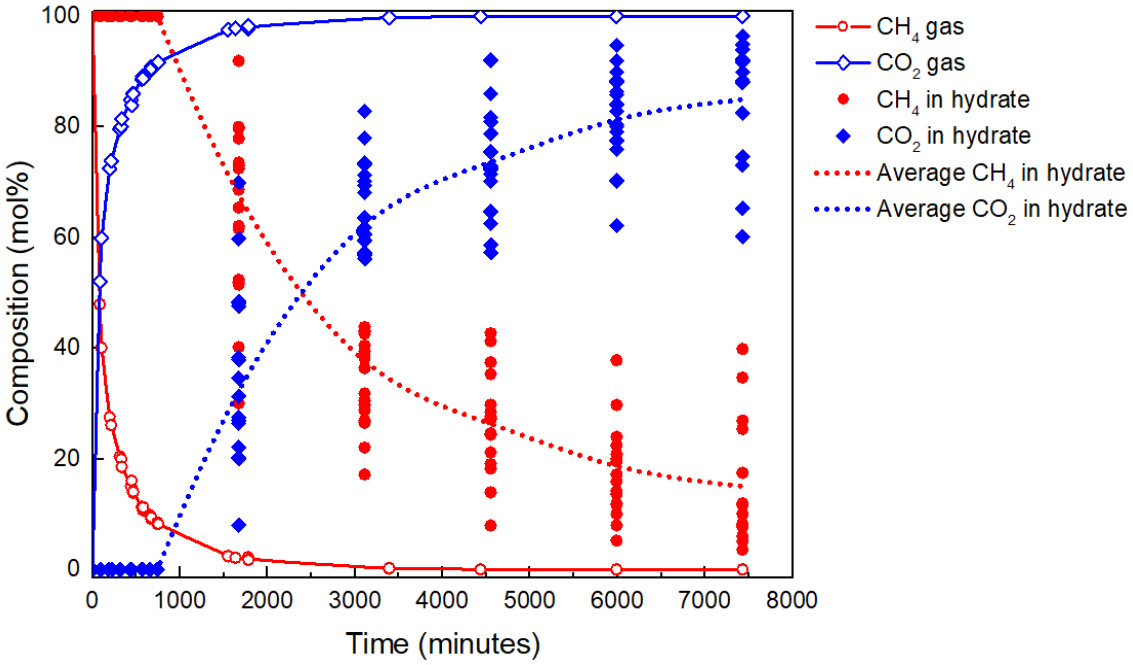

Figure 5.5 Results of Raman spectroscopic measurements on the surfaces of 15 selected hydrate crystals illustrating the exchange process of pure CH_4 hydrates to CO_2-rich mixed hydrates when exposed to CO_2 gas. The dashed lines show the average molar composition changes of CH_4 (red) and CO_2 (blue) in the hydrate phase fitted by smooth curves. The standard deviation of the average molar composition ranged from 0.6 mol% to 5.3 mol% according to the data from 3 repeated experiments.

With the use of confocal Raman spectroscopy and a motorized sample stage, Raman spectra were acquired not only on the surface of the hydrate crystals, but also at different penetration depths inside the crystals by focusing the laser beam at defined depth. In this work, the laser beam was initially focused on the surface of the hydrate crystal and the position of the sample stage was recorded as zero at the z-axis. With the help of the software, this position of the motorized stage was changed vertically in such a way that the focus of the laser beam moved into the hydrate crystal. With a spatial resolution of 6.2 μm in z-direction, measurements were therefore made at penetration depths of 15 μm, 30 μm, 60 μm, and 90 μm into the hydrate crystals to ensure that the measurements had covered the whole range of depths. A curve fit was created in Figure 5.6 for the individual measurement points in order to better illustrate the trend of the transformation process. Each curve represents the average composition changes for 15 different hydrate crystals at a specific depth. The standard deviations of the average composition at specific depths from 3 experiments were served as error bars in Figure 5.6. The measurements on different hydrate crystals and different depths for each crystal served as a better representation for the whole system. The results clearly indicated the incorporation of CO_2 into the hydrate phase with a concentration gradient from the surface to the core of the hydrate particle. It was shown from Figure 5.6 that after the pure CH_4 hydrate crystals were exposed to a CO_2 gas for around 1.5 days, the average conversion to mixed CH_4–CO_2 hydrate composition was 50 mol% CH_4 / 50 mol% CO_2 on the surface of the hydrate crystals. However, at 60 μm depth into the hydrate crystals, the average conversion to mixed CH_4–CO_2 hydrate composition was 80 mol% CH_4 / 20 mol% CO_2 after 1.5 days. With time, a higher conversion to CO_2 hydrate was recorded for all depths. However, after day 6 small fluctuations to the hydrate compositions have been observed at all depths (see supporting information, Figure S2).

It was confirmed that the transformation process from pure CH_4 hydrates to CO_2-rich mixed hydrates took place initially at the interface of CH_4 hydrate and CO_2 gas as the results showed the faster composition changes at the surface. Since there was no direct contact between the inner layers of the hydrate crystal and the CO_2 gas, the reaction into the hydrate crystals became diffusion-limited with depths. Also, the driving force of the concentration gradient decreases with depth. Over longer time, the results from Raman spectroscopy indicated that CO_2 molecules penetrated from the surface to the deeper depths through the hydrate layer. It started with the enclathration of the CO_2 molecules on the surface and

was then followed by the enclathration of the CO_2 molecules into the hydrate structure in deeper layers. Therefore, these observations support in general the hypothesis of the "shrinking-core-model" and are similar to the findings by Lee et al. (2014) [236] and Falenty et al. (2016) [250].

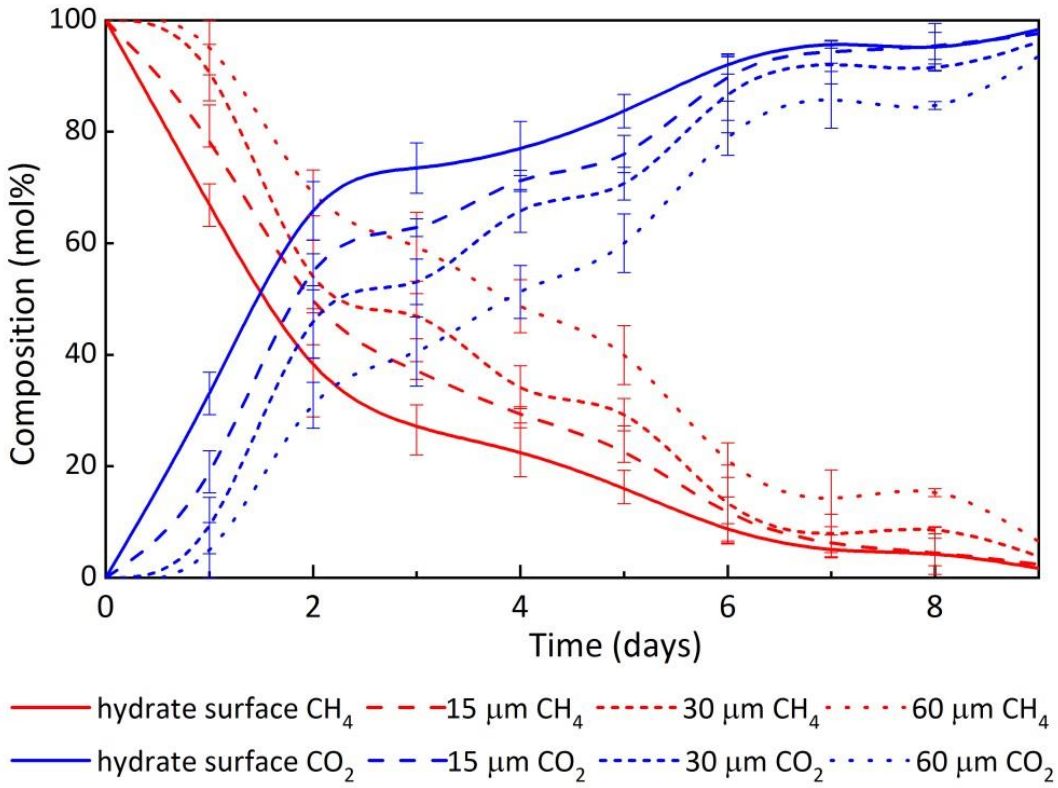

Figure 5.6 Changes of the average composition in mol% of the hydrate phase at defined depths over time after the initial CH_4 hydrate was exposed to a CO_2 gas phase. The standard deviation of the average composition in 3 repeated CH_4–CO_2 exchange experiments were used for the descriptive error bars.

Apart from the single point Raman measurements on the hydrate crystals during the transformation process, line scans and Raman maps were also performed at the surface of the hydrate crystals after 5 days. Figure 5.7a depicts the line scan on one of the well-developed hydrate crystals, where 50 measuring points along 37 µm across the surface were scanned step by step in one direction. This process took over 60 mins for the 50 points. One has to assume that the transformation process will continue during this time. It is therefore not possible to repeat the line scan in order to prove the reproducibility of the measurements. As such, the reproducibility of the Raman line scans was tested before the experiment on a hydrate crystal with only a few measuring points. The average standard deviation was 0.2 mol% for 12 measuring points on a crystal surface

over 3 repeated tests. Therefore, the results presented in Figure 5.7b indicate the measured variations in local composition of the hydrate crystal. Interestingly, the concentration recorded for CO_2 in the mixed hydrate crystal was higher at the edges of the crystal, compared to the CO_2 concentration towards the center of the crystal. Since the edge of this hydrate crystal had a wider contact surface with the gas phase, CO_2 molecules could attack the hydrate crystal from different sides and were available to be incorporated into the hydrate phase. Similar trends were observed while repeating the experiment on different hydrate crystals.

Raman mapping conducted on a specific rectangle area (42 µm x 61 µm) scanning both, in *x*-*y*-directions on the surface of the hydrate crystal (see Figure 5.8) demonstrated the inhomogeneous nature of the formed CH_4–CO_2 mixed hydrates. Also, there was overall a higher CH_4 / CO_2 ratio towards the center of the measured crystal as shown in Figure 5.8b, indicating more CH_4 was left over in the hydrate phase. It should be noted that pixels in Figure 5.8b only show results of each measuring point. X-axis in Figure 5.8b corresponded to the direction parallel to the short side of the rectangle in Figure 5.8a while Y-axis indicated the direction parallel to the long side of the rectangle.

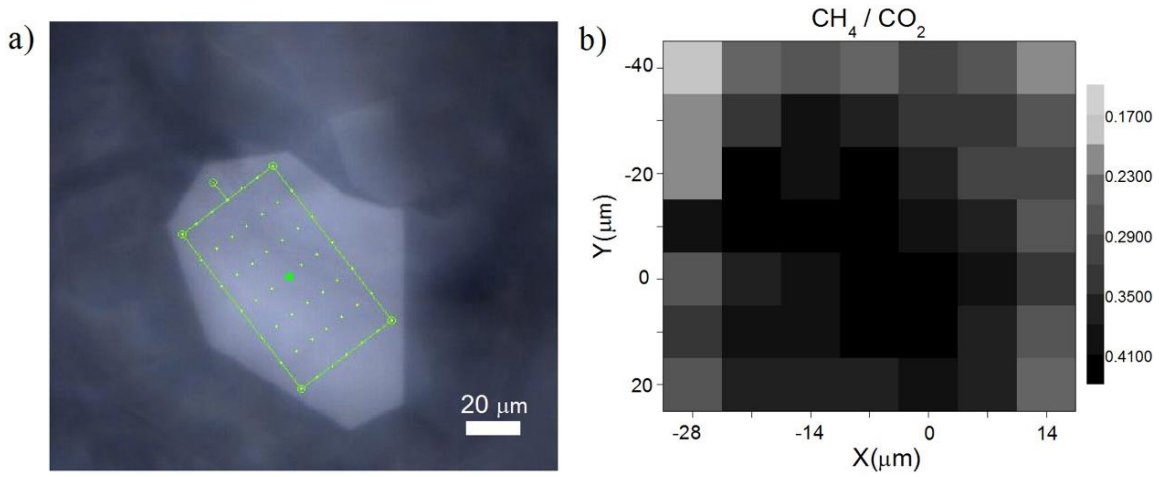

Figure 5.7 (a) Raman line scan across hydrate crystal surface was scanned step by step in one direction, (b) Composition variations for the CH_4 and CO_2 encased into the hydrate phase at 50 measuring points across the formed hydrate crystal. The average standard deviation for the line mapping was 0.2 mol%.

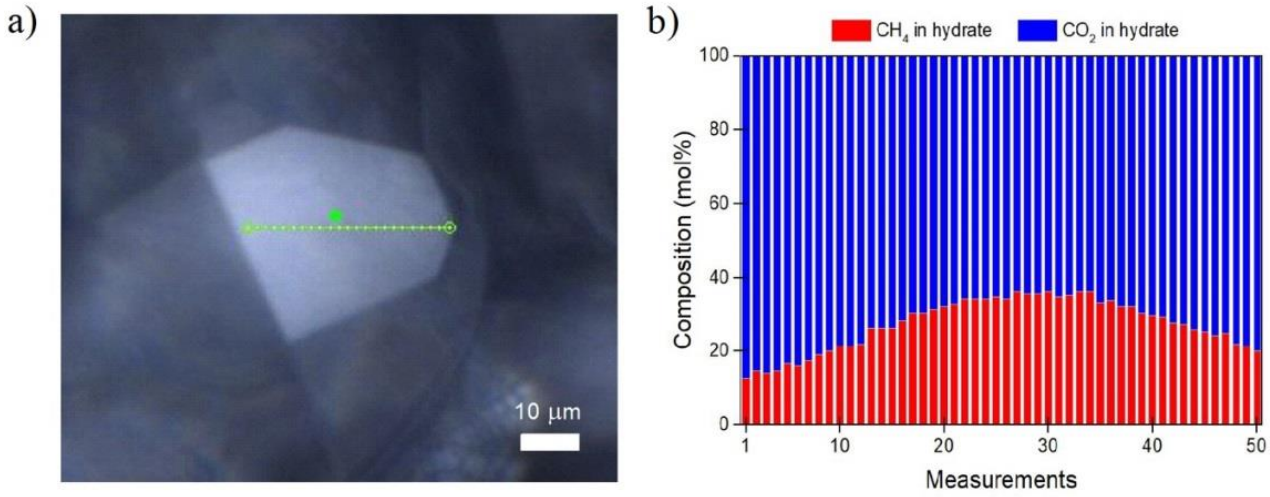

Figure 5.8 (a) Raman mapping on a hydrate crystal surface. 49 (7 x 7) measuring points were chosen to be analyzed to determine the composition of the hydrate crystal. (b) Calculated CH_4/CO_2 ratio in the mapped area based on the integrated Raman band areas of CH_4 and CO_2 respectively, without a correction with Raman scattering cross section factor or instrumental efficiency. Increasing darkness reflects a higher CH_4/CO_2 ratio, whereas lighter points represent a lower CH_4/CO_2 ratio.

3. Changes in morphology of hydrate crystals when exposed to CO_2

For the microscopic observations during the transformation of the initial CH_4 hydrate to mixed gas hydrates, a series of snapshots were acquired periodically using a digital camera mounted on the confocal microscope. These snapshots were used to systematically study the morphology of the pure CH_4 hydrate crystals when the gas phase was changed to CO_2. In this observation, at least ten crystals of pure CH_4 hydrate were initially selected. The ratio of large to small cavities for structure I hydrate has reached 3:1 for these crystals. They were also categorized as well-developed crystals that exhibited polyhedral shape with sharp edges and flat surfaces when they were first exposed to the CO_2 gas. However, when the transformation process started, the crystals' appearance changed significantly over time.

Figure 5.9 presents two crystals as examples showing the evolution of the hydrate crystals from the initial pure CH_4 hydrates to CO_2-rich mixed hydrates. As shown in Figure 5.9a the initial flat rectangular shape surface of the crystal shrank on day 1 and day 2. On day 3, it started to grow again until day 6. However, on the last day of the experiment, the hydrate crystal surface was found to be smaller. The calculation of the diameter for the entire crystal showed

that it decreased by 57.8% on day 7 (39.8 µm) compared to the diameter before it was exposed to CO_2 gas (94.2 µm). As for the crystal in Figure 5.9b, it experienced a continuous dwindling within the 7 days of experiment. Already on day 2, the sharp edges of the crystal were invisible. The complete shape of the crystal disappeared at the end. For this reason, comparison for diameter of the crystal could not be conducted. Other crystals changed their surface morphology over time without showing a clear trend in decrease or increase regarding their sizes. It should be noted that the shrinking of the hydrate crystals was not considered as an effect from the irradiated laser beam during the Raman measurements. No physical damage was observed on the hydrate crystal surfaces where the laser beam was hitting. Besides, no significate changes were recorded in the Raman spectra regarding the shapes and sizes of the O–H stretching bands which indicated that the hydrate crystals were fully intact.

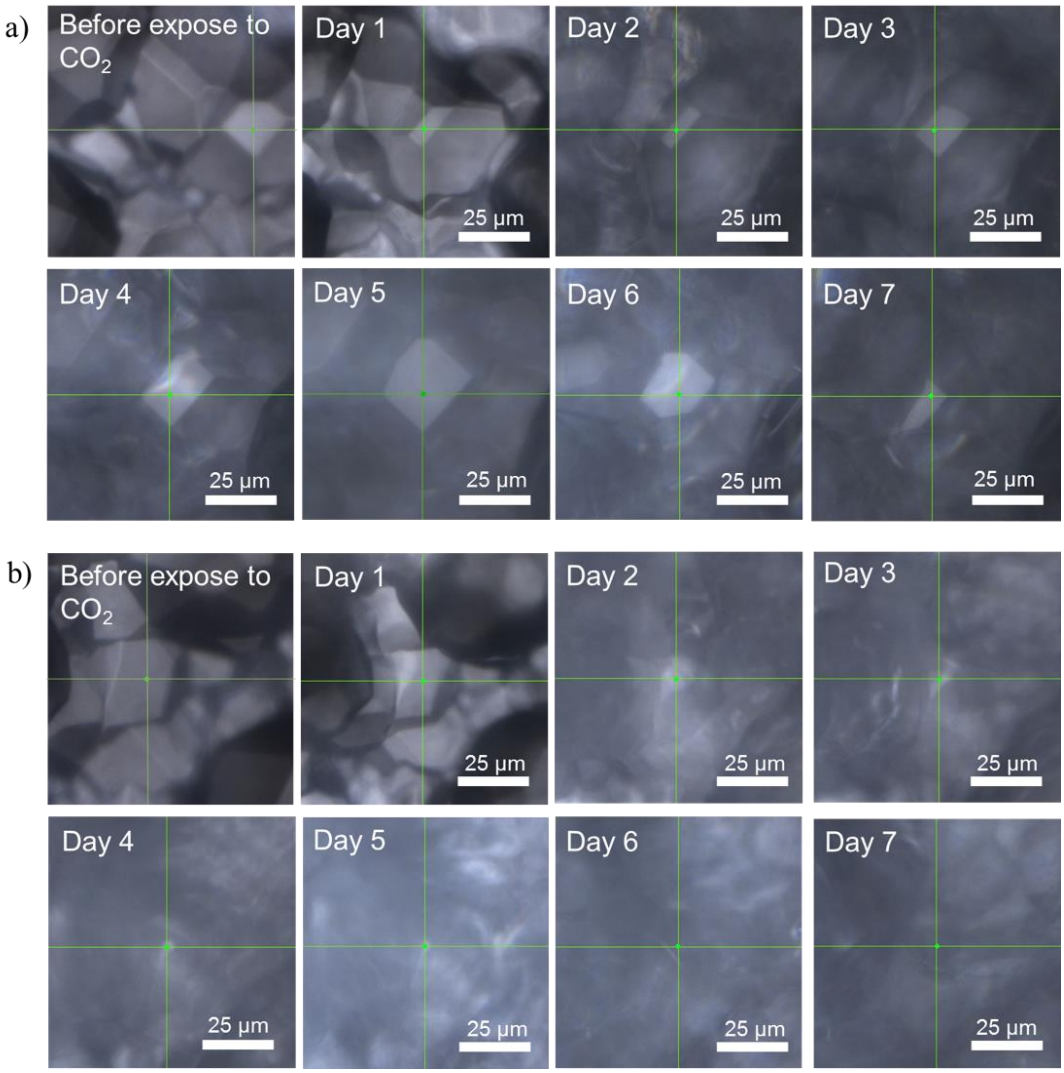

Figure 5.9 Changes in surface morphology on two CH_4 hydrate crystals (shown in (a) and (b) separately) after the shift of gas phase to CO2 gas at experiment conditions of p = 3.2 MPa and T= 274 K. The CH4 hydrate crystal in Figure 5.9a was found to grow in the first a few days followed by a shrinking on the last day. However, the crystal in Figure 5.9b experienced a continuous shrinking and disappeared on day 7. The green point with crossed lines was the exact measuring spot site on hydrate crystal.

It is noteworthy that the crystals which experienced a continuous dwindling according to microscopic observations showed a different transformation profile compared to those crystals which grew or maintained their sizes. Two types of transformation curves can be observed from Figure 5.10 which presents the changes of CH_4 concentration on the surfaces of hydrate crystals over time. Different symbols represented the plots from different crystals. Blue full symbols represented the dwindling crystals which decreased continuously regarding the sizes while red empty ones were the crystals which grew or at least maintained similar sizes. It becomes clear that the dwindling crystals (blue symbols) tend to have a higher CH_4 composition in the hydrate phase which means a slower transformation rate especially at the very beginning when CH_4 hydrates were exposed to a CO_2 gas. The reaction rate was almost constant throughout the whole experimental period. For the crystals that grew or maintained in sizes (red symbols), a faster transformation was observed at the beginning of the reaction which slowed down with time. It should be noted that the growing of hydrate crystal size was not due to the growth of a CO_2 hydrate layer on the initial CH_4 hydrate crystal. This could be proved by the results from Raman measurements. With the present set-up, the formation of an aqueous phase in which the CO_2 could dissolve during the decomposition of the hydrates was not able to be detected. However, the existence of free water molecules could still be possible during the experiments. Since the cage structure has to open to a certain extent for the replacement of guest molecules, the observed dwindling phenomena after the exposure of pure CH_4 hydrate crystal to the CO_2 gas, may be an indication for at least a rearrangement of the molecules.

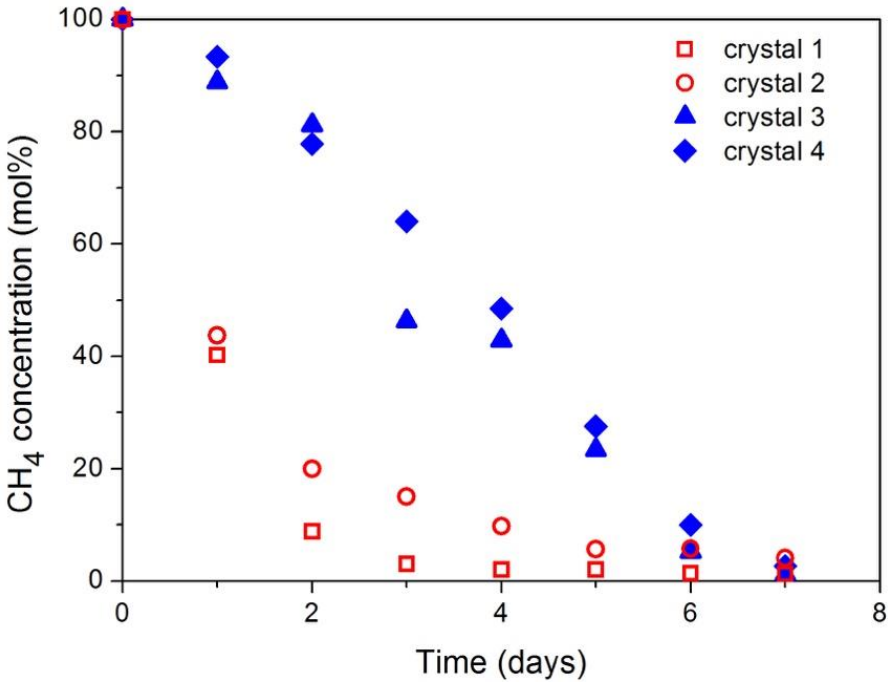

Figure 5.10 Changes of CH_4 concentration on the surface of hydrate crystals over time. Crystals marked in blue experienced a clear decrease regarding their size while those marked in red either grew or maintained their size.

5.1.3 Discussion

There are several theories proposed to explain the mechanisms behind CH_4–CO_2 replacement process. However, whether the transformation refers to a substitution of guest molecules, a re-arrangement of the hydrate cavities or a recrystallization still remains uncertain. Taking a closer insight into the transformation kinetics, experimental data obtained in this work were applied to the Avrami equation and shrinking core model which were widely used for describing the nucleation and growth process of the solid-state reaction [145,148]. Although not developed for the description of hydrate kinetics, they have been successfully applied before to fit data from hydrate formation [139,146,251] and also the CH_4–CO_2 swapping process [147].

Random nucleation followed by the growth of the nuclei is often modelled using the Avrami rate law. The Avrami rate law is in principle also applicable for the initial stage of the CH_4–CO_2 exchange reaction [236]. It assumes that an initial layer of mixed CH_4–CO_2 hydrate is formed with a quick exchange with CH_4 hydrate on the surface after the CH_4 hydrate is exposed to the CO_2 gas. Thereafter, the growth of mixed hydrates slowed down as shown in Figure 5.5 and Figure 5.6 which corresponded to a diffusion-controlled process (the second

stage). The presence of mixed CH_4–CO_2 hydrate on the surface limited the mass transfer for the subsequent hydrate growth. The shrinking core model was employed in this stage when diffusion of the gas and water molecules through a continuously-growing mixed hydrate layer controlled the rate of reaction. Three different equations for the simple shrinking core model (Jander [149], Levenspiel [140], Fujii–Kondo [138]) were applied and their results were compared.

With all the calculations performed using these three different models, the compositions for mixed CH_4–CO_2 hydrates in mol% were back calculated, and the values were compared with the experimental data to find which equation best described the kinetics of the CH_4–CO_2 transformation process. Figure 5.11 shows the results of these calculations for two crystals with different transformation patterns: (a) a "survived" crystal with a remaining or growing size and (b) a dwindling crystal that experienced a continuous decrease regarding the size. For most of the remaining crystals, the results clearly indicated the incorporation of CO_2 into the hydrate phase with two stages involved: (1) a fast surface reaction on the gas–solid interface, and (2) a gradual slow process due to the resistance to diffusion of gas through the formed mixed hydrate layer. The experimental data satisfactorily fitted with the Avrami rate law (Equation 1.6) in the first stage of the exchange process. As for the second stage, all the three equations (Equation 1.7, 1.8, 1.9) fitted the data to certain extents. Among them, the Fujii–Kondo equation suited best compared to Levenspiel and Jander (see Figure 5.11a). Similar findings were also recorded by Lee et al., [236] where they showed well-fitted trend of the Avrami and Fujii–Kondo model with the experimental data. It is also possible that the transformation process is only weakly influenced by the diffusion. Therefore, the Avrami rate law fitted the complete transformation process for some crystals. However, for the dwindling crystal, the experimental data still fitted with the Avrami rate law at the beginning of the process. After about 100 hours the experimental data no longer followed the trend calculated with the Avrami rate law. Also, none of the three kinetic models matched well for the dwindling crystal (as shown in Figure 5.11b) since they were all based on the assumption that the solid crystal did not change the size but only the unreacted core shrank. Instead, a linear regression was achieved between the time and the measured CO_2 composition in the hydrate phase with an R-value of 0.994. This indicated a constant reaction rate during the complete transformation process rather than a two-stage process. The dwindling process of the hydrate crystals as a result of hydrate dissociation may prevent the establishment of a stable CO_2-rich mixed

hydrate phase as a diffusion layer at the surface of the hydrate crystal. Therefore, the chemical disequilibrium between the crystals and the gas phase maintained. This may explain why there is no significant change in the reaction rate shown in Figure 5.11b.

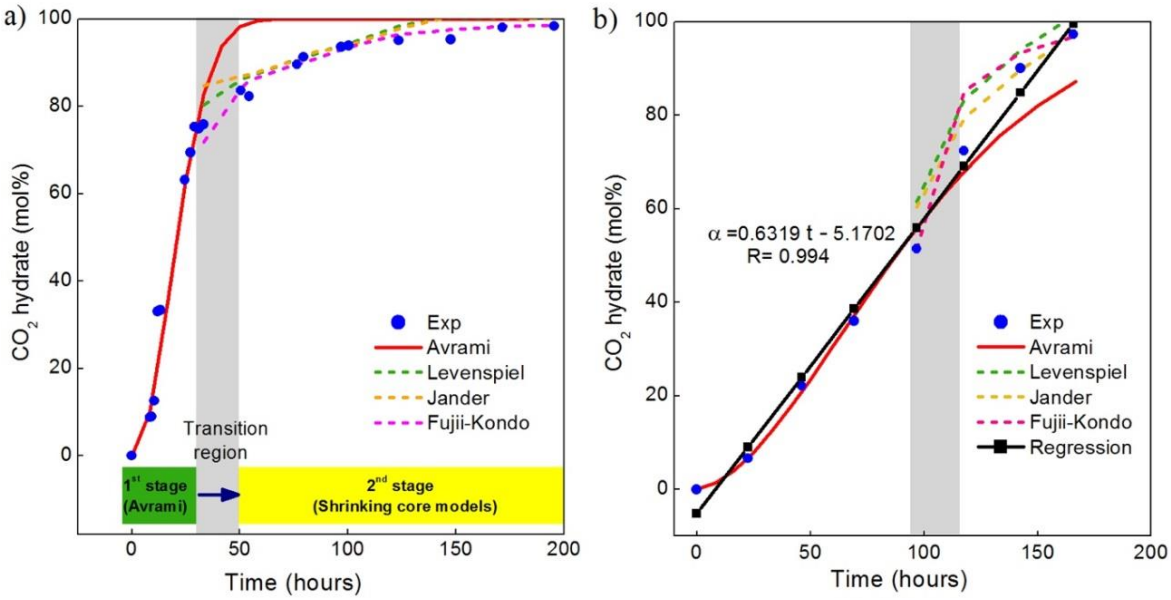

Figure 5.11 Comparison of Avrami (solid line) and shrinking core models (dashed lines) with experimental data for formation reaction of two different mixed CH_4–CO_2 hydrate crystals: (a) a "survived" crystal with a remaining or growing size and (b) a continuously dwindling crystal. Blue dots show the experimental results taken at the surface of each crystal. Black dotted line in Figure 5.11b represents a linear regression for the experimental data and R is the coefficient of correlation.

The parameters for the models are listed in Table 5.2 and 5.3, respectively. Table 5.2 shows the formation rate constants (k) and the Avrami exponents (n) for the enclathration-controlled step for three runs each for 2 crystals. The values for the formation rate constant (k) range over two orders of magnitude. This indicates that the speed of the enclathration-controlled step varies from crystal to crystal significantly. This is applicable for the single experiment as well as for the different runs, which is a further indication of the heterogeneous nature of the transformation process. In addition to the k-values, the Avrami model also provides information about the dimension of crystal growth by the Avrami exponents (n) [251,252]. For the experiments shown here, the values vary between 1 and 2, indicating that the growth of the mixed crystals is one- to two-dimensional. Table 3 shows the rate constants for the diffusion-controlled step,

which were determined according to the Fuji–Kondo model, as well as the radius of the examined crystal. The fitting with this model gives the best results. Although the rate constants are of the same order of magnitude for the three runs, they vary significantly for the individual crystals.

Table 5.2 Formation rate constants (k) and Avrami exponents (n) obtained from enclathration-controlled step for 6.

Crystal number	k/min^{-n}	n	Experiment
1	9.11E-06	1.5829	Run 1
2	9.31E-05	1.2674	Run 1
3	3.23E-05	1.3221	Run 2
4	5.28E-07	1.8317	Run 2
5	5.16E-05	1.2594	Run 3
6	3.55E-07	2.0291	Run 3

Table 5.3 Formation rate constants (k) of Fujii and Kondo equation obtained from diffusion-controlled step for 6 crystals. (The radius of the crystals was obtained from the microscopic images of crystals and determined with the software "ImageJ").

Crystal number	k/min^{-n}	Radius/μm	Experiment
1	4.20E-03	46.2	Run 1
2	1.59E-02	45.5	Run 1
3	7.63E-03	30.2	Run 2
4	2.50E-02	43.4	Run 2
5	2.08E-02	51.0	Run 3
6	1.69E-02	44.9	Run 3

In addition to these kinetic data, microscopic observations on the hydrate phase revealed alterations in hydrate morphology which were an indication for potentially different transformation behaviors of hydrate crystals. Changes of the morphology directly affected the sizes of the hydrate crystals. As a consequence, the crystal would either expand, shrink, or completely disintegrate.

One assumption for the morphology change would be the dissociation of pure CH_4 hydrates and a parallel growth of mixed hydrates. This effect was observed

by Schicks et al., [234] who studied the exchange process of CO_2/N_2–CH_4 in gas hydrates simulating the Iġnik Sikumi field trial. The coexistence of initial pure CH_4 hydrates and secondary mixed gas hydrates containing CH_4, CO_2 and N_2 was detected in the solid phase. While continuously measuring the decomposing CH_4 hydrate crystals, the Raman spectra of the solid phase clearly indicated only the CH_4 molecules in the hydrate phase and the composition did not change until the dissociation process ended. In contrast, coexistence of pure CH_4 hydrate and mixed hydrate was not observed in the solid phase for this study. Within the first few hours (around 8.3 hours) when the enclathration of CO_2 molecules were not detected in the hydrate phase, the morphological changes of hydrate crystals may be attributed to the decomposition of pure CH_4 hydrates. However, after 8.3 hours, only CH_4–CO_2 mixed hydrates were confirmed from the depth profile analysis by applying Raman spectroscopy. All Raman spectra taken from hydrate crystals after this time showed Raman bands at 1277 cm^{-1} and 1382 cm^{-1} assigned as CO_2 in the hydrate phase besides Raman bands at 2905 cm^{-1} and 2915 cm^{-1} for CH_4 in hydrate cavities. The observed shrinking of crystals for most of the remaining time was therefore clearly the dissociation of mixed hydrates. This dissociation process of some mixed hydrate crystals while other mixed hydrate crystals grow or maintain in size is reminiscent of a process similar to Ostwald Ripening.

Ostwald ripening, known as a grain coarsening process, has been observed by previous researchers with different visualization techniques such as X-ray computed tomography [183], optical microscopy [253,254] and X-ray diffraction [255]. The process has been studied not only in simple materials like metals ceramics but also in more complexed crystalline hydrates [182]. It differs from the normal hydrate grain growth process and has a strong effect on hydrate pore-scale habit and spatial distribution, in which larger crystals grow at the expense of the dissolution of smaller crystals [183]. The thermodynamic basis of the ripening is the size-dependence of the stability of a crystal. According to the Gibbs–Thomson effect, solubility limit is inversely proportional to the radius of the spherical particle [256], which means a molecular concentration gradient may develop in the surroundings between a small crystal and a nearby large one [254]. This leads to a diffusive transport from the higher concentrations around smaller crystals toward larger crystals. Eventually, smaller crystals which are energetically less stable are consumed by larger ones to minimize surface area and lower the free energy. In this case, a CO_2 gas concentration gradient surrounding the existing mixed hydrate crystals. Thus, a thermodynamically-

driven spontaneous process is speculated to occur resulting in a net flux of molecules flowing to larger crystals which can be described as a rearrangement of molecules (see Figure 5.12). This shrinking process may take place simultaneously with the diffusion process as described in shrinking core model which partly explained the observed compositions and morphology changes of the crystals in our experiment. It may also lead to small fluctuations in the hydrate compositions in the surrounding area.

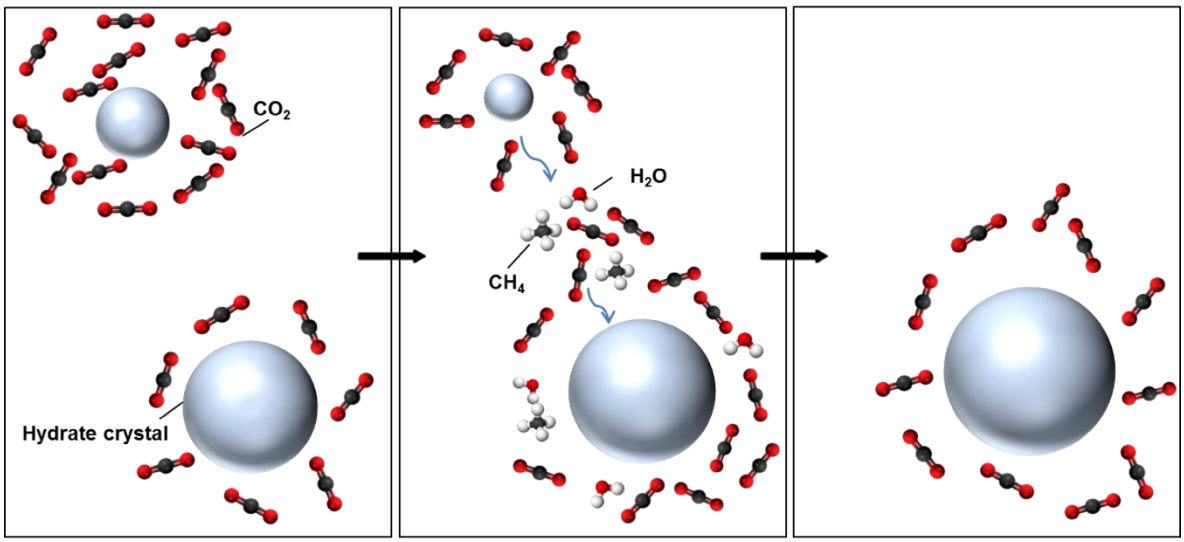

Figure 5.12 Schematic illustration of the growth of CH_4–CO_2 mixed hydrate at the expense of smaller hydrate crystals considering the Ostwald Ripening effect. The left panel indicates a CO_2 molecular concentration gradient between the large and small hydrate crystals based on the Gibbs–Thomson effect. Therefore, the diffusion of CO_2 molecules due to the concentration gradient is initiated from the small crystal towards the large crystal together with CH_4 molecules and water molecules so as to minimize the surface area and lower the free energy. Finally, the large crystal grows and the small crystal disappears as shown in the right panel.

5.1.4 Summary and conclusions

The transformation process of pure CH_4 hydrates into CO_2-rich mixed hydrates was unveiled in this study on a μm scale by use of the time-resolved *in situ* Raman spectroscopic measurements and microscopic observations. The results from Raman spectroscopic measurements clearly indicated the incorporation of CO_2 into the hydrate phase with a concentration gradient at different penetration depths rather than the growth of a CO_2 layer on the existing CH_4 hydrate crystal. The heterogeneity of hydrate composition at defined depths

was confirmed. It was shown from line scans and Raman maps that the transformation process was advanced at the edge of a crystal than that in the center. The analysis of the results suggested that most of the crystals displayed a two-stage reaction supporting in general the hypothesis of the shrinking core model. It involved a fast formation of the mixed hydrates on the surface of the initial CH_4 hydrate crystals which was rate-limiting, followed by a slow diffusion-controlled process that was dominated by the molecules penetrating inwards for the formation of mixed hydrates in deeper depths. This behavior was found for crystals which kept their size or even started to grow after their expose to a CO_2 gas. The formation rate constants for kinetic models varied from crystal to crystal indicating again the heterogeneity of the transformation process.

Microscopic observations indicated that all crystals of the initial CH_4 hydrate phase changed their surface morphology when exposed to a CO_2 gas. Some crystals of the initial CH_4 hydrate phase decreased in size and some completely disappeared over time. In contrast to the two-stage reaction mechanism described above these crystals showed an almost constant reaction rate for the complete transformation process. This observation supports the assumption of a rearrangement of the molecules and a (partial) dissociation followed by the formation of a mixed hydrate phase and not a replacement of the guest molecules in existing hydrate cavities. A possible explanation for the morphology changes would be the Ostwald Ripening effect as the large crystals grow at the expense of small ones resulting in changing sizes and shapes of the mixed hydrate crystals.

In summary, our research provides time-resolved and quantified information for the whole CH_4–CO_2 exchange process on a µm level. The reaction mechanism of the CH_4/CO_2 transformation process seems to be influenced by how the hydrate morphology changes after the crystals are exposed to CO_2 gas. On a long-term perspective, more work should be done to clarify the reaction mechanisms in consideration of CO_2 injection as an attractive gas production method from the natural hydrate reservoirs.

5.2 Transformation process of mixed gas hydrates with external CO_2 gas

Even though the chief constituent in gas hydrates is CH_4, it is quite common for the existence of other hydrocarbon molecules as well as CO_2 and/or H_2S in the hydrate structures in natural reservoirs. These hydrates containing other hydrocarbons besides CH_4 typically exhibit in the form of sII. Due to the

enclathration of higher hydrocarbons, mixed hydrates are thermodynamically more stable than pure sI CH_4 hydrates.

The idea of a combination of CH_4 production from hydrate-bearing sediments and a sequestration of CO_2 as gas hydrates seems to be an elegant way to use natural gas hydrates as an almost CO_2-neutral resource. Most of the previous studies focused on the replacement of CH_4 hydrates with CO_2. Only a few data were available for the swapping process of sII mixed gas hydrates. Park et al. investigated the transformation of sII CH_4–C_2H_6 mixed gas hydrates with CO_2 and CO_2/N_2 gas mixtures. They reported a very high recovery of CH_4 (92% – 95%) and C_2H_6 (93%) from the hydrate phase [86]. Schicks et al. also described in their study the exchange of hydrocarbons with CO_2 in CH_4–C_2H_6 and CH_4–C_3H_8 sII hydrates as a decomposition and reformation process driven by the chemical potential gradient between hydrate phase and the provided gas phase [118]. A recent experiment carried out by Lee et al. [257] verified the coexistence of sI and sII hydrates after the replacement in the CH_4 + C_3H_8 – CO_2 system. Later, Zhang et al., [258] simulated the guest exchange behaviors of CH_4–C_2H_6–C_3H_8 mixed hydrates with CO_2/N_2. They concluded from the results that CO_2 molecules preferably attacked CH_4 compared to C_2H_6 and C_3H_8 in the hydrate phase. However, still less is known about the swapping process of sII hydrates with a more complex composition with CO_2 at higher resolutions.

Gas hydrate samples that recovered from QMP were characterized as sII mixed hydrates with multi-components. In considering the gas production from these complicated mixed hydrates by means of CO_2 injection, we assumed a possible structural transition in which hydrocarbon molecules were in exchange with CO_2 molecules in the hydrate structures. To simulate the production of sII mixed hydrates in natural reservoirs, a gas mixture containing CH_4, C_2H_6, C_3H_8, iso-C_4H_{10}, n-C_4H_{10} and CO_2, from which mixed gas hydrates were initially formed, were exchanged with pure CO_2 gas. For further comparison, the composition of the initial gas hydrate phase was characterized applying *in situ* Raman spectroscopy. The transformation process after gas exchange was continuously monitored both in the gas and hydrate phase until the system reached a steady state, hence to understand the transformation process on a molecular level.

5.2.1 Materials and methods

For the transformation process from sII mixed gas hydrates to CO_2-rich sI hydrates, a gas mixture containing 71 mol% CH_4, 4 mol% C_2H_6, 8 mol% C_3H_8, 1 mol% iso-C_4H_{10}, and 1 mol% n-C_4H_{10} and 15 mol% CO_2 was used for the synthesis of mixed gas hydrates. The high-pressure cell filled with 150 μL deionized water was pressurized with the above gas mixture at 274 K and 3.2 MPa (Figure 5.13), which was exactly the same as the conditions for CH_4–CO_2 exchange experiment. Once well-developed sII hydrate crystals were observed in the system indicating the achievement of a stationary state, the system was pressurized with pure CO_2 gas at 3.2 MPa and 274 K. The moment when the inlet valve was reopened was defined as time zero (t = 0 min).

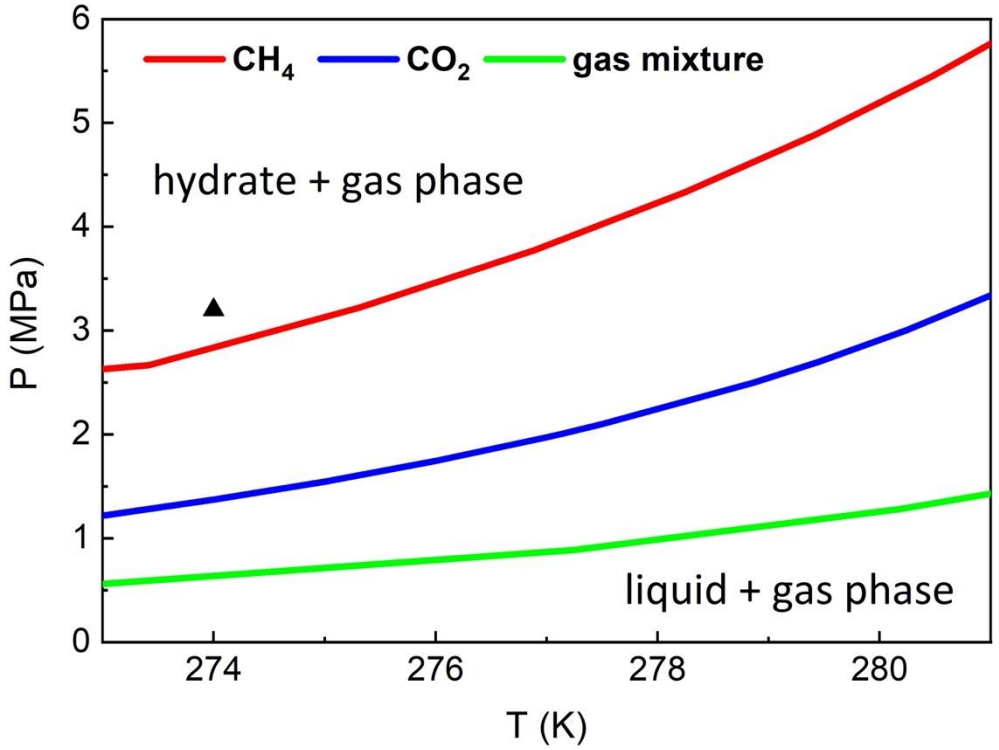

Figure 5.13 Experimental p–T condition that was employed in this study (black triangle) and corresponding equilibrium curves. The red line indicated the equilibrium curve for methane hydrates, the blue line indicated the phase equilibrium for CO_2 hydrates, and the green line was for the mixed gas hydrates.

During the experiment, single-point Raman measurements were performed continuously on the gas phase and hydrate phase. At least 12 selected hydrate crystals were measured with a confocal pinhole of 100 μm to record the progression of the guest replacement in terms of relative hydrate compositions. Additional microscopic observations were facilitated by a digital camera that was mounted on the confocal microscope. The morphology changes of the

hydrate crystals were continuously characterized to show the transformation behaviors of hydrate crystals. Each experiment was repeated for two times and lasted for around 10 days until the secondary hydrate phase was stable in terms of the relative guest composition. The discussion of the preliminary results mainly focused on the period after the gas exchange (t = 0 mins), and were presented in the following sub-chapter.

5.2.2 Results

In order to examine the exchange behavior of multi-guests (CH_4, C_2H_6, C_3H_8, iso-C_4H_{10}, n-C_4H_{10} and CO_2) in hydrate cavities with CO_2, the composition of the initial gas and hydrate phase were measured before replacement. The sII mixed hydrates formed from the gas mixture composed of around 47.9 mol% CH_4, 3.5 mol% C_2H_6, 30.2 mol% C_3H_8, 4.8 mol% iso-C_4H_{10}, 0.7 mol% n-C_4H_{10} and 12.9 mol% CO_2. Again, C_3H_8 and iso-C_4H_{10} were found to be enriched in the hydrate phase.

After the exchange of gas phase from the multi-component mixture to pure CO_2, we observed a sharp decrease in hydrocarbons and enrichment of CO_2 in the gas phase (Figure 5.14). Around 30 mins later, the detected concentrations of hydrocarbon molecules except CH_4 were extremely low in the gas phase. Meanwhile, CH_4 concentration was found to remain nearly constant after the rapid decline. It should be mentioned that CO_2 molecules existed as a component in the original gas phase. Therefore, its concentration increased from 31.8 mol% to nearly 100 mol% after 300 mins implying that the gas mixture was completely replaced by the CO_2 gas.

There's no doubt that the composition of the primary mixed hydrates altered adapting to the varying gas phase. Figure 5.15 presented the hydrate composition of the measured hydrate crystals as a function of time with (a) focusing on CH_4 and CO_2 molecules, (b) illustrating all the rest components. The rapid increase of CO_2 composition in the hydrate phase (Figure 5.15a) was accompanied by the fast decline of hydrocarbons (Figure 5.15b). This indicated that an instant transformation process took place in the initial stage where CO_2 molecules was encased in the cavities and hydrocarbon molecules were excluded from hydrate structures. In particular, C_3H_8 content was reduced fast. Noteworthy, the hydrate phase on the first day after gas exchange still showed the characteristics of sII hydrate even though the composition varied due to the change of the feed gas. It was followed by a slower conversion process since the CO_2 gas had to diffuse into the layers for the reaction with the inner core. Huge variations were monitored for the components especially on the first two days.

Interestingly, changes of CH_4 in the hydrate phase were not straightforward especially on the following two days after the gas replacement. Despite the fact that CH_4 was depleted in the gas phase, specific hydrate crystals were remarkably enriched in CH_4. The decline of CH_4 in the hydrate phase was much slower than the other hydrocarbon components. The end-state hydrate phase on the fifth day contained primarily CO_2 together with an inconsiderable amount of CH_4.

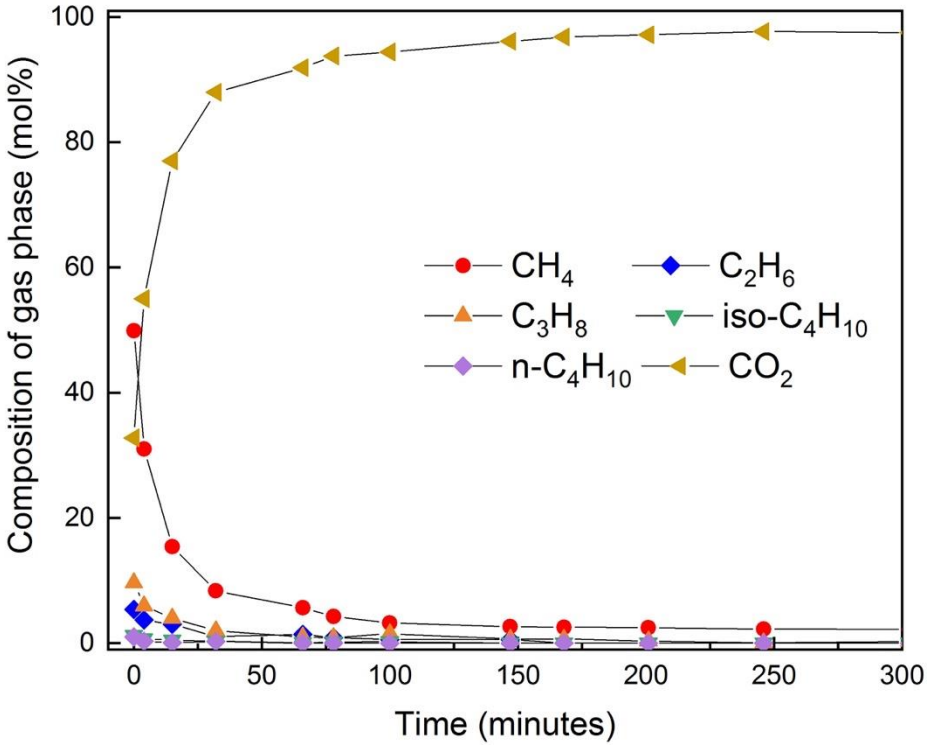

Figure 5.14 Changes of the composition in the gas phase as a function of time within the first 300 minutes. Individual data points represented by different symbols with specific colors corresponded to different guest components.

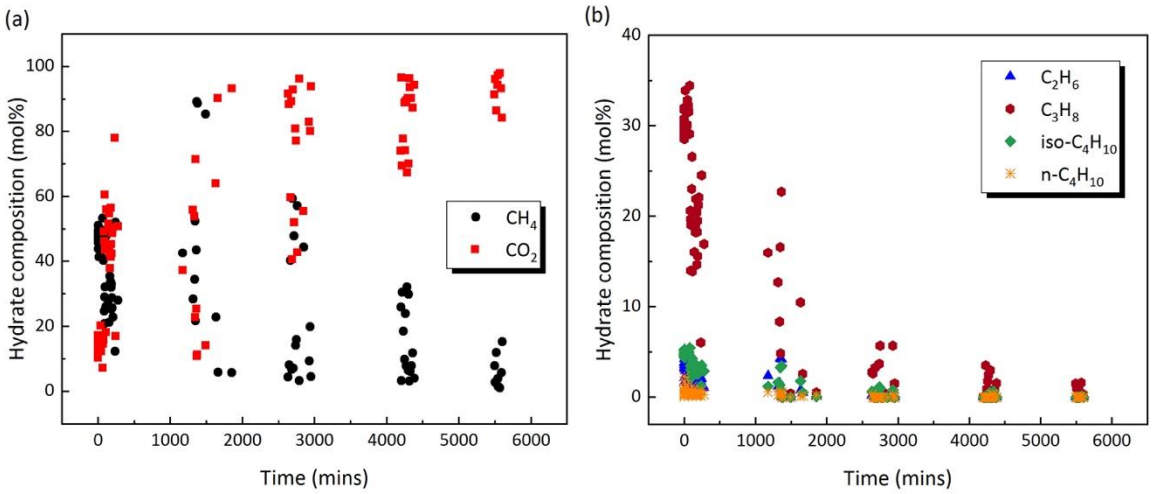

Figure 5.15 Composition changes as a function of time measured on the surface of the selected hydrate crystals after they were exposed to CO_2 gas, (a) CH_4 and CO_2 concentrations, (b) C_2H_6, C_3H_8, iso-C_4H_{10} and n-C_4H_{10} concentrations. Individual data points represented by different symbols with specific colors corresponded to different guest components.

Take a closer look into the changes of hydrate composition over time, particularly the CH_4 concentration, it could be speculated that hydrate crystals experienced three different types of transformation on the second day (Figure 5.16). According to the results of the gas phase, CO_2 prevailed in the system after 300 mins accounting for nearly 100 mol%. Nevertheless, the concentration of CH_4 remained nearly constant or slightly changed in some of the selected hydrate crystals after one day, implying that C_3H_8 and higher hydrocarbons were mainly released with the enclathration of CO_2 molecules and CH_4 was remained in the hydrate cavities (Type 1). An unexpected rise in CH_4 concentration was observed in other crystals (Type 2). Certainly, CO_2 molecules were also enriched in some crystals while CH_4 molecules were released leading to a significant drop in the CH_4 concentration. (Type 3). Since the selected hydrate crystals were monitored continuously throughout the process, the changes shown in Figure 5.16 indicated that both Type 2 and Type 1 crystals gradually transformed towards Type 3 crystals. Ultimately, the difference of composition between the measured crystals became smaller with CO_2 dominating the hydrate cavities and CH_4 occasionally presented.

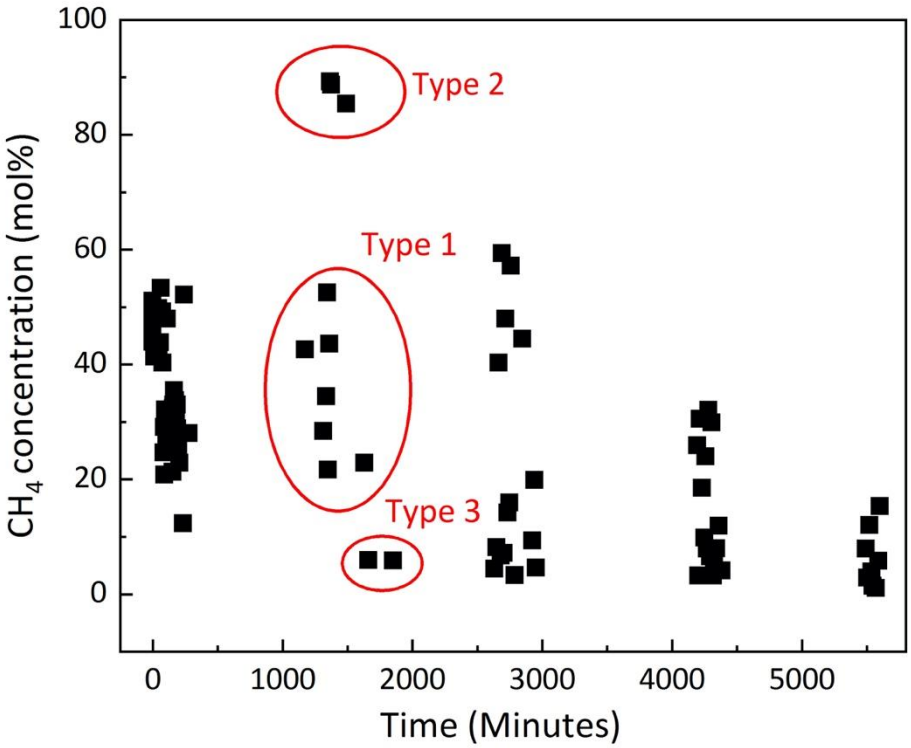

Figure 5.16 Results of CH_4 concentration in the hydrate phase that derived from Figure 5.15.

To better characterize the hydrate crystals on the second day as described above, Raman spectra acquired from the measurements on the surface of 3 hydrate crystals which belonged to different types were compared and presented in Figure 5.17. Type 1 crystals were defined for those with mid-range CH_4 concentrations. Apart from the two prominent Raman bands at 1285 cm^{-1} and 1388 cm^{-1} representing CO_2 gas, the double Fermi diads at 1274 cm^{-1} and 1380 cm^{-1} for CO_2 in the hydrate structures were detected in Type 1 crystals. Two bands occurred at 810 cm^{-1} and 876 cm^{-1} indicating iso-C_4H_{10} and C_3H_8 in sII hydrate structures, respectively. Unfortunately, neither the peak at 991 cm^{-1} which could be assigned to C_2H_6 in large cavities of sII nor the peak at 838 cm^{-1} for n-C_4H_{10} was easily distinguished from Figure 5.17a due to their low concentrations in the hydrate phase. In the C–H stretching vibrational mode region (Figure 5.17b), the enclathration of CH_4 encaged into the $5^{12}6^4$ and 5^{12} cavities of sII hydrates was proved by the occurrence of the Raman bands at 2902 cm^{-1} and 2912 cm^{-1}. Figure 5.17c–d showed the corresponding Raman spectrum for the crystal that contained higher amounts of CH_4 (Type 2). Unlike the spectrum for Type 1 crystals, the integrated intensities of Raman bands at 1274 cm^{-1} and 1380 cm^{-1} were quite low, showing a limited amount of CO_2 in the hydrate structures. An increase of the intensity for the spectral line at 2905 cm^{-1} could be detected,

illustrating that more CH_4 molecules were encaged into the $5^{12}6^2$ cavities. Besides, the characteristic band for CH_4 in the small cavities was shifting from 2912 cm^{-1} to 2915 cm^{-1} leading to the conclusion that the original sII hydrates transformed into CH_4-riched sI hydrates. Higher hydrocarbons were not recorded in this spectrum. More CO_2 molecules were found in the hydrate structures in Type 3 crystals, evident from the higher intensities of Raman bands at 1274 cm^{-1} and 1380 cm^{-1} and lower intensities of peaks at 2905 cm^{-1} and 2915 cm^{-1} (Figure 5.17e–f). Also, the CO_2-rich mixed hydrates were in forms of sI with no detection of higher hydrocarbons. These findings clearly demonstrated the coexistence of sI hydrates and sII hydrates during the replacement process, which indicated that a certain portion of the initial sII hydrate was partially converted into sI hydrates. As the process continued, the ratio of the CH_4 bands changed. Signals for iso-C_4H_{10} and C_3H_8 vanished. In contrast, two bands at 1274 cm^{-1} and 1380 cm^{-1} increased suggesting an advanced swapping of guest molecules with CO_2.

Despite the fact that the hydrate composition varied significantly among hydrate crystals, most of the hydrate crystals still showed the characteristics of sII hydrates on the second day after gas exchange. With longer time, CO_2 continued to encase into the cavities and finally the hydrate phase turned into CO_2-rich sI hydrates (Type 3). Type 1 and Type 2 crystals seemed to be in a transition stage, which transformed into Type 3 crystals as the experiment proceeded. Type 3 crystals maintained their composition until the system reached a steady state suggesting that they were at an advanced stage during the transformation process as compared to Type 1 and Type 2 crystals. A thorough transformation from the sII mixed gas hydrates to sI CO_2-rich hydrates were recorded from a series of snapshots that continuously taken on the surface of one specific hydrate crystal (Figure 5.18). Initially, the hydrate crystal displayed a clear boundary with a flat surface. After a delay of around 12 mins, the surface layer of the hydrate crystal was instantly transformed, leaving a rough outline of the original crystal. This finding indicated that the decomposition happened initially at the surface. Subsequently, the transformation of hydrates was characterized by the appearance of tiny dotted surfaces, either gradually expanded or shrank during swapping process. Finally, well-structured sI hydrates crystals occurred.

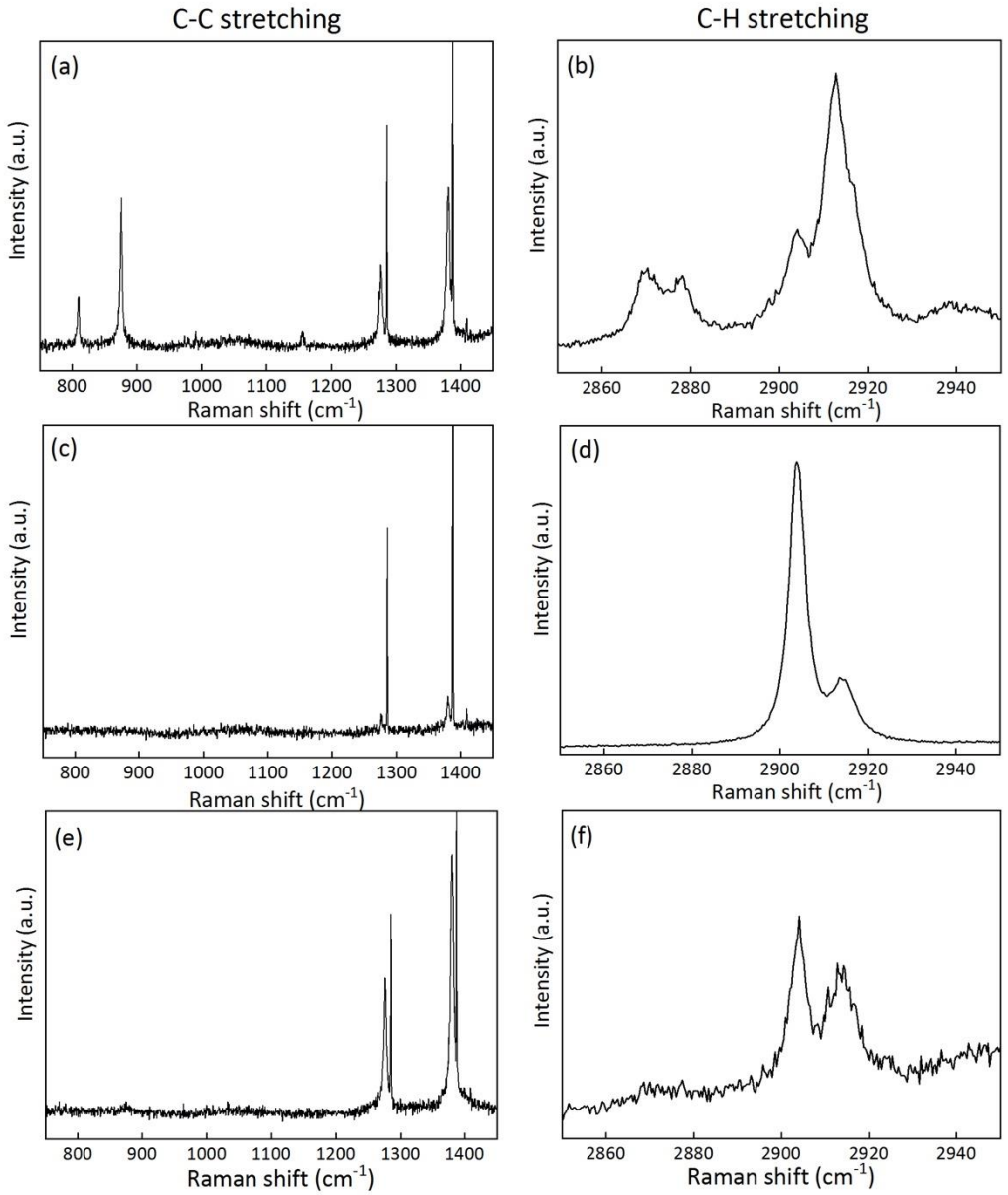

Figure 5.17 Microscopic observations on three hydrate crystals and their corresponding Raman spectra in C–C stretching vibrational mode region and C–H stretching vibrational mode region. (a–b) Type 1 hydrate crystal which remained constant in terms of composition, exhibiting as sII hydrates. (c–d) Type 2 CH_4-rich sI mixed gas hydrates. (e–f) Type 3 CO_2-rich sI mixed gas hydrates.

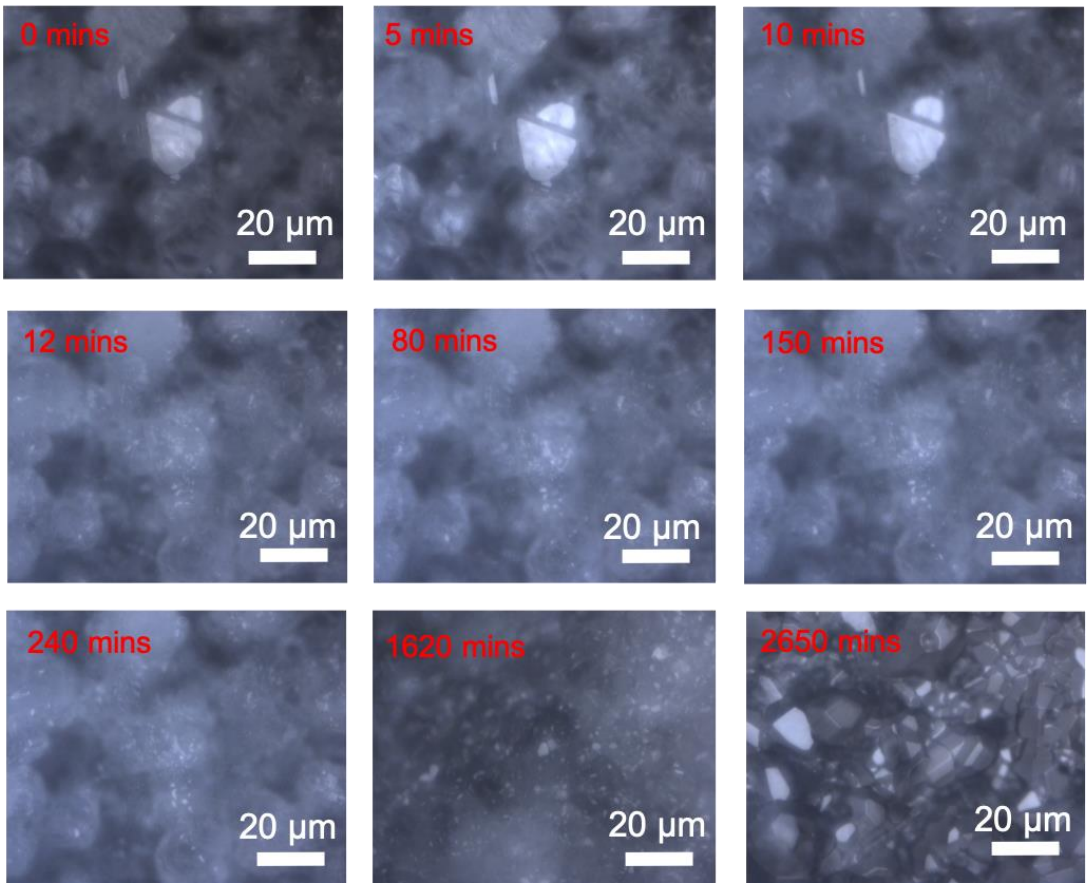

Figure 5.18 Morphology changes observed on the surface of a hydrate crystal during the transformation process from sII mixed hydrates to sI CO_2-rich hydrates. The structural transformation started after 12 mins.

5.2.3 Discussion

The occurrence of sII natural gas hydrates have frequently been reported in the reservoirs with mainly thermogenic origin. They are potential candidates for recovering gas and concomitantly sequestering greenhouse gas CO_2. Previous investigations by Seo et al.[259] presented their simulations on the replacement in CH_4–C_3H_8 hydrates with external CO_2/N_2. They suggested an isostructural and cage specific replacement with CO_2 substituting C_3H_8 in large cavities and N_2 replacing CH_4 in small cavities. Other researches also indicated that both structural transformation and isostructural conversion occurred in the replacement of sII hydrates [257,258]. Schicks et al. [118] also investigated the conversion process of hydrocarbon hydrates into CO_2 hydrates from Raman spectroscopic and PXRD measurements. They suggested the process as a decomposition and reformation process which involved a rearrangement of molecules on a molecular scale. The experimental data in this study provided from Raman spectroscopy showed the conversion of sII mixed gas hydrates to

CO_2 hydrates simulating the production of natural gas from sII hydrates by CO_2 gas injection. Since pure CO_2 gas crystalizes always in a type of sI, a phase transition from sII mixed hydrates to sI CO_2-rich hydrates and the coexistence of sI and sII during the transition process were observed, which corresponded to other literature data [118,198].

It is widely-accepted from the phase diagram that mixed gas hydrates are stable at higher temperatures and lower pressures as compared to simple CO_2 hydrates, as long as they are in chemical equilibrium with the chemical environment. In particular, the initial gas hydrates in this study contained more than 50 mol% of higher hydrocarbons besides CH_4. The observed transformation from stable sII mixed hydrates into CO_2 hydrates demonstrated that the chemical disequilibrium between the gas phase and the originally formed hydrate phase is the crucial factor [118].

The initial chemical equilibrium state was disturbed by the exchange of the gas phase. Right after the gas exchange, hydrates crystals started to destabilize even though most of them still exhibited the characteristics of sII hydrates. Hydrocarbons especially C_3H_8 which accounted for 30 mol% in the initial hydrate phase were largely released from hydrate structures while CO_2 enclathrated in the large $5^{12}6^4$ cavities of sII. The first indication of crystals showing the characteristic of sI hydrates came after a few hours indicating a gradual transformation process. The time taken for the transition can vary from crystal to crystal. In other words, the crystals were going through different transition stages during the measurements. A two-step transformation process was speculated including a destruction of the existing sII cavities and a rearrangement to form sI cavities. In this case, the chemical disequilibrium between the CO_2 gas and the original sII mixed gas hydrates was the driving force for the destruction of sII hydrate cavities after gas phase exchange. It is likely that the hydrate structures were left incomplete and guest molecules were released. With the enrichment of CO_2 in the gas phase, the incomplete structures may rearrange to incorporated CO_2 molecules for the formation of sI hydrates. The transition process lasted for several days until a stationary state was reached where the chemical potential of CO_2 in the gas phase was in equilibrium with the chemical potential in the newly formed hydrate phase. It is very likely that the equilibrium of the system was still not reached within the experimental period.

It is noticeable that the transformation behavior differed distinctly among hydrate crystals (Figure 5.15 and Figure 5.16). An unexpected increase of the CH_4 concentration was recorded in some crystals after the gas exchange. Considering

the decomposition and reformation process, it could be explained by the release of CH_4 which comprised of 47.9 mol% in the original hydrates, from the hydrate cavities especially at the beginning of the transformation. The liberated CH_4 molecules may exist as gas bubbles beneath the solid phase and therefore temporarily led to a distinct enrichment of CH_4 in specific areas. The chosen experimental condition was within the stability field of CH_4 hydrates. For that reason, CH_4 could re-enter the rearranged cavities and formed CH_4-rich hydrates with CO_2 molecules. Nevertheless, the chemical potential of these hydrates was also not in equilibrium with the chemical potential of the surrounding gas. The achievement of a new equilibrium was necessary. Finally, CH_4-rich hydrates turned into CO_2-rich hydrates. The possibility of a CH_4-rich hydrate formation during the decomposition and reformation process should be seriously taken into account to ensure an effective and safe production of the sII natural gas hydrate at conditions within the stability field of CH_4 hydrates.

5.2.4 Conclusions

In this study, we investigated the transformation process of multi-component mixed hydrates to CO_2-rich sI hydrates when exposed to pure CO_2 gas, simulating the gas production via CO_2 injection in sII hydrate reservoirs. Since mixed gas hydrates were thermodynamically more stable than CO_2 hydrates under same temperature and pressure conditions, the driving force of the replacement was the chemical potential gradients between the formed gas hydrates and the coexisting gas phase. Within a certain period of time after gas exchange which usually differed from several hours to tens of hours, hydrate phase showed characteristics of sII. The structural transition was featured by a decomposition of the original hydrates and reformation of a secondary sI hydrates. All sII hydrate crystals, independent of the initial composition, transformed into sI hydrates, demonstrating the availability of natural gas production and CO_2 storage by the induction of CO_2.

With the experimental data presenting time-resolved information of the mixed gas hydrate transformation process on a molecular level, the knowledge of CH_4 production from multi-component hydrates in nature by the induction of CO_2 was enhanced. To ensure a safe and effective gas recovery, more attention should be paid to the formation of a secondary CH_4-rich hydrates during the conversion process when the p–T conditions were within the stability field of CH_4 hydrates.

5.3 Transformation process of CH_4 hydrates when exposed to a multi-component gas mixture

Light hydrocarbons commonly occur in marine or permafrost sediments, where they originate mainly from microbial activities or thermocatalytic decomposition of organic matters. These hydrate-forming gases migrate from the place of origin at deeper depths to the shallower hydrate stability zone for the formation of gas hydrates. Typically, it is assumed that the composition of hydrate-forming molecules in a given feed gas phase would result in a specific hydrate structure, which depends on the molecular sizes of the hydrate formers. However, the coexistence of hydrate phases with different structures and compositions have been reported in various natural deposits as discussed in *Chapter 1.2.1* [40–43]. It is possible that the feed gas fluid is interrupted due to geological events (landslides, earthquakes) and a second gas source which delivers totally different guest components may migrate into hydrate phase in the stability zone. For instance, the initial gas source delivers methane from microbial origin by methyl-type fermentation for the formation of sI methane hydrates. Later on, a second source containing thermogenic hydrocarbons which are associated with deep oil fields may prevail, probably leading to a transition of the hydrate structure and/or a formation of a coexisting hydrate phase. Similar phenomenon was reported in Lake Baikal [260,261] where sI and sII gas hydrates coexisted within the same stratigraphic horizon, implying that they were formed from two gas sources. Yet, the mechanisms of the structural transition and the reason for the coexisting hydrate structures still remained unclear.

In order to further understand how the initially formed hydrates reacted to the changes of gas source with a totally different gas composition, we performed laboratory experimental simulations on the transformation process from sI CH_4 hydrates to sII mixed gas hydrates when exposed to a multi-component gas mixture. In this study, the composition changes in the gas phase and the hydrate phase were constantly characterized by *in situ* Raman spectroscopic measurements after the initial gas was interrupted. The transformation process from the initial hydrate phase to a secondary hydrate phase was recorded and the corresponding coexistence of hydrate phases was documented during the process.

5.3.1 Materials and methods

For the opposite structural transition process from sI to sII hydrates, CH_4 hydrates were first formed from pure CH_4 gas and 150 µl deionized water in the high-pressure cell at identical p-T conditions as in the previous two exchange experiments (274 K, 3.2 MPa) (Figure 5.13). The formation of CH_4 hydrates followed the same procedures as described in *Chapter 2.2.1.* To initiate the

transformation process, CH_4 hydrates at a steady state were exposed to the pre-cooled gas mixture containing CH_4, C_2H_6, C_3H_8, iso-C_4H_{10}, n-C_4H_{10} and CO_2 (same gas mixture as the one used in *Chapter 5.2*) at constant pressure and temperature conditions, following the same procedure as those in the sII to sI transformation process (*Chapter 5.2*).

Raman spectroscopic measurements were taken in both the gas and hydrate phase before the gas exchange. Once well-structured CH_4 hydrates were introduced to the gas mixture, single-point Raman measurements were taken at different penetration depths from the surface to the core of the crystal (0 μm, 30 μm, 60 μm) to record changes in the clathrate structure, composition and cage occupancy. Microscopic pictures were regularly taken for each hydrate crystal during the transformation process. The experiment was repeated for two times and revealed similar results. Same as the previous experiment, the results and discussions mainly focused on the period after gas replacement. The moment when the valve for the gas mixture was opened was designated as time $t = 0$.

5.3.2 Results and discussion

As can be seen from Figure 5.13, sII mixed gas hydrates were thermodynamically more stable than CH_4 hydrates. Unlike the CH_4–CO_2 transformation process discussed in *Chapter 5.1* where both gas molecules form sI hydrates, higher hydrocarbon molecules (e.g. C_3H_8, iso-C_4H_{10} or n-C_4H_{10}) in the gas mixture could only occupy the large cavities of sII hydrates under the experimental condition. Therefore, a potential structural transition from sI to sII was expected when the initial CH_4 hydrates were introduced to the complicated gas mixture.

1. Changes of the composition in the gas phase

Time-dependent Raman spectra revealed the composition changes of the gas phase once the transformation process started. As seen in Figure 5.19, time zero was designated as the moment when the inlet valve was reopened for introducing the gas mixture. The individual data points indicated by different symbols of a specific color corresponded to the six guest components. CH_4 was the only gas component in the system before the gas flow was shifted, accounting for 100 mol% (red circles). After around 7 mins, the CH_4 proportion decreased sharply to around 50 mol% while both the concentrations of C_3H_8 (orange up triangles) and CO_2 (yellow left triangles) increased in the gas phase. The detected concentration of CO_2 in the gas phase was around 38 mol% after 50 mins while C_3H_8 only composed of around 10 mol%. The first detection of C_2H_6

(blue diamonds) was after around 30 mins. 6 mol% of C_2H_6 was detected in the gas phase. As for iso-C_4H_{10}, a delay of 60 mins in detection was reported (green down triangles in Figure 5.19). Unfortunately, Raman signals for n-C_4H_{10} in the gas phase did not occur within the first 400 minutes. The average composition of the gas phase at a steady state contained 50.6 mol% CH_4, 5.6 mol% C_2H_6, 10.2 mol% C_3H_8, 1.3 mol% iso-C_4H_{10}, 0.9 mol% n-C_4H_{10} and 31.3 mol% CO_2.

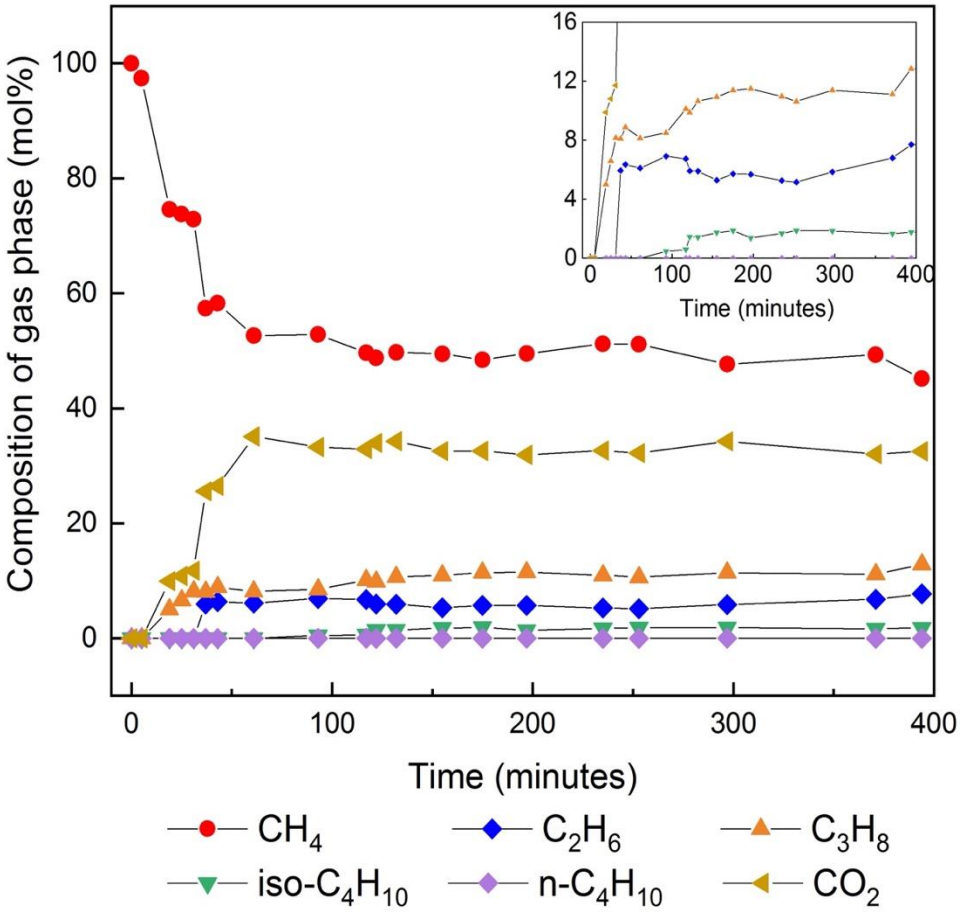

Figure 5.19 Changes of the composition in the gas phase as a function of time within the first 400 minutes. The inset of the figure focused on the concentration changes of hydrocarbons other than CH_4. Individual data points represented by different symbols with specific colors corresponded to different guest components.

2. Composition and morphology changes of the hydrate crystals

Raman spectra of the initial CH_4 hydrates showed typical characteristics of sI hydrates with two Raman bands occurred at 2905 cm^{-1} and 2915 cm^{-1}, which indicated CH_4 in large $5^{12}6^2$ cages and in small 5^{12} cages, respectively (Figure 5.20

black curve). After the gas exchange, Raman band intensities for the existing two bands started to decrease over time. The shrinking of Raman band intensity at 2905 cm^{-1} (I_L) was much faster than the other Raman bands at 2915 cm^{-1}(I_S). This implied that less CH_4 molecules were encased in the large cavities of the hydrate structures. The occurrence of the two Fermi diads at 1274 cm^{-1} and 1381 cm^{-1} came after 25 mins indicating the first encasement of CO_2 in the structures and also the start of the transformation process. Despite a short delay, the enclathration of C_3H_8 in the large cavities was detected at 876 cm^{-1}. Meanwhile, a small Raman band popped up at 991 cm^{-1} which could be assigned to C_2H_6 molecules in the large cavities of sII hydrates. The Raman signal of iso-C_4H_{10} at 810 cm^{-1} was determined at t = 37 mins after gas replacement. However, n-C_4H_{10} band at 838 cm^{-1} was too low to be detected until 5 hours later. With longer time, both Raman bands for CH_4 appeared to have a slight redshift, which corresponded to our previous findings for CH_4 molecules in sII mixed hydrates. Instead of the original peaks at 2905 cm^{-1} and 2915 cm^{-1}, the Raman signals gradually shifted to 2903 cm^{-1} and 2912 cm^{-1} (Figure 5.20 red curve) with a strong dominance of the latter. The structural determination was based on the vibrational modes of hydrocarbons as well as the shape and position of the CH_4 bands. Therefore, it was confirmed that sI CH_4 hydrates transformed into sII mixed gas hydrates when exposed to the gas mixture. Despite the fact that CH_4 dominated mainly the small cavities with a small amount in the large cavities, the other guest components occupied the large cavities of sII hydrates.

It should be emphasized that a high heterogeneity was confirmed for the transformation behavior of different hydrate crystals on the first day after the gas exchange. The C–H stretching bands for CH_4 that measured on the surface of three hydrate crystals were illustrated and compared in Figure 5.21. The development of crystal 1 was slow as it did not experience a structural transition even after 360 mins. Crystal 2 exhibited characteristics similar to sI hydrates after 180 mins. However, the intensity of Raman band at 2905 cm^{-1} was lowered as the reaction proceeded, suggesting a transition into sII hydrates after 360 mins. The transformation of crystal 3 was more advanced as the shape of C–H bands already shared similarities with sII hydrates after 180 mins. It remained constant in terms of the cage occupancy after 360 mins. Obviously, the transformation behavior varied from crystal to crystal especially at the beginning of the process. The crystals experienced a differentiated transition stage after the same period of time. Subsequently, the hydrate phases gradually transformed into typical sII hydrates.

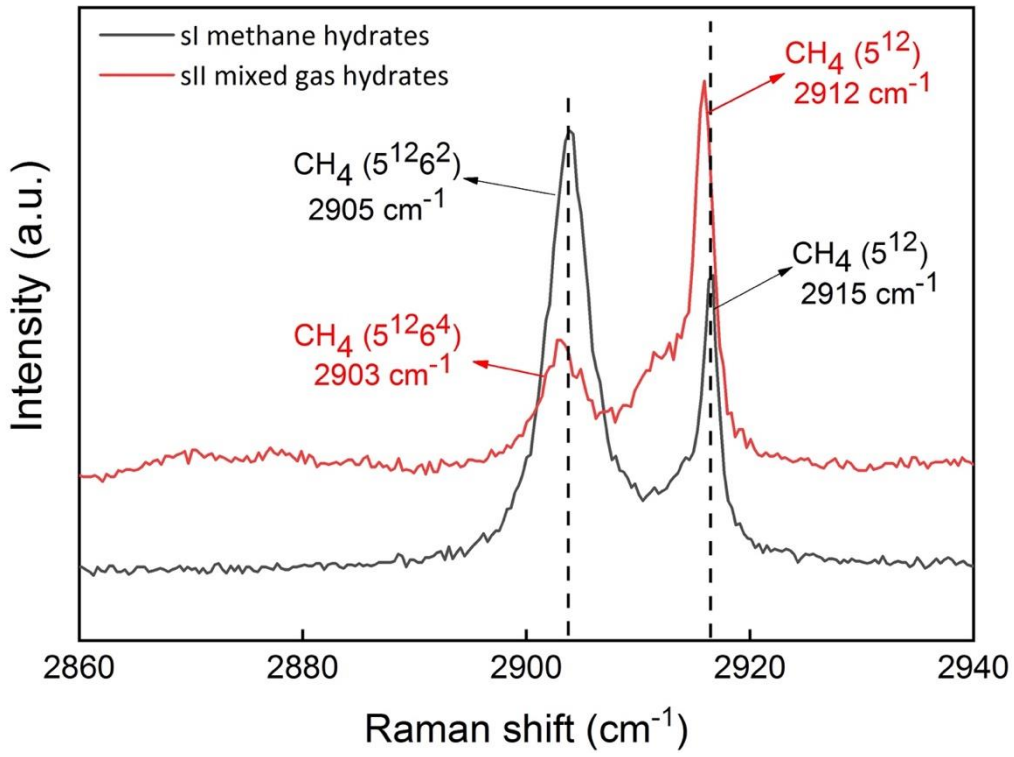

Figure 5.20 Overlap of two Raman spectra showing the C–H stretching vibrational modes from 2860 cm^{-1} to 2940 cm^{-1} obtained before the gas exchange (black curve) and 48 hours after exchange (red curve). The black curve depicted two Raman bands at 2905 cm^{-1} and 2915 cm^{-1}, which could be assigned to CH_4 in large and small cavities of sI hydrates, respectively. The red curve showed two redshifted Raman bands at 2903 cm^{-1} and 2912 cm^{-1}, indicating CH_4 in large and small cavities of sII hydrates with a dominance in the latter one.

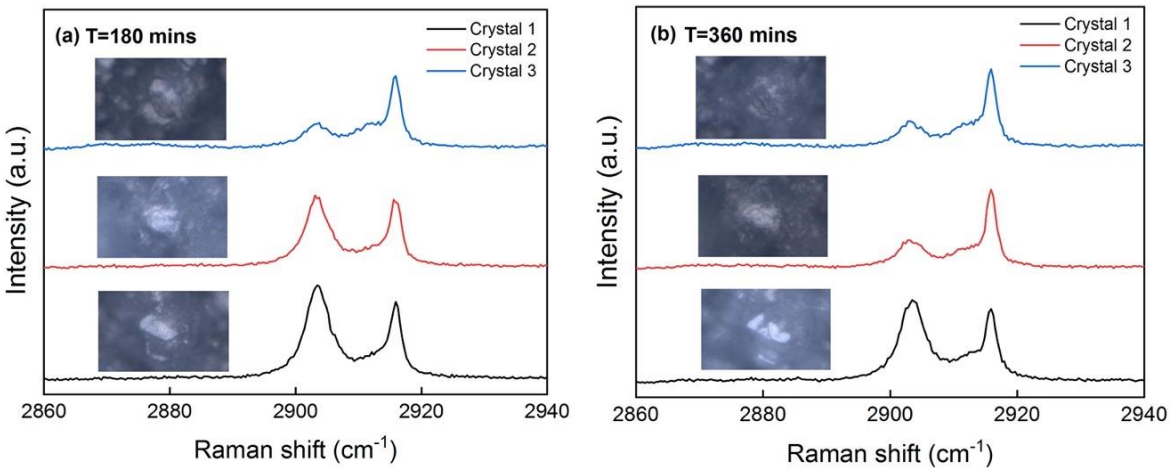

Figure 5.21 Comparison of the C–H stretching vibrational modes for three hydrate crystals after 180 mins (a) and after 360 mins (b). The corresponding surface morphology of specific crystals were also attached in the figure.

As seen in Figure 5.22, the hydrate composition became instantly depleted in CH_4 and rich in C_2–C_4 and CO_2 molecules at the beginning of the experiment since CH_4 in hydrates were continuously released. This indicated that C_2H_6, C_3H_8, iso-C_4H_{10}, n-C_4H_{10} and also CO_2 could enclathrate in the cavities in initial stage of transformation while CH_4 gas molecules were released. In particular, the CO_2 concentration was added up to 30 mol% while C_3H_8 was enriched accounting for 10 mol% in the hydrate phase. The fast replacement in the early stage was in accordance with the phenomenon observed during CH_4–CO_2, mixed hydrates–CO_2 swapping processes. The hydrate composition was found to remain nearly constant as the experiment proceeded. The end-state hydrate phase at a steady state contained around 42.8 mol% CH_4, 2.6 mol% C_2H_6, 33.1 mol% C_3H_8, 5.2 mol% iso-C_4H_{10}, 0.6 mol% n-C_4H_{10} and 15.8 mol% CO_2, indicative of a preferential enclathration of C_3H_8 and iso-C_4H_{10} molecules in the hydrate phase compared to their concentration in the gas phase.

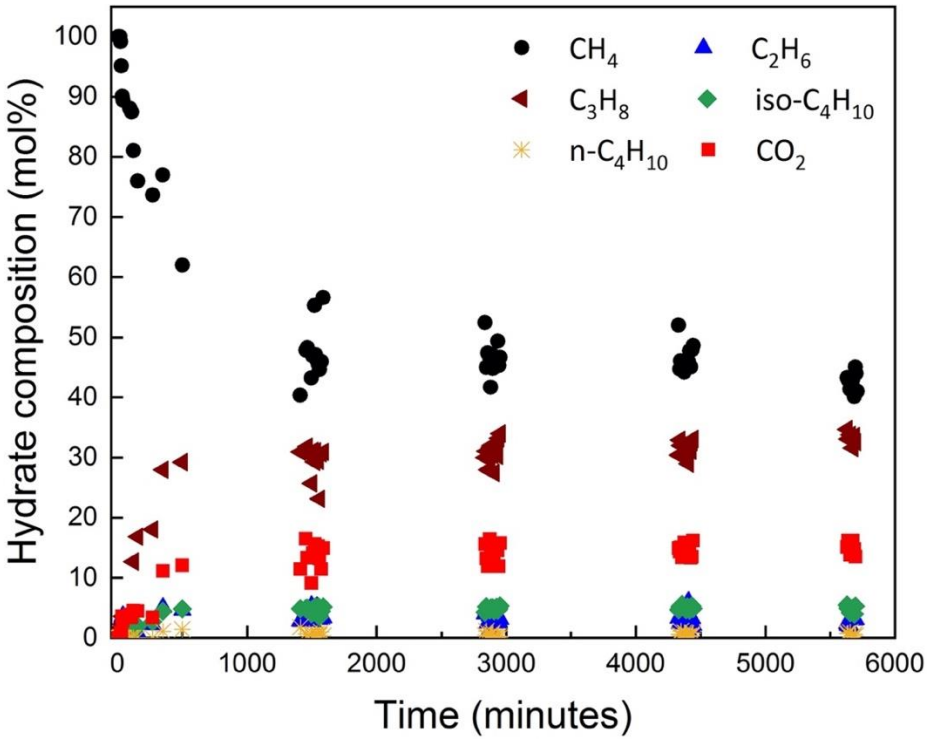

Figure 5.22 Changes of hydrate composition as a function of time measured on the surface of the selected hydrate crystals. The individual data point represented the measuring result from one single hydrate crystal.

It is well-established that a unit cell of sI hydrates contains two 5^{12} cavities and six $5^{12}6^2$ cavities [5]. Assuming that the cavities are completely occupied, the CH_4 peak intensity ratio in large (I_L) and small (I_S) cavities achieves 3.0. In our experiments, the ratio of peak intensity for CH_4 in large and small cavities (I_L/I_S) was provided in Figure 5.23. Initially, the ratio reached around 3.5, which was slightly higher than the theoretical value. This indicated that CH_4 molecules were mostly in the large $5^{12}6^2$ cavities of sI with a relatively low concentration in the small 5^{12} cavities. With increasing amounts of higher hydrocarbons and CO_2 encasing into the large cavities, CH_4 molecules were highly excluded from the large cavities, leading to a rapid decline of the ratio. Consequently, a ratio of less than 0.5 was recorded which was in good agreement with the results from Raman spectra indicating that CH_4 mainly occupied small cavities with partial occupation in large cavities while the other molecules enclathrated into large cavities. Correspondingly, variations of CH_4 proportion in the hydrate phase (Figure 5.22) displayed a similar trend with that in Figure 5.23, showing a rapid decrease on the first day and afterwards a gradual stabilization process with smaller variations among the selected hydrate crystals.

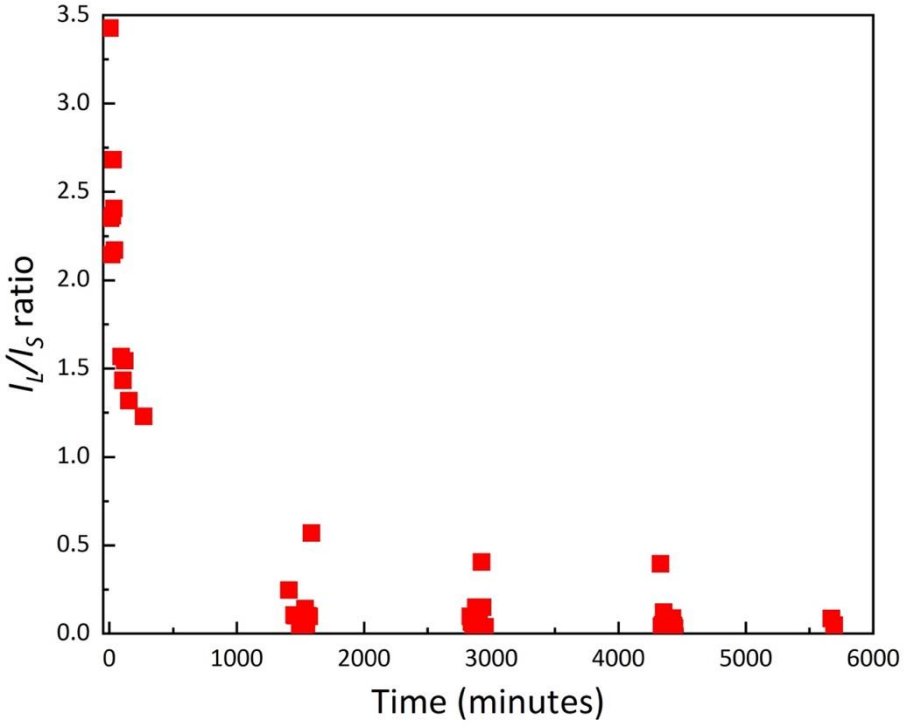

Figure 5.23 Peak intensity ratios of CH_4 in large and small cavities during the transformation process.

Figure 5.24 compared the relative composition of the gas and resulting hydrate phase. This hydrate composition at a steady state did not yet correspond to the

composition calculated from CSMGem at equilibrium state with 41.6 mol% CH_4, 2.3 mol% C_2H_6, 28.4 mol% C_3H_8, 0.5 mol% iso-C_4H_{10}, 4.0 mol% n-C_4H_{10} and 23.2 mol% CO_2 (Figure 5.24). However, the composition of the hydrates which were synthesized directly from the multi-component gas mixture as described in *Chapter 5.2* was quite similar to the resulting hydrate phase after transition process, implying that the transition process did not influence the final composition of the hydrate phase.

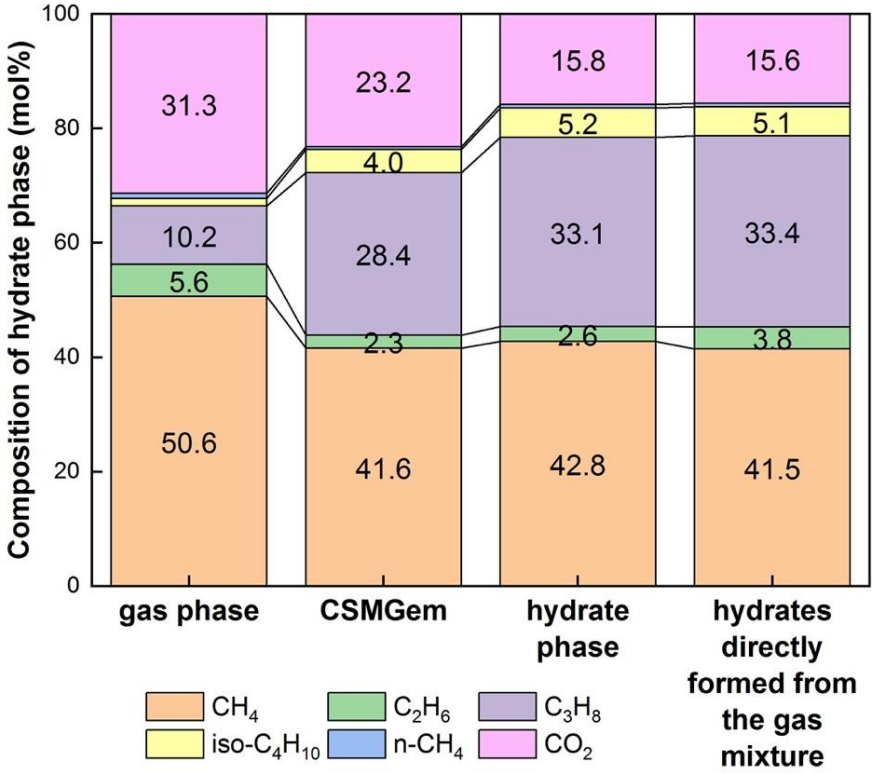

Figure 5.24 Comparison of the actual gas phase composition and the respective hydrate composition which were measured from experiments and calculated from CSMGem, respectively. The composition of the hydrates synthesized directly from the gas mixture were also added in this figure for comparison.

Continuous observations of the hydrate crystals showed a clear transformation behavior in terms of the surface morphology (Figure 25). Notably, well-structured hydrate crystals with sharp edges were observed in CH_4 hydrates before the gas exchange. Even after 17 mins, the surface morphology of the hydrate crystals showed similar characteristics as those in the pure CH_4 hydrates. At t = 19 mins, hydrate crystals with sharp edges were covered by a layer with an uneven surface. Instantly, this layer expanded in specific directions and finally covered the entire vision. It was noteworthy that the contours of the initial CH_4 hydrate crystals survived and hydrate structures did not collapse as a whole

even though the surface morphology changed thoroughly within two minutes. Thereafter, the microscopic observations gradually became blurred and the shape of the original hydrate crystals become indistinguishable as the experiment proceeded. Based on the insights on the transformation process of CH_4–CO_2 [227], a partial dissociation of CH_4 hydrates on the surface layer accompanied by a rapid recrystallization of sII mixed gas hydrates would be a possible explanation for this phenomenon.

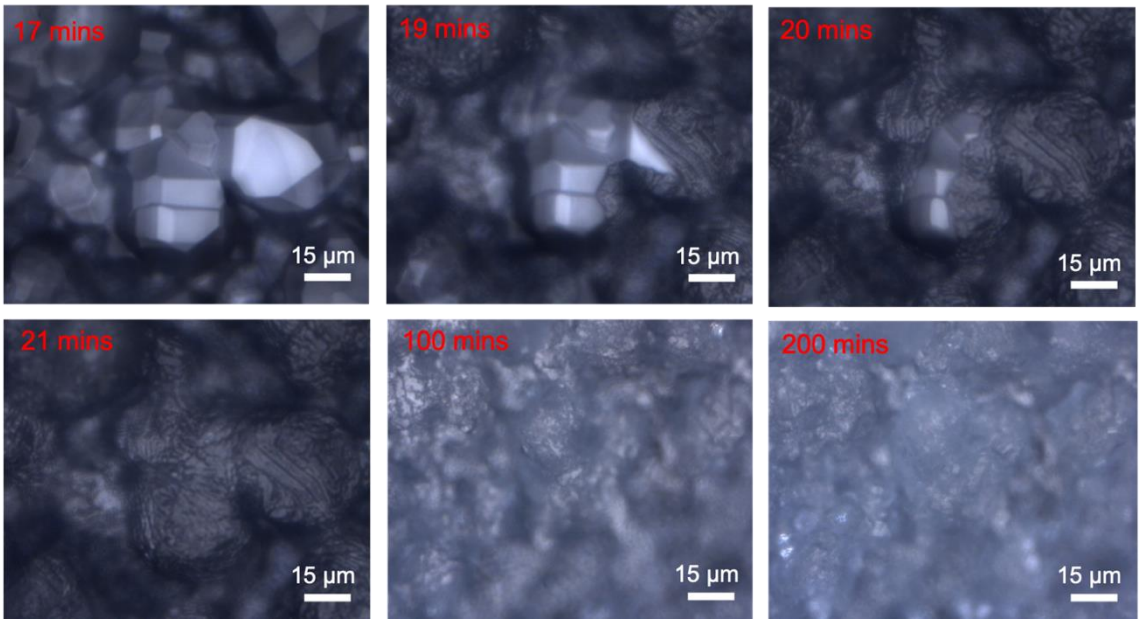

Figure 5.25 Snapshots of hydrate crystals illustrating the surface morphology changes during the transformation process.

In order to advance our understanding on the newly formed layer and the hydrates beneath it, Raman spectroscopic measurements were also performed at different penetration depths from the surface to the core of the hydrate crystal at 0 µm, 30 µm, 60 µm. With the help of the motorized sample stage which could be adjusted vertically, the laser beam was able to focus at defined depth. Under the chosen experimental condition, the spatial resolution in z-direction reached 6.2 µm. The high-resolution measurements revealed the changes of CH_4 concentrations at different depths over time (Figure 5.26). As can be seen from the figure, red squares which represented the results measured on the surface of hydrate crystals exhibited an early decrease followed by blue diamonds (measured at 30 µm depth) and green triangles (measured at 60 µm depth). The surface of hydrate crystals always had the lowest CH_4 proportion in the hydrate phase as compared to that in the deeper depths. This observation of the lower

CH_4 amount in the hydrate phase was confirmed in various hydrate crystals, illustrating that the transformation process took place initially at surface. This was in good agreement with the findings of morphology changes. The time-consuming inward diffusion process of large hydrocarbon molecules led to a slower decrease of the CH_4 concentration in the hydrate phase.

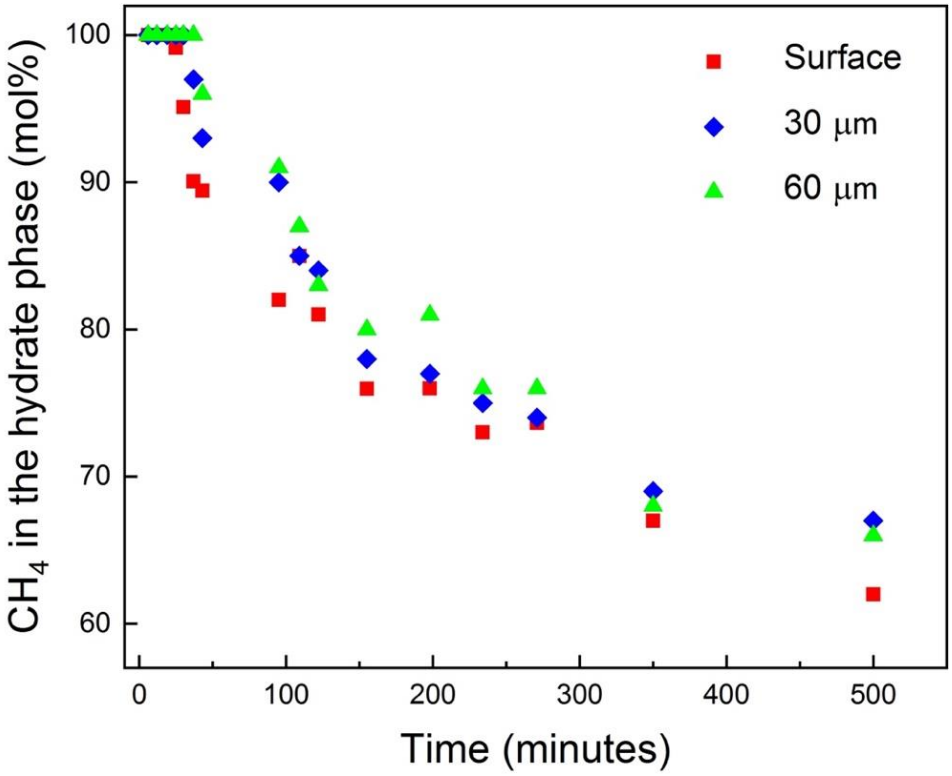

Figure 5.26 Variations of CH_4 concentration in the hydrate phase that measured at different penetration depths, surface (red squares), 30 μm (blue diamonds) and 60 μm (green triangles).

5.3.3 Discussions

In situ Raman spectroscopy was used to evaluate on the molecular level the structural transition process from sI CH_4 hydrates to sII multi-component mixed hydrates. After the formation of CH_4 hydrates, CH_4 content in the gas phase was diluted by adding a mixture of hydrocarbons(C_1–C_4) and CO_2 into the system. The reason for the structural transition was the large size of these newly offered molecules which made them preferentially suitable for large cavities in sII hydrates. Even though sII mixed gas hydrates were stable than pure CH_4 hydrates at the chosen experimental condition (Figure 5.13), it was believed that the chemical disequilibrium between the replaced gas phase and the CH_4 hydrates was the main driving force for the structural transition.

As indicated from both microscopic observations and Raman spectroscopy, the transition of guests in hydrate structures took place initially at the hydrate particle surface. The rate of surface reaction was indicated by the steep slope in Figure 5.22. Thereafter, the rate of conversion slowed down distinctly, demonstrating a two-step transformation process similar to the isostructural conversion of CH_4 to CO_2 (*Chapter 5.1*) and the structural conversion from sII mixed gas hydrates to sI by CO_2 gas injection (*Chapter 5.2*). Nevertheless, the results from sII to sI transformation process suggested an transition period for all the crystals ranged from several hours to tens of hours, during which the hydrate phase still showed the characteristics similar to sII hydrates. Only after the transition time could we detect the well-developed sI hydrate crystals containing primarily CO_2 (with partial CH_4). In this experiment, the formation of a secondary hydrate showing the characteristics of sII were observed within the first hour with C_2H_6, C_3H_8, iso-C_4H_{10} and CO_2 encased in the hydrates cavities besides CH_4. Expressly, the conversion of sI CH_4 hydrate into a sII mixed hydrate proceeded faster than the previous experiment started from the mixed gas hydrates containing C_1–C_4 and CO_2. In contrast, a previous study from Schicks et al. [118] observed a faster transformation process from sII binary CH_4 + C_2H_6/C_3H_8 hydrates to sI CO_2-rich hydrates and a slower reverse process from sI to sII after the feed gas changed back to the gas mixture. It was summarized from the comparison of these results that the rate of structural transition was closely related to the composition of the gas and hydrate phase. The rate of transformation depended on the concentration gradient for each component in the surrounding gas and hydrate phase, rather than the direction of the structural transition (either from sI to sII or from sII to sI). In this study, the concentration of CO_2 reached 30 mol% in the initial mixed hydrate phase. The incoming CO_2 gas was diluted through the presence of other components which led to the assumption that the concentration gradient between the gas phase and CO_2 in the hydrate structures was not as strong as it would be for the pure CH_4 hydrates surrounded by a multi-component gas mixture. In the reverse transformation process from sI to sII, none other guests except CH_4 was found in the original hydrate structures. The mole fractions of higher hydrocarbons and CO_2 were zero in the hydrate structures but accounted for around 50 mol% in the feed gas phase.

Driven by the large difference of mole fraction for hydrocarbons and CO_2 in the coexisting phases, both cavities were unstable but the large $5^{12}6^2$ cavities in sI CH_4 hydrates may break down faster. The release of CH_4 from the large cavities

resulted in a significant drop of the I_L/I_S ratio as shown in Figure 5.23. Evident from the microscopic observations and Raman spectra, the large hydrocarbon molecules and CO_2 accompanied by a small proportion of the released CH_4 molecules were assumed to promptly interact with neighboring labile water molecules to form new large $5^{12}6^4$ cavities on the particle surface. Since the pentagonal dodecahedrons (5^{12}) was the basic building block in both structures, large amount of CH_4 still remained in small cavities. These results suggested a decomposition of large cavities in sI hydrates and a reformation of the large cavities for sII mixed hydrates incorporating higher hydrocarbons, CO_2 and released CH_4. Since the replacement behavior differed from crystal to crystal, sI and sII hydrates may coexist throughout the experiment. To achieve further equilibrium, these large molecules transported through the formed sII layer on the surface for the rearrangement of cavities in deeper layers.

5.3.4 Conclusions

In this study, we presented time-resolved and semi-quantitative information on the transformation process from sI to sII hydrate phase with a discussion of possible molecular mechanisms. This was achieved by performing *in situ* Raman spectroscopic measurements on the crystal growth starting with simple sI CH_4 hydrates but exposed to a multi-component gas mixture containing C_1–C_4 and CO_2 besides CH_4. The changes of composition for gas and hydrate phase, cage occupancy ratio and surface morphology after the gas replacement were regularly recorded in order to characterize the entire structural transition process. Following conclusions can be draw from the results:

1. The study demonstrated that the key driving force for the exchange was the aim to reach an equilibrium stage for the chemical potential of all components between coexisting phases. The concentration gradient of each component between the gas and hydrate phases also affected the rate of structural transition.

2. Similar to other solid–gas reactions, the transformation process from sI to sII hydrates also involved overall two stages: a fast surface reaction with the rearrangement of hydrate cavities with a much slower diffusion-controlled process in deeper depths.

3. After the exchange of the offered gas, both large and small cavities of sI CH_4 hydrates became unstable and collapsed when CH_4 escaped from them. However, the small cavities may survive at least in parts. This resulted in the partial decomposition of sI CH_4 hydrates involving the I_L/I_S ratio no longer retained the required value of 3:1. In this case, $5^{12}6^2$ cavities rearranged into

larger ones ($5^{12}6^4$) encasing higher hydrocarbons and CO_2 for the construction of a sII lattice with excess small cavities (5^{12}) to be formed.

Towards a scenario of feed gas perturbation due to geological events, a potential shift in the hydrate composition and structure was foreseeable which provided insights for the coexistence of hydrate phases with different structures in natural reservoirs.

Chapter 6

6 Summary

The aim of this thesis is to obtain a systematic overview of the thermodynamic properties of multi-component mixed hydrates together with their formation, dissociation and transformation behaviors. The experiments are mainly based on the natural reservoir conditions in Qilian Mountain permafrost, China for the reason that gas hydrates recovered from this area are characterized by a more complicated gas component with a shallower burial depth below thinner permafrost when compared to other well-documented permafrost hydrate reservoirs all over the world. Also, the occurrence of the hydrate reservoir is found in a middle-latitude region of high elevation which makes the reservoir in QMP more unique. A proper and advanced understanding of the complex mixed gas hydrates is therefore a prerequisite for the assessment of potential risks and efficiency of the hydrate resource production in this region. Furthermore, general concepts and fundamental information with regard to the mixed gas hydrate formation/dissociation/transformation process can be extracted from the experimental simulation results, which are applicable to other natural reservoirs containing sII mixed hydrates on a world-wide perspective.

Apparently, the investigation of mixed gas hydrates requires a comprehensive and in-depth literature review on the basic properties of gas hydrates. In this case, the composition, structure, mechanical properties, natural occurrences, widely-adopted exploitation techniques were introduced. A brief summary of the gas hydrate system in Qilian Mountain permafrost laid a solid foundation for the experimental simulation. To further discuss the hydrate dissociation behaviors, the background of global climate warming was emphasized. The thermodynamic properties involving the phase behavior and driving forces were described. The existing kinetic models explaining hydrate formation from water/ice were introduced and compared. This information not only provides the state-of-the-art background in hydrate research but also clarifies the motivation and necessity of this study.

To mimic the mixed gas hydrates in natural reservoirs, an analytical tool which enables the *in situ* observation of the formation/dissociation/transformation process is requested for the delivery of fast and reliable results. For this purpose, a confocal Raman spectroscopy was selected as a powerful method since it can easily determine the overall composition and cage occupancy of hydrate phases. A new experimental setup was developed and tested in the framework of this thesis which involves a high-pressure cell that is integrated into the confocal Raman spectroscopy. The pressure cell can work with a continuous gas flow system which assures a constant composition of the feed gas during the experiments. With the help of the valves located outside the cell, the cell is also possible to simulate as a closed or semi-closed system with a disturbing gas. Another unique feather of the system is the availability of *in situ* Raman measurements on x-y- and z- directions utilizing the motorized software-controlled sample stage. The integrated optical microscopy allows a continuous observation of the ongoing process in the pressure cell. All the instrumental parameters adopted for the experiment were optimized in advance to guarantee a precise characterization with high resolution. Most of the experimental simulations presented in the thesis were carried out with this specialized setup, supplemented by other setups and analytical tools. A peer-review paper which introduced the new experimental setup was already published.

The outcome of the thesis can be distinguished mainly into 3 parts involving 7 independent experimental sets. These experiments were carried out under specifically chosen conditions to maximize the simulation of the hydrates in natural reservoirs.

The first part consisted of two experimental sets to investigate the formation process of mixed gas hydrates, in consideration of the effects from the feed gas flow and surrounding sediments (*Chapter 3*). Although there are several hypotheses, the reasons for the existence of coexisting hydrate phases have not yet been clarified. *Chapter 3.1* (published results) presents the experimental simulations on the formation process of complex mixed hydrates based on the reservoir conditions in QMP to verify a possible explanation. The setup was operated as an open, closed and semi-closed system respectively during the first experiment. Through continuous characterization on the gas and hydrate phase over several days, important information about the gas enclathration on a µm-scale were revealed, indicating a competitive enclathration of guest molecules into the hydrate crystal lattice depending on their guest-to-cavity ratio and solubility. Another interesting result of our experiments was the observation that

despite a change in the gas composition, no coexisting hydrate phase was formed, which provided new insights and may refute the hypothesis of the coexistence of hydrate phases due to a changing feed gas phase. To come closer to the natural conditions, powdered natural sediments from QMP and coarse artificial quartz sands were added to the system for a comparison with the hydrate formation process without sediments under identical p–T conditions (*Chapter 3.2*, preparing for publication). By a combination of the *ex situ* experiment in three batch pressure vessels and the *in situ* Raman spectroscopic measurements, the formation kinetics and equilibrium curve of the mixed gas hydrates were determined. A promoting effect of sediments especially the powdered natural samples was confirmed on the rate of hydrate nucleation and growth. However, the stability field of the mixed hydrates was not affected due to the limited amount of sediments. The formation patterns were different as shown by the time-resolved information on hydrate composition in three systems. The presence of QMP sediments led to a coexisting solid phase which could be probably explained from the effects from existing hydrophobic minerals and organic compounds in its surrounding areas.

The investigations of the hydrate dissociation process mainly addressed two research questions about the interactions between sediments and hydrate crystals as well as the dissociation behavior of guest molecules in response to climate warming (*Chapter 4*). An unexpected and significant drop in permeability was measured on the hydrate-bearing core sample from QMP during CH_4 hydrate decomposition induced by depressurization. This was the first time to report the formation damage by fines mobilization and migration during hydrate decomposition. It was explained as a result of freshwater release from hydrate dissociation and the fact that the simultaneous release of a large methane volume displaced the saline pore water and separated it from the produced freshwater. These findings were critical for the risk assessment of gas production especially in clayey sand reservoirs with high hydrate saturations (*Chapter 4.1*, published results). To illustrate the dissociation behavior of different guest molecules in hydrate structures, three different hydrates were decomposed by thermal stimulation mimicking the atmospheric warming (*Chapter 4.2*, preparing for publication). Taking the advantage of the confocal Raman spectroscopy and optical microscopy, the dissociation process of hydrates was visualized, providing advanced insights at a μm scale. The results indicated that CH_4 molecules in large cavities of sI CH_4 hydrates were released faster than those in small cavities at the end of the dissociation. The occurrence of C_3H_8 besides CH_4

in the binary hydrate system led to an opposite trend where the break-down of small cavities was rapid, followed by the liberating of CH_4 and C_3H_8 in large cavities of sII. Since the hydrate cavities were better stabilized by the inclusion of guests with suitable molecular sizes, it was easier for those cavities with low guest-to-cavity ratios to be collapsed when the system was heated. Nevertheless, the presence of large guests in the mixed gas hydrates may pose significant effects on the neighboring cavities. CH_4 happened to escape the cavities much faster than C_2H_6 and CO_2. The trend for C_3H_8 was not clear and needs further investigation.

The third part of the thesis was made up by three separate hydrate transformation experiments (*Chapter 5*). Noteworthy, these transformation processes were observed on a micrometer scale at different stages. Experiments began with the simplest isostructural conversion from sI CH_4 hydrates to sI CO_2-rich hydrates (*Chapter 5.1,* published results). The incorporation of CO_2 into the hydrate phase with a concentration gradient from the surface to the core of the hydrate particle supported in general the shrinking core model with two steps: a fast surface reaction and a slow diffusion-controlled process. Microscopic observations indicated that all the crystals changed their surface morphology whereby some of the initial CH_4 hydrate crystals grew or maintained while at the same time other crystals decreased in sizes and even disappeared over time. This was the first time that a second transformation behavior was documented. The results were fitted to the existing models for further discussion. This experiment was followed by two structural transition processes from sII mixed gas hydrates to sI CO_2-rich hydrates and from sI CH_4 hydrates to sII mixed gas hydrates (*Chapter 5.2 and 5.3*, preparing for publication). Regarding the driving force of the structural transition, the results showed that it was the chemical potential difference between the coexisting hydrate phase and the surrounding gas phase that induced the transformation. The highlight of these two experiments was to visualize and characterize the different stages of transition for hydrate crystals during the structural transformation process.

In conclusion, this study presented systematic experimental simulations of the formation, dissociation and transformation process of mixed gas hydrates on a μm-scale based on natural reservoir conditions. The thesis aims to provide fundamental knowledge and new insights on sII mixed gas hydrates which might be crucial for the risk prediction and efficiency assessment in future gas production in natural reservoirs.

Supporting Information

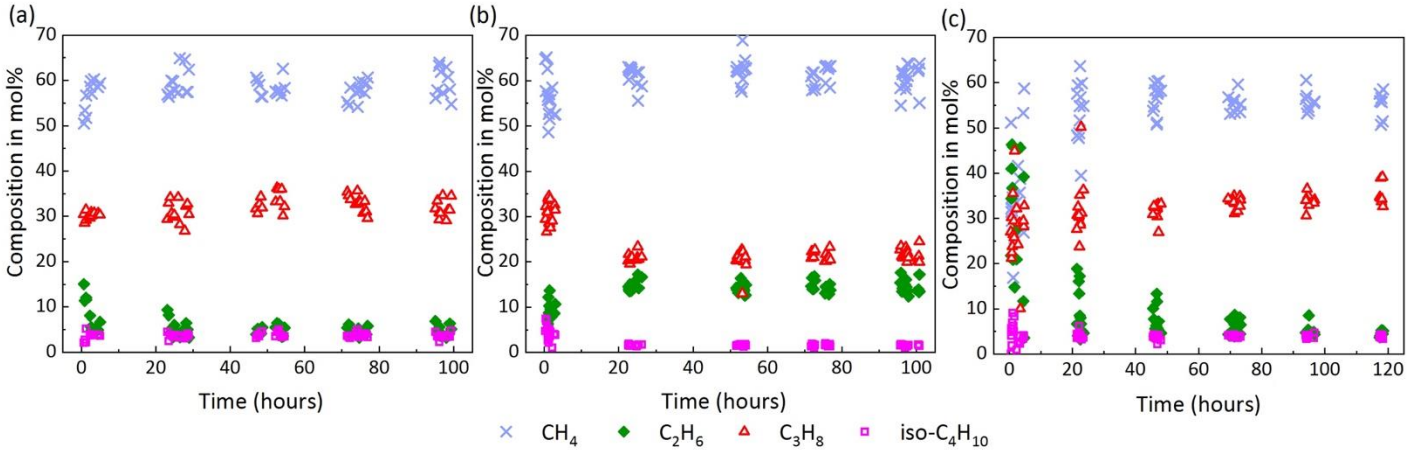

Figure S1 Composition changes measured on the surface of mixed hydrate crystals during a repeated test in the open system (Figure S1a), the closed system (Figure S1b), and the semi-closed system (Figure S1c).

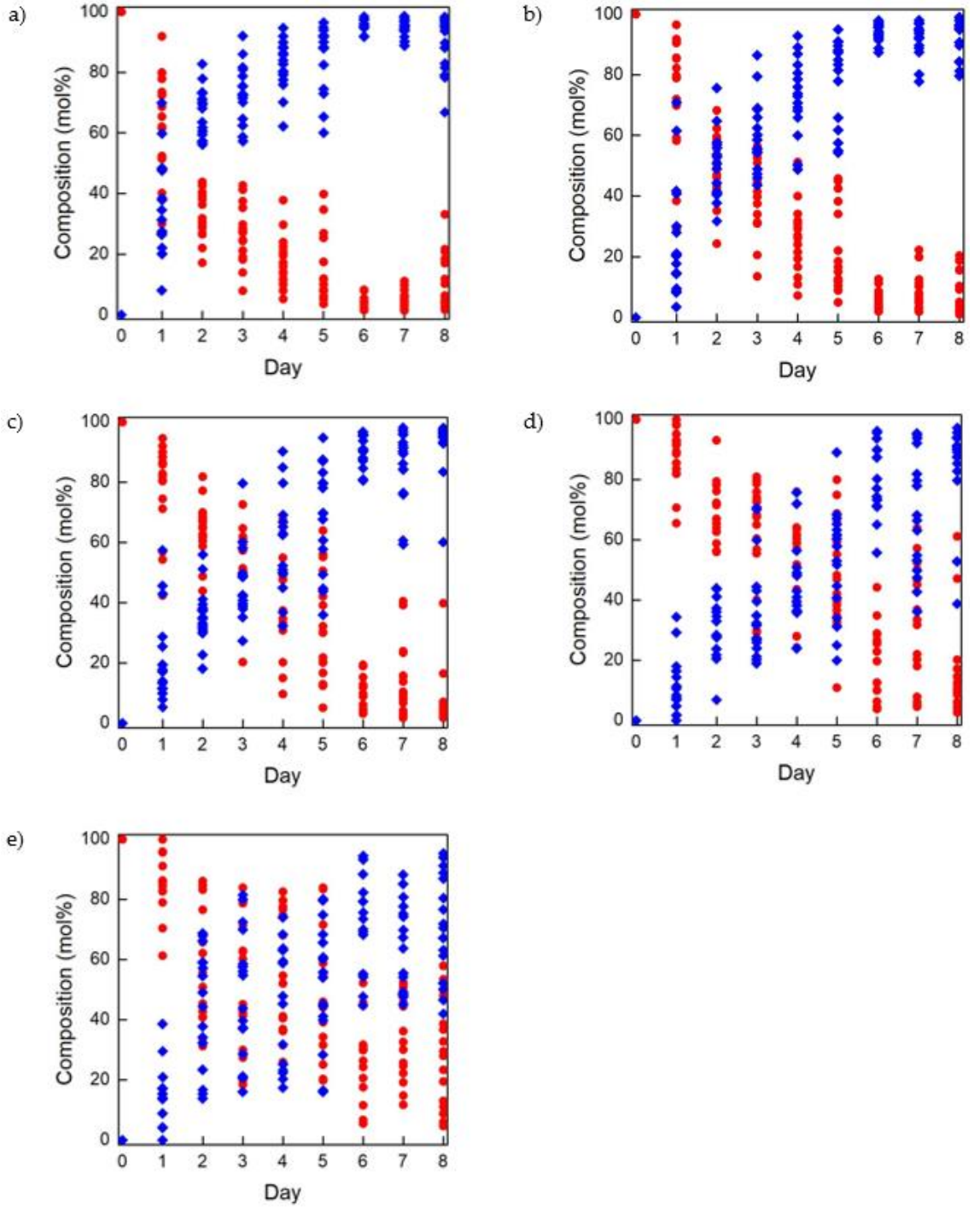

Figure S2 Composition of the selected hydrate crystals as a function of time at penetration depths of (a) surface, (b) 15 μm, (c) 30 μm, (d) 60μm, and (e) 90 μm, after the exchange from CH_4 gas to CO_2 gas. Full circle symbol (●) is for CH_4 in hydrate phase, and full diamond symbol (♦) represents CO_2 in hydrate phase.

References

1. Davy, H. VIII. On a combination of oxymuriatic gas and oxygene gas. *Philos. Trans. R. Soc. London* **1811**, *101*, 155–162.
2. Hammerschmidt, E.G. Formation of Gas Hydrates in Natural Gas Transmission Lines. *Ind. Eng. Chem.* **1934**, *26*, 851–855.
3. Makogon, Y.F. Hydrate formation in the gas-bearing beds under permafrost conditions. *Gazov. Promyshlennost* **1965**, *5*, 14–15.
4. von Stackelberg, M. Feste Gashydrate. *Naturwissenschaften* **1949**, *36*, 327–333.
5. Sloan, E.D.; Koh, C.A. *Clathrate hydrates of natural gases*; 3rd ed.; CRC Press Taylor and Francis Group: Boca Raton, FL, USA, 2008;
6. Jeffrey, G.A. Hydrate inclusion compounds. *J. Incl. Phenom.* **1984**, *1*, 211–222.
7. Chazallon, B.; Focsa, C.; Charlou, J.L.; Bourry, C.; Donval, J.P. A comparative Raman spectroscopic study of natural gas hydrates collected at different geological sites. *Chem. Geol.* **2007**, *244*, 175–185.
8. Tse, J.S.; Powell, B.M.; Sears, V.F.; Handa, Y.P. The lattice dynamics of clathrate hydrates. An incoherent inelastic neutron scattering study. *Chem. Phys. Lett.* **1993**, *215*, 383–387.
9. Jeffrey, G.A.; McMullan, R.K. The Clathrate Hydrates. In *Progress in Inorganic Chemistry*; Albert Cotton, F., Ed.; John Wiley & Sons, Ltd, 1967; pp. 43–190.
10. Ripmeester, J.A.; Tse, J.S.; Ratcliffe, C.I.; Powell, B.M. A New Clathrate Hydrate Structure. *Nature* **1987**, *325*, 135–136.
11. Subramanian, S.; Kini, R.A.; Dec, S.F.; Sloan, E.D. Evidence of structure II hydrate formation from methane plus ethane mixtures. *Chem. Eng. Sci.* **2000**, *55*, 1981–1999.
12. Ismail, N.A. Interfacial and kinetic studies of clathrate hydrates, Colorado School of Mines, 2021.
13. Schrader, D.L.; Connolly Jr, H.C.; Lauretta, D.S.; Nagashima, K.; Huss, G.R.; Davidson, J.; Domanik, K.J. The formation and alteration of the Renazzo-like carbonaceous chondrites II: Linking O-isotope composition and oxidation state of chondrule olivine. *Geochim. Cosmochim. Acta* **2013**, *101*, 302–327.
14. Lederhos, J.P.; Christiansen, R.L.; Sloan, E.D. A first order method of hydrate equilibrium estimation and its use with new structures. *Fluid Phase Equilib.* **1993**, *83*, 445–454.
15. Subramanian, S.; Sloan, E.D. Trends in vibrational frequencies of guests trapped in clathrate hydrate cages. *J. Phys. Chem. B* **2002**, *106*, 4348–4355.
16. Lu, Z.; Zhu, Y.; Zhang, Y.; Wen, H.; Li, Y.; Liu, C. Gas hydrate occurrences in the Qilian Mountain permafrost, Qinghai Province, China. *Cold Reg. Sci. Technol.* **2011**, *66*, 93–104.
17. Davidson, D.W.; Garg, S.K.; Gough, S.R.; Hawkins, R.E.; Ripmeester, J.A. Characterization of natural gas hydrates by nuclear magnetic resonance and dielectric relaxation. *Can. J. Chem.* **1977**, *55*, 3641–3650.
18. Szasz, G.J.; Sheppard, N.; Rank, D.H. Spectroscopic studies of rotational isomerism. I. Liquid n-butane and the assignment of the normal modes of vibration. *J. Chem. Phys.* **1948**, *16*, 704–711.
19. Luzi, M.; Schicks, J.M.; Naumann, R.; Erzinger, J.; Udachin, K.; Moudrakowski, I.; Ripmeester, J.A.; Ludwig, R. Investigations on the Influence of Guest Molecule characteristics and the presence of multicomponent gas mixtures on gas hydrate properties. In Proceedings of

the Proceedings of the 6th International Conference on Gas Hydrates; 6-10 July, Vancouver, British Columbia, Canada, 2008.
20. Kvenvolden, K.A. Gas hydrates - geological perspective and gobal change. *Rev. Geophys.* **1993**, *31*, 173–187.
21. Kvenvolden, K.A.; Lorenson, T.D. The global occurrence of natural gas hydrate. In *Natural Gas Hydrates: Occurrence, Distribution, and Detection*; Paull, C.K., Dillon, W.P., Eds.; American Geophysical Union: Washington D C, 2001.
22. Kvenvolden, K.A. Methane hydrate — A major reservoir of carbon in the shallow geosphere? *Chem. Geol.* **1988**, *71*, 41–51.
23. Beaudoin, Y.C.; Boswell, R.; Dallimore, S.; Waite, W. *Frozen Heat: A UNEP Global Outlook on Methane Gas Hydrates*; United Nations Environment Programme, GRID-Arendal, 2014;
24. Kirschke, S.; Bousquet, P.; Ciais, P.; Saunois, M.; Canadell, J.G.; Dlugokencky, E.J.; Bergamaschi, P.; Bergmann, D.; Blake, D.R.; Bruhwiler, L.; et al. Three decades of global methane sources and sinks. *Nat. Geosci.* 2013, *6*, 813–823.
25. Lorenson, T.D.; Dougherty, J.A.; Flocks, J.G. Hydrocarbon Gases from Giant Piston Cores in the Northern Gulf of Mexico : Results from the IMAGES VIII / PAGE 127 cruise of the RV Marion Dufresne , July 2002. In *Initial reports of the IMAGES VIII/PAGE 127 gas hydrate and paleoclimate cruise on the RV Marion Dufresne in the Gulf of Mexico,2-18 2002*; Winters, W.J., Lorenson, T.D., Paull, C.K., Eds.; 2004; Vol. 1358.
26. Koh, C.A.; Sloan, E.D.; Sum, A.K.; Wu, D.T. Fundamentals and applications of gas hydrates. *Annu. Rev. Chem. Biomol. Eng.* **2011**, *2*, 237–257.
27. Waite, W.F.; Ruppel, C.D.; Boze, L.-G.; Lorenson, T.D.; Buczkowski, B.J.; McMullen, K.Y.; Kvenvolden, K.A. Preliminary global database of known and inferred gas hydrate locations. *U.S. Geol. Surv. data release* **2020**.
28. Trofimuk, A.A.; Cherskiy, N.V.; Tsarev, V.P. Accumulation of natural gases in zones of hydrate formation in the hydrosphere. *Dokl. Akad. Nauk SSSR* **1973**, *212*, 931–934.
29. Hester, K.C.; Brewer, P.G. Clathrate Hydrates in Nature. *Ann. Rev. Mar. Sci.* **2009**, *1*, 303–327.
30. Pang, X.Q.; Chen, Z.H.; Jia, C.Z.; Wang, E.Z.; Shi, H.S.; Wu, Z.Y.; Hu, T.; Liu, K.Y.; Zhao, Z.F.; Pang, B.; et al. Evaluation and re-understanding of the global natural gas hydrate resources. *Pet. Sci.* **2021**, *18*, 323–338.
31. Milkov, A. V. Global estimates of hydrate-bound gas in marine sediments: How much is really out there? *Earth-Science Rev.* **2004**, *66*, 183–197.
32. Solovev, V.A. Global estimation of gas content in submarine gas hydrate accumulations. *Russ. Geol. Geophys.* **2002**, *43*, 609–624.
33. Boswell, R.; Collett, T.S. Current perspectives on gas hydrate resources. *Energy Environ. Sci.* **2011**, *4*, 1206–1215.
34. Dickens, G.R. Down the rabbit hole: Toward appropriate discussion of methane release from gas hydrate systems during the Paleocene-Eocene thermal maximum and other past hyperthermal events. *Clim. Past* **2011**, *7*, 831–846.
35. Klauda, J.B.; Sandler, S.I. Global Distribution of Methane Hydrate in Ocean Sediment. *Energy & Fuels* **2005**, *19*, 459–470.
36. Boswell, R.; Collett, T.S.; Frye, M.; Shedd, W.; McConnell, D.R.; Shelander, D. Subsurface gas hydrates in the northern Gulf of Mexico. *Mar. Pet. Geol.* **2012**, *34*, 4–30.
37. Haeckel, M.; Suess, E.; Wallmann, K.; Rickert, D. Rising methane gas bubbles form massive hydrate layers at the seafloor. *Geochim. Cosmochim. Acta* **2004**, *68*, 4335–4345.

38. Bahk, J.J.; Kim, D.H.; Chun, J.H.; Son, B.K.; Kim, J.H.; Ryu, B.J.; Torres, M.E.; Riedel, M.; Schultheiss, P. Gas hydrate occurrences and their relation to host sediment properties: Results from Second Ulleung Basin Gas Hydrate Drilling Expedition, East Sea. *Mar. Pet. Geol.* **2013**, *47*, 21–29.
39. Dai, S.; Santamarina, J.C.; Waite, W.F.; Kneafsey, T.J. Hydrate morphology: Physical properties of sands with patchy hydrate saturation. *J. Geophys. Res. B Solid Earth* **2012**, *117*, 11205.
40. Lu, H.; Seo, Y.; Lee, J.; Moudrakovski, I.; Ripmeester, J.A.; Chapman, N.R.; Coffin, R.B.; Gardner, G.; Pohlman, J. Complex gas hydrate from the Cascadia margin. *Nature* **2007**, *445*, 303–306.
41. Klapp, S.A.; Murshed, M.M.; Pape, T.; Klein, H.; Bohrmann, G.; Brewer, P.G.; Kuhs, W.F. Mixed gas hydrate structures at the Chapopote Knoll, southern Gulf of Mexico. *Earth Planet. Sci. Lett.* **2010**, *299*, 207–217.
42. Wei, J.; Fang, Y.; Lu, H.; Lu, H.; Lu, J.; Liang, J.; Yang, S. Distribution and characteristics of natural gas hydrates in the Shenhu Sea. *Mar. Pet. Geol.* **2018**, *98*, 622–628.
43. Hachikubo, A.; Khlystov, O.; Manakov, A.; Kida, M.; Krylov, A.; Sakagami, H.; Minami, H.; Takahashi, N.; Shoji, H.; Kalmychkov, G.; et al. Model of formation of double structure gas hydrates in Lake Baikal based on isotopic data. *Geophys. Res. Lett.* **2009**, *36*, 1–5.
44. Uchida, T.; Moriwaki, M.; Takeya, S.; Ikeda, I.Y.; Ohmura, R.; Nagao, J.; Minagawa, H.; Ebinuma, T.; Narita, H.; Gohara, K.; et al. Two-step formation of methane-propane mixed gas hydrates in a batch-type reactor. *AIChE J.* **2004**, *50*, 518–523.
45. Klapp, S.A.; Bohrmann, G.; Kuhs, W.F.; Mangir Murshed, M.; Pape, T.; Klein, H.; Techmer, K.S.; Heeschen, K.U.; Abegg, F. Microstructures of structure I and II gas hydrates from the Gulf of Mexico. *Mar. Pet. Geol.* **2010**, *27*, 116–125.
46. Uchida, T.; Takeya, S.; Kamata, Y.; Ohmura, R.; Narita, H. Spectroscopic measurements on binary , ternary , and quaternary mixed-gas molecules in clathrate structures. *Ind. Eng. Chem. Res.* **2007**, *46*, 5080–5087.
47. Jin, Y.; Kida, M.; Yoneda, J.; Konno, Y.; Oshima, M.; Tenma, N.; Nagao, J. Natural Gas Hydrates Recovered from the Umitaka Spur in the Joetsu Basin, Japan: Coexistence of Two Structure-I Hydrates with Distinctly Different Textures and Gas Compositions within a Massive Structure. *ACS Earth Sp. Chem.* **2019**, *4*, 77–85.
48. Schicks, J.M.; Luzi-Helbing, M. Kinetic and thermodynamic aspects of clathrate hydrate nucleation and growth. *J. Chem. Eng. Data* **2015**, *60*, 269–277.
49. Manakov, A.Y.; Khlystov, O.M.; Hachikubo, A.; Ogienko, A.G. A physicochemical model for the formation of gas hydrates of different structural types in K-2 mud volcano (Kukui Canyon, Lake Baikal). *Russ. Geol. Geophys.* **2013**, *54*, 475–482.
50. Zhu, Y.; Zhang, Y.; Wen, H.; Lu, Z.; Jia, Z.; Li, Y.; Li, Q.; Liu, C.; Wang, P.; Guo, X. Gas Hydrates in the Qilian Mountain Permafrost, Qinghai, Northwest China. *Acta Geol. Sin. Ed.* **2010**, *84*, 1–10.
51. Zhou, Y.W.; Guo, D.X.; Cheng, G.D.; et al. *China Permafrost*; Science Press: Beijing, 2000;
52. Feng, Y. Investigatory summary of the Qilian orogenic belt, China: history, presence and prospect. *Adv. earth Sci.* **1997**, *12*, 307–314.
53. Lu, Z.; Rao, Z.; He, J.; Zhu, Y.; Zhang, Y.; Liu, H.; Wang, T.; Xue, X. Geochemistry of drill core headspace gases and its significance in gas hydrate drilling in Qilian Mountain permafrost. *J. Asian Earth Sci.* **2015**, *98*, 126–140.

54. Fu, J.H.; Zhou, L.F. Carboniferous-Jurassic stratigraphic provinces of the southern Qilian Basin and their petro-geological feature. *Northwest Geosci.* **1998**, *19*, 47–54.
55. Fu, J.H.; Zhou, L.F. Triassic stratigraphic rovinces of the southern Qilian basin and their petro-geological features. *Northwest Geosci.* **2000**, *21*, 64–72.
56. Lu, Z. quan; Tang, S. qi; Luo, X. ling; Zhai, G. yi; Fan, D. wen; Liu, H.; Wang, T.; Zhu, Y. hai; Xiao, R. A natural gas hydrate-oil-gas system in the Qilian Mountain permafrost area, northeast of Qinghai-Tibet Plateau. *China Geol.* **2020**, *3*, 511–523.
57. Zhu, Y.; Wang, P.; Pang, S.; Zhang, S.; Xiao, R. A Review of the Resource and Test Production of Natural Gas Hydrates in China. *Energy & Fuels* **2021**, *35*, 9137–9150.
58. Wang, P.; Zhu, Y.; Lu, Z.; Huang, X.; Pang, S.; Zhang, S.; Jiang, S.; Li, Q.; Yang, K.; Li, B. Geochemistry and genesis of authigenic pyrite from gas hydrate accumulation system in the Qilian Mountain permafrost, Qinghai, northwest China. *Sci. China-Earth Sci.* **2014**, *57*, 2217–2231.
59. Wang, P.; Zhu, Y.; Lu, Z.; Guo, X.; Huang, X. Gas hydrate in the Qilian Mountain permafrost and its distribution characteristics. *Geol. Bull. China* **2011**, *30*, 1839–1850.
60. Wang, P.K.; Zhu, Y.H.; Lu, Z.Q.; Huang, X.; Pang, S.J.; Zhang, S. Gas hydrate stability zone migration occurred in the Qilian mountain permafrost, Qinghai, Northwest China: Evidences from pyrite morphology and pyrite sulfur isotope. *Cold Reg. Sci. Technol.* **2014**, *98*, 8–17.
61. Lu, Z.; Zhu, Y.; Liu, H.; Zhang, Y.; Jin, C.; Huang, X.; Wang, P. Gas source for gas hydrate and its significance in the Qilian Mountain permafrost, Qinghai. *Mar. Pet. Geol.* **2013**, *43*, 341–348.
62. Huang, X.; Zhu, Y.; Wang, P.; Guo, X. Hydrocarbon gas composition and origin of core gas from the gas hydrate reservoir in Qilian Mountain permafrost. *Geol. Bull. China* **2011**, *30*, 1851–1856.
63. Cheng, B.; Xu, J.; Lu, Z.; Li, Y.; Wang, W.; Yang, S.; Liu, H.; Wang, T.; Liao, Z. Hydrocarbon source for oil and gas indication associated with gas hydrate and its significance in the Qilian Mountain permafrost, Qinghai, Northwest China. *Mar. Pet. Geol.* **2018**, *89*, 202–215.
64. Lu, Z.; Zhai, G.; Zhu, Y.; Zhang, Y.; Li, Y.; Wang, W.; Wang, T.; Liu, H.; Tang, S.; Tan, P. Fault control of gas hydrate accumulation in Qilian Mountain Permafrost. *Int. J. Offshore Polar Eng.* **2016**, *26*, 199–205.
65. Wang, A.; Li, J.; Wei, Y.; Yang, C.; Nie, J.; Cao, D. Gas migration for terrestrial gas hydrates in the Juhugeng mining area of Muli basin, Qilian Mountains, Northwest China. *Energy Explor. Exploit.* **2020**, *38*, 989–1013.
66. Zhao, J.F.; Zhu, Z.H.; Song, Y.C.; Liu, W.G.; Zhang, Y.; Wang, D.Y. Analyzing the process of gas production for natural gas hydrate using depressurization. *Appl. Energy* **2015**, *142*, 125–134.
67. Zhai, G.Y.; Lu, Z.Q.; Lu, H.L.; Zhu, Y.H.; Yu, C.Q.; Chen, J.W. Gas Hydrate Geological System in the Qilian Mountain Permafrost. *Mineral. Petrol.* **2014**, *34*, 79–92.
68. Liu, C.; Meng, Q.; He, X.; Li, C.; Ye, Y.; Lu, Z.; Zhu, Y.; Li, Y.; Liang, J. Comparison of the characteristics for natural gas hydrate recovered from marine and terrestrial areas in China. *J. Geochemical Explor.* **2015**, *152*, 67–74.
69. Xia, N.; Liu, C.; Ye, Y.; Meng, Q.; Lin, X.; He, X. Study on determination method of natural gas hydrates by Micro-Laser Raman Spectroscopy. *Rock Miner. Anal.* **2011**, *30*, 416–422.
70. Rydzy, M.B.; Schicks, J.M.; Naumann, R.; Erzinger, J. Dissociation enthalpies of synthesized multicomponent gas hydrates with respect to the guest composition and cage occupancy. *J. Phys. Chem. B* **2007**, *111*, 9539–

9545.
71. Schicks, J.M.; Luzi-Helbing, M. Cage occupancy and structural changes during hydrate formation from initial stages to resulting hydrate phase. *Spectrochim. Acta Part A Mol. Biomol. Spectrosc.* **2013**, *115*, 528–536.
72. Heeschen, K.U.; Abendroth, S.; Priegnitz, M.; Spangenberg, E.; Thaler, J.; Schicks, J.M. Gas Production from Methane Hydrate: A Laboratory Simulation of the Multistage Depressurization Test in Mallik, Northwest Territories, Canada. *Energy & Fuels* **2016**, *30*, 6210–6219.
73. Clennell, M.B.; Hovland, M.; Booth, J.S.; Henry, P.; Winters, W.J. Formation of natural gas hydrates in marine sediments 1. Conceptual model of gas hydrate growth conditioned by host sediment properties. *J. Geophys. Res. Earth* **1999**, *104*, 22985–23003.
74. Cha, S.B.; Oaur, H.; Wildman, T.R.; Sloan, E.D. A third-surface effect on hydrate formation. *J. Phys. Chem.* **1988**, *92*, 6492–6494.
75. Lu, Z.Q.; Zhu, Y.H.; Zhang, Y.Q.; Wen, H.J.; Li, Y.H.; Wang, P.K. Estimation method of gas hydrate resources in the Qilian Mountain permafrost area, Qinghai, China— A case of the drilling area. *Geol. Bull. China* **2010**, *29*, 1310–1318.
76. Moridis, G.J.; Collett, T.S.; Boswell, R.; kurihara, M.; reagan, M.T.; Koh, C.A.; Sloan, E.D. Toward production from gas hydrates: current status, assessment of resources, and simulation-based evaluation of technology and potential. *SPE Reserv. Eval. Eng.* **2009**, *12*, 745–771.
77. Moridis, G.J.; Kowalsky, M.B.; Pruess, K.; Lawrence Berkeley Nat, L. Depressurization-Induced Gas Production From Class 1 Hydrate Deposits. *Soc. Pet. Eng.* **2007**, *10*, 458–481.
78. Bonnefoy, O.; Gruy, F.; Herri, J.M. Van der Waals interactions in systems involving gas hydrates. *Fluid Phase Equilib.* **2005**, *231*, 176–187.
79. Koh, D.-Y.; Kang, H.; Lee, J.-W.J.J.Y.; Park, Y.; Kim, S.-J.; Lee, J.-W.J.J.Y.; Lee, J.-W.J.J.Y.; Lee, H. Energy-efficient natural gas hydrate production using gas exchange. *Appl. Energy* **2016**, *162*, 114–130.
80. Li, S.; Zheng, R.; Xu, X.; Chen, Y. Dissociation of Methane Hydrate by Hot Brine. *Pet. Sci. Technol.* **2015**, *33*, 671–677.
81. Schicks, J.M.; Spangenberg, E.; Giese, R.; Luzi-Helbing, M.; Priegnitz, M.; Beeskow-Strauch, B. A counter-current heat-exchange reactor for the thermal stimulation of hydrate-bearing sediments. *Energies* **2013**, *6*, 3002–3016.
82. Wang, D.Y.; Ma, X.J.; Qiao, J. Impact Factors of Natural Gas Hydrate Dissociation by Depressurization: A review. *Explor. Process. Miner. Resour.* **2014**, *868*, 564–567.
83. Gunn, D.A.; Nelder, L.M.; Rochelle, C.A.; Bateman, K.; Jackson, P.D.; Lovell, M.A.; Hobbs, P.R.N.; Long, D.; Rees, J.G.; Schultheiss, P.; et al. Towards improved ground models for slope instability evaluations through better characterization of sediment-hosted gas-hydrates. *Terra Nov.* **2002**, *14*, 443–451.
84. Ersland, G.; Husebø, J.; Graue, A.; Kvamme, B. Transport and storage of CO2 in natural gas hydrate reservoirs. *Energy Procedia* **2009**, *1*, 3477–3484.
85. Everett, S.M.; Rawn, C.J.; Chakoumakos, B.C.; Keffer, D.J.; Huq, A.; Phelps, T.J. Insights into the structure of mixed CO2/CH4 in gas hydrates. *Am. Mineral.* **2015**, *100*, 1203–1208.
86. Park, Y.; Kim, D.-Y.; Lee, J.J.-W.J.; Huh, D.-G.; Park, K.-P.; Lee, J.J.-W.J.; Lee, H. Sequestering carbon dioxide into complex structures of naturally occurring gas hydrates. *Proc. Natl. Acad. Sci.* **2006**, *103*, 12690–12694.
87. Khlebnikov, V.N.; Antonov, S.V.; Mishin, A.S.; Bakulin, D.A.; Khamidullina, I.V.; Liang, M.; Vinokurov, V.A.; Gushchin, P.A. A new

method for the replacement of CH4 with CO2 in natural gas hydrate production. *Nat. Gas Ind. B* **2016**, *3*, 445–451.
88. Hancock, S.; Collett, T.S.; Dallimore, S.; Satoh, A.; Inoue, T.; Huenges, E.; Al., E. Overview of thermal-stimulation production-test results for the JAPEX/JNOC/GSC etc. Mallik 5L-38 gas hydrate production research well. In *Scientific Results from the Mallik 2002 Gas Hydrate Production Research Well Program, Mackenzie Delta, Northwest Territories, Canada*; Dallimore, S.R., Collett, T.S., Eds.; Geological Survey of Canada, 2005; Vol. 585, p. 15.
89. Hunter, R.B.; Collett, T.S.; Boswell, R.; Anderson, B.J.; Digert, S.A.; Pospisil, G.; Baker, R.; Weeks, M. Mount Elbert Gas Hydrate Stratigraphic Test Well, Alaska North Slope: Overview of scientific and technical program. *Mar. Pet. Geol.* **2011**, *28*, 295–310.
90. Collett, T.S.; Bahk, J.J.; Frye, M.; Goldberg, D.S.; Husebo, J.; Koh, C.A.; al., et; Leadership, C. for O. *Historical methane hydrate project review .*; Washington D.C., 2013;
91. Kurihara, M.; Sato, A.; Funatsu, K.; Ouchi, H.; Yamamoto, K.; Numasawa, M.; Ebinuma, T.; Narita, H.; Masuda, Y.; Dallimore, S.R.; et al. Analysis of production data for 2007/2008 mallik gas hydrate production tests in Canada. In Proceedings of the International oil and gas conference and exhibition in China; Society of petroleum engineers: Beijing, China, 2010; pp. 2908–2931.
92. Zhang, Y.Q.; Li, X.Y.M.Y.M.; Li, X.Y.M.Y.M.; Wang, Z.G. Technical Process of Gas Hydrate Production in Permafrost and Research on Oceanic Gas Hydrate Production. *Explor. Eng. (Rock Soil Drill. Tunneling)* **2016**, *43*, 154–159.
93. Boswell, R.; Schoderbek, D.; Collett, T.S.; Ohtsuki, S.; White, M.; Anderson, B.J. The Iġnik Sikumi field experiment, Alaska North Slope: Design, operations, and implications for CO2-CH4 exchange in gas hydrate reservoirs. *Energy and Fuels* **2017**, *31*, 140–153.
94. Zhu, Y.H. Land field gas hydrate resources exploration and trial production obtains a series of achievements. *News Lett. China Geol. Surv.* **2017**, *3*, 1–5.
95. Yamamoto, K.; Terao, Y.; Fujii, T.; Ikawa, T.; Seki, M.; Matsuzawa, M.; Kanno, T. Operational overview of the first offshore production test of methane hydrates in the Eastern Nankai Trough. In Proceedings of the Offshore Technology Conference; Houston, Texas, USA, 2014; pp. 1–15.
96. Li, J.; Ye, J.; Qin, X.; Qiu, H.; Wu, N.; Lu, H.; Xie, W.; Lu, J.; Peng, F.; Xu, Z.; et al. The first offshore natural gas hydrate production test in South China Sea. *China Geol.* **2018**, *1*, 5–16.
97. Ruppel, C.D.; Kessler, J.D. The interaction of climate change and methane hydrates. *Rev. Geophys.* **2017**, *55*, 126–168.
98. Intergovernmental Panel on Climate Change (IPCC) *Climate Change 2013: The Physical Science Basis. Contribution of Working Group I to the Fifth Assessment Report of the Intergovernmental Panel on Climate Change*; Cambridge University Press: Cambridge, U.K. and New York, 2013;
99. Dickens, G.R.; Oneil, J.R.; Rea, D.K.; Owen, R.M. Dissociation of Oceanic Methane Hydrate as a Cause of the Carbon Isotope Excursion at the end of the Paleocene. *Paleoceanography* **1995**, *10*, 965–971.
100. Kennett, J.P.; Cannariato, K.G.; Hendy, C.H. *Methane Hydrates in Quaternary Climate Change: The Clathrate Gun Hypothesis*; Washington D C, 2003;
101. Ruppel, C.D. Methane hydrates and contemporary climate change. *Natl. Educ. Knowl.* **2011**, *3*, 1–29.
102. Wang, J.S.; Logan, J.A.; McElroy, M.B.; Duncan, B.N.; Megretskaia, I.A.;

Yantosca, R.M. A 3-D model analysis of the slowdown and interannual variability in the methane growth rate from 1988 to 1997. *Global Biogeochem. Cycles* **2004**, *18*.
103. Fung, I. Three-dimensional model synthesis of the global methane cycle. *J. Geophys. Res.* **1991**, *96*.
104. Lelieveld, J.; Crutzen, P.J.; Dentener, F.J.; Lelieveld1, J.; Crutzen2, P.J.; Dentener1, F.J. Changing concentration, lifetime and climate forcing of atmospheric methane. *Tellus* **2016**, *50*, 128–150.
105. Collett, T.; Bahk, J.J.; Baker, R.; Boswell, R.; Divins, D.; Frye, M.; Goldberg, D.; Husebo, J.; Koh, C.; Malone, M.; et al. Methane Hydrates in Nature-Current Knowledge and Challenges. *J. Chem. Eng. Data* **2015**, *60*, 319–329.
106. de Garidel-Thoron, T.; Beaufort, L.; Bassinot, F.; Henry, P. Evidence for large methane releases to the atmosphere from deep-sea gas-hydrate dissociation during the last glacial episode. *Proc. Natl. Acad. Sci.* **2004**, *101*, 9187–9192.
107. Bock, J.; Martinerie, P.; Witrant, E.; Rôme Chappellaz, J. Atmospheric impacts and ice core imprints of a methane pulse from clathrates. *Earth Planet. Sci. Lett.* **2012**, *349–350*, 98–108.
108. Chuvilin, E.; Davletshina, D.; Ekimova, V.; Bukhanov, B.; Shakhova, N.; Semiletov, I. Role of warming in destabilization of intrapermafrost gas hydrates in the arctic shelf: Experimental modeling. *Geosci.* **2019**.
109. Madhusudhan, B.N.; Clayton, C.R.I.; Priest, J.A. The Effects of Hydrate on the Strength and Stiffness of Some Sands. *J. Geophys. Res. Solid Earth* **2019**, *124*, 65–75.
110. Luzi-Helbing, M.; Naumann, R.; Girod, M.; Schicks, J.M. Dissociation kinetics of CH4 hydrate, mixed CH4+CO2 hydrate and mixed SII hydrates. . *Proc. 9th Int. Conf. Gas Hydrates* 2017.
111. Wu, Q.; Lu, Z.; Liu, Y. Permafrost changes in the Tibetan Plateau. *Adv. Clim. Chang. Res.* **2006**, *2*, 77–80.
112. Luo, J.; Yin, G.; Niu, F.; Lin, Z.; Liu, M. High spatial resolution modeling of climate change impacts on permafrost thermal conditions for the Beiluhe basin, Qinghai-Tibet Plateau. *Remote Sens.* **2019**, *11*, 1294.
113. Wang, Y.; Pan, M.; Mayanna, S.; Schleicher, A.M.; Spangenberg, E.; Schicks, J.M. Reservoir formation damage during hydrate dissociation in sand-clay sediment from Qilian Mountain permafrost, China. *Appl. Energy* **2020**, *263*, 114619.
114. Gibbs, J.W. On the equilibrium of heterogeneous substances. In *Transaction of the Connecticut Academy of Arts and Sciences*; Academy: New Haven; pp. 108–248.
115. Atkins, P.W. *Physikalische Chemie*; 3rd Editio.; Wiley-VCH Verlag GmbH: Weinheim, Germany, 2001;
116. Jhaveri, J.; Robinson, D.B. Hydrates in the methane-nitrogen system. *Can. J. Chem. Eng.* **1965**, *43*, 75–78.
117. Kashchiev, D.; Firoozabadi, A. Driving force for crystallization of gas hydrates. *J. Cryst. Growth* **2002**, *241*, 220–230.
118. Schicks, J.M.; Luzi, M.; Beeskow-Strauch, B. The Conversion Process of Hydrocarbon Hydrates into CO2 Hydrates and Vice Versa: Thermodynamic Considerations. *J. Phys. Chem. A* **2011**, *115*, 13324–13331.
119. Radhakrishnan, R.; Trout, B.L. A new approach for studying nucleation phenomena using molecular simulations: Application to CO2 hydrate clathrates. *J. Chem. Phys.* **2002**, *117*, 1786–1796.
120. Long, J. Gas Hydrate Formation Mechanism and its Kinetic Inhibition, Ph.D. thesis, Colorado School of Mines, 1994.
121. Kvamme, B. A new theorie for kinetics of hydrate formation. In

Proceedings of the Proceedings of the 2nd International Conference on Natural Gas Hydrates.; 2-6 June, Toulouse, France, 1996; pp. 139–146.
122. Beeskow-Strauch, B.; Schicks, J.M.; Spangenberg, E.; Erzinger, J. The influence of SO2 and NO2 impurities on CO2 gas hydrate formation and stability. *Chem. - A Eur. J.* **2011**, *17*, 4376–4384.
123. Sloan, E.D.; Fleyfel, F. A molecular mechanism for gas hydrate nucleation from ice. *AIChE J.* **1991**, *37*, 1281–1292.
124. Christiansen, R.L.; Sloan, E.D. Mechanisms and Kinetics of Hydrate Formation. *Ann. N. Y. Acad. Sci.* **1994**, *715*, 283–305.
125. Ludwig, R. The importance of tetrahedrally coordinated molecules for the explanation of liquid water properties. *ChemPhysChem* **2007**, *8*, 938–943.
126. Walsh, M.R.; Koh, C.A.; Sloan, E.D.; Sum, A.K.; Wu, D.T. Microsecond simulations of spontaneous methane hydrate nucleation and growth. *Science (80-.).* **2009**, *326*, 1095–1098.
127. Jacobson, L.C.; Hujo, W.; Molinero, V. Amorphous precursors in the nucleation of clathrate hydrates. *J. Am. Chem. Soc.* **2010**, *132*, 11806–11811.
128. Jacobson, L.C.; Hujo, W.; Molinero, V. Nucleation pathways of clathrate hydrates: Effect of guest size and solubility. *J. Phys. Chem. B* **2010**, *114*, 13796–13807.
129. Subramanian, S.; Sloan, E.D. Molecular measurements of methane hydrate formation. *Fluid Phase Equilib.* **1999**, *158–160*, 813–820.
130. Igor L. Moudrakovski; Anivis A. Sanchez; Christopher I. Ratcliffe, and; Ripmeester*, J.A. Nucleation and Growth of Hydrates on Ice Surfaces: New Insights from 129Xe NMR Experiments with Hyperpolarized Xenon. *J. Phys. Chem. B* **2001**, *105*, 12338–12347.
131. Hwang, M.J.; Wright, D.A.; Kapur, A.; Holder, G.D. An experimental study of crystallization and crystal growth of methane hydrates from melting ice. *J. Incl. Phenom. Mol. Recognit. Chem.* **1990**, *8*, 103–116.
132. Uchida, T.; Hondoh, T.; Mae, S.; Duval, P.; Lipenkov, V.Y. In-Situ Observations of Growth Process of Clathrate Air-Hydrates Under Hydrostatic Pressure. In *Physics and chemistry of ice*; Norikazu, M., Hondoh, T., Eds.; Hokkaido University Press: Sapporo, Japan, 1992; pp. 121–125.
133. Uchida, T.; Hondoh, T.; Mae, S.; Duval, P.; Lipenkov, V.Y. Effects of temperature and pressure on the transformation rate from air bubbles to air-hydrate crystals in ice sheets. *Ann. Glaciol.* **1994**, *20*, 143–147.
134. Stern, L.A.; Hogenboom, D.L.; Durham, W.B.; Kirby, S.H.; Chou, I.-M. Optical-Cell Evidence for Superheated Ice under Gas-Hydrate-Forming Conditions. *J. Phys. Chem. B* **1998**, *102*, 2627–2632.
135. Kuhs, W.F.; Klapproth, A.; Gotthardt, F.; Techmer, K.; Heinrichs, T. The formation of meso- and macroporous gas hydrates. *Geophys. Res. Lett.* **2000**, *27*, 2929–2932.
136. Henning, R.W.; Schnitz, A.J.; Thieu, V.; Halpern, Y. Neutron diffraction studies of CO2 clathrate hydrate: formation from deuterated ice. *J. Phys. Chem. A* **2000**, *104*, 5066–5071.
137. Jander, W. Reaktionen im festen Zustande bei höheren Temperaturen. Reaktionsgeschwindigkeiten endotherm verlaufender Umsetzungen. *Zeitschrift für Anorg. und Allg. Chemie* **1927**, *163*, 1–30.
138. Fujii, K.; Kondo, W. Kinetics of the Hydration of Tricalcium Silicate. *J. Am. Ceram. Soc.* **1974**, *57*, 492–497.
139. Wang, X.; Schultz, A.J.; Halpern, Y. Kinetics of methane hydrate formation from polycrystalline deuterated ice. *J. Phys. Chem. A* **2002**, *106*, 7304–7309.
140. Levenspiel, O. Chemical reaction engineering. In *Industrial and Engineering Chemistry Research*; Wiley, J., Sons, Eds.; 1999; pp. 4140–4143.
141. Salamatin, A.N.; Kuhs, W.F. Formation of Porous Gas Hydrates. In

Proceedings of the the Fourth International Conference on Gas Hydrates; 2002.
142. Kuhs, W.F.; Hansen, T.C. Time-resolved Neutron Diffraction Studies with Emphasis on Water Ices and Gas Hydrates. *Rev. Mineral. Geochemistry* **2006**, *63*, 171–204.
143. Genov, G.; Kuhs, W.F.; Staykova, D.K.; Goreshnik, E.; Salamatin, A.N. Experimental studies on the formation of porous gas hydrates. *Am. Mineral.* **2004**, *89*, 1228–1239.
144. Genov, G.Y. Physical processes of the CO 2 hydrate formation and decomposition at conditions relevant to Mars, Georg-August-Universität zu Göttingen, 2005.
145. Avrami, M. Kinetics of phase change. I: General theory. *J. Chem. Phys.* **1939**, *7*, 1103–1112.
146. Susilo, R.; Ripmeester, J.A.; Englezos, P. Methane conversion rate into structure H hydrate crystals from ice. *AIChE J.* **2007**, *53*, 2451–2460.
147. Zhao, J.; Zhang, L.; Chen, X.; Fu, Z.; Liu, Y.; Song, Y. Experimental Study of Conditions for Methane Hydrate Productivity by the CO2 Swap Method. *Energy and Fuels* **2015**, *29*, 6887–6895.
148. Schmalzried, H. *Chemical Kinetics of Solids*; VCH: Weinheim, Germany, 1995;
149. Jander, W. Reaktionen im festen Zustande bei höheren Temperaturen. Reaktionsgeschwindigkeiten endotherm verlaufender Umsetzungen. *Zeitschrift für Anorg. und Allg. Chemie* **1927**, *163*, 1–30.
150. Schicks, J.M.; Pan, M.; Giese, R.; Poser, M.; Aminatulmimi, N.I.; Luzi-Helbing, M.; Bleisteiner, B.; Lenz, C. A new high-pressure cell for systematic in situ investigations of micro-scale processes in gas hydrates using confocal micro-Raman spectroscopy. *Rev. Sci. Instrum.* **2020**, *91*, 115103.
151. Sum, A.K.; Burruss, R.C.; Sloan, E.D. Measurement of clathrate hydrates via Raman spectroscopy. *J. Phys. Chem. B* **1997**, *101*, 7371–7377.
152. Tulk, C.A.; Ripmeester, J.A.; Klug, D.D. The Application of Raman Spectroscopy to Chemical Analysis. *Ann. N. Y. Acad. Sci.* **2006**, *912*, 859–872.
153. Schicks, J.M.; Ziemann, M.A.; Lu, H.; Ripmeester, J.A. Raman spectroscopic investigations on natural samples from the Integrated Ocean Drilling Program (IODP) Expedition 311: Indications for heterogeneous compositions in hydrate crystals. *Spectrochim. Acta Part a-Molecular Biomol. Spectrosc.* **2010**, *77*, 973–977.
154. Luzi-Helbing, M.; Prinz, J.; Bald, I.; Schicks, J.M. Investigation of heterogeneously composed Gas Hydrates via Raman Mapping. In Proceedings of the 9th International Conference on Gas Hydrates; Denver, USA, 2017.
155. Huo, Z.; Hester, K.; Sloan, E.D.; Miller, K.T. Methane hydrate nonstoichiometry and phase diagram. *AIChE J.* **2003**, *49*, 1300–1306.
156. Celli, M.; Zoppi, M.; Zaghloul, M.A.S.; Ulivi, L. High pressure optical cell for synthesis and in situ Raman spectroscopy of hydrogen clathrate hydrates. *Rev. Sci. Instrum.* **2012**, *83*, 113101.
157. Joon Shin, H.; Lee, Y.J.; Im, J.H.; Won Han, K.; Lee, J.W.; Lee, Y.; Dong Lee, J.; Jang, W.Y.; Yoon, J.H. Thermodynamic stability, spectroscopic identification and cage occupation of binary CO2 clathrate hydrates. *Chem. Eng. Sci.* **2009**, *64*, 5125–5130.
158. Ruffine, L.; Donval, P.; Charlou, L.; Cremi, A.; Zehnder, H. Experimental study of gas hydrate formation and destabilisation using a novel high-pressure apparatus. **2010**, *27*, 1157–1165.
159. WJ, L.; IM, C.; RC, B.; MZ, Y. In situ study of mass transfer in aqueous solutions under high pressures via Raman spectroscopy: a new method for

the determination of diffusion coefficients of methane in water near hydrate formation conditions. *Appl. Spectrosc.* **2006**, *60*, 122–129.
160. Chou, I.M.; Sharma, A.; Burruss, R.C.; Shu, J.F.; Mao, H.K.; Hemley, R.J.; Goncharov, A.F.; Stern, L.A.; Kirby, S.H. Transformations in methane hydrates. *Proc. Natl. Acad. Sci. U. S. A.* **2000**, *97*, 13484–13487.
161. Hirai, H.; Takahara, N.; Kawamura, T.; Yamamoto, Y.; Yagi, T. Structural changes and preferential cage occupancy of ethane hydrate and methane-ethane mixed gas hydrate under very high pressure. *J. Chem. Phys.* **2008**, *129*, 224503.
162. Wang, Z.; He, D.; Zhang, W.; Li, W.; Li, W.; Qin, J.; Lei, L.; Zou, Y.; Yang, X. Portable high pressure sapphire anvil cell for gas hydrates research. *Rev. Sci. Instrum.* **2010**, *81*, 085102.
163. Kumar, R.; Linga, P.; Moudrakovski, I.; Ripmeester, J.A.; Englezos, P. Structure and kinetics of gas hydrates from methane/ethane/propane mixtures relevant to the design of natural gas hydrate storage and transport facilities. *AIChE J.* **2008**, *54*, 2132–2144.
164. Kumar, D.; Dash, R.; Dewangan, P. Methods of gas hydrate concentration estimation with field examples. *Geohorizons* **2009**, *78*, 76–86.
165. Schicks, J.M.; Naumann, R.; Erzinger, J.; Hester, K.C.; Koh, C.A.; Sloan, E.D. Phase transitions in mixed gas hydrates: experimental observations versus calculated data. *J. Phys. Chem. B* **2006**, *110*, 11468–11474.
166. Spangenberg, E.; Seyberth, K.; Heeschen, K.U.; Priegnitz, M.; Schicks, J.M. A Quick Look Method to Assess the Dependencies of Rock Physical Sediment Properties on the Saturation With Pore-Filling Hydrate. *J. Geophys. Res. Earth* **2018**, *123*, 5588–5598.
167. Washburn, E.W. The Dynamics of Capillary Flow. *Phys. Rev.* **1921**, *17*, 273.
168. Adolphs, J.; Setzer, M.J.; Heine, P. Changes in pore structure and mercury contact angle of hardened cement paste depending on relative humidity. *Mater. Struct. Constr.* **2002**, *35*, 477–486.
169. Bergmann, J.; Friedel, P.; Kleeberg, R. BGMN — a new fundamental parameters based Rietveld program for laboratory X-ray sources, its use in quantitative analysis and structure investigations. *Comm. Powder Diffraction, Int. Union Crystallogr. CPD Newsl.* **1998**, *20*, 5–8.
170. Wedler, G.; Freund, H.-J. *Lehrbuch der Physikalischen Chemie*; 6th ed.; Wiley-VCH Verlag GmbH & Co. KGaA: Weinheim, Germany, 2012;
171. Burke, E.A.J. Raman microspectrometry of fluid inclusions. *Lithos* **2001**, *55*, 139–158.
172. Schrader, B. *Infrared and Raman Spectroscopy: Methods and Applications*; VCH Verlagsgesellschaft mbH: Weinheim, Germany, 1995;
173. Schrötter, H.W.; Klöckner, H.W. Raman scattering cross sections in gases and liquids. In *Raman Spectroscopy of Gases and Liquids. Topics in Current Physics, vol 11*; Weber, A., Ed.; Springer Berlin Heidelberg, 1979; pp. 123–166.
174. Qin, J.; Kuhs, W.F. Quantitative analysis of gas hydrates using Raman spectroscopy. *AIChE J.* **2013**, *59*, 2155–2167.
175. Kiefer, J.; Seeger, T.; Steuer, S.; Schorsch, S.; Weikl, M.C.; Leipertz, A. Design and characterization of a Raman-scattering-based sensor system for temporally resolved gas analysis and its application in a gas turbine power plant. *Meas. Sci. Technol.* **2008**.
176. Pan, M.; Schicks, J.M. Influences of gas supply changes on the formation process of complex mixed gas hydrates. *Molecules* **2021**, *26*, 3039.
177. Pan, M.; Schicks, J.M. *Raman spectroscopic data from gas hydrates formed from a complex gas mixture with different gas supply conditions*; GFZ Data Services, 2021;

178. Uchida, T.; Takeya, S.; Kamata, Y.; Ikeda, I.Y.; Nagao, J.; Ebinuma, T.; Narita, H.; Zatsepina, O.; Buffett, B.A. Spectroscopic observations and thermodynamic calculations on clathrate hydrates of mixed gas containing methane and ethane: Determination of structure, composition and cage occupancy. *J. Phys. Chem. B* **2002**, *106*, 12426–12431.
179. Subramanian, S.; Kini, R.A.; Dec, S.F.; Sloan, E.D. Structural transition studies in methane + ethane hydrates using Raman and NMR. *Ann. N. Y. Acad. Sci.* **2000**, *912*, 873–886.
180. Walrafen, G.E.; Yang, W.H.; Chu, Y.C. Raman evidence for the clathratelike structure of highly supercooled water. *ACS Symp. Ser.* **1997**, *676*, 287–308.
181. Schicks, J.M. Der Einfluss molekularer Eigenschaften von Gasen auf die Hydratbildungsprozesse, die thermodynamischen Eigenschaften und die Reaktionen von einfachen und gemischten Gashydraten, Habilitation thesis, 2013.
182. Chaouachi, M.; Neher, S.H.; Falenty, A.; Kuhs, W.F. Time Resolved Coarsening of Clathrate Crystals: The Case of Gas Hydrates. *Cryst. Growth Des.* **2017**, *17*, 2458–2472.
183. Chen, X.; Espinoza, D.N. Ostwald ripening changes the pore habit and spatial variability of clathrate hydrate. *Fuel* **2018**, *214*, 614–622.
184. Collett, T.S.; Johnson, A.H.; Knapp, C.C.; Boswell, R. Natural gas hydrates: a review. In *Natural Gas Hydrates - Energy Resource Potential and Associated Geologic Hazards.*; Boswell, R.M., Knapp, C., Johnson, A., Collett, T., Eds.; AAPG Memoir, 2009; pp. 146–219.
185. Heeschen, K.U.; Schicks, J.M.; Oeltzschner, G. The promoting effect of natural sand on methane hydrate formation: Grain sizes and mineral composition. *Fuel* **2016**, *181*, 139–147.
186. Torres, M.E.; Tréhu, A.M.; Cespedes, N.; Kastner, M.; Wortmann, U.G.; Kim, J.H.; Long, P.; Malinverno, A.; Pohlman, J.W.; Riedel, M.; et al. Methane hydrate formation in turbidite sediments of northern Cascadia, IODP Expedition 311. *Earth Planet. Sci. Lett.* **2008**, *271*, 170–180.
187. Winters, W.J.; Dallimore, S.R.; Collett, T.S.; Jenner, K.A.; Katsube, J.T.; Cranston, R.E.; Wright, J.F.; Nixon, F.M.; Uchida, T. Relation between Gas Hydrate and Physical Properties at the Mallik 2L-38 Research Well in the Mackenzie Delta. *Ann. N. Y. Acad. Sci.* **2000**, *912*, 94–100.
188. Østergaard, K.K.; Anderson, R.; Llamedo, M.; Tohidi, B. Hydrate phase equilibria in porous media: effect of pore size and salinity. *Terra Nov.* **2002**, *14*, 307–312.
189. Uchida, T.; Takeya, S.; Chuvilin, E.M.; Ohmura, R.; Nagao, J.; Yakushev, V.S.; Istomin, V.A.; Minagawa, H.; Ebinuma, T.; Narita, H.; et al. Decomposition of methane hydrates in sand, sandstone, clays, and glass beads. *J. Geophys. Res. Solid Earth* **2004**, *109*, 1–12.
190. Kleinberg, R.L.; Flaum, C.; Griffin, D.D.; Brewer, P.G.; Malby, G.E.; Peltzer, E.T.; Yesinowski, J.P. Deep sea NMR: Methane hydrate growth habit in porous media and its relationship to hydraulic permeability, deposit accumulation, and submarine slope stability. *J. Geophys. Res. Solid Earth* **2003**, *108*, 2508.
191. Mizuno, Y.; Hanafusa, N. Studies of surface properties of ice using Nuclear Magnetic Resonance. *J. Phys. Colloq.* **1987**, *48*, 511–517.
192. Zhang, Y.; Li, X. Sen; Chen, Z.Y.; Li, G.; Wang, Y. Effects of particle and pore sizes on the formation behaviors of methane hydrate in porous silica gels. *J. Nat. Gas Sci. Eng.* **2016**, *35*, 1463–1471.
193. Blackwell, V.R. Formation processes of clathrate hydrates of carbon dioxide and methane, California Institute of Technology, Pasadena, California, 1998.

194. Uchida, T.; Ebinuma, T.; Takeya, S.; Nagao, J.; Narita, H. Effects of Pore Sizes on Dissociation Temperatures and Pressures of Methane, Carbon Dioxide, and Propane Hydrates in Porous Media. *J. Phys. Chem. A* **2002**, *106*, 820–826.
195. Lu, H.; Kawasaki, T.; Ukita, T.; Moudrakovski, I.; Fujii, T.; Noguchi, S.; Shimada, T.; Nakamizu, M.; Ripmeester, J.; Ratcliffe, C. Particle size effect on the saturation of methane hydrate in sediments – Constrained from experimental results. *Mar. Pet. Geol.* **2011**, *28*, 1801–1805.
196. Malagar, B.R.C.; Lijith, K.P.; Singh, D.N. Formation & dissociation of methane gas hydrates in sediments: A critical review. *J. Nat. Gas Sci. Eng.* **2019**, *65*, 168–184.
197. Bhawangirkar, D.R.; Nair, V.C.; Prasad, S.K.; Sangwai, J.S. Natural Gas Hydrates in the Krishna-Godavari Basin Sediments under Marine Reservoir Conditions: Thermodynamics and Dissociation Kinetics using Thermal Stimulation. *Energy and Fuels* **2021**, *35*, 8685–8698.
198. Beeskow-Strauch, B.; Schicks, J.M. The Driving Forces of Guest Substitution in Gas Hydrates-A Laser Raman Study on CH4-CO2 Exchange in the Presence of Impurities. *Energies* **2012**, *5*, 420–437.
199. Al-Yaseri, A.; Ali, M.; Ali, M.; Taheri, R.; Wolff-Boenisch, D. Western Australia basalt-CO2-brine wettability at geo-storage conditions. *J. Colloid Interface Sci.* **2021**, *603*, 165–171.
200. Sa, J.H.; Kwak, G.H.; Lee, B.R.; Park, D.H.; Han, K.; Lee, K.H. Hydrophobic amino acids as a new class of kinetic inhibitors for gas hydrate formation. *Sci Rep* **2013**, *3*, 2428.
201. Waite, W.F.; Santamarina, J.C.; Cortes, D.D.; Dugan, B.; Espinoza, D.N.; Germaine, J.; Jang, J.; Jung, J.W.; Kneafsey, T.J.; Shin, H.; et al. Physical properties of hydrate-bearing sediments. *Rev. Geophys.* **2009**, *47*, RG4003.
202. Nimblett, J.; Ruppel, C. Permeability evolution during the formation of gas hydrates in marine sediments. *J. Geophys. Res.* **2003**, *108*, 2420.
203. Delli, M.L.; Grozic, J.L.H. Experimental determination of permeability of porous media in the presence of gas hydrates. *J. Pet. Sci. Eng.* **2014**, *120*, 1–9.
204. Moridis, G.J. Numerical studies of gas production from methane hydrates. In Proceedings of the SPE Gas Technology Symposium; Society of Petroleum Engineers, 2003.
205. Moridis, G.J.; Collett, T.S.; Dallimore, S.R.; Satoh, T.; Hancock, S.; Weatherill, B. Numerical studies of gas production from several CH4 hydrate zones at the Mallik site, Mackenzie Delta, Canada. *J. Pet. Sci. Eng.* **2004**, *43*, 219–238.
206. Song, W.; Kovscek, A.R. Direct visualization of pore-scale fines migration and formation damage during low-salinity waterflooding. *J. Nat. Gas Sci. Eng.* **2016**, *34*, 1276–1283.
207. Hussain, F.; Zeinijahromi, A.; Bedrikovetsky, P.; Badalyan, A.; Carageorgos, T.; Cinar, Y. Enhanced oil recovery through low salinity fines-assisted waterflooding: Laboratory and mathematical modelling. In Proceedings of the Society of Petroleum Engineers - SPE Asia Pacific Oil and Gas Conference and Exhibition, APOGCE 2014 - Changing the Game: Opportunities, Challenges and Solutions; 2014.
208. Zeinijahromi, A.; Al-Jassasi, H.; Begg, S.; Bedrikovetski, P. Improving sweep efficiency of edge-water drive reservoirs using induced formation damage. *J. Pet. Sci. Eng.* **2015**, *130*, 123–129.
209. Krueger, R.F. An overview of formation damage and well productivity in oilfield operations. *J. Pet. Technol.* **1986**, *38*, 131–152.
210. Wilson, M.J.; Wilson, L.; Patey, I. The influence of individual clay minerals on formation damage of reservoir sandstones: a critical review with some

new insights. *Clay Miner.* **2014**, *49*, 147–164.
211. Wilson, L.; Wilson, M.J.; Green, J.; Patey, I. The influence of clay mineralogy on formation damage in North Sea reservoir sandstones: A review with illustrative examples. *Earth-Science Rev.* **2014**, *134*, 70–80.
212. Konno, Y.; Fujii, T.; Sato, A.; Akamine, K.; Naiki, M.; Masuda, Y.; Yamamoto, K.; Nagao, J. Key Findings of the World's First Offshore Methane Hydrate Production Test off the Coast of Japan: Toward Future Commercial Production. *Energy & Fuels* **2017**, *31*, 2607–2616.
213. Katagiri, J.; Konno, Y.; Yoneda, J.; Tenma, N. Pore-scale modeling of flow in particle packs containing grain-coating and pore-filling hydrates: Verification of a Kozeny–Carman-based permeability reduction model. *J. Nat. Gas Sci. Eng.* **2017**, *45*, 537–551.
214. Li, G.; Wu, D.-M.; Li, X.-S.; Lv, Q.-N.; Li, C.; Zhang, Y. Experimental measurement and mathematical model of permeability with methane hydrate in quartz sands. *Appl. Energy* **2017**, *202*, 282–292.
215. Zhao, J.; Fan, Z.; Dong, H.; Yang, Z.; Song, Y. Influence of reservoir permeability on methane hydrate dissociation by depressurization. *Int. J. Heat Mass Transf.* **2016**, *103*, 265–276.
216. Revil, A.; Darot, M.; Pezard, P.A. From surface electrical properties to spontaneous potentials in porous media. *Surv. Geophys.* **1996**, *17*, 331–346.
217. Civan, F. *Reservoir Formation Damage*; Gulf Professional Publishing: USA, 2015;
218. Khilar, K.C.; Fogler, H.S. The Existence of a Critical Salt Concentraion for Particle Release. *J. Colloid Interface Sci.* **1984**, *101*, 215–400.
219. Wu, Z.R.; Li, Y.H.; Sun, X.; Wu, P.; Zheng, J.N. Experimental study on the effect of methane hydrate decomposition on gas phase permeability of clayey sediments. *Appl. Energy* **2018**, *230*, 1304–1310.
220. Truong-Lam, H.S.; Seo, S.D.; Kim, S.; Seo, Y.; Lee, J.D. In Situ Raman Study of the Formation and Dissociation Kinetics of Methane and Methane/Propane Hydrates. *Energy and Fuels* **2020**, *34*, 6288–6297.
221. Sun, Y.H.; Su, K.; Li, S.L.; Carroll, J.J.; Zhu, Y.H. Experimental Investigation into the Dissociation Behavior of CH4-C2H6-C3H8 Hydrates in Sandy Sediments by Depressurization. *Energy & Fuels* **2018**, *32*, 204–213.
222. Gupta, A.; Dec, S.F.; Koh, C.A.; Sloan, E.D. NMR Investigation of Methane Hydrate Dissociation. *J. Phys. Chem. C* **2007**, *111*, 2341–2346.
223. Zhou, X.; Long, Z.; Liang, S.; He, Y.; Yi, L.; Li, D.; Liang, D. In Situ Raman Analysis on the Dissociation Behavior of Mixed CH4-CO2 Hydrates. *Energy and Fuels* **2016**, *30*, 1279–1286.
224. Tang, C.; Zhou, X.; Li, D.; Zhao, X. In situ Raman investigation on mixed CH4 -C3H8 hydrate dissociation in the presence of polyvinylpyrrolidone. *Fuel* **2018**, *214*, 505–511.
225. Ballard, A.L.; Sloan, E.D. Structural transitions in methane+ethane gas hydrates — Part II: modeling beyond incipient conditions. *Chem. Eng. Sci.* **2000**, *55*, 5773–5782.
226. Subramanian, S.; Ballard, A.L.; Kini, R.A.; Dec, S.F.; Sloan, E.D. Structural transitions in methane+ethane gas hydrates - Part I: Upper transition point and applications. *Chem. Eng. Sci.* **2000**, *55*, 5763–5771.
227. Pan, M.; Ismail, N.A.; Luzi-Helbing, M.; Koh, C.A.; Schicks, J.M. New Insights on a μm-Scale into the Transformation Process of CH4 Hydrates to CO2-Rich Mixed Hydrates. *Energies* **2020**, *13*, 5908.
228. Lee, H.; Seo, Y.; Seo, Y.T.; Moudrakovski, I.L.; Ripmeester, J.A. Recovering Methane from Solid Methane Hydrate with Carbon Dioxide. *Angew. Chemie - Int. Ed.* **2003**, *42*, 5048–5051.
229. Hirohama, S.; Shimoyama, Y.; Wakabayashi, A.; Tatsuta, S.; Nishida, N.

Conversion of CH4-hydrate to CO2-hydrate in liquid CO2. *J. Chem. Eng. Japan* **1996**, *29*, 1014–1020.
230. Ota, M.; Morohashi, K.; Abe, Y.; Watanabe, M.; Lee Smith, R.; Inomata, H. Replacement of CH4 in the hydrate by use of liquid CO2. *Energy Convers. Manag.* **2005**, *46*, 1680–1691.
231. Zhou, X.; Fan, S.; Liang, D.; Du, J. Replacement of methane from quartz sand-bearing hydrate with carbon dioxide-in-water emulsion. *Energy and Fuels* **2008**, *22*, 1759–1764.
232. Xiong, L.J.; Li, X.-S.; Zeng, Z.Y.; Li, G.; Chen, Z.Y.; Zhang, Y.; Li, Q.P. Experimental investigation into replacement of CH4 in hydrate in porous sediment with liquid CO2 injection. In Proceedings of the 7th international conference on gas hydrate; Edinburgh, Scotland, United Kingdom, 2011.
233. Deusner, C.; Bigalke, N.; Kossel, E.; Haeckel, M. Methane production from gas hydrate deposits through injection of supercritical CO2. *Energies* **2012**, *5*, 2112–2140.
234. Schicks, J.M.; Strauch, B.; Heeschen, K.U.; Spangenberg, E.; Luzi-Helbing, M. From Microscale (400 μl) to Macroscale (425 L): Experimental Investigations of the CO2/N2-CH4 Exchange in Gas Hydrates Simulating the Iġnik Sikumi Field Trial. *J. Geophys. Res. Solid Earth* **2018**, *123*, 3608–3620.
235. Falenty, A.; Murshed, M.M.; Salamatin, A.N.; Kuhs, W.F. Gas replacement in clathrate hydrates during CO2 injection - Kinetics and micro-structural mechanism. In Proceedings of the Proceedings of the ISOPE Ocean Mining Symposium; Szczecin, Poland, 2013; pp. 109–115.
236. Lee, B.R.; Koh, C.A.; Sum, A.K. Quantitative measurement and mechanisms for CH4 production from hydrates with the injection of liquid CO2. *Phys. Chem. Chem. Phys.* **2014**, *16*, 14922–14927.
237. Murshed, M.M.; Schmidt, B.C.; Kuhs, W.F. Kinetics of methane-ethane gas replacement in clathrate-hydrates studied by time-resolved neutron diffraction and Raman spectroscopy. *J. Phys. Chem. A* **2010**, *114*, 247–255.
238. Ota, M.; Abe, Y.; Watanabe, M.; Smith, R.L.; Inomata, H. Methane recovery from methane hydrate using pressurized CO2. *Fluid Phase Equilib.* **2005**, *228*, 553–559.
239. Kvamme, B.; Graue, A.; Buanes, T.; Kuznetsova, T.; Ersland, G. Storage of CO2 in natural gas hydrate reservoirs and the effect of hydrate as an extra sealing in cold aquifers. *Int. J. Greenh. Gas Control* **2007**, *1*, 236–246.
240. Yoon, J.H.; Kawamura, T.; Yamamoto, Y.; Komai, T. Transformation of methane hydrate to carbon dioxide hydrate: In situ Raman spectroscopic observations. *J. Phys. Chem. A* **2004**, *108*, 5057–5059.
241. Mok, J.; Choi, W.; Seo, Y. Time-dependent observation of a cage-specific guest exchange in sI hydrates for CH4 recovery and CO2 sequestration. *Chem. Eng. J.* **2020**, *4*, 1–10.
242. Falenty, A.; Qin, J.; Salamatin, A.N.; Yang, L.; Kuhs, W.F. Fluid Composition and Kinetics of the in Situ Replacement in CH4–CO2 Hydrate System. *J. Phys. Chem. C* **2016**, *120*, 27159–27172.
243. Zhou, X.; Lin, F.; Liang, D. Multiscale Analysis on CH4-CO2 Swapping Phenomenon Occurred in Hydrates. *J. Phys. Chem. C* **2016**, *120*, 25668–25677.
244. Kang, H.; Koh, D.Y.; Lee, H. Nondestructive natural gas hydrate recovery driven by air and carbon dioxide. *Sci. Rep.* **2014**, *4*, 1–8.
245. Shin, K.; Park, Y.; Cha, M.; Park, K.P.; Huh, D.G.; Lee, J.; Kim, S.J.; Lee, H. Swapping phenomena occurring in deep-sea gas hydrates. *Energy and Fuels* **2008**, *22*, 3160–3163.
246. Cha, M.; Shin, K.; Lee, H.; Moudrakovski, I.L.; Ripmeester, J.A.; Seo, Y. Kinetics of methane hydrate replacement with carbon dioxide and nitrogen

gas mixture using in situ NMR spectroscopy. *Environ. Sci. Technol.* **2015**, *49*, 1964–1971.
247. Salamatin, A.N.; Falenty, A.; Kuhs, W.F. Diffusion Model for Gas Replacement in an Isostructural CH4-CO2 Hydrate System. *J. Phys. Chem. C* **2017**, *121*, 17603–17616.
248. Eaves, J.D.; Loparo, J.J.; Fecko, C.J.; Roberts, S.T.; Tokmakoff, A.; Geissler, P.L. Hydrogen bonds in liquid water are broken only fleetingly. *Proc. Natl. Acad. Sci. U. S. A.* **2005**, *102*, 13019–13022.
249. Pakoulev, A.; Wang, Z.; Dlott, D.D. Vibrational relaxation and spectral evolution following ultrafast OH stretch excitation of water. *Chem. Phys. Lett.* **2003**, *371*, 594–600.
250. Falenty, A.; Qin, J.; Salamatin, A.N.; Yang, L.; Kuhs, W.F. Fluid composition and kinetics of the in situ replacement in CH4-CO2 hydrate system. *J. Phys. Chem. C* **2016**, *120*, 27159–27172.
251. Luzi, M.; Schicks, J.M.; Naumann, R.; Erzinger, J. Systematic kinetic studies on mixed gas hydrates by Raman spectroscopy and powder X-ray diffraction. *J. Chem. Thermodyn.* **2012**, *48*, 28–35.
252. Pradell, T.; Crespo, D.; Clavaguera, N.; Clavaguera-Mora, M.T. Diffusion controlled grain growth in primary crystallization: Avrami exponents revisited. *J. Phys. Condens. Matter* **1998**, *10*, 3833.
253. Kuang, Y.; Feng, Y.; Yang, L.; Song, Y.; Zhao, J. Effects of micro-bubbles on the nucleation and morphology of gas hydrate crystals. *Phys. Chem. Chem. Phys.* **2019**, *21*, 23401–23407.
254. Jung, J.W.; Santamarina, J.C. Hydrate formation and growth in pores. *J. Cryst. Growth* **2012**, *345*, 61–68.
255. Uchida, T.; Kishi, D.; Shiga, T.; Nagayama, M.; Gohara, K. Sintering process observations on gas hydrates under hydrate-stable and self-preservation conditions. *J. Chem. Eng. Data* **2015**, *60*, 284–292.
256. Perez, M. Gibbs-Thomson effects in phase transformations. *Scr. Mater.* **2005**, *52*, 709–712.
257. Lee, Y.; Choi, W.; Shin, K.; Seo, Y. CH4-CO2 replacement occurring in sII natural gas hydrates for CH4 recovery and CO2 sequestration. *Energy Convers. Manag.* **2017**, *150*, 356–364.
258. Zhang, G.B.; Jiang, S.H.; Li, S.L.; Guov, W.; Li, B.; Ma, X.L.; Sun, Y.H. Guest-exchange Behaviors of Different Hydrocarbons with CO2 + N2 Occurring in SII Mixed Hydrates. *KnE Mater. Sci.* **2018**, *4*, 204.
259. Seo, Y.-J.; Park, S.; Kang, H.; Ahn, Y.-H.; Lim, D.; Kim, S.-J.; Lee, J.; Lee, J.Y.; Ahn, T.; Seo, Y.; et al. Isostructural and cage-specific replacement occurring in sII hydrate with external CO 2 /N 2 gas and its implications for natural gas production and CO 2 storage. *Appl. Energy* **2016**, *178*, 579–586.
260. Manakov, A.Y.; Khlystov, O.M.; Hachikubo, A.; Minami, K.; Yamashita, S.; Khabuev, A.; Ogienko, A.G.; Ildyakov, A. V.; Kalmychkov, G. V.; Rodionova, T. V. Structural studies of Lake Baikal natural gas hydrates. *J. Struct. Chem.* **2019**, *60*, 1437–1455.
261. Kida, M.; Khlystov, O.; Zemskaya, T.; Takahashi, N.; Minami, H.; Sakagami, H.; Krylov, A.; Hachikubo, A.; Yamashita, S.; Shoji, H.; et al. Coexistence of structure I and II gas hydrates in Lake Baikal suggesting gas sources from microbial and thermogenic origin. *Geophys. Res. Lett.* **2006**, *33*, L24603.

List of publications

Peer-reviewed articles

- Wang Y, **Pan M.**, Mayanna S, Schleicher AM, Spangenberg E, Schicks J. Reservoir formation damage during hydrate dissociation in sand-clay sediment from Qilian Mountain permafrost, China. Applied Energy 2020, 263, 114619. **(co-first author)**
- Schicks, J., **Pan, M.**, Giese, R., Poser, M., Ismail, N. A., Luzi-Helbing, M., Bleisteiner, B., Lenz, C. A new high-pressure cell for systematic in situ investigations of micro-scale processes in gas hydrates using confocal micro-Raman spectroscopy. Review of Scientific Instruments 2020, 91, 11, 115103. https://doi.org/10.1063/5.0013138.
- **Pan, M.**, Ismail, N. A., Luzi-Helbing, M., Koh, C. A., Schicks, J. New Insights on a μm-Scale into the Transformation Process of CH_4 Hydrates to CO_2-Rich Mixed Hydrates. Energies 2020, 13, 22, 5908. https://doi.org/10.3390/en13225908.
- **Pan, M.**, Schicks, J. Influence of gas supply changes on the formation process of complex mixed gas hydrates. Molecules 2021, 26, 3039. https://doi.org/10.3390/ molecules26103039.

Conferences contributions

- **Pan, M.**, Schicks, J. Experimental simulations of mixed gas hydrates dissociation in response to temperature changes in Qilian Mountain permafrost, China. EGU General Assembly, online 2021.
- **Pan, M.**, Wang, Y., Mayanna, S., Schleicher, A.M., Spangenberg, E., Schicks, J., Li, X.-S. Changes of permeabilities as a result of hydrate dissociation in sand-clay sediment from Qilian Mountain permafrost, China. EGU General Assembly, Vienna, Austria 2019.
- Schicks, J., Luzi-Helbing, M., Strauch (Beeskow-Strauch), B., Heeschen, K., Spangenberg, E., Giese, R., **Pan, M.**, Ismail, N., Priegnitz, M., Deusner, C., Haeckel, M. A clean solution?-The potential and limitations of the CH_4-CO_2 exchange in gas hydrates. AAPG Asia Pacific Region Geosciences Technology Workshop, Auckland, New Zealand 2019.
- **Pan, M.**, Schicks, J. Experimental simulations for the mixed gas hydrate formation process in Qilian Mountain permafrost, China. 36th International Geological Congress, New Delhi, India 2020 (postponed).

- **Pan, M.**, Schicks, J. Towards understanding the formation process of complex mixed gas hydrates in Qilian Mountain permafrost, China. 10th International Conference on Gas Hydrates. Singapore 2020 (Postponed).
- Schicks, J., **Pan, M.**, Ismail, N., Luzi-Helbing, M. New guests in old cavities- The transformation process of CH_4 hydrates to CO_2-rich mixed hydrates. 10th International Conference on Gas Hydrates, Singapore, 2020 (Postponed).
- Schicks, J., **Pan, M.**, Giese R., Poser, M., Ismail, N., Luzi-Helbing, M. A new experimental setup for systematic in situ investigations of molecular processes in gas hydrates using micro Raman spectroscopy. 10th International Conference on Gas Hydrates, Singapore, 2020 (Postponed).
- Ismail, N., **Pan, M.**, Beeskow-Strauch, B., Koh, CA., Schicks, JM. Structural analysis of mixed CO_2/C_2H_6 hydrate system using Raman spectroscopy and powder X-ray diffraction. 10th International Conference on Gas Hydrates, Singapore, 2020 (Postponed)

Data publication

- **Pan, Mengdi**, Schicks, Judith M. (2021): Raman spectroscopic data from gas hydrates formed from a complex gas mixture with different gas supply conditions. GFZ Data Services. https://doi.org/10.5880/GFZ.3.1.2021.0